Stochastic models on residual scales in LES of sprays in diesel-like conditions : spray formation, turbulent dispersion and evaporation of droplets

Surya Kaundinya Oruganti

N° d'order NNT : 2020LYSEC42

THESE de DOCTORAT DE L'UNIVERSITE DE LYON
opérée au sein de l'Ecole centrale de Lyon

Ecole Doctorale MEGA N° 162
Mécanique – Energétique -Génie Civil -Acoustique

Spécialité de doctorat : Mécanique des fluides

Soutenue publiquement le 08/12/2020, par :
V. M. Surya Kaundinya Oruganti

Stochastic models on residual scales in LES of sprays for diesel-like conditions: spray formation, turbulent dispersion and evaporation of droplets

---

Devant le jury composé de :

Cuenot Bénédicte	Project leader (HDR)	CERFACS	Rapporteur
Patrick Jenny	Professor	ETH Zurich	Rapporteur
Noureddine Guerrassi	Chief Engineer (HDR)	BorgWarner	Examinateur
Ricardo Novella	Associate Professor	CMT Motores Termicos - UPV	Présidente
Mikael Gorokhovski	Professor	Ecole Centrale de Lyon	Directeur de thèse

Dedicated to my beloved parents

Shri. V.S. Subrahmanya Sastry Oruganti

&

Smt. Parvathi Oruganti

ACKNOWLEDGEMENTS

This thesis would not have been possible without the financial support of the French National Association for Research and Technology (ANRT) and Volvo Group Trucks Technologies (GTT) under the CIFRE fellowship programme. I would like to thank Guillaume Millet, Chief Engineer at Combustion Department of Volvo GTT, whose sincere efforts resulted in initiating this project in collaboration with Prof. Mikhael Gorokhovski of Laboratoire de Mecanique des Fluides et d'Acoustique (LMFA).

I would like to express my sincere gratitude to my thesis supervisor Prof. Mikhael Gorokhovski without whose ideas, constant encouragement, constructive criticism this thesis would not have reached its present form. I am indebted to him for all his invaluable time spent on enlightening me with his immense knowledge on turbulence, sprays and combustion physics. This thesis is a culmination of his ideas and combined efforts of his previous students Alexis Barge and Remi Zamansky over the past decade. I would like to specifically thank Alexis Barge for sharing his work and also for all the valuable discussions in the initial phase of my thesis. I am also grateful to all the jury members for agreeing to examine the work done during this thesis. I would like to thank Dr. Ricardo Novella for his suggestions and guidance with respect to spray modelling in OpenFOAM and connecting me with the activities of the Engine Combustion Network (ECN) community.

All the computational work in this thesis is carried out on the PSMN cluster of Ecole Normale Superior de Lyon, PMCS2I cluster of Ecole Centrale de Lyon and Volvo internal clusters. A special thanks to all the IT and administrative members both at Volvo and LMFA for their logistical help throughout this thesis. I would also like to express my regards for all those colleagues and friends who helped me during the last three years making my stay in Lyon very memorable.

A special thanks to my college teacher Dr. P.V. Krishnan for being a constant source of inspiration and for kindling in me the spirit for true intellectual pursuit. I am forever indebted to my parents, who sacrificed their lives for helping me pursue my goals. Finally, this journey would not have been a cherishable experience if not for my wife Bhavishya.

CONTENTS

1 INTRODUCTION

1.1 Future of combustion engines – relevance of sprays

Transportation of people and goods across the globe is traditionally driven by combustion of liquid fuels - either through the use of reciprocating internal combustion engines (ICE) for land and marine transport or jet engines for air transport. The high energy density and ease of storage of the liquid fuels have made them the most preferred choice for power generation for these applications. But with increasing concerns over climate change and geo-political reasons pertaining to energy security, various countries across the globe (1) are strongly pushing towards diversification of their transportation fleet through a mix of propulsion technologies ranging from ICE with alternative fuels and advanced combustion modes to fully battery electric vehicles (BEV). In the aftermath of the "*dieselgate*" scandal there has been a strong push for the total replacement of ICE with the "*zero emissions*" BEV. But a complete life-cycle analysis of BEV (2,3) taking into the non-renewable energy sources for electricity generation and toxic wastes from end-of life disposal result in higher emissions than an ICE. Moreover, the limitations on battery size and charging durations of the BEV's especially for long haul commercial transport, make combustion engines the predominant power plant for such applications at least for a foreseeable future. Therefore, it is imperative for scientific and policy making communities to invest resources in further improvement of low cost and more efficient ICE's with lower environmental impact. There are two types of ICE – spark ignition (SI) engines used primarily in passenger cars and the compression ignition (CI) engines used predominantly in commercial transport and marine sectors. Gasoline is used to fuel the

SI engines whereas the diesel is used for CI engines. Conventionally, the CI diesel engines are considered to be "*cleaner*" because of the lower greenhouse gas emissions which is directly related to their higher fuel efficiency compared to their SI engine counterparts. In conventional diesel engines, a high-pressure liquid fuel is injected into a hot compressed air at the top dead center (TDC). The in-cylinder temperatures and mixture equivalence ratios (φ) are controlled by the "*rate of fuel-air mixing*" before combustion is initiated. Given the short ignition delay (ID) of the diesel fuel, a heterogenous mixture with localized pockets of fuel rich and high temperature zones results in formation of *"pollutants"* like NOx and soot particles which are hazardous to public health. As shown in *Figure 1-1(a)* the NOx formation usually occurs at high temperature and low equivalence ratios ($\varphi < 2$), whereas the soot formation occurs at high equivalence ratio and moderate temperatures. Over the past three decades, different in-cylinder combustion control strategies and exhaust after-treatment methods have helped to meet the stringently increasing restrictions on the pollutant emissions as shown in *Figure 1-1(b)*. Usually the exhaust aftertreatment methods end up increasing the fuel-consumption and also the overall cost of the engine.

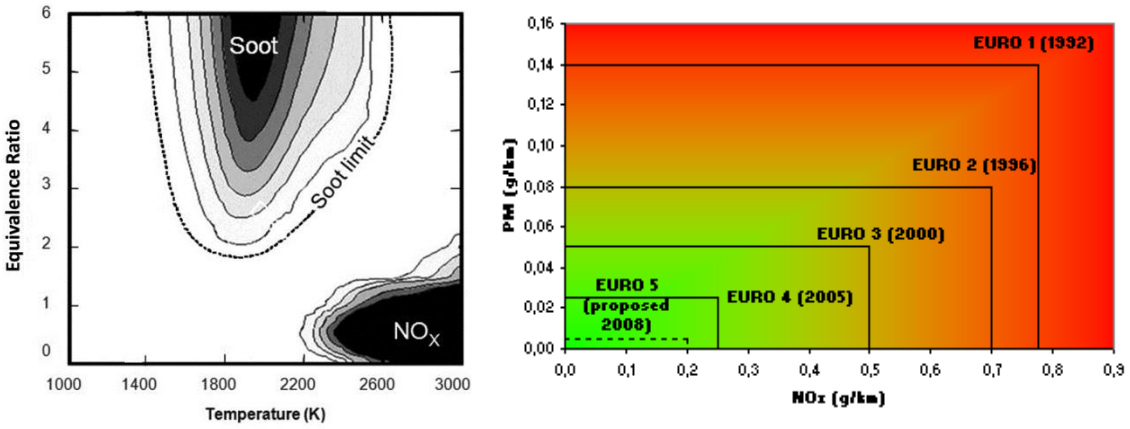

Figure 1-1: (a) φ-Temperature dependence diagram showing the conditions for soot-NOx formation (4) (b) European emission regulations on diesel cars since early 90's (source Wikipedia)

On the other hand, (5) has argued that in the next few decades the fuel demand will be highly skewed towards diesel in-order to meet the future requirements of commercial transport sector, making the gasoline surrogates more readily available. So, there is a growing emphasis (6,7) on co-designing efficient fuel/engine systems with advanced combustion concepts with non-diesel alternatives to directly reduce the in-cylinder emissions. The vast majority of these combustion concepts are classified as *"Low*

temperature combustion (LTC)". The goal is to use gasoline fuel with longer ignition delay in a CI engine, in order to achieve sufficient mixing of the fuel and air in a dilute environment prior to start of combustion. This pre-mixed charge avoids localized pockets of high equivalence ratios, thereby reducing the soot formation. The dilution of the mixture either by adding air or using high exhaust gas re-circulation (EGR) reduces the in-cylinder temperatures, subsequently reducing the NOx formation.

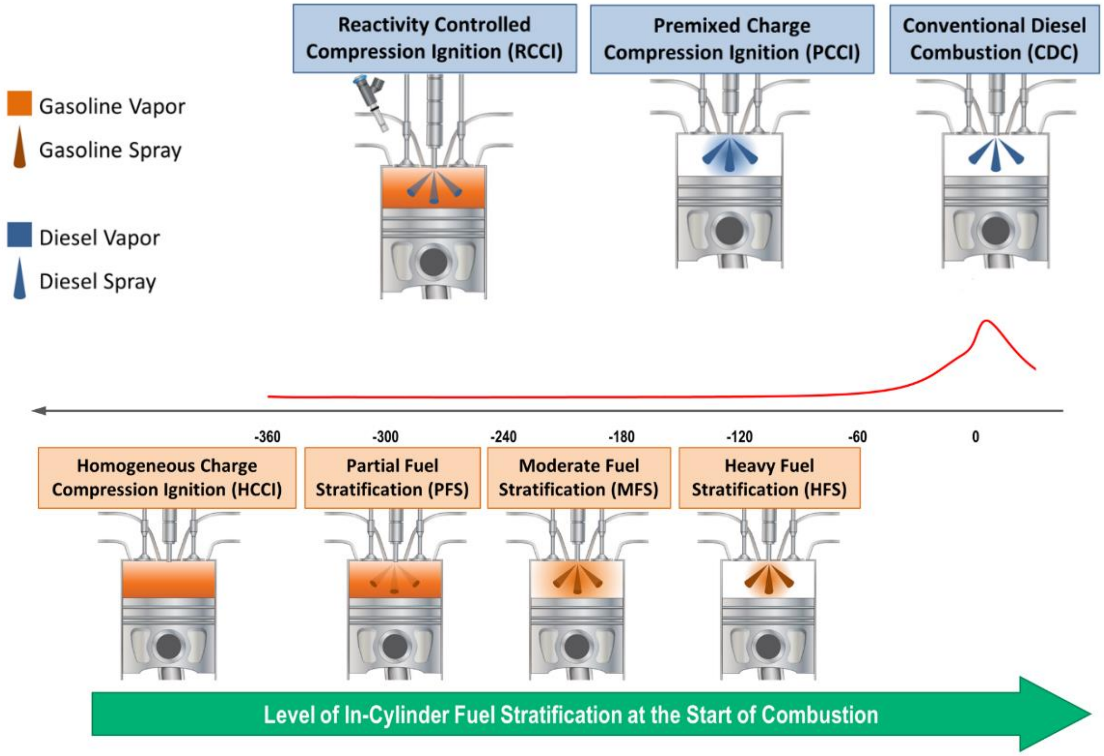

Figure 1-2: Classification of LTC concept based on fuel-stratification strategies controlling the start and duration of fuel injection (8)

The overall efficiency and range of operability of the different LTC concepts is largely dependent on the level of fuel-stratification (8). As shown in *Figure 1-2*, this is realized by injecting the fuel earlier in the compression stroke allowing pre-mixing at lower cylinder temperatures. In either case, i.e. diesel engines or LTC with gasoline, understanding the physical processes controlling fuel-injection and spray development leading up to the formation of fuel-air mixture hold the key to improving their efficiency.

1.2 Experimental studies on spray characterization

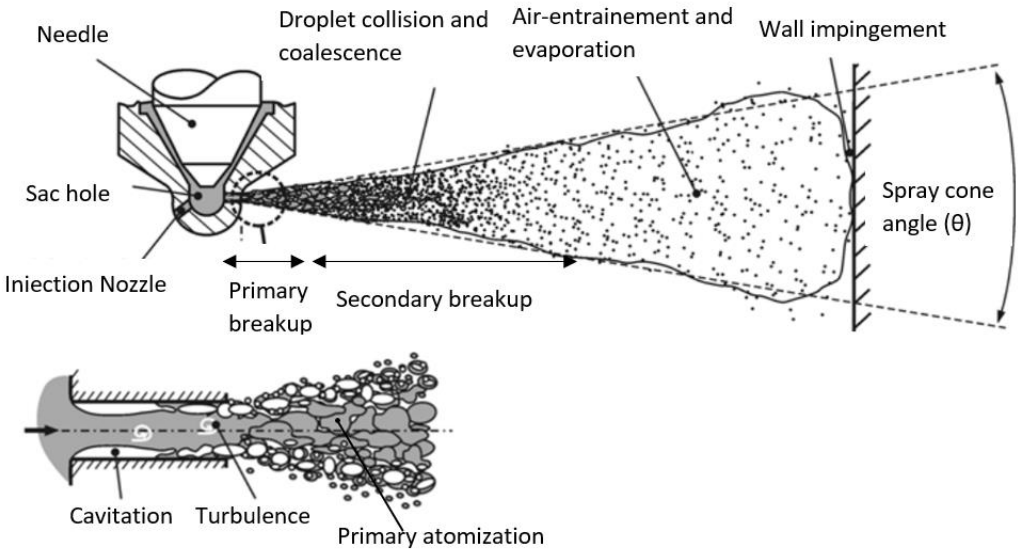

Figure 1-3: Schematic of fuel injection system with different spray sub-processes adapted from (9)

In order to achieve efficient mixing of liquid fuel with the oxidizer on very short time scales (typically few milliseconds or less), the fuel is injected in the form of highly atomized "*sprays"*. A spray is an ensemble of liquid droplets evolving in a surrounding gaseous medium. Each droplet has its own diameter and velocity and may breakup, collide and coalesce with other droplets. The important spray characteristics are the droplet-size distribution, droplet temperature, droplet velocity, number density (i.e. number of particles per unit volume) and their spatial distribution (i.e. local volume fraction). Understanding the spray characteristics either by experiments or numerical modelling has been a very challenging task because of its inherently stochastic nature. The stochastic nature of sprays is attributed to the non-linear interactions between complex physical phenomenon starting from the turbulence and cavitation inside the injector nozzle leading to surface instabilities on the issuing jet, growth of these instabilities resulting in atomization, subsequent secondary breakup, finally heat and mass transfer to surrounding gas resulting in spray vaporization. A schematic of fuel injection and different spray sub-processes are shown in *Figure 1-3*. The most apparent method for characterization of spray dynamics is the experiments. A detailed review of the advances in spray measurement techniques over the years in provided by Fansler & Parrish (10) and the references therein. They classified the experimental studies into the *spray formation region* and *developed spray region*. The spray formation studies are concerned with in-nozzle flow development and subsequent atomization. On the other

hand, the developed spray region studies focus on entrainment of droplets by turbulent gaseous flow and subsequent vaporization. A short review of experimental studies concerning different spray physics is presented in this section.

1.2.1 Spray Atomization

Atomization process is a mechanism to rapidly disintegrate the liquid jet into a large number of small droplets thereby increasing the ratio of surface to mass in the liquid. This enhances the vaporization rate and the efficiency of fuel-air mixing on very short time scales. From a general point of view the atomization process is determined by two phenomena namely, intensity of initial disturbances in the liquid jet and mechanisms responsible for amplifying these disturbances resulting in the formation of liquid fragments. This process of producing liquid fragments from surface instabilities on a liquid jet is often referred to as *"primary breakup"*. Further fragmentation of these primary ligaments into smaller droplets continues repeatedly until the surface tension forces are strong enough to ensure cohesion of these small droplets. This step is referred to as "*secondary breakup"*. The relevance of each of these atomization processes depends on the initial energy of the liquid jet and the ambient gas conditions. Retiz & Bracco (11), have shown that different mechanisms can influence spray atomization. Some of the main mechanisms identified are the aerodynamic shear due to relative velocity between the liquid and gas, viscosity, surface tension, in-nozzle flow turbulence and cavitation. They concluded by sequential elimination of each mechanism that atomization can still occur and no one mechanism is always necessary. The *jet-stability curve* shown in *Figure 1-4* is the most commonly used tool by experimentalists (12,13) to study the relevance of different breakup mechanisms depending on the global characteristics like jet velocity *(U)* and the breakup length (L_{BU}). The breakup length L_{BU} is defined as the length of the continuous jet attached to the nozzle. Four main breakup regimes based on significance of liquid inertia, surface tension, and aerodynamic forces on jet breakup are identified by Reitz & Bracco (11). These have been named as the Rayleigh regime, the first wind-induced regime, the second wind-induced regime, and the atomization regimes. At low injection velocities, breakup process is initiated by *Rayleigh's* capillary instabilities on large wavelength (Λ) disturbances growing on the jet surfaces. As the velocity of the jet increases the aerodynamic shear forces induced by the relative velocity between the liquid jet and the ambient gas increase the growth rate of disturbances, resulting in much faster breakup of the jet i.e. reduction in the breakup length as seen in the region C. This breakup

regime is called as the "*First wind induced regime"*. The droplet sizes are comparable to the jet diameter in the Rayleigh and First wind induced regimes. But as the jet velocities increase further the flow becomes turbulent. Jet breakup is then characterized by growth of short wavelength (Λ) surface waves initiated by turbulence near the nozzle exit and amplified by the aerodynamic forces. This breakup regime is called as the "*Second wind induced regime"*. At very high injection velocities, typical of engine fuel sprays, Lefebvre (14) observed complete disruption of jet right at the nozzle exit producing very droplets much smaller than the jet diameter. This regime is referred to as "*Atomization regime"*.

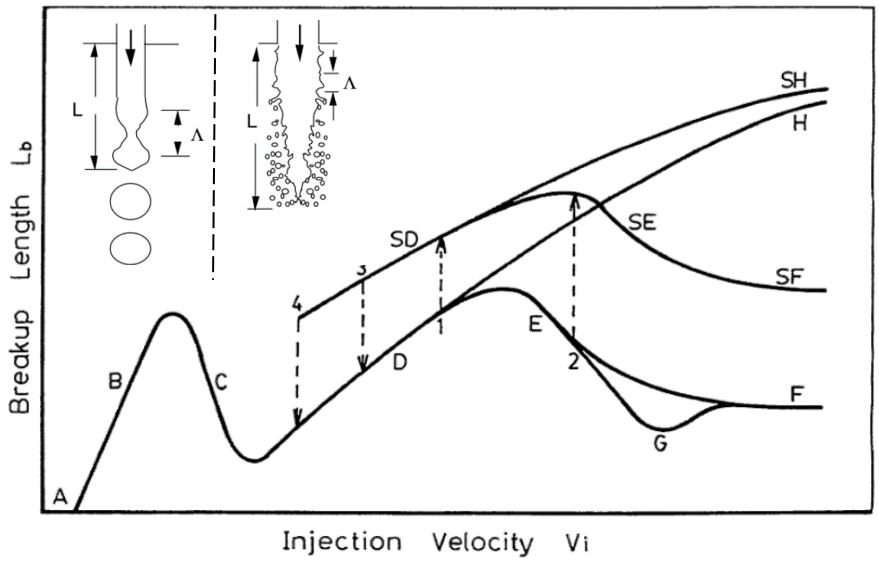

Figure 1-4: Jet stability curve showing different atomization regimes showing influence of different atomization mechanisms. Adapted from (13)

Experimental studies of Wu & Faeth (15-18) have shown that the degree of flow development inside the nozzle and presence of turbulence at nozzle exit characterizes the spray atomization. They systematically tested the influence of turbulence induced breakup from other known breakup mechanisms, such as cavitation through careful design of the injection system. In sufficiently low ambient density environments with liquid/gas density ratios greater than 500, they (16) argued that breakup occurs when the radial turbulent velocity fluctuations inside the jet, are strong enough to overcome the surface tension forces. They also hypothesized that the resulting droplet sizes correlate with the smallest turbulent eddies in the liquid jet responsible for the breakup, which are usually inertial sub-range of the turbulent energy spectrum. On the other hand, in high ambient density environment, they (18) observed that the size of droplets was influenced by aerodynamic effects. They hypothesized that the acceleration of the gas at the liquid

jet interface reduces the local pressure. This reduction in aerodynamic pressure enhances the turbulent kinetic energy of the jet to overcome the surface tension forces. A schematic of aerodynamically enhanced turbulent atomization mechanisms is shown in *Figure 1-5*.

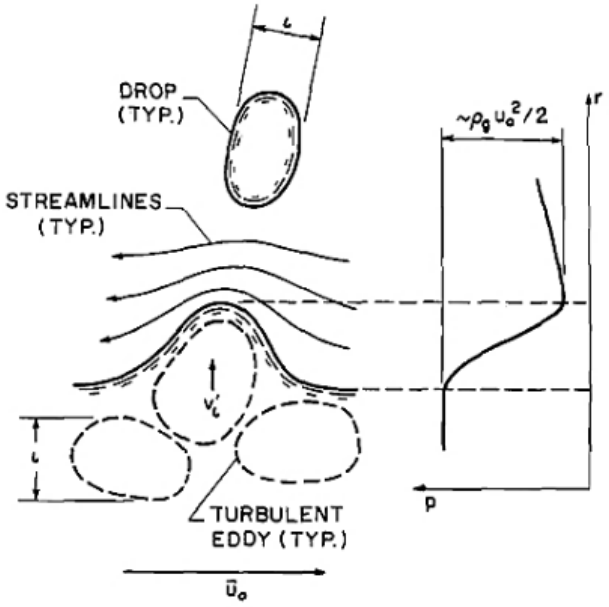

Figure 1-5: Schematic of aerodynamically enhanced turbulent atomization mechanism of Wu and Faeth. The size of the droplets formed scales with the eddy size (L_i) and the fluctuating radial velocity component (v'_L) is responsible for breakup (18).

Hiroyasu et al (19-20) studied the effects of nozzle geometry on the internal flow development and subsequent primary breakup characteristics in atomization regime. They studied two different types of nozzle inlet geometry namely round and sharp. Their studies showed a hysteresis in the jet-stability curve. They attributed the hysteresis development to cavitation inside the nozzle. As shown in *Figure 1-6(a,b)* while no cavitation was found in short nozzles or nozzles with rounded inlets, the nozzles with sharp inlet geometries i.e. *Figure 1-6(c,d)* have shown the presence of cavitation. They argued that cavitation increases the jet turbulence and thereby enhances atomization. Therefore, a jump in breakup length is seen at lower jet velocities in case of cavitating nozzles. Further at sufficiently high velocities, the cavitating flow does not reattach to the nozzle wall, making it turbulent free and the breakup length increases further like in the case of a non-turbulent jets without boundary layers. This regime is referred to as *super-cavitation*. Experimental studies of transparent diesel injectors by Kim et al (21) have shown that level of turbulence in the nozzle is characterized by the needle lift. They have shown that at smaller needle lifts during the needle opening and closing higher turbulence

is generated which results in a wider spray. Similar studies were conducted by Arcoumanis & Gavaises (22) to study cavitation behaviour of multi-hole injectors using transient injector nozzles. They also noticed the presence of string vortices in the sac volume, which seemed to develop transiently and periodically between adjacent holes and then interacted with the cavitation films in the nozzle.

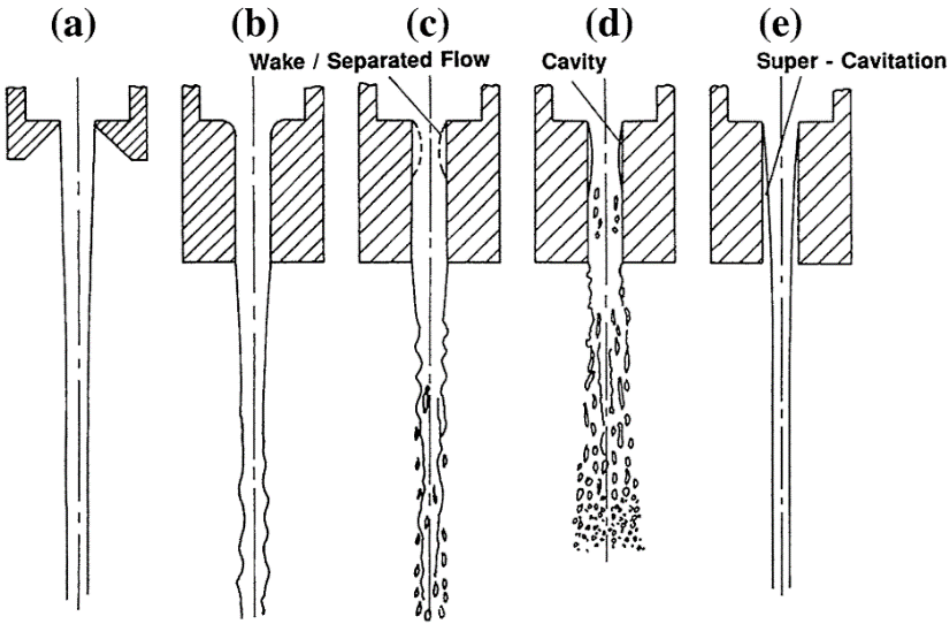

Figure 1-6: Schematic representation of nozzle flow development and its effect on primary breakup. (a) short nozzle (b) rounded inlet (c, d, e) sharp inlet. Adapted from (23)

In a detailed review of experimental studies, Dumouchel (23) argues that though it is widely agreed that the in-nozzle flow has a paramount effect on spray atomization, there are a lot of discrepancies between different experimental studies with respect to main contributing mechanisms and the extent of their influence on atomization. This is mostly attributed to differences in nozzle internal designs and operating conditions. Another most commonly used classification of atomization regimes is on the basis of non-dimensional numbers like:

1. *Liquid and Gas Weber number* (We_l, We_g), which is the ratio of aerodynamic forces and surface tension forces.

$$\mathbf{We_l} = \frac{\rho_l U_{rel}{}^2 r}{\sigma} \quad \textbf{and} \quad \mathbf{We_g} = \frac{\rho_g U_{rel}{}^2 r}{\sigma} \qquad \textbf{1-1}$$

2. *Reynolds number (Re),* which is the ratio of inertial and viscous forces.

$$\mathbf{Re_l} = \frac{U_{rel}\, r}{\nu_l} \qquad \textbf{1-2}$$

3. *Ohnesorge number (Z):* which is a non-dimensional number independent of the jet velocity while considering all important fluid properties.

$$\mathbf{Z} = \frac{\sqrt{\mathbf{We_l}}}{\mathbf{Re_l}} = \frac{\boldsymbol{\nu_l}}{\sqrt{\mathbf{2\sigma\rho_l r}}} \qquad \textbf{1-3}$$

4. *Taylor number (T):* which is a non-dimensional number to characterize the relative importance of liquid/gas density ratio, liquid turbulence and aerodynamic forces on atomization.

$$\mathbf{T} = \frac{\boldsymbol{\rho_l}}{\boldsymbol{\rho_g}} \frac{\mathbf{Re_l^2}}{\mathbf{We_l^2}} \qquad \textbf{1-4}$$

where namely, ρ_l is the liquid density, ρ_g is the ambient gas density, r is the nozzle radius ν_l is the liquid viscosity, σ surface tension and U_{rel} is the relative velocity between liquid and gas phases. Dumouchel (23) summarized the criteria for jet breakup from different experimental works as shown in *Table 1-1*. He has shown that while regimes B and C are associated with Ohnesorge number *(Z)* and gaseous weber number (We_g), the regimes D and E are characterized by Taylor number *(T)* and gaseous weber number We_g.

Disintegration regime	Primary breakup Conditions
Rayleigh breakup	$We_L > 8$ and $We_g < 1.2 + 3.41Z^{0.96}$
First wind induced breakup	$1.2 + 3.41Z^{0.96} < We_g < 13$
Second wind induced breakup	$13 < We_g < 43$
Atomization regime	$We_g > 43$ and $\frac{\rho_l}{\rho_g} > \frac{744}{(\sqrt{A}-1.15)} f(T)^2$ where $f(T) = \frac{\sqrt{3}}{6}(1 - e^{-10T})$

Table 1-1: Criteria of liquid jet disintegration regimes summarized from different experimental studies (23)

Secondary breakup is another important process of dense sprays, through its effect on droplet size distributions as the dilute spray region is approached. Fragmentation of ligaments formed from primary breakup continues until aerodynamic drag has reduced the relative velocity between the droplets and the ambient gas to a level where disruptive forces are no longer large enough to overcome the restorative surface tension forces. Pilch & Erdman (24) and Hsiang & Faeth (25) provided a detailed review of different secondary breakup mechanisms. They characterized the different breakup regimes in terms of the gaseous Weber number (We_g). The conditions for different breakup regimes as

summarized by Guildenbecher (26) in his detailed review of experimental studies on secondary breakup is shown in *Table 1-2*.

Disintegration regime	Breakup Conditions
Vibrational	$0 < We_g < 11$
Bag	$11 < We_g < 35$
Multimode	$35 < We_g < 80$
Sheet thinning	$80 < We_g < 350$
Catastrophic	$We_g > 350$

Table 1-2: Criteria of aerodynamic secondary breakup regimes from different experimental studies as summarized in (26)

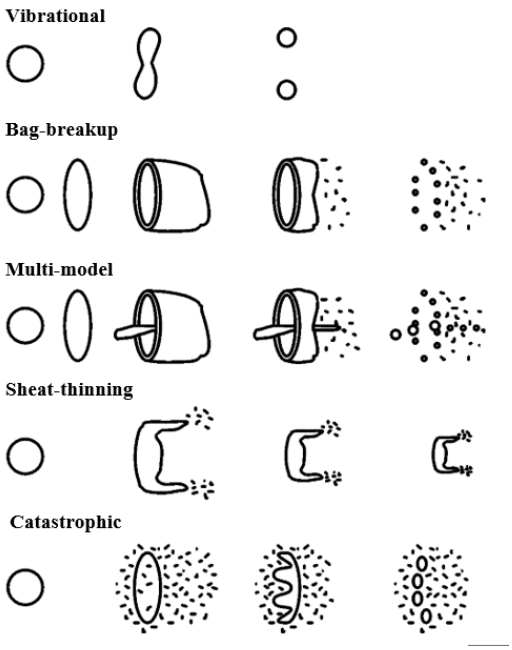

Figure 1-7: Different secondary breakup regimes characterized by gas weber numbers (26)

A schematic representation of the physical nature of breakup in different regimes is shown in *Figure 1-7*. The vibrational breakup consists of oscillations at the natural frequency of the drop and produces only a few fragments whose sizes are comparable to those of the parent drop. The bag breakup geometry is composed of a thin hollow bag attached to a thicker toroidal rim. The bag disintegrates first, followed by the toroidal rim. The former results in a larger number of small fragments, while the latter results in smaller number of large fragments. Multi-mode breakup is similar to bag breakup, but with the addition of a stamen oriented against the direction of the drop motion. Like bag breakup, the bag

is the first to disintegrate, followed by the rim and the stamen producing multiple droplets of various sizes. In sheet stripping (or sheet-thinning), a film is continuously eroded from the drop surface. It disintegrates rapidly. This results in a plethora of small droplets and, in some cases, a core whose size is comparable to that of the parent drop. Finally, during catastrophic breakup the drop surface is corrugated by waves of large amplitude and long wavelengths. They form a small number of large fragments that in turn break up into even smaller units. Another class of studies on spray characterization are based on *fractal analysis* quantifying the disparity in length scales of the liquid fragments formed as a result of the atomization process. The fractal dimension is a measure of the fragmentation of a surface that is self-similar over a range of scales, i.e. similar structures can be observed at different magnifications. Shavit and Chigier (27) were the first to apply fractal analysis to study spray atomization in co-axial jet flow. They have shown that there is no preferred single dominant disturbance on the liquid surface and a wide range of perturbations deform the liquid-gas interface resulting in formation of liquid fragments with different length-scales. More recent experimental studies of Dumouchel et al (28,29) applied fractal analysis on large number of liquid flow images of a fuel spray issuing from an injector nozzle. They found that while the local fractal dimension of spray in the near-nozzle region correlates with Reynolds number of the issuing jet, the mean fractal dimension of the overall spray structure scales with the liquid Weber number. Moreover, the smallest fragment size for all downstream distances from the nozzle is found to be directly proportional to capillary length-scales, signifying the importance of surface tension as the controlling mechanism of atomization. Based on these results they argued that similar to turbulence the atomization process could be described as a cascade of structures of different length-scales, wherein the role of the viscosity in turbulence is being played by surface tension.

1.2.2 Turbulent Spray Evaporation

In case of isolated droplets in a turbulent flow, Birouk and Gökalp (30) have shown that the vaporization rate is enhanced by turbulence. The effect of turbulence on evaporation rate is characterized by a non-dimensional Damköhler number $Da=\frac{\tau_f}{\tau_{vap}}$, which is the ratio of characteristic turbulent time scale (τ_f) to the timescale of droplet evaporation (τ_{vap}).

$$\dot{m}_{tv}/\dot{m}_v = (1.0 + 0.0948Da^{-0.765}) \qquad \textbf{1-5}$$

Higher the turbulence intensity, smaller is the turbulent time scale and the Damköhler number (*Da*) and higher is the turbulent evaporation rate $\dot{m}_{tv}$ in comparison to the classical d²-law, $\dot{m}_v$ as shown in Eq.1-5. Verwey and Birouk (31,32) conducted experiments of isolated droplets at elevated temperatures and pressures for different fuels to understand the physical mechanisms governing turbulent evaporation. It was demonstrated that the enhancement in vaporization rate by turbulence is because of the rapid dispersion of the vapor by turbulent eddies smaller than the droplet size. This creates an increased vapor mass fraction gradient at the droplet surface increasing the diffusion potential for further evaporation. This effect is characterized in terms of the ratio Kolmogorov length scale to the initial droplet size i.e. $\frac{\eta}{d_0}$. Based on their results they concluded that while evaporation rate of larger droplets is affected by small-scale turbulent fluctuations, the small droplets within the sub-Kolmogorov scale range experience only the relative effect of the mean flow. Villermaux (33,34) described the droplet evaporation in a mono-dispersed dense spray as a *scalar mixing* process, wherein the rate of evaporation is determined by the rate of mixing of the vapor concentration field surrounding a droplet. As a result, the lifetime of a droplet is shown to be much longer than the d² -law. Experimental studies of Sahu et al (35) on poly-dispersed sprays have further shown that evaporation process is coupled to *turbulent dispersion*, in addition to the scalar mixing process. Monchaux et al (36) showed that the turbulent dispersion of droplets in poly-disperse sprays results in preferential accumulation of droplets in clusters. The effect of dispersion is characterized by a non-dimensional *Stokes number St*, which is defined as the ratio of droplet to fluid inertia as given by Eq. 1-6.

$$\mathbf{St} = \frac{\tau_p}{\tau_f} = \left(\frac{d}{\eta}\right)^2 \frac{1+2\Gamma}{36} \qquad \mathbf{1\text{-}6}$$

where τ_p is the droplet response time to fluid solicitations and Γ is the ratio of droplet density to the gas density. Haradalupas et al (37,38) showed that while maximum clustering occurs when *St* is equal to 1, the dimension of the clusters increases with *St.* Also, it was demonstrated that the typical length scale of the cluster is of few orders of magnitude of Kolmogorov length scale η showing the importance of small-scale turbulence characteristics of spray dispersion. Sahu et al (35) showed that droplet clustering resulting in smaller inter-droplet spacing than the average, reduces the droplet evaporation rate. It was demonstrated that the spray evaporation is characterized by group vaporization of droplet clusters in the spray center and single droplet evaporation in the spray periphery. Most of these experiments were performed in simple flow configurations

at low injection velocities compared to typical diesel sprays. Earlier experimental studies of diesel sprays (39-41) characterized the dispersion and vaporization process in terms of macroscopic properties like liquid/vapor penetration lengths and spray spreading angle obtained using high-speed schlieren imaging as shown in *Figure 1-8*. In non-evaporating sprays they showed that increasing the injection pressure/ambient gas density decreases the penetration length because of the increased dispersion of spray by entrainment of surrounding air. On the other hand, while there is no significant influence of injection pressure on spreading angle, increasing the gas density increases the spray spreading angle. In case of evaporating sprays, the vapor penetration rate and spreading angle of an evaporating spray were both lower than that of a non-evaporating spray, which was attributed to vaporization cooling that contracts the spray. Moreover, Siebers (42,43) quantified the intensity of vaporization in terms of maximum liquid penetration length and has shown that the evaporation process is controlled by turbulent mixing or entrainment of air by the spray. With the advent of advanced optical measurement techniques, recently there has been an increasing focus on quantitave description of the microscopic features of sprays. To this end (44, 45) performed quantitative measurements of mixture fraction, temperature and velocities fields in evaporating sprays using Rayliegh scattering and Particle image velocimetry (PIV) techniques. Experiments showed a strong variations in instantaneous flow fields from one realization to another due to small fluctuations in operating conditions. So the ensemble average statistics and the corresponding uncertainty in measurements for different flow quanities are calculated. While the velocity fields are useful to quantify the entrainment of the hot gases by the spray, the mixture fraction and temperature fields provides a detailed understanding of mass and heat transfer processes between the two phases.

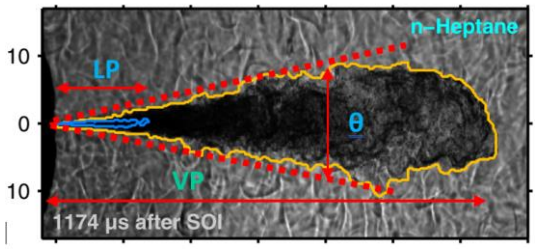

Figure 1-8: Schlieren image of spray with schematic representation of liquid penetration length (LP), vapor penetration length (VP) and spray spreading angle θ (41)

1.2.3 Engine combustion network (ECN) – experimental database

While these advanced experiments provide insight into individual processes, understanding the stochastic nature of sprays require insights into the non-linear interactions between these processes. This would require simultaneous measurement of the aforementioned physical quantities at engine relevant conditions. Such simultaneous application of multiple diagnostics would significantly increase the cost and complexity of the experiment due to the disparity in length and time scales of the different processes involved. The more suitable alternative to understand the interactive spray dynamics resolving the wide range of spatial and temporal scales is to use numerical modeling of the multiphase flows. Therefore, in recent times a combined approach of developing reliable predictive numerical models with the help of standardized experimental datasets is gaining traction. To this end *Engine Combustion Network (ECN),* a consortium of research organizations from across the world have accumulated an extensive database of well documented experiments performed by round-robin testing of standardized injectors at engine relevant conditions. Usually the ECN spray experiments (47,48) are performed in a *constant volume* cubical vessel of size 108 mm on each side. The high pressure and temperatures corresponding to real engine conditions are generated by spark igniting a pre-mixed combustible gas mixture. After the pre-mixed combustion, due to the heat transfer to the chamber walls from the combustion products the chamber temperature and pressure gradually reduces. Once the desired conditions are attained the spray in injected into the chamber. In order to quantify the in-nozzle flow effects on primary atomization standard injector geometries are used. Different measurement techniques (49) are used to characterize the three dimensional geometrical features of the injectors. A schematic of the different ECN experimental techniques is shown in *Figure 1-9*.

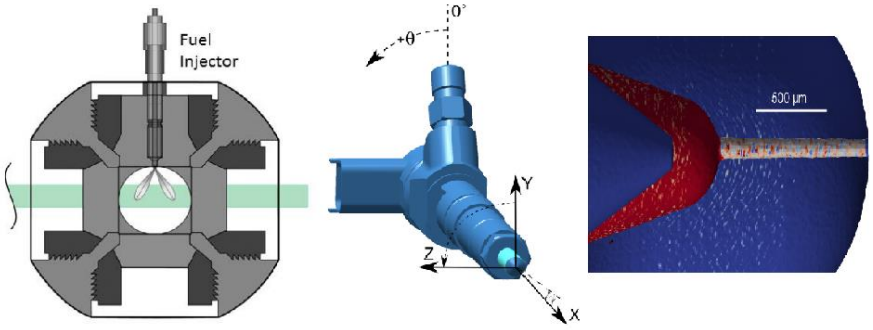

Figure 1-9:ECN measurements techniques: (a) Constant volume spray combustion chamber (b) Spray-A injector configuration (c) X-ray phase contrast imaging for needle lift (d) X-ray tomography measurement of injector nozzle geometry (49).

1.2.4 Main questions – Intermittency and cycle-cycle variations in diesel spray estimates

Experimental studies have shown that at engine relevant conditions with relatively high flow Reynolds numbers, different spray processes like atomization, dispersion and evaporation are governed by turbulence at small spatial scales. Recent experimental studies of Mordant et al (49,50) and Voth et al (51,52) on Lagrangian statistics in turbulence at high-Reynolds numbers showed strong intermittency in the fluid-particle acceleration. They showed that the acceleration is log-normally distributed and has very strong variations greater than its standard deviation. It has also been observed that the correlation time of the norm of the acceleration is of the order of that of the integral scales, while the correlation time of its components is of the order of Kolmogorov's time, thus showing that the properties of acceleration depend on the Re. Intermittency implies that small spatial scales are usually concentrated in vortex tubes or sheets surrounded by a extensive regions of fluid where they are absent. The presence of alternating highly turbulent and non-turbulent regions makes the fluid acceleration highly non-gaussian in nature. Localized intense fluid accelerations may induce strong fluctuations in the population of liquid drops, and their vaporization rates. Consequently, such events of strong fluid acceleration can be responsible for "spontaneous" extinction or ignition sites in the combustion chamber. Secondly, the experimental studies have shown that interaction between different spray processes is so non-linear that even small fluctuations in the operating conditions leads to a completely different realization of the spray structure. In light of these observations the main questions concerning numerical modelling of sprays pertains to :

1. Within one cycle there are strong effects of intermittency. So how to account for the intermittency of small spatial scales on different physcial processes like atomization, dispersion and evaporation of liquid fuel droplets?

2. Due to cycle to cycle variations in operating conditions the flow properties are stochastic in nature. So another important question is how to simulate the different spray sub-processes stochastically?

1.3 Governing equations for Euler-Lagrangian modelling of sprays

In a typical diesel engine, the number of fuel droplets injected per cycle is approximately in the order of 10^7 - 10^8 depending on the operating conditions. It is a too difficult task to numerically model the fluid dynamics of such large number of droplets. So, fuel sprays are modelled using lagrangian tracking of "parcels or computational particles" moving in a Eulerian gas flow. A parcel is a point particle which represents an ensemble of physical droplets with similar properties. The gas flow quantities affecting the spray like velocity, temperature, and mixture fraction are to be interpolated at the particle's positions from the Eulerian grid. This approach is based on the assumption that the spray is volumetrically dilute. The Lagrangian Monte Carlo approach was first proposed by Dukowicz (53) and later further improved upon by Amsden & O'Rourke (54) for modelling fuel-spray processes like atomization, evaporation and dispersion. The Euler-Lagrangian governing equations used for the spray modelling are briefly re-visited here.

1.3.1 Navier Stokes Equations – gaseous phase

The Navier Stokes Equation for the gaseous phase describing the mass, momentum, energy conservation and species mass fraction are given by Eq. 1-7 to 1-10.

$$\frac{\partial \rho}{\partial t} + \nabla . \rho \mathbf{u} = \boldsymbol{M_{liq}} \qquad \textbf{1-7}$$

$$\frac{\partial \rho \mathbf{u}}{\partial t} + \boldsymbol{\nabla} . (\rho \mathbf{u}\mathbf{u}) = -\boldsymbol{\nabla} . \boldsymbol{p} - \boldsymbol{\nabla} . \boldsymbol{\tau} + \boldsymbol{S_{liq}} \qquad \textbf{1-8}$$

$$\frac{\partial \rho \mathbf{e}}{\partial t} + \nabla . (\rho \mathbf{u}\mathbf{e}) = -\nabla . (\mathbf{q}) - \nabla . (\mathbf{p}\mathbf{u}) - \nabla . (\boldsymbol{\tau} . \mathbf{u}) + \mathbf{Q_{liq}} \qquad \textbf{1-9}$$

$$\frac{\partial \rho Y_k}{\partial t} + \nabla . (\rho \boldsymbol{u} Y_k) = -\rho \mathbf{D}_k \nabla . Y_k + \boldsymbol{\rho_k} \qquad \textbf{1-10}$$

Here ρ, u, p, e, are the gas phase density, velocity, pressure, internal energy respectively. The terms D_k and Y_k in Eq. 1-10 are the diffusivity and mass fraction of species *k* in the gaseous mixture. In momentum equation i.e. Eq. 1-8, the term τ is the viscous stress tensor expressed as product of kinematic viscosity ν and the strain rate *S* as given by Eq. 1-11. Next in the energy equation, the term q is the heat flux vector expressed as product of thermal conductivity λ and temperature gradient of the gaseous mixture ∇T.

$$\boldsymbol{\tau} = -2\rho \boldsymbol{\nu} \boldsymbol{S} \qquad \textbf{1-11}$$

$$\boldsymbol{S} = \frac{1}{2}(\nabla \boldsymbol{u} + \nabla \mathbf{u}^{\boldsymbol{T}}) \qquad \textbf{1-12}$$

$$\boldsymbol{q} = -\boldsymbol{\lambda}\boldsymbol{\nabla}.\boldsymbol{T} \quad \textbf{1-13}$$

And M_{liq}, S_{liq}, Q_{liq} and ρ_k are the source terms accounting for the exchange of mass, momentum and energy between two phases. The formulations of these terms are explained later in Section 1.3.3.

1.3.2 Lagrangian modelling – dispersed liquid phase

The motion of each lagrangian droplet, moving in an Eulerian framework, is governed by the Newton's second law i.e.

$$\mathbf{m_p a_p} = \mathbf{m_p}\frac{\mathbf{du_p}}{\mathbf{dt}} = \sum \mathbf{F_{i,p}} \quad \textbf{1-14}$$

Here m_p, a_p and $F_{i,p}$ are the droplet mass, acceleration and forces acting on the particle. While different forces accounting lift, rotation and buoyancy of particles are usually considered in the equation of motion, they are negligible because of the high-density ratio between the liquid fuel droplet and ambient gas. What remains is the *aerodynamic drag* force due to the relative velocity between the two phases. Including this drag force term in the right-hand side of Eq. 1-14, the equation of motion for a droplet can be re-written as shown in Eq.1-15.

$$\boldsymbol{a_p} = \frac{\boldsymbol{du_p}}{\boldsymbol{dt}} = \frac{\boldsymbol{\rho}}{\boldsymbol{\rho_p d_p}}\frac{\mathbf{3}}{\mathbf{4}}\boldsymbol{C_d}\left|\mathbf{u}-\mathbf{u_p}\right|\left(\mathbf{u}-\mathbf{u_p}\right) \quad \textbf{1-15}$$

$$\boldsymbol{a_p} = \frac{\boldsymbol{du_p}}{\boldsymbol{dt}} = \frac{\mathbf{u}-\mathbf{u_p}}{\boldsymbol{\tau_p}} \quad \textbf{1-16}$$

$$\boldsymbol{\tau_p} = \frac{\mathbf{4}}{\mathbf{3}}\frac{\mathbf{1}}{\mathbf{C_d}\left|\mathbf{u}-\mathbf{u_p}\right|}\frac{\boldsymbol{\rho_p}\,\mathbf{d_p}}{\boldsymbol{\rho_g}} \quad \textbf{1-17}$$

In above equations, d_p is the droplet size, τ_p is the particle response time to fluid solicitations, u_p is the droplet velocity, ρ_g and ρ_p are the densities of gas and droplet respectively. The drag coefficient C_d is a function of droplet Reynolds number $\left(Re_p = \frac{\rho_g d_p \left|\mathbf{u}-\mathbf{u_p}\right|}{\nu}\right)$. At low velocities, it is assumed that the boundary layer around the droplet experiences a transition from laminar to turbulent and the drag coefficient is strongly dependent on Re_p. For much higher velocities, the boundary layer is assumed to be fully developed with vortices of different length scales being shed from the droplet. In this regime the drag coefficient is roughly constant.

$$C_d = \begin{cases} \frac{24}{Re_p}\left(1 + 0.15 Re_p^{0.687}\right) & Re_p < 1000 \\ 0.42 & \mathrm{Re_p} > 1000 \end{cases} \quad \text{1-18}$$

Next the droplet evaporation is modelled using the Spalding's (55) classical d²-law with the Frossling's (56) correction for the convective flow. The model is based on the assumption that the droplet evaporation is controlled by the rate of diffusion of vapor from droplet surface to the surrounding gas. Other assumptions of this model are:

1. The diffusion process is spherically symmetric and interaction between droplets are neglected.
2. Infinite conductivity of the droplets resulting in a constant temperature inside the droplet.
3. Rapid mixing of vapor diffusing from the droplet surface by the surrounding gas.

The rate of evaporation of a droplet $\dot{m}_p$ is obtained by equating it with the mass flux leaving the droplet surface (ζ) into the surrounding ambient gas (∞).

$$\dot{m}_p = \frac{dm_p}{dt} = -2\pi d_p \rho \mathrm{D_{f\nu}}\, B_M\, \mathrm{Sh_d} \quad \text{1-19}$$

where Sh_d is the Sherwood number which represents the ratio of convective to diffusive mass transport, B_M is the Spalding's mass transfer number, D_{fv} is the fuel vapor diffusivity in air.

$$\mathrm{Sh_d} = \left(1 + 0.3 \mathrm{Re}_p^{\frac{1}{2}} \mathrm{Sc}_p^{\frac{1}{3}}\right) \frac{ln(1+B_M)}{B_M} \quad \text{1-20}$$

$$B_M = {(Y_{F\zeta} - Y_{F\infty})}\Big/{(1 - Y_{F\zeta})} \quad \text{1-21}$$

Here $Y_{F\zeta}$ is the vapor mass fraction at the droplets surface, $Y_{F\infty}$ is the vapor mass fraction in the far-field and $Sc_p = \frac{\mu}{\rho_p D_{fv}}$ is the Schmidt number, where μ is the viscosity of the gaseous mixture. $Y_{F\zeta}$ is obtained by assuming that the flow at the droplet surface is saturated. Using molar fraction of the fuel vapor at the surface $X_{F\zeta}$, the molar weight of the fuel, W_F, and, the molar weight of the mixture of all species other than the fuel $W_{nF,\zeta}$, the saturated vapor fraction $Y_{F\zeta}$ is calculated as shown in Eq. 1-22.

$$Y_{F\zeta} = {(X_{F\zeta}\, W_F)}\Big/{(X_{F\zeta}\, W_F + (1 - X_{F\zeta})\, W_{nF,\zeta})} \quad \text{1-22}$$

The fuel molar fraction $X_{F\zeta}$ can be written using the partial pressure of the fuel species, which in turn is calculated from the Clausius-Clapeyron law.

$$X_{F\zeta} = {}^{p_{F\zeta}}/_{p} \quad \textbf{1-23}$$

$$p_{F\zeta} = p_0 e^{\frac{W_F L_v}{R}\left(\frac{1}{T_0} - \frac{1}{T_\zeta}\right)} \quad \textbf{1-24}$$

where p_0, T_0 correspond to reference pressure and temperature on the saturation curve, R is the universal gas constant and L_v is the latent heat of vaporization. The droplet temperature is calculated from the energy balance equation, which states that the energy supplied to the droplet is either used to heat the droplet or supplies heat for vaporization.

$$\rho_p \frac{4}{3}\pi r^3 C_{pl} \frac{dT_p}{dt} - 4\pi r^2 L_v = 4\pi r^2 Q_p \quad \textbf{1-25}$$

where r is the droplet radius, T_p is the droplet temperature, C_{pl} is the liquid specific heat and Q_p is the rate of conduction of heat to the droplet per unit surface area. The heat conduction rate Q_p is calculated using the Ranz-Marshall (57) correlation.

$$Q_p = k(T - T_p)\frac{Nu_d}{2r} \quad \textbf{1-26}$$

where, k is the thermal conductivity of the liquid droplet, Nu_d is the Nusselt number which is the ratio of convective to conductive heat transfer between the droplet and the surrounding.

$$Nu_d = \left(1 + 0.3 Re_p^{\frac{1}{2}} Pr_p^{\frac{1}{3}}\right) \quad \textbf{1-27}$$

where $Pr_p = \frac{\mu C_p}{k}$ is the Prandtl number and C_p is the specific heat at constant pressure of the gaseous mixture. Next, the spray breakup models (58, 59) usually describe the rate of change of size of a computational particle by a breakup rate expression of the form:

$$\frac{dr}{dt} = \frac{r - r_{bu}}{\tau_{bu}} \quad \textbf{1-28}$$

Here r is the radius of the computational particle, and r_{bu}, τ_{bu} are the characteristic particle size and breakup time scale which determine the rate of breakup. Different formulations have been defined for these parameters depending on the breakup mechanisms described earlier in Section 1.2.1. These parameters are usually function of the liquid-gas density ratio and the magnitude of relative velocity i.e. $|u - u_p|$.

1.3.3 Source terms – two-way coupling

In case of high-pressure fuel sprays, the relative velocities between liquid-gas phases are significantly high (usually in the order of 100-400 m/s). So, in addition to the mass transfer from liquid-gas phase due to droplet evaporation, the impact of momentum transfer from liquid droplets on the dynamics of the carrier gas phase has to be considered. The source terms are modelled as the volume average contributions of all the droplets in a Eulerian cell. In case of momentum source term, there are two contributing factors namely, the drag force and the momentum exchange due to evaporation of droplets. Similarly, the energy source term considers the contributions of the phase change due to evaporation, heat conduction from droplet to gas and the work done by the drag force on the droplet.

$$\boldsymbol{M_{liq}} = \frac{\mathbf{1}}{\mathbf{V_{cell}}} \sum_{\mathbf{m=1}}^{\mathbf{N_p}} \dot{\mathbf{m}}_{\mathbf{p,m}} \mathbf{n}_{\mathbf{p,m}} \qquad \textbf{1-29}$$

$$\boldsymbol{S_{liq}} = \frac{\mathbf{1}}{\boldsymbol{V_{cell}}} \sum_{\boldsymbol{m=1}}^{\boldsymbol{N_p}} (\boldsymbol{F_{p,m}} + \dot{\boldsymbol{m}}_{\boldsymbol{p,m}} \boldsymbol{u_{p,m}}) \boldsymbol{n_{p,m}} \qquad \textbf{1-30}$$

$$\boldsymbol{Q_{liq}} = \frac{\mathbf{1}}{\boldsymbol{V_{cell}}} \sum_{\boldsymbol{m=1}}^{\boldsymbol{N_p}} (\boldsymbol{F_{p,m}} \left| \boldsymbol{u} - \boldsymbol{u_{p,m}} \right| + \dot{\boldsymbol{m}}_{\boldsymbol{p,m}} \boldsymbol{L_v} + \boldsymbol{C_{p,l}} \boldsymbol{m_{p,m}} \frac{\boldsymbol{dT_{p,m}}}{\boldsymbol{dt}}) \boldsymbol{n_{p,m}} \qquad \textbf{1-31}$$

Here for a given parcel m, $n_{p,m}$ is the number of droplets, $m_{p,m}$ is the droplet mass, $F_{p,m}$ is the drag force (Eq. 1-14), $\dot{m}_{p,m}$ is the vaporization rate (Eq. 1-19) , L_v is the latent heat of vaporization, $C_{p,l}$ is the specific heat at constant pressure, $\frac{dT_{p,m}}{dt}$ is the rate of change of droplet temperature (Eq. 1-25) and V_{cell} is volume of the computational cell. In case of the species transport equation, the source term ρ_k is zero for all species except for the fuel vapor, where $\rho_v = M_{liq}$.

1.3.4 Main question – Under-resolved spray simulations

One of the main challenges in numerical modelling in fluid-mechanics pertains to the problem of tubulence. Turbulent flows are characterized by a wide range of length and time scales. The largest eddies are typically in the size of the geometrical domain (*L)* and are characterized by the mean flow, whereas the smallest eddies are characterized by the rate of dissipation of energy down to the molecular scales. In case of single phase flows, the length scale of smallest eddies represented by Kolmogorov length scales (η) is inversely proportional to the flow Reynolds number (Re) i.e. $\eta \sim LRe^{-3/4}$. In the case of multiphase flows like sprays, the smallest length scale is governed by the smallest droplet size which could be smaller than the Kolmogorov length scale. Let us consider the

example of modelling ECN spray chamber which is a cube with size of roughly $L = 100mm$ on each side. Assuming the smallest droplet size of the atomized spray to be of the order of $d = 10\mu m$,the number of grid points required to resolve all the flow length scales will be in the order of $10^{12} - 10^{13}$. So in such conditions, the direct numerical resolution (DNS) of small energetic scales characterizing intermittency effects is hampered due to limitations in available computational resources, thereby the flow simulation becomes "*under-resolved*". This requires simulation of contribution of discarded scales. On the other hand, Reynolds averaged Navier Stokes (RANS) method where ensemble averaged conservation equations for the mean flow quantitites are solved, while modelling the higher order terms like turbulent production and dissipation rate of kinetic energy is widely used for spray simulations because of their low computational costs. While RANS represents correctly the esemble averaged statistics of cycle-cycle flow variations it does not correctly represent flow turbulence in one-flow cycle making it difficult to account for the intermittency effects of small-scale turbulence. On the other hand while LES resolves turbulence in aflow-cycle, but it does not resolve the small-scales characterizing intermittency effects. So still the pertinent question for under-resolved diesel spray simulations remains the same i.e. how to account for the intermittency effects of un-resolved turbulent length scales on spray processes?

1.4 Large eddy simulations (LES) of sprays

Large Eddy Simulations (LES) offers a comprimise between DNS and RANS approaches. LES usually solves for spatially filtered Navier Stokes equations where the filter size is comparable to the computational grid. This approach directly resolves the instantaneous flow structures larger than the filter size and the effect of unresolved scales is modeled using simple sub-grid scale (SGS) turbulence models. Moreover the engine combustion chamber domain is confined and moderate in size and the flow Reynolds numbers are modest, usually in the order of $10^4 - 10^5$. For these reasons the requirements for application of LES for engine flows are within the reasonable limits of the modern day computational resources.

1.4.1 Filtered Navier Stokes Equations for gaseous phase

The basic formulation of LES was developed by Smagorinsky (60) for atmospheric flows in early 1960's as an alternative to resolving all the scales of motion using DNS. The concept of LES is based on Kolmogorov's classical hypothesis (61,62) of small-scale

turbulence. Kolmogorov argued that while the large-scale structures are anisotropic and strongly influenced by the geometrical boundary conditions, the directional bias is lost at smaller scales by the chaotic scale-reduction process. So, he hypothesized that at sufficiently high Reynolds numbers the statistics of small-scale turbulent motions have a universal form and are dependent only on the rate of energy transfer ϵ from large-scales to smaller scales. Therefore, in LES the principle idea is to solve directly for the large scales of motion, while modelling the small scales. The first step of LES modelling is to perform some kind of *spatial filtering* operation to separate the large scales of motion from the smaller scales. The filtering process involves locally derived weighted average of flow properties over a volume of fluid. One of the important parameters of filtering operation is the filter width or grid scale (Δ), which is a representative length scale demarcating the *resolved* scales of motion solved by the governing equations from the *sub-grid* scales which needed to be modelled. Any given flow variable f in LES is decomposed into resolved component ($\bar{f}$) and the sub-grid scale (SGS) component f'.

$$\mathbf{f} = \bar{\mathbf{f}} + \mathbf{f}' \qquad \textbf{1-32}$$

The resolved scale component is obtained from a filtering operation, which is defined as:

$$\bar{\mathbf{f}} = \oint \mathbf{G}(\mathbf{x}, \mathbf{x}'; \Delta)\mathbf{f}(\mathbf{x}')\mathbf{dx}' \qquad \textbf{1-33}$$

where Δ is the filter width which is proportional to smallest length scale retained by the filtering operation. $G(x, x'; \Delta)$ is the filter kernel satisfying the normalization condition given by Eq.1-34.

$$\oint \mathbf{G}(\mathbf{x}, \mathbf{x}'; \Delta)\mathbf{dx}' = \mathbf{1} \qquad \textbf{1-34}$$

A schematic representation of filtering process is shown in *Figure 1-10* with arbitrary filter kernel and a randomly fluctuating one dimensional (1-D) variable *f*. While there are different types of filter kernels, the most commonly used one in finite volume-based solvers is the *top-hat* filter, which is simply an average over a rectangular region within an interval of $x - \frac{1}{2}\Delta < x' < x + \frac{1}{2}\Delta$ for a 1-D case.

$$\mathbf{G}(\mathbf{x}, \Delta) = \begin{cases} \mathbf{1}/\Delta & \mathbf{f}|\mathbf{x}'| < \Delta/\mathbf{2} \\ \mathbf{0} & \mathbf{otherwise} \end{cases} \qquad \textbf{1-35}$$

The filtered flow variables derived from Navier Stokes equations of the Eulerian gas-phase equations are given by:

$$\frac{\partial \bar{\rho}}{\partial t} + \nabla . \bar{\rho}\,\bar{\mathbf{u}} = \bar{M}_{liq} \qquad \textbf{1-36}$$

$$\frac{\partial \bar{\rho}\bar{u}}{\partial t} + \nabla . (\bar{\rho}\bar{u}\bar{u}) = -\nabla . \bar{p} - \nabla . (\tau + \tau_{sgs}) + \bar{S}_{liq} \qquad \textbf{1-37}$$

$$\frac{\partial \bar{\rho}\bar{e}}{\partial t} + \nabla . (\bar{\rho}\bar{\mathbf{u}}\bar{\mathbf{e}}) = -\nabla . (\bar{\mathbf{q}}) - \nabla . (\bar{\mathbf{p}}\bar{\mathbf{u}}) - \nabla . (\boldsymbol{\tau} . \bar{\mathbf{u}}) + \bar{Q}_{liq} - \nabla . \mathbf{h}_{sgs} \qquad \textbf{1-38}$$

$$\frac{\partial \bar{\rho}\bar{Y}_k}{\partial t} + \nabla . (\bar{\rho}\bar{\mathbf{u}}\bar{Y}_k) = -\bar{\rho}\mathbf{D}_k \nabla . \bar{Y}_k - \nabla . (\boldsymbol{\phi}_{sgs,k}) + \overline{\rho_k} \qquad \textbf{1-39}$$

In order to close the filtered equations given by Eq. 1-36 to 1-39, further modelling of the sub-grid scale (SGS) stress tensor $\boldsymbol{\tau}_{sgs}$ and sub-grid scale heat and species flux terms h_{sgs} and $\phi_{sgs,k}$ are necessary. The most important characteristic of LES is resolving the instantaneous flow structures, which are usually related to the non-linear terms $\nabla . (\bar{\rho}\bar{u}\bar{u})$ in the momentum equation given by Eq. 1-37. Thus, the expected increase in resolved scale flow structures in LES must come from these terms and not from the turbulence model for $\boldsymbol{\tau}_{sgs}$. To achieve the increased flow structures, the non-linear terms must be allowed to function sufficiently. This is usually achieved either through the use of smaller filter widths (Δ) or a less dissipative SGS turbulence model.

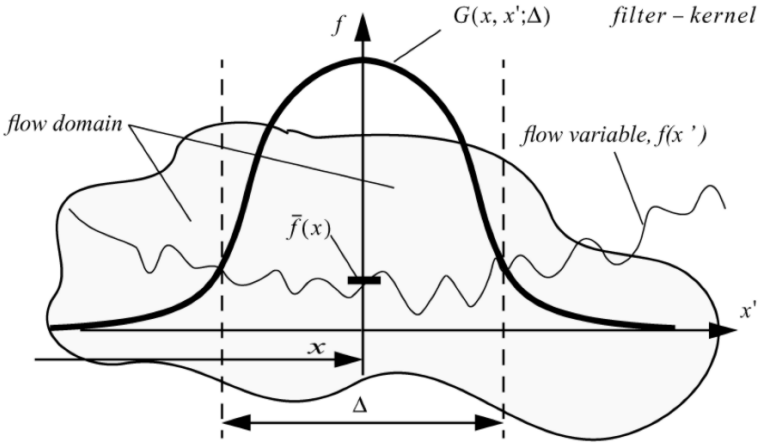

Figure 1-10: 1-D representation of filtering process with an arbitrary filter function (adapted from thesis of Eugene de Villiers (63))

1.4.2 Sub-grid scale (SGS) turbulence models

The formulation of the different SGS turbulence models is based on the eddy viscosity model. The basic hypothesis of eddy viscosity model is that the non-uniform component of the SGS stress tensor is locally aligned with the resolved non-uniform part of the rate

of strain tensor. The normal stresses are taken as isotropic and are expressed in terms of the SGS kinetic energy.

$$\boldsymbol{\tau_{sgs} - \frac{1}{3}\mathbf{tr}(\tau)\mathbf{I} = \tau_{sgs} - \frac{2}{3}\mathbf{k_{sgs}}\mathbf{I} = \nu_{sgs}(\nabla\bar{u} + \nabla\bar{u}^{T}) = -2\nu_{sgs}\bar{S}} \quad \textbf{1-40}$$

where $\bar{\mathbf{S}}$ is the resolved strain rate tensor and $\mathbf{k_{sgs}}$ is the sub-grid scale kinetic energy.

$$\mathbf{k_{sgs}} = \frac{1}{2}\sum_i \tau_{ii} \quad \textbf{1-41}$$

$$\bar{\mathbf{S}} = \frac{1}{2}(\nabla\bar{u} + \nabla\bar{u}^{T}) \quad \textbf{1-42}$$

Following the same analogy used for modelling the SGS shear stress, the heat and mass terms i.e. $\mathbf{h_{sgs}}$ **and** $\boldsymbol{\phi_{sgs,k}}$ expressed in the following way:

$$h_{sgs} = -\bar{\rho}\nu_{sgs}C_p\nabla.\bar{T} \quad \textbf{1-43}$$

$$\phi_{sgs,k} = -\bar{\rho}\nu_{sgs}\nabla.\bar{Y}_k \quad \textbf{1-44}$$

1.4.2.1 Smagorinsky model

Smagorinsky (60) first derived a relation for the sub-grid scale eddy-viscosity, assuming that the small scales are in equilibrium and dissipate all the energy received from the resolved scales instantaneously. The expressions for SGS viscosity and kinetic energy are given by Eqn. 1-45 and 1-46.

$$\mathbf{\nu_{sgs} = (C_s\Delta)^2|\bar{S}|} \quad \textbf{1-45}$$

$$\mathbf{|\bar{S}| = (\bar{S}:\bar{S})^{1/2}} \quad \textbf{1-46}$$

The value of the parameter $\boldsymbol{C_s}$, referred to as the Smagorinsky 'constant', has been determined from isotropic turbulence decay and is in range of 0.15-0.25. However, this value is not universal and depends on the flow conditions. The model gives excessive dissipation for non-homogenous flows like near-wall boundary layers, free shear flows, separating and re-attaching flows. In-order to rectify this either very small filter widths must be used or the values of $\boldsymbol{C_s}$ must be scaled accordingly. This is the main drawback of Smagorinsky model.

1.4.2.2 One Equation Model

In order to address the non-equilibrium effects of energy transfer, a new eddy viscosity model based on solution of transport equation for the sub-grid scale turbulent kinetic

energy $\boldsymbol{k_{sgs}}$ is first developed by Yoshizawa (64) for atmospheric flows and later adapted for general engineering applications by Kim and Menon (65). The transport equation for SGS turbulent energy can be derived by first subtracting the filtered equations of motion from their exact non-filtered counterparts to give a relation for the fluctuating component of velocity u′. Multiplying the result by the sub-grid velocity vector and contracting the equation gives the following transport equation (Eq. 1-47) for $\boldsymbol{k_{sgs}}$.

$$\frac{\partial \bar{\rho} k_{sgs}}{\partial t} + \nabla.\left(\bar{\rho}\bar{u}k_{sgs}\right) = -\bar{\rho}\tau : S - \nabla.\left(\bar{\rho}\nu_{sgs}\nabla.k_{sgs}\right) + \varepsilon_{sgs} \qquad \textbf{1-47}$$

$$\nu_{sgs} = C_k\, \Delta k_{sgs}^{\frac{1}{2}} \text{ and } \varepsilon = C_\epsilon \Delta^{-1} k_{sgs}^{\frac{3}{2}} \qquad \textbf{1-48}$$

where $\boldsymbol{\epsilon}$ is the rate of energy dissipation and $\boldsymbol{C_k}, \boldsymbol{C_\epsilon}$ are the modelling coefficients. The one equation model has shown advantages when used to model transitional flows or flows with large scale unsteadiness. A study of the performance of different SGS models in channel flows by (66) and in non-reactive in-cylinder engine flows by (67-68) has shown the one-equation model to be quite effective and superior to Smagorinsky model. So, this SGS model is used throughout this thesis.

1.4.3 Filtered Lagrangian equations for dispersed phase

In case of classical LES approach, the relative velocity in drag force equation and the breakup rate are approximated in terms of the filtered gas-phase velocity at the droplets position $\bar{u}$, discarding the influence of unresolved scale. Similarly, in case of evaporation model, assuming rapid mixing of vapor by the surrounding gas, $Y_{v\infty}$ is approximated by the filtered vapor mass fraction $\overline{Y_v}$ in the Eulerian cell. The filtered lagrangian equations are given by Eq. 1.49 to 1.51. In Eq. 1-51, $\bar{r}_{bu}$ and $\bar{\tau}_{bu}$ show that the relaxation radius and the breakup time scale are expressed in terms of filtered flow quantities like $|\bar{u} - u_p|$.

$$a_p = \frac{du_p}{dt} = \frac{\bar{u} - u_p}{\tau_p} \qquad \textbf{1-49}$$

$$\dot{m}_p = \frac{dm_p}{dt} = -2\pi d_p \rho D_{fv}\, Sh_d\, \frac{(Y_{F\zeta} - \overline{Y_v})}{(1 - Y_{F\zeta})} \qquad \textbf{1-50}$$

$$\frac{dr}{dt} = \frac{r - \bar{r}_{bu}}{\bar{\tau}_{bu}} \qquad \textbf{1-51}$$

1.4.4 Main question – Choice of model parameter for introducing intermittency effects in the framework of LES

The classical LES modeling approach is based on Kolmogorov's hypotheses describing the universality of turbulent scales much smaller than the geometrical domain. It is assumed that the flow at such small scales is isotropic and is characterized by the mean rate of energy dissipation $\overline{\varepsilon}$. But Landau (69) has agrued that the energy dissipation (ε) in itself is *non-homogenous* and *highly intermittent* i.e., ε is a spatially varying random variable fluctuating together with the velocity field and is strongly dependent on the local Reynolds number (Re). Corrsin (70) demonstrated experimentally that while the thickness of the large queiscent flow regions are of the order of external turbulent length scale (L), the thickness of highly energetic turbulent regions scale with Kolmogorov length scales(η). Kolmogorov and Obhukov (71,72) have proposed a refined hypothesis accounting for the fluctuations in the dissipation rate (ε), wherein it was shown that the dissiparion rate has a log-normal distribution whose variance is dependent on ratio of length scales (L/η).As the disparity in length scales i.e. (L/η) increases at higher Re, intermittent character of small spatial scales also become more prevalent. In order to model the SGS fluctuations in flow velocity field, Bellan (73) has proposed to reconstruct fluctuating SGS velocity at the particles position either by:

a) random sampling of the perturbations from a Gaussian distribution around the root mean square (RMS) value of flow variables. The frequency of these fluctuations is obtained from the life time of the particle in an eddy of the size of filter width (Δ).
b) deterministic approach wherein the SGS fluctuations are modelled from the Laplacian of resolved field.

Several other SGS models have been developed based on the idea of reconstructing the unresolved scale velocity field either stochastically or deterministically. In all these approaches the magnitude of SGS velocity usually scales with the filter width. Assuming that the filter width Δ is in the inertial range of turbulence cascade (i.e. $\eta << \Delta << L$) it can be concluded that SGS velocity fluctuations are much smaller than the filtered velocity as shown in Eq. 1-52.

$$|\boldsymbol{u}_{sgs}| << |\overline{\boldsymbol{u}}| \sim |\boldsymbol{u}| \qquad \textbf{1-52}$$

Therefore such models are invariant on the local flow Reynolds number, hence disregard the intermittency effects on subgrid-scales. But on the other hand Sabelnikov, Chtab and

Gorokhovski (74) have shown that the residual acceleration is substantially greater than the filtered acceleration at high-Reynolds-numbers. This can be seen in terms of classical Kolmogorov's scaling (e.g. Eq.1-53) by the following estimation: $(\bar{a}_k\bar{a}_k)^{1/2} \approx u_\Delta^2/\Delta$, $(a'_k a'_k)^{1/2} \approx v_\eta^2/\eta$, $u_\Delta^2 \approx (\langle\varepsilon\rangle\Delta)^{2/3}$, $v_\eta^2 \approx (\langle\varepsilon\rangle\eta)^{2/3}$ and then

$$\frac{(\bar{a}_k\bar{a}_k)^{1/2}}{(a'_k a'_k)^{1/2}} = \left(\frac{\eta}{\Delta}\right)^{1/3} = \left(\frac{L}{\Delta}\right)^{1/3} Re^{\frac{-1}{4}} \qquad \textbf{1-53}$$

From Eq. 1-53, it is evident that unlike the unresolved velocity, the magnitude of SGS acceleration can exceed the resolved scale acceleration by several orders of magnitude at high Re, thus allowing the expression of the intermittent properties of small scales. Therefore if any SGS model aims to account for the intermittency effects then the unresolved scale acceleration has be to the key variable for modelling. So the main questions is how to model the SGS flow acceleration field in the context of turbulent sprays?

1.5 Sub-grid scale acceleration models

Over the past decade, Gorokhovski et al (74-79) have developed two different classes of approaches to account for the intermittency effects on unresolved scales in LES modelling of particle laden flows. The first approach is to provide in the filtered momentum equation of the Eulerian phase an access to the fluid acceleration on residual scales. This approach based on the stochastic forcing of filtered momentum equations, is often referred to as stochastic subgrid acceleration model or LES-SSAM. The idea of LES-SSAM model was first introduced in Sabelnikov, Chtab and Gorokhovski (74) and improved further in Barge & Gorokhovski (75, 76). The second approach is to directly model the effects of unresolved flow on droplet motion by coupling the droplet lagrangian equation of motion with the stochastic properties of the instantaneous dissipation rate field 'seen' by the particle along its trajectory. This model is referred to as Stochastic Response of Inertial Particles or LES-STRIP. The idea of LES-STRIP was first introduced in Gorokhovski & Zamansky (77,78) and further improved in Barge (79). The generic formulations of these two approaches are outline in the following sections.

1.5.1 LES-SSAM – Stochastic modelling of sub-grid scale acceleration

Similar to the velocity field decomposition in classical LES, in LES-SSAM the acceleration field is decomposed into resolved component which is directly modelled by LES and an unresolved component which needs to be modelled.

$$\mathbf{a} = \bar{\mathbf{a}} + \mathbf{a}' \qquad \textbf{1-54}$$

For the sake of simplicity we consider the flow to be incompressible and the dispersed flow is dilute so that the momentum source term can be neglected. Then the total resolved flow acceleration obtained from the filtered Navier Stokes Equation (Eq. 1-37) can be written using Eq. 1-55.

$$\bar{\mathbf{a}} = \frac{\mathbf{D}\bar{\mathbf{u}}}{\mathbf{Dt}} = \frac{\partial \bar{\mathbf{u}}}{\partial \mathbf{t}} + \bar{\mathbf{u}}\boldsymbol{\nabla}.(\bar{\mathbf{u}}) = -\frac{\mathbf{1}}{\boldsymbol{\rho}}\boldsymbol{\nabla}.\bar{\mathbf{p}} + \boldsymbol{\nabla}.\ (\mathbf{2}\nu\bar{\mathbf{S}}) \qquad \textbf{1-55}$$

The second term in Eq. 1-54 represents the the total flow acceleration at the unresolved scales and is given by Eq. 1-56.

$$\mathbf{a}' = \frac{\mathbf{Du}'}{\mathbf{Dt}} = \frac{\partial \mathbf{u}'}{\partial \mathbf{t}} + \mathbf{u}'\boldsymbol{\nabla}.(\mathbf{u}') = -\frac{\mathbf{1}}{\boldsymbol{\rho}}\boldsymbol{\nabla}.\mathbf{p}' + \boldsymbol{\nabla}.\ (\mathbf{2}\boldsymbol{\nu}\boldsymbol{s}) \qquad \textbf{1-56}$$

The first assumption of LES-SSAM is to replace Eq. 1-56 with the following expression:

$$(\boldsymbol{a}')_{\mathbf{mod}} = -\frac{\mathbf{1}}{\boldsymbol{\rho}}\boldsymbol{\nabla}.\mathbf{p}^* + \boldsymbol{a}^* \qquad \textbf{1-57}$$

where a^* is the stochastic term, which replicates the total acceleration at unresolved scales. Since, the modelled acceleration a^* is not solenoidal, the *pseudo pressure* term *i.e.* $p*$ is introduced in Eq. 1-57 in order to maintain the incompressibility of the velocity field. The second assumption is to use the eddy viscosity model for the SGS stress tensor τ_{sgs} similar to classical LES. The third assumption is that the sum of $(\bar{\mathrm{a}} + a^*)$ is approximated to the instantaneous total acceleration $\hat{a}$ which solves for a surrogate velocity field $\hat{u}$. This leads to the formulation of *Stochastic Navier Stokes Equations (SNSE)*.

$$\hat{\mathbf{a}} = \frac{\partial \hat{\mathbf{u}}}{\partial \mathbf{t}} + \hat{\mathbf{u}}\,\boldsymbol{\nabla}.(\hat{\mathbf{u}}) = -\frac{\mathbf{1}}{\boldsymbol{\rho}}\boldsymbol{\nabla}.\ \overbrace{(\bar{\mathbf{p}} + \mathbf{p}^*)}^{\hat{\mathbf{p}}} + +\boldsymbol{\nabla}.\ (\mathbf{2}(\mathbf{v} + \mathbf{v_{sgs}})\hat{\mathbf{S}}) + \mathbf{a}^* \qquad \textbf{1-58}$$

The role of a^* is to stochastically force the acceleration of unresolved scales onto the filtered Navier Stokes equations, inorder to obtain statistical properties of acceleration similar to those reported in the literature (49-52). The experiments showed that the intermittency was manifested by long range correlation in time of the magnitude of

acceleration: a fluid particle trapped in the intertwined helical motion, preserved the magnitude of acceleration much longer than its direction. The latter was correlated on the Kolmogorov's timescale while correlation of the magnitude of acceleration was characterized by a few integral timescales. Such a dual-scale nature of the fluid acceleration is modelled by decomposing the SGS acceleration term a^* into two independent stochastic processes, one for the norm $a^*(t)$ and the other for the unit directional vector with components $e_i(t)$.

$$\mathbf{a^*(t) = a^*(t)e_i(t);\ \ e_i e_i = 1} \qquad \textbf{1-59}$$

The acceleration norm is simulated by the log-normal process. The log-normal stochastic differential equation for the sug-grid scale acceleration is given by Eq. 1-60.

$$\mathbf{da^* = -a^*\left(\ln\left(\frac{a^*}{a_\eta}\right) - \frac{3}{16}\sigma^2\right)\frac{dt}{T} + \frac{3}{4}a^*\sqrt{\frac{2\sigma^2}{T}}dW(t)} \qquad \textbf{1-60}$$

where $dW(t)$, is the increment of a standard Brownian process,$\langle dW\rangle$=0, $\langle dW^2\rangle$=dt. The dispersion term σ^2 is dependent on the local Reynolds number $\mathrm{Re}_\Delta = \frac{\nu_t}{\nu}$, through the Kolmogorov length scale η. The relaxation time T is correlated to the integral flow time scale.

$$\mathbf{\sigma^2 = \ln\frac{\Delta}{\eta} \quad and \quad T^{-1} = \frac{\nu_t}{\Delta^2}} \qquad \textbf{1-61}$$

The orientation of the SGS unit directional vector at each spatial point is emulated by Brownian random walk over a unit surface sphere, where the diffusion coefficient is inversely proportional to Kolmogorov time scale τ_η. In cartesian co-ordinates, the *Ornstein-Uhlenbeck (OU) process* for direction vector components is given by

$$\mathbf{de_i = -2\tau_\eta^{-1}e_i dt + \left(\delta_{ij} - e_i e_j\right)\sqrt{2\tau_\eta^{-1}}dW_{xj}} \qquad \textbf{1-62}$$

where W_{xj} represent independent components of Brownian motion W_x at spatial point x. Sabelnikov, Chtab and Gorokhovski (74) could not formulate an efficient algorithm for conserving the norm of unit vector. So, the evolution of orientation vector is approximated by randomly sampling the direction vector once in each time-step of the order of Kolmogorov's timescale, τ_η. The fluid particle statistics of LES-SSAM were compared with those of a standard LES and experiments (49). Compared to the classical LES, the results showed a much better prediction of Lagrangian acceleration and intermittent effects on speed increments. Recently Sabelnikov, Barge and Gorokhovski (75) derived

an efficient algorithm for directly integrating Eq.1-62 in cartesian co-ordinates. Additionally, they completed the stochastic equation by adding a relaxation term towards the direction of local vorticity vector calculated from resolved scales. The Eq. 1-62 was re-written into its equivalent form in Stratanoivch calculus and then integrated by using the mid-point method. The complete form of OU process with relaxation term in Stratanoivch sense is given by Eq. 1-63.

$$\mathbf{de_i = -h_{\perp,i} T_{rel}^{-1} dt - 2\tau_\eta^{-1} e_i dt + \sqrt{2\tau_\eta^{-1}} \epsilon_{ijk} dW_j \circ e_k} \qquad \mathbf{1\text{-}63}$$

Here ($\circ$) represents the Stratanoivch calculus and ϵ_{ijk} is the Levi-Civata symbol. And the first term represents the stochastic relaxation towards a presumed direction with its components h_i and its projection form $h_{\perp,i} = h_i - (h_j e_j) e_i$. The presumed direction vector h relaxes towards the unit vector $e_{\omega,i} = \frac{\omega_i}{|\omega|}$, where ω_i are the components of local resolved vorticity field. T_{rel} denotes the typical time of such relaxation which is inversely proportional to the resolved strain rate $\bar{S}$. This method is then assessed and compared with the DNS results of the lagrangian statistics of inertial particles in homogenous isotropic turbulence (HIT) and homogenously sheared turbulence (76, 79). In both the cases the LES-SSAM was able to account for both the non-Gaussian statistics of the inertial particle acceleration and the short auto-correlation time of the direction vector on relatively coarse grid compared to classical LES. Following the solution of SNSE, the lagrangian particle equation of motion can be re-written in terms of the surrogate velocity field characterizing the intermittency effects as shown in Eq. 1-64.

$$\boldsymbol{a_p = \frac{du_p}{dt} = \frac{\hat{u} - u_p}{\tau_p}} \qquad \mathbf{1\text{-}64}$$

1.5.2 LES-STRIP – Stochastic response of inertial particles

One of the main drawbacks of LES-SSAM method is that the stochastic models for acceleration are written in a Lagrangian way for fluid particles but realized locally on fixed grid points. This can be remedied to some extent by directly modelling the effects of unresolved scales directly on the particle dynamics. This has motivated Zamansky & Gorokhovski (77,78) to develop a stochastic SGS model for particle acceleration. In turbulent flows, the velocity of the droplet relative to the fluid is a random quantity. Along the particle trajectory, the main contribution to the statistics of this random quantity comes from turbulent fluctuations with frequencies of the order of τ_p^{-1} and higher. Part

of those frequencies is unresolved in LES when approximating the relative velocity in terms of filtered gas velocity. Applying the formula from (80): $\langle(u_f - u_p)^2\rangle = \int_0^\infty E(\omega)\frac{(\omega\tau_p)^2}{1+(\omega\tau_p)^2}d\omega$, where brackets denote averaging along the droplet trajectory, ω is the frequency and taking the spectral density of velocity fluctuations along the droplet trajectory as $E(\omega) \sim {\langle\varepsilon\rangle}/{\omega^2}$ the following expression can be derived:

$$\langle(\mathbf{u_f} - \mathbf{u_p})^2\rangle \sim \langle\boldsymbol{\varepsilon}\rangle\boldsymbol{\tau_p} \quad \textbf{1-65}$$

where $\langle\varepsilon\rangle$ is the mean dissipation rate along the particle path. Additionally, from Eq. 1-65 in case of statistical stationarity i.e. $\frac{d}{dt}\langle u_p{}^2\rangle$ =0, the correlation between the fluid velocity u_f and the droplet acceleration a_p can be obtained in terms of dissipation rate $\langle\varepsilon\rangle$.

$$\langle\mathbf{u_f a_p}\rangle \sim \langle\boldsymbol{\varepsilon}\rangle \quad \textbf{1-66}$$

Eq. 1-66 shows that the influence of fluid velocity on the droplet acceleration statistics is best defined in terms of the dissipation rate ε. Bec et al. (81) in their DNS study of inertial particles in homogenous isotropic turbulence (HIT), showed that the dissipation rate ε along the particle trajectory is highly intermittent, with large scale fluctuations spanning over a few Kolmogorov time scales. For these reasons it can be concluded that the dissipation rate presents itself as an interesting variable to model the intermittency effects of unresolved scales on droplet acceleration. The main idea of LES-STRIP is therefore to couple the particle equation of motion with the stochastic properties of the instantaneous dissipation field 'seen' by the particle along its trajectory. In LES-STRIP the particle acceleration is decomposed into resolved and SGS components as shown in Eq.1-67. While the first term represents the response to the large-scale sweeps governed by the resolved fluid velocity field and the second term is random and represents the particle acceleration conditionally averaged on the instantaneous dissipation rate ε along the particle path.

$$\mathbf{a_p} = \bar{\mathbf{a}}_\mathbf{p} + \left.\frac{\mathbf{du_p}}{\mathbf{dt}}\right|_{\boldsymbol{\varepsilon}} \quad \textbf{1-67}$$

In order to emulate the dual-scale nature of Lagrangian acceleration as explained in experiments (49-52) the SGS component is modelled as a product of two independent stochastic processes one for the norm of the acceleration $|\boldsymbol{a}|$ and the other for the orientation vector $\overrightarrow{\mathbf{e_p}}$.

$$\left.\frac{du_p}{dt}\right|_{\varepsilon} = |\boldsymbol{a}| \times \overrightarrow{\mathbf{e_p}} \qquad \textbf{1-68}$$

Two different strategies are used for modelling the droplet acceleration depending on droplet size. For droplets larger than Kolmogorov length scale i.e. $d_p > \eta$ an effective droplet response time is introduced by accounting for the turbulent viscosity at the scale of the droplet size, $\boldsymbol{\upsilon_{p,t}}$. The effective droplet response time is given by the following expression:

$$\boldsymbol{\tau_{p,t}} = \frac{\rho_p {d_p}^2}{18\rho\,(\upsilon + \upsilon_{p,t})} \qquad \textbf{1-69}$$

where $\upsilon_{p,t}$ is estimated from Eq. 1.70 using Prandtl's mixing length and Kolmogorov's scaling.

$$\boldsymbol{\upsilon_{p,t}} = \boldsymbol{\varepsilon^{1/3} d_p^{4/3}} \qquad \textbf{1-70}$$

Reformulating the droplet equation of motion in terms of effective response time $\tau_{p,t}$, the droplet acceleration can be re-written in the following form:

$$\mathbf{a_p} = \frac{\bar{u}-u_p}{\tau_{p,t}} = \frac{\bar{u}-u_p}{\tau_p} + 18\frac{\rho}{\rho_p}\frac{\varepsilon^{1/3}}{d_p^{2/3}}(\bar{\mathbf{u}} - \mathbf{u_p}) \qquad \textbf{1-71}$$

Assuming that the filter width Δ is greater than the droplet size, the norm of the relative velocity is approximated using the Kolmogorov scaling $|\bar{u} - u_p| \sim \varepsilon^{1/3} d_p^{1/3}$. Using this approximation Eq. 1-72 can be re-casted in the following manner:

$$\mathbf{a_p} = \frac{\bar{u}-u_p}{\tau_p} + 18\frac{\rho}{\rho_p}\frac{\varepsilon^{2/3}}{d_p^{1/3}}\overrightarrow{\mathbf{e_p}} \qquad \textbf{1-72}$$

For droplets smaller than Kolmogorov length scale i.e. $d_p < \eta$, assuming a similar decomposition of acceleration as shown in Eqn. 1-67 and estimating the norm of SGS fluctuations of relative velocity in terms of Eq.1-65 i.e. $|\bar{u}_f - u_p|_{sgs} = \sqrt{\varepsilon\tau_p}$ the expression for SGS acceleration can written as

$$\left.\frac{du_p}{dt}\right|_{\varepsilon} = \frac{|\bar{u}_f - u_p|_{sgs}}{\tau_p}\overrightarrow{\mathbf{e_p}} = \sqrt{\frac{\varepsilon}{\tau_p}}\overrightarrow{\mathbf{e_p}} \qquad \textbf{1-73}$$

Both the models require modelling of the statistical properties of dissipation rate ε and the unit directional vector $\overrightarrow{e_p}$. The evolution of the instantaneous dissipation rate ε along the particle trajectory is modelled using the stochastic equation for log-normal process of ε as proposed by Pope & Chen (82).

$$d\varepsilon = -\varepsilon\left(\ln\left(\frac{\varepsilon}{\bar{\varepsilon}}\right) - \frac{1}{2}\sigma^2\right)\frac{dt}{T} + \varepsilon\sqrt{\frac{2\sigma^2}{T}}dW(t) \qquad 1\text{-}74$$

where dW(t), is the increment of a standard Brownian process, ⟨dW⟩=0, ⟨dW^2⟩=dt. In difference to Pope & Chen (82) the dispersion term σ^2 is dependent on the local Reynolds number $Re_\Delta = \frac{\nu_t}{\nu}$, through the Kolmogorov length scale η. The relaxation time T is correlated to the integral flow time scale.

$$\sigma^2 = \ln\frac{\Delta}{\eta} \quad \text{and} \quad T^{-1} = \frac{\nu_t}{\Delta^2} \qquad 1\text{-}75$$

The locally resolved/filtered dissipation rate is used instead of its mean value. The second stochastic equation is for the unit directional vector which is modelled by a random process over a unit sphere. The orientation increments are expressed in terms of angular velocity of a point on the surface of the sphere which evolves according to an Ornstein-Uhlenbeck process and a projection factor ensuring that the norm of the orientation vector remains unity. Barge (79) in his PhD thesis improved the stochastic model for orientation vector of particle acceleration by modelling the evolution of the orientation vector in terms of Eq. 1-63 i.e. implicitly solving the Ornstein-Ulhenbeck process given by Eq. 1-62 in cartesian co-ordinates using the mid-point shceme.

1.5.3 Further motivation in LES-STRIP in the context of this thesis

In case of LES-SSAM, the stochastic models for the acceleration on residual scales in formulated in Lagrangian terms and at the same time is realized as local forcing without spatial correlation. On the other hand, LES-STRIP directly models the unresolved scale turbulence effects on particle motion in a lagrangian way with both spatial and temporal correlations. But in case of LES-STRIP, the forcing of the unresolved scale acceleration on the gas flow requires two-coupling of momentum transfer as shown in Eq. 1-30. This two-way coupling is very much relevant for diesel sprays given the high injection pressures.

1.6 In-Nozzle flow

1.6.1 Characterizing in-nozzle flow effects on atomization

The Lagrangian modelling of sprays do not consider the injector nozzle geometrical effects on atomization process and consequently the spray structure. But as discussed in Section 1.2.1, the flow development inside the injector nozzle has a paramount influence

on the near-nozzle spray formation process. While the in-cylinder parameters that affect spray-atomization are interrelated and cannot be controlled, the nozzle geometry is the only truly independent parameter that can be controlled to produce desired spray breakup characteristics. However, the internal flow and its effect on the spray breakup are not well understood due to complexities arising from flow asymmetries resulting from nozzle geometry, needle motion, turbulence, and flow cavitation. Hiroyasu et al (19) argued that cavitation is an additional source for enhancing the turbulent fluctuations inside the nozzle which are responsible for initiation of instabilities on the liquid jet surface. Moreover, experimental studies of Kim et al (21) and Arcoumanis et al (22) have shown that besides the geometrical origins of cavitation, cavitation could also be induced dynamically by turbulent structures in the sac volume, which seemed to develop transiently and periodically between adjacent nozzle holes as a function of the needle lift. Viewing in-nozzle flow turbulence as a precursor to cavitation in diesel sprays, we limit ourselves to non-cavitating turbulent flows in this thesis. Assuming the nozzle flow turbulence to be fully developed, Jiao et al (83) attempted to characterize the effect of turbulence intensity at the nozzle exit on primary atomization using DNS of a periodic pipe flow in conjunction with DNS of primary atomization. They showed the presence of different types of liquid structures separating from the liquid jet at different axial locations. But in reality, given the short nozzle length to diameter ratios of real-nozzles, the turbulence may not be fully developed. Owing to the small dimensions and high speed of the flow in real-nozzles, obtaining a complete realization of the flow dynamics using DNS is not possible. Bode et al (84) used wall-resolved LES to study the effect of nozzle taper ratio on turbulence intensity and subsequent atomization for variants of *ECN Spray-A* injector. It was shown that in comparison to non-convergent nozzles, the convergent nozzles have lower turbulence intensities but higher radial velocities. Agarwal & Trujillo (85) studied the effects of nozzle surface features on the prediction of spray atomization characteristics using wall resolved LES of in-nozzle flow. They have studied two representative geometries of *ECN Spray-A* injector with varying intensities of nozzle surface features. It was shown that even small differences of the order of 1μm in the surface features result in a difference of upto 1mm in the spray breakup length. At the nozzle exit, while both geometries have similar turbulence intensities, the differences were more profoundly seen in the non-axial velocity components. This highlights the relative importance of the non-axial velocity components on atomization process. Guerrassi et al (86, 87) used hybrid-LES approach for studying the nozzle flow

dynamics in non-cavitating injectors by comparing the resulting spray morphologies with experimental near-nozzle spray images. While small scale vortices were found inside the nozzle, large-scale string vortices were attributed to flow recirculation in the sac and flow acceleration into the nozzle hole. A strong correlation between the in-nozzle flow vortices and the surface instabilities on the liquid jet surface were shown. Guerrassi et al (88) also performed a similar study earlier using hybrid-LES for in-nozzle flow to characterize the influence of the needle lift on atomization process. While experimental studies of Kim et al (21) showed that lower needle lifts produce faster atomization and wider sprays, the main contributing factor for such behaviour was identified by (88) to be the non-axial turbulent kinetic energy.

1.6.2 LES modelling of nozzle flow – problem of near-wall turbulence

The main challenge in LES modelling of in-nozzle flow pertains to the *"near-wall problem of LES in wall-bounded flows".* As described by Jiménez (89), the near-wall region is characterized by the presence of low velocity streaks and thin elongated vortices of different length scales depending on their distance from the wall. The interactions between the multi-scale coherent structures makes the modelling of turbulence challenging. The wall-bounded flow is usually divided into an inner and outer layer. While the effects of viscosity and wall shear stress are important in the inner layer, their direct effects of mean velocity are negligible in the outer layer. At high Reynolds numbers an overall region ("log-layer") develops between the viscous and outer layers. The estimates of Chapman (90) have shown that the computational cost in terms of number of grid points 'N' to resolve a given fraction of turbulent kinetic energy using LES in the outer layer is independent of Re. On the other hand, the number of grid points required for resolving the viscous layer using LES is very demanding and is of the order of $N \sim O(Re^2)$. This cost scaling is referred to as the "*near-wall problem of LES*". This makes LES as costly as DNS. A schematic of the rough estimate of number of points required for resolved LES modelling as a function of Reynolds number is shown in Figure 1-11 . An alternative approach is to compute using classical LES approach with grid sizes determined by the size of the outer flow eddies and model the under-resolved velocity gradients in the viscous layer. In order to account for the effects of the discarded scales, various ideas and analytical frameworks have been proposed. The two widely used approaches for "*wall modelled LES"* are: hybrid RANS/LES methods or LES with SGS model. A detailed review of different "wall-resolved LES" models is provided by

Piomelli & Balaras (91), Bose & Park (92) and Larrson et al (93) and the references therein.

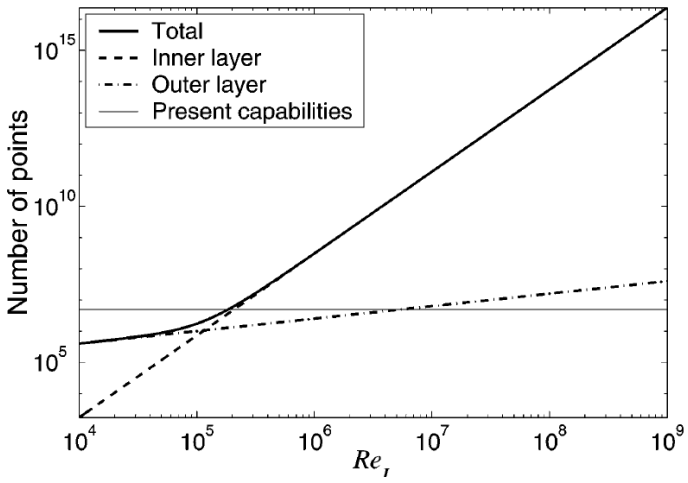

Figure 1-11 Number of grid points required to resolve a boundary layer (90)

1.6.3 Modelling wall-bounded flows using LES-SSAM model

At high Reynolds numbers when the near-wall turbulence is not well-resolved, Bose et al (95) have shown that the LES models tend to largely over-predict the streamwise velocity fluctuations and underpredict the cross-stream velocity fluctuations. Inaccurate predictions of cross-stream turbulence statistics are attributed to the inability of turbulence models to account for the dynamics of streak ejection and sweeps in the near-wall region. Streaks are typically low velocity regions which upon moving away from the wall interact with high speed quasi-streamwise vortices, making the flow highly intermittent. Given the relative importance of cross-stream velocity fluctuations on atomization, accurate modelling of in-nozzle flow effects on atomization requires accounting for the intermittency effects of near-wall turbulence. Recent DNS investigations (96-98) on acceleration characteristics in a channel flow have shown that the acceleration is a strongly intermittent variable. It was demonstrated that while the intermittency is linked to the dynamics of quasi-streamwise elongated vortical structures, the intensity of the intermittent nature is attributed to the presence of streaks in the viscous wall layer. Based on analysis of acceleration statistics obtained from DNS of channel flow, Zamansky, Vinkovic & Gorokhovski (99) have applied the LES-SSAM method for modelling intermittency effects in the near-wall region. They modelled the norm of acceleration as a product of characteristic velocity increment $\Delta u(y)$ at any given distance y from the wall and the frequency f at which this increments changes. The frequency is assumed to be a random variable, characterized by high frequency events near the wall

and low frequency events at the centerline of channel. A stochastic equation based on fragmentation process evolving along the wall normal distance is used to model the frequency *f*. And the acceleration orientation vector is modelled by random walk over a unit sphere, statistically relaxing towards isotropy as the wall distance increases i.e. moving away from the wall towards the centerline all directions become equally probable. The LES–SSAM approach is then assessed against the DNS data for channel flow of Jimenez & Hoyas (100) and Moser & Kim (101) at different flow Reynolds numbers. The model has shown better prediction of important statistics of velocity, acceleration and the energy spectra at small scales in comparison with classical wall modelled LES. But the LES-SSAM formulation used in (102) is specifically formulated for rectilinear coordinate systems and is difficult to be extended for modelling complex nozzle flow geometries. So, in this thesis, we attempt to model the SGS acceleration norm in terms of resolved dissipation rate $\bar{\varepsilon}$ and turbulent viscosity ν_{sgs} as shown in Eq. 1-76 and 1-77. Turbulent viscosity is obtained using the mixing-length eddy viscosity model. While in the near-wall region the turbulent length scale is assumed to be proportional to the wall distance y, in the outer layer the mixing length scale is assumed to be proportional to filter width.

$$|\boldsymbol{a}| = \left(\frac{\boldsymbol{\varepsilon^3}}{\boldsymbol{\nu_{sgs}}}\right)^{\mathbf{0.25}} \quad \textbf{1-76}$$

$$\boldsymbol{\nu_{sgs}} = \boldsymbol{min}(\,\boldsymbol{\kappa y}\,(\mathbf{1}-\boldsymbol{e}^{-\boldsymbol{y}/\boldsymbol{\delta_\nu A^+}})\,,\boldsymbol{C_s}\,\boldsymbol{\Delta})\,|\bar{\boldsymbol{S}}|^2 \quad \textbf{1-77}$$

Here δ_ν is the viscous length scale, κ and A^+ are the model constants assumed to take the values of 0.41 and 26 respectively. The orientation vector is modelled using the Ornstein-Uhlenbeck process given by Eq. 1-63 without the relaxation towards local vorticity field, making all directions equiprobable.

1.7 Primary atomization

While the phenomenological breakup models using the lagrangian spray modelling approach provide a good understanding of overall spray development process, a more detailed understanding of the physical coupling between in-nozzle geometry on the primary atomization requires detailed modelling of the growth of surface instabilities leading up to the jet breakup in the near-nozzle region. Commonly the one-fluid modelling approaches based on integration of the Navier-Stokes equations, identifying the gas-liquid interface at each time step are used to model primary atomization.

1.7.1 Interface tracking methods

In this section, a general description of governing equations as presented in Hermann & Gorokhovski (103) are shortly revisited, followed by outlining the challenges in modelling primary atomization in the context of LES. With assumption that the primary atomization process occurs at low Mach numbers and liquid-gas are immiscible, the flow is modelled by unsteady incompressible Navier Stokes Equations with variable density.

$$\nabla . \mathbf{u} = 0 \qquad \textbf{1-78}$$

$$\frac{\partial \rho \mathbf{u}}{\partial t} + \mathbf{u} . \nabla \rho \mathbf{u} = -\nabla . \bar{p} + \nabla . (\rho \nu (\nabla \bar{\mathbf{u}} + \nabla \bar{\mathbf{u}}^{T})) + \mathbf{T}_{\sigma} \qquad \textbf{1-79}$$

where T_σ represents the surface tension force acting at the interface. The liquid-gas interface is represented by a material surface whose motion is described by

$$\frac{d\mathbf{x}_f}{dt} = \mathbf{u}(\mathbf{x}_f, t) \qquad \textbf{1-80}$$

One way to describe the motion of interface is to solve the for a collection of marker particles placed on the interface. Here a pre-fixed number of marker particles are used to track the interface which could limit accuracy of interface description. This method was introduced by Harlow and Welch (104) and is referred to as *Marker and Cell (MAC)* method. Another interface tracking method uses an additional lagrangian grid to track the interface, while solve the flow velocity field on an under-lying Eulerian grid. Defining the complex interaction between the interface solved on two-different grids poses a challenge. This method developed by Tryggvason et al (105) is referred to as the *Front tracking method.* Alternative to the interface tracking approaches described above, the motion of liquid-gas interface is solved on a fixed Eulerian gird by solving the transport equation of a scalar marker function Ψ. This class of models are referred to as the *interface capturing methods.*

$$\frac{\partial \Psi}{\partial t} + \mathbf{u} . \nabla \Psi = 0 \qquad \textbf{1-81}$$

One way to solve the marker function is using the *Level Set Method* developed by Sussman et al (106), wherein Ψ represents the distance from the interface assuming a constant value Ψ_0 at the interface i.e. in the liquid $\Psi > \Psi_0$ and in the gas phase $\Psi < \Psi_0$. The main drawback of Level Set Methods is that they do not inherently preserve the liquid mass. Another widely used method is the *Volume of Fluid (VOF)* method developed by Hirt & Nicholas (107) wherein Ψ represents the liquid volume fraction in each computational cell.

$$\Psi = \frac{1}{V}\oint H(x - x_f)dx \quad \textbf{1-82}$$

$$H(x,t) = \begin{cases} 0 & \text{if x is in the gas} \\ 1 & \text{if x is in the liquid} \end{cases} \quad \textbf{1-83}$$

where *H* is a phase indicator function. The major advantage of VOF is that it is possible to construct algorithms for solving the volume fraction Ψ conserving the liquid mass. At the same time, owing to the discontinuous nature of Ψ the algorithms should ensure avoiding excessive numerical diffusion of Ψ. The accuracy of the VOF methods depends on the grid resolution which is also used for resolving the flow field. A more detailed review of different VOF methods is presented by Mirjalili et al (108). A general taxonomy of the different numerical approaches for interface tracking and capturing methods is shown in *Figure 1-12*. Since the smallest scales resolved even in a DNS is larger than the thickness of the interface itself, the presence of interface constitutes discontinuity in material properties on the resolved scales. Therefore, any material property α (either viscosity or density) is defined as the control volume averaged value of the two fluids, assuming that the individual fluid material properties are constant values.

$$\alpha_{cv} = \frac{1}{V_{cv}}\oint \alpha(x)\, dx = \alpha_l + \Psi(\alpha_l - \alpha_g) \quad \textbf{1-84}$$

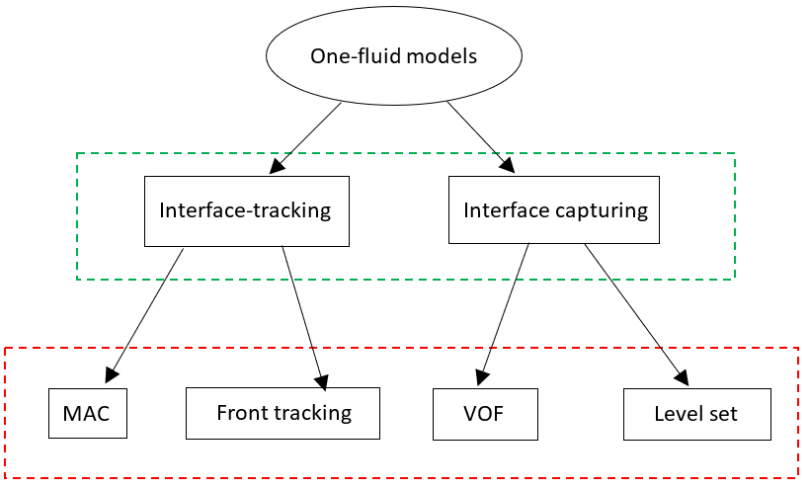

Figure 1-12 Classification of one fluid methods used for modelling primary atomization (105)

Next, even-though the Weber numbers of the liquid jet is very large, the primary atomization occurs on scales much smaller than the integral length scales, where the local Weber numbers are smaller, making the surface tension forces a relevant mechanism for breakup. Hence the accurate treatment of surface-tension forces is crucial even in DNS.

The most common method for calculating the surface tension forces is based on the continuum surface force (CSF) method proposed by Brackbill et al (109).

$$\mathbf{T_\sigma} = \boldsymbol{\sigma\kappa\,\nabla\Psi} \qquad \textbf{1-85}$$

where κ is the mean surface curvature.

1.7.2 Modelling SGS interface dynamics using LES-SSAM

Several DNS studies (110-113) of atomizing sprays with different interface tracking approaches have been performed for conditions approaching realistic injectors. But they are still far beyond the reach of general computing capabilities and for performing parametric studies for real injector configurations. On the other hand, several studies (114-117) use classical LES formulation in the single-phase regions of the flow and extend that formalism to regions containing the phase interface, neglecting effects of SGS dynamics of liquid-gas interface and its interaction with the turbulence. This kind of approach is usually referred to as *"quasi-DNS or high-fidelity LES"* and can be as expensive as the classic DNS. The actual filtered equations are expressed in the following way:

$$\frac{\partial\bar{\rho}\bar{\mathbf{u}}}{\partial t} + \bar{\mathbf{u}}\nabla.\overline{\rho\mathbf{u}} = -\nabla.\bar{\mathbf{p}} - \nabla(\bar{\tau} + \boldsymbol{\tau_{sgs}}) + \overline{\mathbf{T_\sigma}} \qquad \textbf{1-86}$$

The material properties like density and viscosity in Eq. 1-84 can be obtained from the filtered volume fraction $\bar{\Psi}$. So, the three terms that require modelling in Eq. 1-86 are $\bar{\Psi}$, $\overline{T_\sigma}$ and τ_{sgs}. The filtered transport equation for the volume fraction is given by Eq. 1-87.

$$\frac{\partial\bar{\Psi}}{\partial t} + \bar{\mathbf{u}}.\nabla\bar{\Psi} + \nabla.\overline{\mathbf{u}'\Psi'} = \mathbf{0} \qquad \textbf{1-87}$$

In case of atomization at high Weber numbers, the jet destabilization is localized at the subgrid level wherein even small perturbations in flow velocity field can result in distortion of the liquid/gas interface. Therefore, wrinkling of the SGS interface has a strong correlation with the intermittency of turbulence at small scales and modelling the unclosed term $u'\Psi'$ in Eq. 1-87 is essential for accurate description of the liquid-gas interface. Chesnel et al (118) have performed a priori DNS study and shown that the subgrid contribution of this term is significant and its effect on overall spray structure accumulates over time. Herrmann & Gorokhovski (119) attempted to formulate a dual scale approach to model the SGS interface dynamics. Their idea was to obtain a fully resolved interface geometry by modelling SGS velocity required to move the fully

resolved interface on an auxiliary grid using refined level set grid approach. Once knowing the fully resolved phase interface geometry, the unclosed terms associated with the material properties and surface-tension forces in the filtered Navier-Stokes equations can be directly closed using explicit filtering. As shown in Eqn. 1-88, replacing the filtered velocity with the fully resolved velocity u = $\bar{u} + u_{sgs}$, modelling of the term $u'\Psi'$ was avoided.

$$\frac{\partial \bar{\Psi}}{\partial t} + \left(\bar{\mathbf{u}} + \mathbf{u_{sgs}}\right).\nabla\bar{\Psi} = 0 \qquad \textbf{1-88}$$

The sub-grid scale velocity is expressed as the sum of three different terms: (a) u' is due to the effect of SGS eddies, (b) δu is the increment in the SGS velocity due to relative motion between two phases and (c) u_σ is the unresolved velocities induced by SGS surface tension forces. The detailed formulations of these terms are provided in (119). The idea was not tested yet for modelling primary atomization. Similar to the principles outlined in (119) we attempt to model SGS interface dynamics using LES-SSAM approach considering only the effects of unresolved scale turbulence. The idea is to account for the SGS acceleration in the filtered momentum equation (Eq. 1-86) using LES-SSAM method and solve for the Stochastic Navier Stokes Equation (Eq. 1-89).

$$\frac{\partial \overline{\rho u}}{\partial t} + \bar{\mathbf{u}}\nabla.\overline{\rho \mathbf{u}} = -\nabla.\bar{\mathbf{p}} - \nabla(\bar{\tau} + \boldsymbol{\tau}_{\mathbf{sgs}}) + \overline{\mathbf{T}_\sigma} + \bar{\rho}.\mathbf{a}_\mathbf{i}^*(\mathbf{t}) \qquad \textbf{1-89}$$

The SGS acceleration vector is decomposed into rapidly fluctuating orientation vector and the slowly changing norm of acceleration.

$$\mathbf{a}_\mathbf{i}^*(\mathbf{t}) = |\boldsymbol{a}|(\mathbf{t})\mathbf{e}_\mathbf{i}(\mathbf{t}) \qquad \textbf{1-90}$$

The norm is then modelled by stochastic log-normal process given by Eq. 1-60 and the evolution of orientation vector is modelled using the Ornstein-Uhlenbeck process given by Eq. 1-63. Using the surrogate velocity field obtained from the solution of Eq. 1-89, the interface is then constructed geometrically using *isoAdvection* VOF method recently proposed by Roenby et al (120-123).

1.8 Thesis overview and structure

The main objective of this thesis is to further the ideas presented in earlier sections for LES modelling of different spray sub-process by accounting for intermittency effects of unresolved scales and assess their performance in comparison with ECN experimental datasets with conditions reflective of high pressure diesel sprays. The first part of the

thesis concerns with development of a generalized class of stochastic models for different spray processes within the framework of Largrangian modeling of sprays based on the idea of LES-STRIP i.e. coupling the physical parameters governing the particle motion, breakup and evaporation with the stochastic properties of the viscous dissipation field 'seen' by the particle along its trajectory. The second part of this thesis deals with assessment of stochastic sub-grid models for acceleration in the simulation of in-nozzle flow and then to extend it for primary atomization in combination with VOF based on the ideas of LES-SSAM method. All the formulations are implemented and tested in OpenFOAM software (123). The OpenFOAM-v6.0 is used in the first part of the thesis for implementing and testing LES-STRIP models. In the second part of the thesis, OpenFOAM-v1812 is used for implementing and testing of LES-SSAM formulations. The important ideas as addressed chapterwise in the rest of the thesis are briefly described below:

1. A new stochastic breakup model based on the idea presented by Gorokhovski et al (124) is formulated to account for the intermittency effects on droplet breakup. In the rate equation expression for breakup given by Eq. 1-28 the parameters, breakup frequency and the critical radius are assumed to be stochastic random variables. Based on Gorokhovski (125), the definition of the critical radius is expressed by accounting for the inertia of the droplets. On the other hand, the frequency of linear relaxation towards such a critical radius is modelled stochastically in terms of the viscous dissipation rate "seen" by the droplet thereby accounting for the intermittency effects. The stochastic properties of dissipation rate are then modelled using the log-normal process given by Eq. 1-74. The performance of this model is then assessed with the ECN spray experiments and in comparison, to the state of art breakup models available in literature. The detailed description of the formulations of different spray breakup models, experimental conditions of non-evaporating and evaporating test cases and the computational results are presented in Chapter 2.
2. The LES-STRIP formulation as described in (77,78) was used for particle tracking in homogenous box turbulence with one-way coupling i.e. the particle motion does not affect the background fluid flow turbulence. In direct injection engines, given the high Reynolds numbers of the liquid spray, the momentum transfer from spray to the ambient gas flow is essential for flow dynamics. Moreover Barge (79) introduced into LES-STRIP the improved simulation of SGS acceleration

orientation vector using OU process. So this motivates us to assess the improved LES-STRIP approach within the framework of two-way coupling.

3. A new stochastic sub-grid scale model for droplet evaporation is formulated to account for the effects of SGS turbulent mixing. The classical d^2 law given by Eq. 1-19 approximates the vapor mass fraction "seen" by the droplet with the filtered vapor mass fraction in the cell. This is based on the assumption that the vapor diffused from the droplet surface is instantaneously mixed by the surrounding ambient air. This hypothesis is contradicted by experimental studies of individual droplets in a turbulent flow and as well as in sprays. Therefore, a new model is proposed wherein, the vapor mass fraction "seen" by the particle is modelled in terms of two competing phenomena i.e. rate of diffusion of vapor from the droplet surface and a finite rate of SGS turbulent mixing. The characteristic turbulent mixing time scale is then assumed to be a random variable, whose statistics are again described in terms of the log-normal process for the dissipation rate. The detailed description and assessment of the evaporation and dispersion models in comparison with the non-reacting ECN diesel spray experiments and evaporating spray experiments in co-axial combustion chamber performed by Sommerfeld and Qui (126) is provided in Chapter 3.
4. The formulations of the stochastic equations for the acceleration norm in LES-SSAM method for channel flow proposed by Zamansky et al (99) is too convoluted for modelling wall turbulence in complex injector nozzle geometries. Moreover in earlier formulation of LES-SSAM model, the evolution of the unit direction vector of SGS acceleration was modelled by random walk method. So an improved LES-SAM approach with simplified formulations for the acceleration norm with OU process for the evolution of the direction vector are proposed in Eq. 1-78 and Eq. 1-79. The performance of the new LES-SSAM formulations are validated by comparing with the DNS data for channel flow at high Reynolds numbers. Then the nozzle flow is simulated using the LES-SSAM method to generate the turbulence data for primary atomization modelling.
5. In the approach of Herrmann & Gorkhovski (119) they tried to obtain a fully resolved interface by modelling the effect of SGS velocity on advection of interface in the transport equation of filtered vapor mass fraction using level set method. A similar approach is adapted in thesis. As described in Section 1.7.2, we attempt to account for the SGS acceleration terms in momentum equation using

LES-SSAM method and obtain a fully realized velocity field . Then the interface is constructed using *iso-advector method*, a new geometrical VOF method recently proposed by Roenby et al (120). This methodology is applied for modelling primary atomization of a diesel spray jet issuing form a standardized ECN injector. The detailed description of the formulations of *iso-advector* VOF method, experimental conditions and the computational results of both in-nozzle flow and primary atomization are enumerated in Chapter 4.

2 STOCHASTIC MODEL FOR SPRAY BREAKUP

Over the past two decades the Lagrangian Monte Carlo procedure proposed by Dukowicz (53) has been the basis for modelling liquid sprays in turbulent flows owing to its non-diffusive character and simplicity in implementation. As explained in the introduction chapter, the spray is modelled as an ensemble of discrete "*parcels or computational droplets",* each representing a certain number of physical droplets with same properties like velocity, size, temperature etc. The lagrangian description of the spray is used in conjunction with the Eulerian description of the turbulent gas phase and different '*sub-models*' describing the interaction between the two-phases. Even though this approach is valid for the volumetrically dilute regions, it is extended to the dense spray region for modelling of the atomization processes using phenomenological spray breakup models. These phenomenological breakup models assume that the primary atomization process and subsequent fragmentation of ligaments by secondary breakup are indistinguishable. Based on this idea, the initial liquid jet development is modelled using large "*spherical liquid blobs*" typically of the size of the nozzle diameter, which undergo a series of breakup events mimicking a certain breakup mechanism. The different breakup models in literature can be classified into two categories: deterministic and stochastic models. The first class of models are mostly based on idea of *"instability mechanisms"* formulated by Reitz & Bracco (11), describing the growth rate of unstable waves on the surface of a liquid droplet which when sufficiently amplified results in its breakup. The breakup frequency and size of child droplets are assumed to be proportional to the frequency and wavelength of the largest perturbation resulting in breakup of the parent droplet. While Reitz's model considers instabilities leading to the primary breakup, Reitz & Diwakar (58) developed a breakup rate expression, with breakup time correlations corresponding to the "*bag*" and "*stripping*" modes of secondary breakup. Pilch & Erdman (59) used experimental data to develop correlations for breakup frequency and maximum stable radius corresponding to all the different modes of secondary breakup. Reitz & Baele (127) developed a generalized hybrid model wherein the rate of breakup is governed by growth of Kelvin-Helmholtz (KH) instabilities in the near-nozzle region and by Rayleigh-Taylor

(RT) instabilities in the far-field spray region. This model often referred to as "*KH-RT"* is widely used for modelling the high-pressure diesel sprays. Among the instability-based breakup models, the *Taylor-Analogy breakup (TAB)* model proposed by Amsden & O'Rourke (54) is another important and widely used approach. The TAB model represents the oscillations of the parent droplets as a spring-mass system, with breakup presumed to occur when the oscillations in the parent droplet exceed a certain critical value. Wehrfritz & Vuorinen (128) recently characterized the performance of these breakup models using an implicit LES by quantitatively comparing integral spray quantities like liquid/vapor penetration lengths for high-pressure ECN diesel spray experiments. They have shown that a good agreement with experimental data is obtained only at sufficiently fine mesh resolutions (approximately 32-62.5µm). Such a fine mesh implies resolving more and more turbulent scales implicitly by LES. This indicates that the SGS turbulence effects on spray breakup is not well accounted for, by these deterministic models.

On the other hand, experimental studies of Shavit & Chigier and Grout & Dumouchel (27-29) have shown that the characteristic feature of turbulent spray atomization is its fractal nature i.e. atomization is a non-deterministic process with no preferred breakup length/time scales. This may result in formation of a large spectrum of droplets with different sizes. But the aforementioned deterministic models produce "single-scale" droplets with sizes proportional to wavelength of fastest-growing instabilities. So Gorokhovski (126) first proposed a stochastic breakup model wherein the droplet size distribution in long-time limit relaxes towards an exponential distribution. Also, a new formulation for the critical radius, towards which the size distribution relaxes to, was hypothesized based on inertial response of droplet to turbulent fluctuations. Gorokhovski & Saveliev (129-130) showed that due to scaling symmetry, solution of the general fragmentation equation with constant fragmentation frequency goes through two universal asymptotics with increase in time. They showed that the initial droplet size distribution upon fragmentation over a certain time attains the Kolmogorov's (131) log-normal distribution (first asymptotic) and with further progress in time, it reaches a fractal/power distribution (second asymptotic). It was shown that while the first asymptotic solution can be modelled using two parameters namely first and second moments of fragmentation intensity spectrum, the second asymptotic solution needs only one parameter i.e. the ratio of the first two moments. From first universality, it was argued that the fragmentation equation reduces exactly to a Fokker-Plank equation. Gorokhovski

& Apte (132,133) formulated a stochastic breakup model based on analytical solution of the Fokker Plank equation for LES modelling of sprays. They also defined the closures for the logarithmic moments in terms of local flow field properties in the context of LES. But still the time scale characterizing the breakup was based on TAB model (74) for low weber numbers and is a deterministic parameter. So Habchi (134) further extended the stochastic model by defining the breakup time scale and the maximum stable droplet radius as a function of local gaseous weber number representing different breakup regimes. More recently Jones & Letteiri (135) proposed a stochastic model where the breakup time scale is decomposed into a deterministic component calculated from the TAB model (74) and a randomly fluctuating component expressed in terms of the resolved dissipation rate field. The size of the child droplets is sampled from a presumed size distribution function derived based on binary breakup mechanism of Lasheras et al (136).

In this thesis, we use a new stochastic model based on the idea proposed by Gorokhovski et al (125) to account for the intermittency effects of SGS turbulence on the spray breakup. For this a new expression for the critical radius was introduced in terms of the instantaneous dissipation rate field (ε) and the droplet inertia, showing that the droplet breaks-up in response to strong fluctuations in gas-phase turbulence compared to droplet inertia. In order to account for the intermittency effects of unresolved scales, ε was randomly sampled from Obukhov-62 (137) log-normal distribution once over the breakup time. In this thesis we use the same idea for modelling spray breakup in the context of LES, wherein instead of the random-sampling of dissipation rate, the stochastic log-normal process for dissipation rate proposed by Pope & Chen (82) as given by Eq. 1-74 is used to simulate the fluctuations in dissipation rate 'seen' by the droplet along its trajectory. The main objective of this chapter is to study the performance of the new breakup model in comparison with the state of art models and experimental data corresponding to ECN spray conditions. Hereafter a brief description of different breakup models is provided.

2.1 Lagrangian Breakup models

2.1.1 Instability mechanisms – KH-RT model

Early theoretical studies on liquid jet breakup are based on *linear stability analysis* of unstable waves growing at the liquid-gas interface. This approach was first developed by

Rayleigh (138) to study capillary instabilities on an inviscid liquid jet. The hypothesis of this theory is that even an infinitesimally small disturbance on the surface of a liquid column would exponentially grow over time and result in its breakup under a capillary based instability (i.e. surface tension is the pre-dominant mechanism for breakup). Further he hypothesized that the disturbance with maximum growth rate is responsible for the jet breakup and the resulting droplet size is of the same order of magnitude of wavelength of this disturbance. Later Weber (139), Sterling & Sliecher (140) further extended the linear stability analysis of Rayleigh by including the viscous and aerodynamic force effects on the jet breakup. The fundamental ideas of the temporal linear stability theory as presented in Sirignano and Mehring (141) is shortly revisited here. A circular jet of radius r is perturbed by an axisymmetric wave with a Fourier component of the form:

$$\boldsymbol{\eta = \eta_0 e^{(\omega t + ikx)}} \qquad \textbf{2-1}$$

In Eq. 2-1, η is the displacement of the liquid surface in response to the perturbation, x is the axial direction in which the jet evolves , η_0 is the magnitude of initial perturbation at the nozzle exit, k is wavenumber of the perturbation and ω is the complex frequency whose real part, ω_r represents the growth rate of the perturbation. Linearizing the conservation equations governing the evolution of the liquid jet and also the liquid-gas boundary conditions in terms of small perturbations of the form shown in Eq.-2-1 results in a *dispersion equation*. Depending on the initial conditions for the perturbations, the dispersion equation results in a different type of instability. In case of primary atomization, Reitz & Bracco (11) used *Kelvin-Helmholtz (KH)* instability to describe the growing surface waves due to the aerodynamic shear force induced by the relative velocity between the liquid and gas phase. The analytical solution of the dispersion equation for KH-instability gives the maximum growth rate ($\omega = \Omega$) and the corresponding wavelength ($\lambda = \Lambda_{KH}$) in terms of non-dimensional numbers like Taylor number T, Ohnesorge number Z and gaseous Weber number We_g. The expressions for Λ_{KH} and Ω_{KH} are given by Eq. 2-2 and 2-3.

$$\frac{\boldsymbol{\Lambda_{KH}}}{\boldsymbol{r}} = \mathbf{9.02}\frac{\boldsymbol{(1+Z^{0.5})(1+0.4T^{0.7})}}{\boldsymbol{(1+0.87We_g^{1.67})^{0.6}}} \qquad \textbf{2-2}$$

$$\boldsymbol{\Omega_{KH}}\frac{\boldsymbol{\rho_l r^3}}{\boldsymbol{\sigma^{0.5}}} = \frac{\boldsymbol{(0.34+0.38We_g^{1.5})}}{\boldsymbol{(1+Z)(1+1.4T^{0.6})}} \qquad \textbf{2-3}$$

where ρ_l, σ are the liquid density and surface tension. On the other hand, the experimental studies of Hwang and Reitz (142) characterized the secondary breakup of droplets in high

velocity fuel sprays using the *Rayleigh-Taylor (RT) instabilities.* The RT instability describes the growth of surface waves at the interface when a heavier fluid is accelerated in a lighter fluid. In case of the secondary breakup the liquid droplet with higher density is accelerated into the ambient gas with significantly lower density by aerodynamic drag force. As a result, the droplet surface is susceptible to growth of RT instabilities. Using linear stability analysis to obtain dispersion equation for RT instability, Bellman and Pennington (143) derived the expressions for maximum growth rate ($\omega = \Omega_{RT}$) and the corresponding wavelength ($\lambda = \Lambda_{RT}$). The expressions for Λ_{RT} and Ω_{RT} are given by Eq. 2-4 and 2-5.

$$\Lambda_{RT} = 2\pi \sqrt{\frac{3\sigma}{a_p(\rho_l - \rho_g)}} \quad \textbf{2-4}$$

$$\Omega_{RT} = 2\pi \sqrt{\frac{2}{3\sqrt{3\sigma}}\left[a_p(\rho_l/\rho_g - 1)\right]^{1.5}} \quad \textbf{2-5}$$

where a_p, ρ_g are the droplet acceleration and gaseous density. A schematic of the two instability mechanisms is shown in *Figure 2-1*.

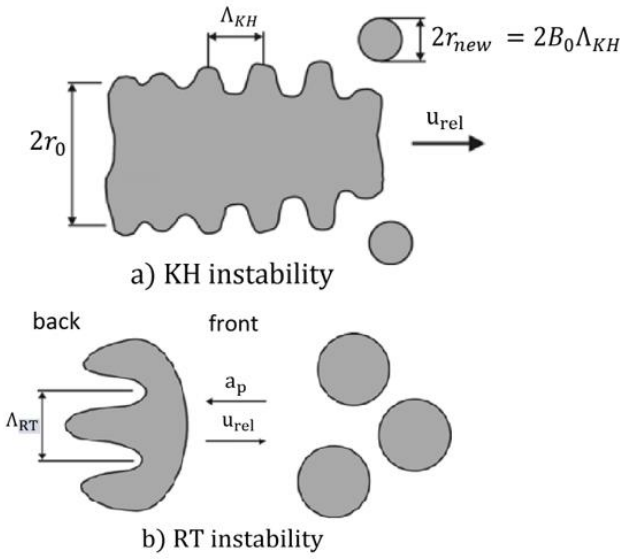

Figure 2-1 Schematic representation of (a) Kelvin-Helmholtz (b) Rayleigh-Taylor instabilities (9).

A hybrid spray breakup model based on KH-RT instabilities developed by Reitz and Baele (127) is widely used for Lagrangian spray modelling. In the near nozzle region, the KH instability is applied, wherein new child droplets are created from surface waves stripped off from a parent droplet with radius *r*. A new parcel containing product drops

of size r_{new} is created and added to the computations. The size of these child droplets is assumed to be proportional to the wavelength as shown in Eq.2-6, where $B_0 = 0.61$.

$$r_{new} = B_0 \Lambda_{KH} \quad \textbf{2-6}$$

The rate of change of droplet size at any given time *t*, depends on the difference between the actual droplet radius *r* and an equilibrium droplet size which is equal to the child droplet radius r_{new} and the characteristic breakup time τ_b. The breakup rate expression is given by Eq. 2-7.

$$\frac{dr}{dt} = \frac{r - r_{new}}{\tau_b} \quad \textbf{2-7}$$

$$\tau_b = B_1 \frac{r}{\Omega_{KH} \Lambda_{KH}} \quad \textbf{2-8}$$

When using KH instability for modelling primary atomization the influence on nozzle flow parameters are not accounted for. This is implicitly modelled through the adjustable model constant B_1. Too small values of B_1result in much faster stripping of the parent blobs producing a large number of child droplets, while too large values B_1 do not accurately represent the breakup rate. Kitaguchi et al (144) has performed optimization studies using LES modelling of spray breakup and found $B_1 \sim 10$ as a good choice for balancing between the accuracy and the computational costs. So, we use the same value for B_1 throughout this study. The secondary breakup of droplets is modelled using the RT instability. The breakup time is found to be equal to the inverse of the frequency of the fastest growing wave i.e. $\tau_b = \Omega_{RT}^{-1}$. At a time $t = \tau_b$, the parent droplet completely breaks down into small droplets whose size is proportional to the wavelength this disturbance i.e. $r_{new} = \Lambda_{RT}$. A schematic of the KH-RT model is shown in *Figure 2-2*.

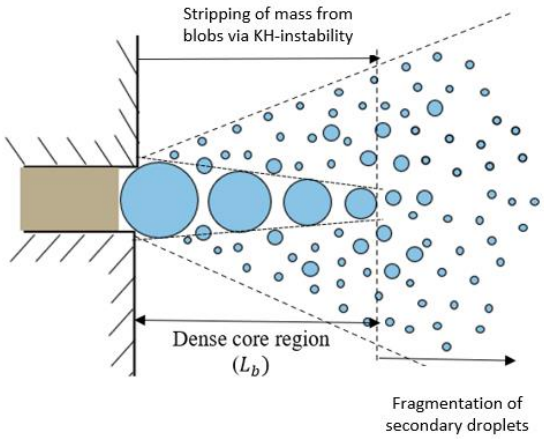

Figure 2-2 Schematic of hybrid KH-RT breakup model

2.1.2 Fragmentation theory – FOKKBREAK model

In this section we revisit briefly the stochastic breakup model based on Gorokhovski & Savelivev's (129) Fokker-Plank equation for fragmentation of droplets. This model is referred hereafter to as the *Fokkbreak* model. Kolmogorov considered the breakup of solid particles as a random discrete process. He assumed that the probability of breaking each parent particle into a given number of parts is independent of the size of the parent particle. In the context of the central limit theorem he predicted that, after a large number of breakup events, such a discrete process would yield a log-normal distribution of particle sizes. Using a scaling formulation, Kolmogorov's (131) scenario states that each breakup event reduces the typical length of fragments, $r \Rightarrow \alpha r$,by an independent random multiplier $\alpha, 0 \leq \alpha \leq 1$. In the framework of Kolmogorov's scenario, consider the drop, which breaks up at the large Weber number. The breakup of the droplets into secondary droplets is theorized to be independent of the instantaneous size of the individual parent drop. A given drop is assumed to break with the frequency ν_0 (the number of breakups per unit time) to form, in mean, the number of new droplets (q_0) after each breakup action. Let r_1 be a characteristic length scale (or radius) of the parent drop. Suppose that the radius of each product droplet is within the interval $r_1[\alpha, (\alpha + d\alpha)]$ with the probability $q(\alpha)d\alpha$,

$$\int_0^1 \boldsymbol{q(\alpha)d\alpha = 1} \qquad \textbf{2-9}$$

Then, $q_0 q(\alpha)d\alpha$ is the probable number of new droplets in the interval $r_1[\alpha, (\alpha + d\alpha)]$. Here, according to Kolmogorov's hypothesis, the probability density $q(\alpha)$and the mean number of new born particles, q_0 , are independent of radius r_1. Let the number of parent drops in the interval dr_1 be given by $F(r_1)dr_1$, where $F(r_1)$ is the number distribution function of parent drops. Then, $\nu_0(r_1)\mathrm{F}(r_1)dr_1$ is the probable number of parent drops undergoing breakup per unit time and $\nu_0(r_1)\mathrm{F}(r_1)dr_1 q_0 q(\alpha)d\alpha$ is the probable number of new droplets formed per unit time in the interval $r_1[\alpha, (\alpha + d\alpha)]$. From all the produced particles, we only select those that fall within the interval of length scales *[r, r+dr]*. This is achieved by the characteristic function of a small interval :

$$\boldsymbol{dr.\delta(r - \alpha r_1)} = \begin{cases} \boldsymbol{1} & \boldsymbol{if\ \alpha r_1 \in [r, r + dr]} \\ \boldsymbol{0} & \boldsymbol{if\ \alpha r_1 \notin [r, r + dr]} \end{cases} \qquad \textbf{2-10}$$

where $\delta(r-\alpha r_1)$ is Dirac delta function. The total number of new droplets that enter into *[r, r+dr]* per unit time can be written in the following way : $dr\int_0^{\infty}\int_0^1 q_0 q(\alpha)\delta(r-\alpha r_1)\nu_0(r_1)F(r_1)d\alpha dr_1$. After integration over r_1, the population balance equation reduces to Eq. 2-11.

$$\frac{\partial F(r)}{\partial t} = \left(q_0\hat{I}_+ - 1\right)\nu_0(r)F(r) \qquad \textbf{2-11}$$

Here the breakup operator $\hat{I}_+F$ is given by Eq. 2-12.

$$\hat{I}_+F = \int_0^1 F\left(\frac{r}{\alpha}\right)q(\alpha)\frac{d\alpha}{\alpha} \qquad \textbf{2-12}$$

Integrating population balance equation (Eq. 2-11) over the entire *r* spectrum yields an equation for the number of particles $n(t)=\int_0^{\infty}F(r,t)dr$:

$$\frac{\partial n}{\partial t} = \langle\nu_0\rangle_f(q_0-1)n \qquad \textbf{2-13}$$

Here, $\langle\nu_0\rangle_f = \int_0^{\infty}\nu_0(r)F(r)dr$ is the mean rate of fragmentation. Eq. 2-11 can be rewritten for the normalized distribution function, $f(r,t) = \left({}^1/_n\right)F(r,t); \int_0^{\infty}f(r)dr = 1$, in the following form:

$$\frac{\partial f}{\partial t} = \left(\hat{I}_+ - 1\right)\nu f + \left(1-\frac{1}{q_0}\right)(\nu - \langle\nu\rangle_f) \qquad \textbf{2-14}$$

where

$$\hat{I}_+\nu f = \int_0^1 \nu\left(\frac{r}{\alpha}\right)f\left(\frac{r}{\alpha}\right)q(\alpha)\frac{d\alpha}{\alpha} \qquad \textbf{2-15}$$

$\hat{I}_+\nu f$ is the breakup operator, $\nu(r) = q_0\nu_0(r)$ is the production frequency of new particles, and, correspondingly $\langle\nu\rangle_f = q_0\langle\nu_0\rangle_f$. When the breakup frequency is independent of particle size ($\nu = \langle\nu\rangle$), Eq. 2-14 becomes

$$\frac{\partial f}{\partial t} = \nu\left(\hat{I}_+ - 1\right)f \qquad \textbf{2-16}$$

Gorokhovski & Saveliev (130) under scaling symmetry assumptions obtained the asymptotic solution (Eq. 2-17) of fragmentation equation (Eq. 2-16).

$$f(r,t) = \lim_{t\to\infty}\frac{1}{R}\frac{1}{\sqrt{2\pi\langle ln^2\alpha\rangle\nu t}}exp\left(-\frac{\langle ln\alpha\rangle^2}{2\langle ln\alpha\rangle}\nu t\right)$$

$$\times exp\left(-\frac{(ln(r/R))^2}{2\langle ln^2\alpha\rangle\nu t}\right)\left(\frac{R}{r}\right)^{1-\langle ln\alpha\rangle/\langle ln^2\alpha\rangle} \qquad \textbf{2-17}$$

where R is initial length scale at time t_0, $R = e^{(lnr)_{t_0}}$. From Eq. 2-17 it follows that with increasing time, the initial size distribution indeed goes through the Kolmogorov's log-normal distribution (first intermediate asymptotics), with only two parameters first and second logarithmic moment of fragmentation intensity spectrum $q(\alpha)$ i.e. $\langle ln\alpha \rangle$ and $\langle ln^2\alpha \rangle$. But with the further progress of time, the log-normal multiplier in the Eq. 2-17 tends to unity and a new final asymptotics appears with fractal distribution, with only one parameter i.e. ratio of first two logarithmic moments $\langle ln\alpha \rangle / \langle ln^2\alpha \rangle$. Since the first asymptotic depends only on the first two logarithmic moments, which means that changing of higher moments $\langle ln^k\alpha \rangle$ does not affect its solution at larger times in comparison with lifetime of breaking droplet, Gorokhovski & Saveliev (130) argued that the higher moments can be set to zero and the fragmentation equation can be reduced exactly to Fokker-Plank equation given by Eq. 2-18.

$$\frac{\partial f(r)}{\partial t} = \left[-\frac{\partial}{\partial r} r \langle ln\alpha \rangle + \frac{1}{2!} \frac{\partial}{\partial r} r \frac{\partial}{\partial r} r \langle ln^2\alpha \rangle \right] \nu f(r) \qquad \textbf{2-18}$$

Gorokhovski & Apte (132) then applied the steady-state solution of the Fokker-Plank equation for sampling the droplet size after breakup. Assuming a Dirac-delta function for the logarithm of radius (x_0) of a parent droplet breaking up in the time interval $[\, t_i, t_{i+1}]$, the change of initial delta function is governed by Fokker Plank equation shown in Eq. 2-18 and as time progresses to $\nu t = 1$, the distribution of $x = ln(r)$ is given by Eq. 2-19.

$$\mathbf{T(x_0)} = \frac{1}{\sqrt{2\langle \ln^2 \alpha \rangle}} \exp\left(-\frac{(x - x_0 - \langle \ln \alpha \rangle)^2}{2\langle \ln^2 \alpha \rangle} \right) \qquad \textbf{2-19}$$

where $\langle \ln \alpha \rangle$, $\langle \ln^2 \alpha \rangle$ are the model parameters. Therefore, the sampling procedure for new droplets is realized by the following function:

$$\int_{-\infty}^{x} T(x)\, dx = \frac{1}{2}\left[1 + \operatorname{erf}\left(\frac{x - x_0 - \langle \ln \alpha \rangle}{\sqrt{2\langle \ln^2 \alpha \rangle}} \right) \right] = \eta \qquad \textbf{2-20}$$

Here $\eta \in [0,1]$, is the random number for sampling droplet size after breakup. The breakup frequency ν given by Eq. 2-21 is based on expression obtained by Faeth et al (25) for the characteristic timescale for aerodynamic shear breakup of droplets.

$$\nu^{-1} = \frac{r}{U_{rel}} \sqrt{\frac{\rho_l}{3\rho_g}} \qquad \textbf{2-21}$$

Kolmogorov argued that in case of turbulent mixing of two liquids with existence of capillary forces between them, the filament of one liquid involved in turbulent motion with another will be stretched by the turbulent stresses upto the moment when a balance

with the capillary forces is reached. At this moment droplets of near critical radius are produced. The force balance between the capillary forces and the turbulent shear forces on droplet surface is given by Eq. 2-22.

$$\frac{2\sigma}{r_{cr}} \sim \frac{1}{2}\rho_g \langle U_{rel}^2 \rangle \qquad \textbf{2-22}$$

Here r_{cr} is the critical radius, ρ_g is the gas density, σ is the surface tension and $\langle U_{rel}^2 \rangle$ is the relative droplet to gas velocity. Gorokhovski (125) developed a new formulation for critical radius as shown in Eq. 2-24 by accounting for droplet inertia when estimating the as shown in Eq. 2-23.

$$\langle U_{rel}^2 \rangle = \bar{\varepsilon}\tau_p \qquad \textbf{2-23}$$

$$r_{cr} = K_1 \left(\frac{\sigma v}{\rho_l \bar{\varepsilon}}\right)^{1/3} \qquad \textbf{2-24}$$

Here K_1 is the modelling constant assume to be of order of unity. And while ρ_l is density of the liquid phase, v, $\bar{\epsilon}$ are the viscosity and the resolved dissipation rate in the gas phase respectively. From the first moment of size distribution, Gorokhovski & Apte (132) showed that the choice of the parameters for $\langle ln\ \alpha \rangle$ and $\langle ln^2\ \alpha \rangle$ should satisfy the Eq. 2-25 in order to ensure disintegration of droplets.

$$\langle ln\ \alpha \rangle + \frac{1}{2}\langle ln^2\ \alpha \rangle < 0 \qquad \textbf{2-25}$$

In view of the fractal nature of the turbulent atomization process at high Weber numbers, there exists no preferred length scale between the parent droplet size and the maximum stable droplet size for the child droplet formed after the breakup. Based on this hypothesis, the first moment of the size distribution can be expressed by Eq. 2-26. And, the ratio of the logarithmic moments is modelled using Eq. 2-27 by Gorokhovski & Apte (132).

$$\langle ln\ \alpha \rangle = ln\left(r_{crit}/r\right) \qquad \textbf{2-26}$$

$$-\frac{\langle ln^2\ \alpha \rangle}{\langle ln\ \alpha \rangle} = K_2\ ln\left(r/r_{crit}\right) \qquad \textbf{2-27}$$

After some initial testing, $K_1 = 1$ and $K_2 = 0.1$ are found to give good prediction of spray characteristics for ECN Spray conditions. Therefore, this choice of parameters is used all throughout this study.

2.1.3 Sub-grid scale intermittency - Stochastic Breakup model

Gorokhovski et al (124) formulated a new stochastic breakup model accounting for the SGS intermittency effects. Their idea is based on Kolmogorov's hypothesis that breakup of droplets occurs when shear force induced by gas phase turbulence exceeds the restorative capillary forces. The breakup rate is modelled using the relaxation equation (Eq. 2-28), wherein the breakup frequency and relaxation radius are assumed to be characterized by the turbulent dissipation rate in the gas phase ε, liquid density ρ_l and surface tension σ.

$$\frac{dr}{dt} = \frac{r - r*}{\tau*} \qquad \textbf{2-28}$$

Similar to Eq. 2-24, the expression for critical relaxation radius $\boldsymbol{r*}$ was based on Gorokhovski (125). Unlike in Eq. 2-24, the strongly fluctuating instantaneous dissipation rate is used to model the critical radius (Eq. 2-29) showing that the breakup of the droplets occurs in response to strong turbulent fluctuations in the gaseous phase. And the intermittency effects on breakup is introduced by modelling the breakup frequency in terms of instantaneous dissipation rate $\boldsymbol{\varepsilon}$. The breakup frequency is obtained by dimensional analysis of the aforementioned physical parameters as shown in Eq. 2-30. The constant $\boldsymbol{C_\tau}$ is used to scale the breakup frequency to obtain correct breakup rate matching the experimental data. Gorokhovski et al (124) assumed the constant to be of the order unity i.e. $\boldsymbol{C_\tau = 1}$.

$$r^* = K_1 \left(\frac{\upsilon\sigma}{\varepsilon\rho_l}\right)^{1/3} \qquad \textbf{2-29}$$

$$\tau^* = \mathrm{C_\tau} \left(\frac{\sigma^2}{\varepsilon^3 \rho_l^2}\right)^{1/5} \qquad \textbf{2-30}$$

In order to introduce the SGS intermittency effects in Eq. 2-28, the instantaneous dissipation rate ε was sampled randomly from Obhukhov's (137) log-normal distribution (Eq. 2-31) once over a breakup time by Gorokhovski et al (124).

$$\mathrm{P(x)dx} = \frac{1}{\sqrt{(2\pi\sigma^2)}} \frac{\mathrm{dx}}{\mathrm{x}} \exp\left[-\left(\frac{\ln \mathrm{x} - \mu}{\sigma}\right)^2\right] \qquad \textbf{2-31}$$

where $\mu = -\frac{1}{2}\sigma^2 = 0.4\mathrm{Re_p}^{3/4}$, $\mathrm{Re_p}$ is the particle Reynolds number, $\mathrm{x} = \frac{\varepsilon}{\langle\varepsilon\rangle}$, ε is the instantaneous dissipation rate and $\langle\varepsilon\rangle$ is the mean dissipation rate. The random sampling approach does not account for the temporal correlations of the instantaneous dissipation

rate field (ε) along the particle trajectory. So instead of the randomly sampling ε, we propose to use the log-normal stochastic process (84) given by Eq. 1-74 for modelling the fluctuations of ε along the droplet trajectory. The Eq. 1-74 is re-written here as for the sake of consistency.

$$d\varepsilon = -\varepsilon\left(ln\left(\frac{\varepsilon}{\bar{\varepsilon}}\right) - \frac{1}{2}\sigma^2\right)\frac{dt}{T} + \varepsilon\sqrt{\frac{2\sigma^2}{T}}dW(t) \qquad \textbf{2-32}$$

where dW(t), is the increment of a standard Brownian process, ⟨dW⟩=0, ⟨dW^2⟩=dt. The dispersion term σ^2 is dependent on the local Reynolds number $Re_\Delta = \frac{\nu_t}{\nu}$, through the Kolmogorov length scale η. The relaxation time T is correlated to the integral flow time scale. The local filtered dissipation rate $\bar{\varepsilon}$ is here used instead of its mean value ⟨ε⟩.

$$\sigma^2 = \ln\frac{\Delta}{\eta} \quad \text{and } T^{-1} = \frac{\nu_t}{\Delta^2} \qquad \textbf{2-33}$$

Here Δ is the filter width proportional to computational grid size, η is the Kolmogorov length scale.

2.2 Experimental and Computational details

2.2.1 ECN Spray experiments

A standardized fuel injector with a convergent hydro-ground nozzle with a diameter of 90 µm is used in this study. The spray experiments were performed using *n-dodecane* as a surrogate, in a constant volume spray chamber as described in Section 1.2.3. This experimental configuration is usually referred to as "*ECN Spray-A*". First the non-evaporating spray experimental data (145,146) for two different injection pressures i.e. 150MPa and 50MPa, to evaluate the performance of the three breakup models described in earlier section. The detailed parameters for non-evaporating spray conditions are listed in . In case of non-evaporating sprays, the performance of the breakup models is characterized in terms of following parameters:

1. *Spray tip penetration* which is defined as the distance where the accumulated liquid droplet mass reaches 95% of the total liquid mass injected at any given instance of time.
2. *Sauter mean diameter* is the characteristic size of spray droplets defined as the ratio of total volume to total surface area of all the droplets in the spray.

$$d_{32} = \frac{\sum d^3}{\sum d^2} \qquad \textbf{2-34}$$

3. *Breakup Length* is defined as the distance from the injection location until which the droplets reach a stable diameter and no further breakup occurs. This determines the rate of spray breakup and is quantified in terms of the evolution of the gaseous Weber number along the spray centerline.

Non-evaporating spray conditions		
Experimental conditions	ECN-A1	ECN-A2
Injection pressure (MPa)	150	50
Ambient pressure (MPa)	3	2
Fuel temperature (K)	363	333
Ambient temperature (K)	440	343
Injected mass (mg)	3.46	7
Injection duration (ms)	1.5	5
Nozzle diameter (µm)	90	90

Table 2-1 : Non-evaporating spray experimental conditions

Evaporating spray conditions	
Experimental conditions	ECN-A1v
Injection pressure (MPa)	150
Ambient pressure (MPa)	6
Fuel temperature (K)	363
Ambient temperature (K)	900
Injected mass (mg)	3.46
Injection duration (ms)	1.5
Nozzle diameter (µm)	90

Table 2-2: Evaporating spray experimental conditions

Next in order to study the influence of spray breakup on fuel-air mixing in non-reacting conditions, an evaporating ECN Spray-A experiment (45,46) is numerically modelled. The different parameters corresponding to the evaporating spray condition is listed in *Table 2-2*. The vaporization process and subsequent fuel-air mixing are characterized in terms of following parameters:

1. *Liquid Penetration Length:* The spray tip penetration for an evaporating spray attains steady state value, where the total evaporation rate is equal to the fuel

injection rate. Therefore, it is a direct measure of the overall spray vaporization rate.

2. *Local Gas phase velocities and vapor mass fraction profiles*. While the gas phase velocities quantify the air-entrainment process which is a direct result of interaction between the liquid spray and turbulent gas-phase flow, the vapor mass fraction distributions quantify the local evaporation and fuel-air mixing.

2.2.2 Numerics – mesh, initial and boundary conditions

The simulation approach is based on a weakly-compressible flow solver with an implicit pressure treatment based on the PISO-algorithm. While for discretization of spatial gradients second order numerical schemes are used, an implicit first-order Euler scheme is used for the time integration. The specific details of the finite volume discretization and interpolation methods used in OpenFOAM are available in (147). A cylindrical domain of length 100mm and a diameter 50mm is used to computationally represent the spray chamber as shown in *Figure 2-3(c)*. The O-Grid technique with fully hexahedral cells is used to discretize the computational domain. The base coarse mesh referred to "*C-Grid"* consists of a uniform cell size of 250µm both in axial and radial directions. Another finer mesh referred to as *"F-Grid"* with a cell size linearly varying from 125µm to 250µm both in axial and radial directions is used to study the effects of mesh resolution. The mesh refinement is used in the high shear flow regions close to the injector-nozzle exit (region-1 shown in Figure 2-1(c)). Several studies (128, 148-149) have reported computations with much smaller grid sizes close to 32µm. But in principle, for Lagrangian particle tracking of droplets the cell grid size should be typically larger than the droplet size. In this study, we used the classical "blob" approach of Amsden & O'Rourke (54), wherein the initial size of all the droplets injected is assumed to be the same as the nozzle diameter. Therefore, the minimum grid size should be greater than or equal to the magnitude of nozzle diameter which in this case is 90µm. So, we limit our studies to maximum cell size of 125 µm. The blob velocity u_p is calculated from the mass flow rate profile $\dot{m}(t)$ as shown in Eq. 2-35.

$$\boldsymbol{u_p = \frac{\dot{m}(t)}{\rho C_d A}} \qquad \textbf{2-35}$$

Here C_d is the discharge coefficient and A is the area of the injector orifice. The mass flow rate profiles are obtained from the experimental measurements. The orientation of the initial velocity is defined randomly within a user-specified *"spray cone angle"*. A

schematic representation of the mass flow rate profile and the spray cone angle are shown in *Figure 2-3(a-b)*. The number of parcels injected is determined by the computational time step (Δt) and the total number of parcels to be injected per second (PPS) which is pre-defined manually. In this study a spray cone angle of 12 degrees is used along with a fixed PPS of 2×10^7. The time step is defined by the maximum Courant number $Co_{max} = \frac{\Delta t}{\Delta x}$ where Δx is the cell size. In all the calculations, a Co_{max} of 0.2 is used.

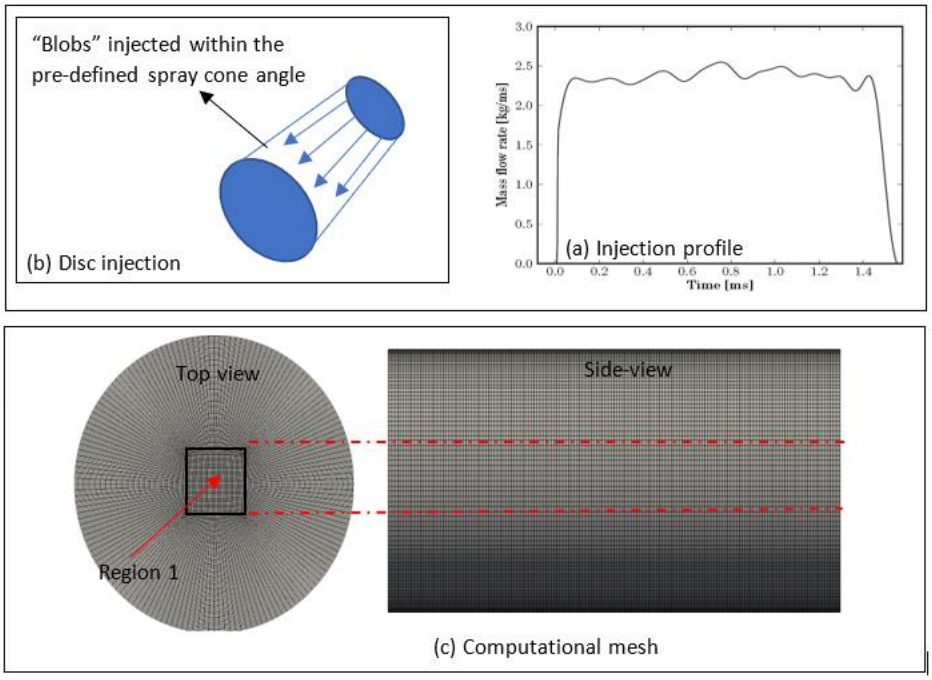

Figure 2-3: Schematic representation of the spray initial conditions and mesh

2.3 Results & discussion

2.3.1 High pressure non-evaporating spray

In this section, first the results from *Spray-A1* experiment corresponding to high pressure fuel spray injection are discussed in this section. *Figure 2-4* shows the comparison of temporal evolution of the spray tip penetration with the experimental data for the three breakup models investigated using two different computational grids. While all the three breakup models over-predict the penetration on *C-grid* as shown in *Figure 2-4(a)*, the stochastic breakup model gives much better prediction of the spray evolution compared to the other two models. On the other hand for *F-grid*, while both the stochastic and Fokkbreak models accurately represent the spray tip evolution, the KH-RT breakup model still over-predicts the penetration with an error of about 20% in comparison to the experiment at a time *t=1.5ms* after start of injection (ASOI). As the *F-grid* predicts the

spray evolution more accurately, the droplet statistics obtained from *F-grid* are used for further investigation of results.

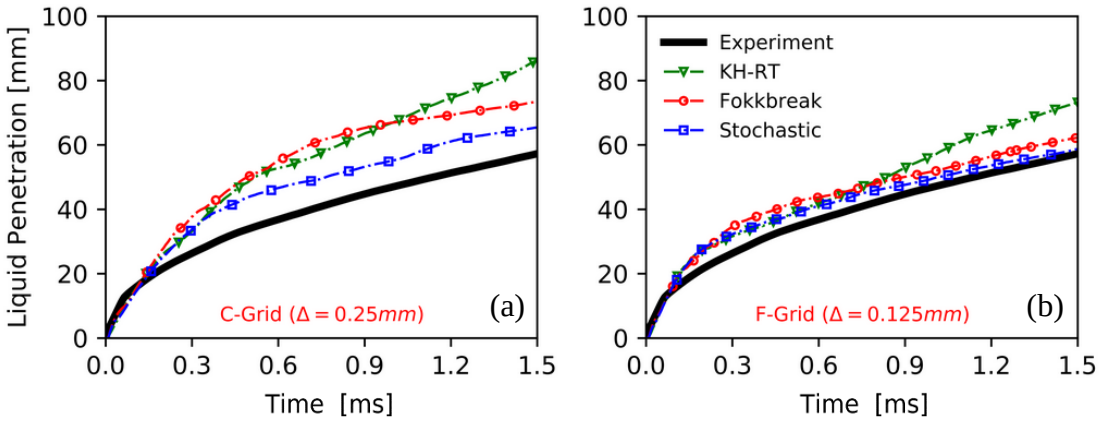

Figure 2-4 : Comparison of temporal evolution of spray tip penetration for different breakup models for the test case Spray A1 test case.

Figure 2-5 shows the comparison of the spatial evolution of the sauter mean diameter (SMD) along the spray centreline for the three breakup models. The SMD is calculated for a fully developed state of spray *i.e.* at *t= 1.5ms ASOI.* The experimental SMD in the near-nozzle region shows that the spray breakup is in the turbulent atomization regime, where disintegration of the liquid jet starts right from the nozzle exit. Contrary to the experimental findings, the KH-RT breakup model shows a gradual decrease in SMD with large droplets proliferating downstream upto a distance of about 10mm from nozzle exit. The rate of decrease in the SMD for the stochastic breakup model is in-between the KH-RT and Fokkbreak models. A close-up of the SMD distribution in the near-nozzle region shows the stable SMD predicted by different models in comparison to the experiment. Similar to the breakup rate, the stable SMD predicted by the stochastic model is in-between that predicted by Fokkbreak (which is closer to the experiment) and the KH-RT models. Another important parameter to characterize the spray breakup is the spatial evolution of mean gaseous Weber number (We_g) as defined by Kastengren et al (145). They defined We_g in terms of the SMD and the average axial velocity of liquid spray (V) at a given axial distance x from the injector as shown in Eq. 2-36.

$$We_g(x) = \frac{\rho_g V^2 SMD}{\sigma} \qquad \textbf{2-36}$$

Experimental studies Zhao et al (150) have shown that the typical critical Weber number is around i.e. $We_{cr} \sim 10$. But Kastengren et al (145), calculated We_g in terms of the mean droplet velocity and not the local relative velocities between the droplet and the turbulent

gas. So, it was argued that the critically stable radius is obtained at much higher We_g values i.e. at We_{cr} ~80. And the distance from the nozzle exit where the We_g attains this critical value We_{cr} is referred to as the *breakup length*, where atomization is almost complete.

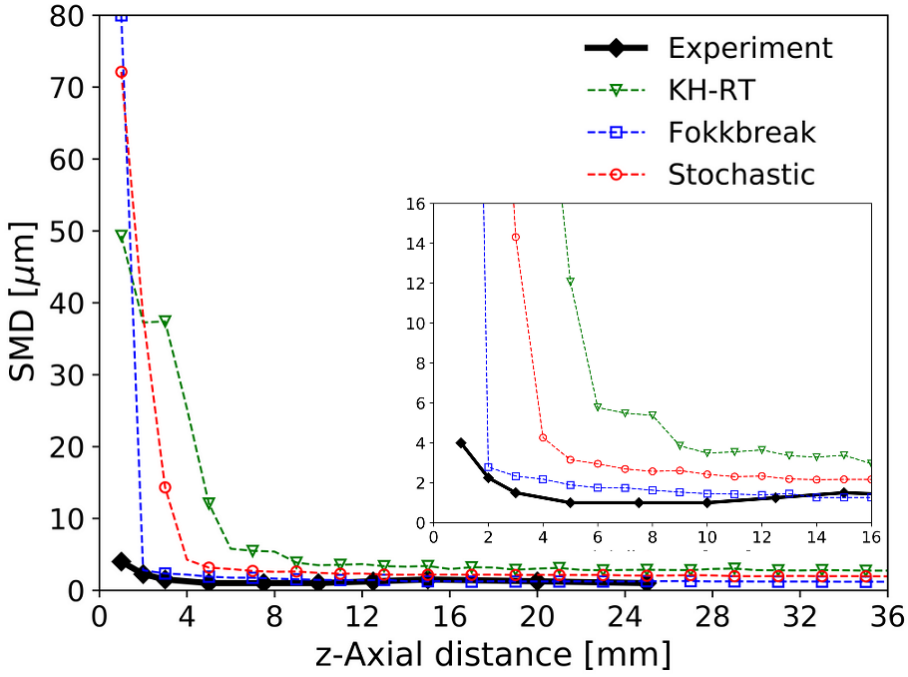

Figure 2-5: Evolution of the Sauter mean diameter (SMD) axially along the centreline of the spray at time t=1.5ms ASOI for Spray A-1 test case

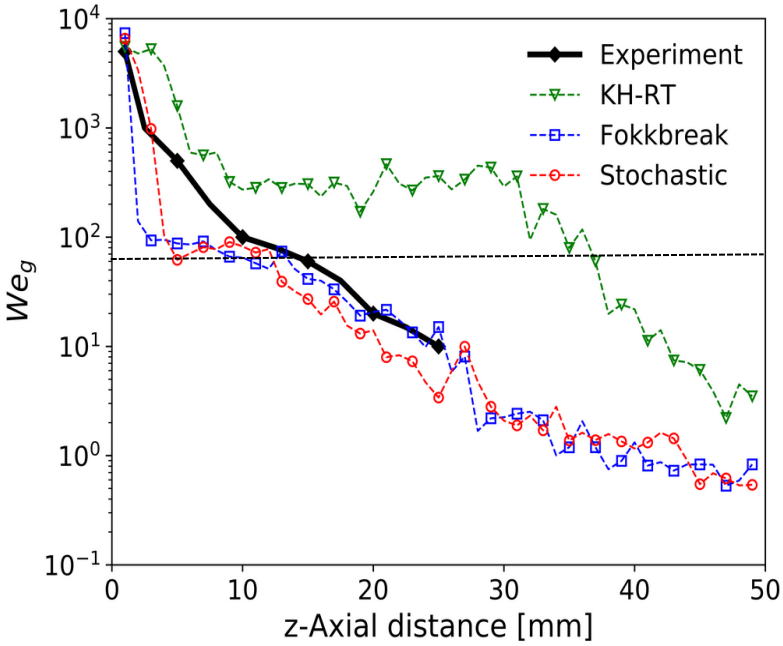

Figure 2-6: Comparison of the spatial variation of We_g predicted by different models at time t=1.5ms ASOI for Spray A-1 test case.

The experiments (145) also pointed out that a larger of number of droplets are in the size range of 0.5-2µm. So, a comparison of the droplet size distribution predicted by the different breakup models is shown in *Figure 2-7*. The Fokkbreak model predicts a smaller spectrum of droplet sizes concentrated in the 0.5-2 µm range with a high probability of droplets close to the SMD (~1.25 µm). On the other hand, the stochastic breakup model has broad spectrum of droplets clustered in the range of 1-3 µm and does not predict the presence of any droplets in the sub-micron range. Unlike these models with a continuous size distribution, in case of KH-RT model we observe two distinct size distributions. The broad spectrum of larger droplets in the range of 2-4 µm can be because of the continuous stripping of the droplets from the *blobs* by the KH instability and the smaller spectrum of sub-micron droplets could be attributed to catastrophic breakup by the RT instability. But in reality, the experiments have not indicated the presences of such kind of discontinuity in the droplet size-distribution.

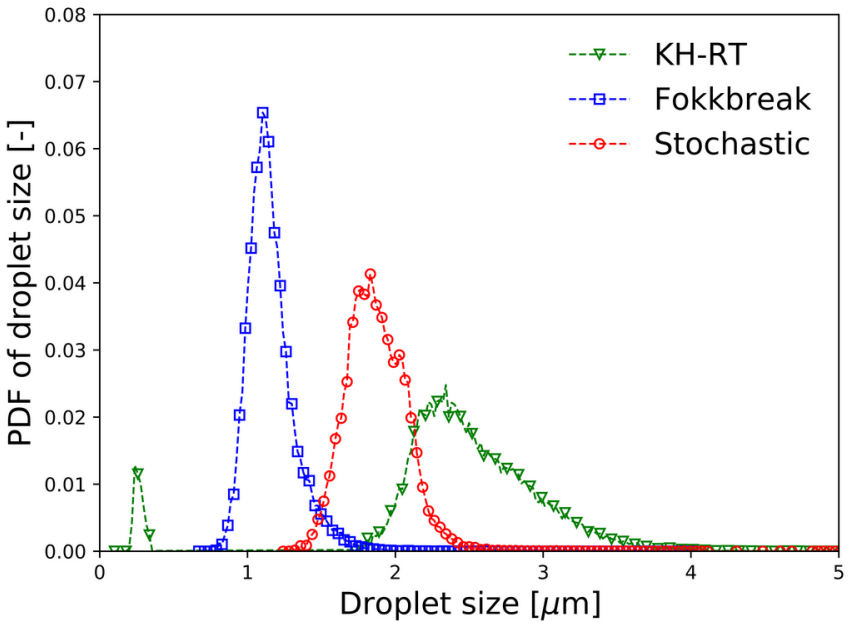

Figure 2-7: Probability distribution function (PDF) of droplet size at t= 1.5ms ASOI with the vertical dashed line representing the SMD values predicted by the breakup models

Figure 2-8 shows the instantaneous spray structure predicted by KH-RT breakup model with the computational parcels scaled by their droplet size. Also, the intensity of the gray scale represents the droplet size.

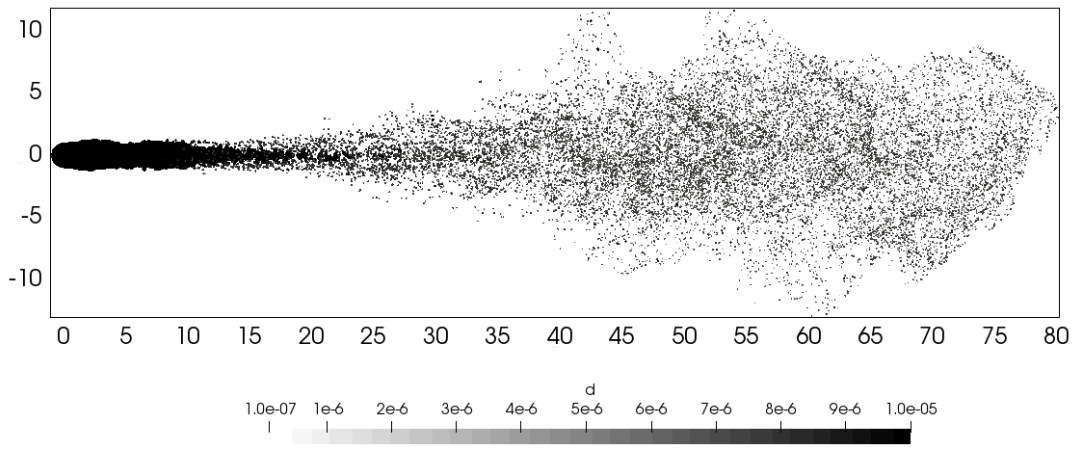

Figure 2-8: Instantaneous spray image of KH-RT breakup model at t=1.5ms ASOI

From the spray structure, we can notice that the presence of two distinct regions characterized by droplets of different sizes. First is the presence of a prolonged intact spray core extending upto a distance of 25 mm with parcels with sizes much larger than 10µm as shown in *Figure 2-9 (a)*. This shows that stripping of parcels through KH instability is the dominant mechanism in this region. This is followed by rapid disintegration of parcels in the downstream region upto 35-40 mm by RT instability forming large spectrum of parcels ranging between 0.1-5µm. This is shown in *Figure 2-9 (b)*. Then there is a transient spray region where dispersion of smaller parcels by turbulent gas phase becomes more relevant.

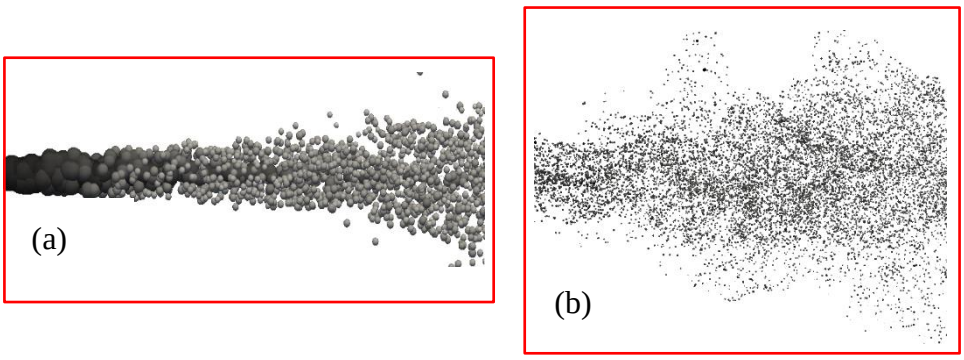

Figure 2-9: Close-up of KH-RT spray structure (a) stripping of droplets by KH instability in the near-nozzle region (b) droplet size in far-field spray region

Figure 2-10 shows the instantaneous spray images of the Fokkbreak and Stochastic breakup models. The spray images corroborate with the droplet size distribution i.e. Fokkbreak model gives much smaller droplets in the size range of 0.5-1µm than the Stochastic model. The presence of much smaller droplets which tend to follow the gaseous flow could explain higher spray tip penetration in case of Fokkbreak model. On the other hand, we notice that the stochastic breakup model gives a much wider spectrum

of parcel sizes ranging from 1-10 µm spread all over the spray. Usually we use a finite number of parcels to statistically represent the spray. The number of actual droplets in a parcel is calculated from mass conservation after each breakup event. *Figure 2-11* shows a more realistic representation of the spray structure in terms number of droplets per parcel for Fokkbreak and Stochastic breakup models. Here while the parcel size is scaled by the droplet size, the number of droplets per parcel is shown on a logarithmic gray scale. The larger parcels have very few droplets compared to the smaller parcels as shown by the color intensity scaling. Usually the droplet statistics like size-distribution or the SMD, are weighted averaged by the number of droplets per parcel and hence filter out the presence of larger parcels shown in the spray images. Even though Fokkbreak model shows a wide spectrum of parcels, a significantly large number of parcels have sizes close to its SMD value. The stochastic model on the other hand has higher probability of parcels with sizes much larger than the SMD. This shows that the stochastic model gives a most realistic statistical representation of the spray compared to the Fokkbreak model.

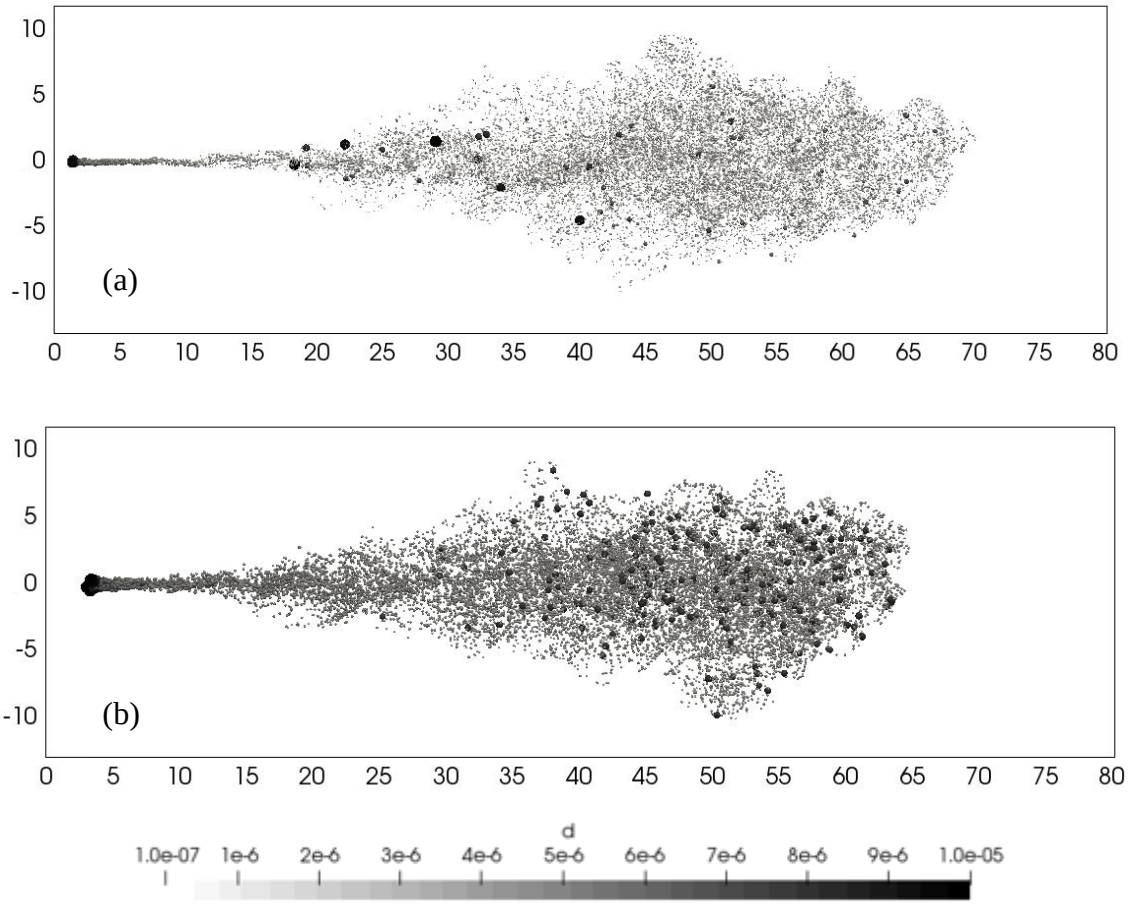

Figure 2-10: Instantaneous spray images of (a) Fokkbreak (b) Stochastic breakup models at t=1.5ms ASOI

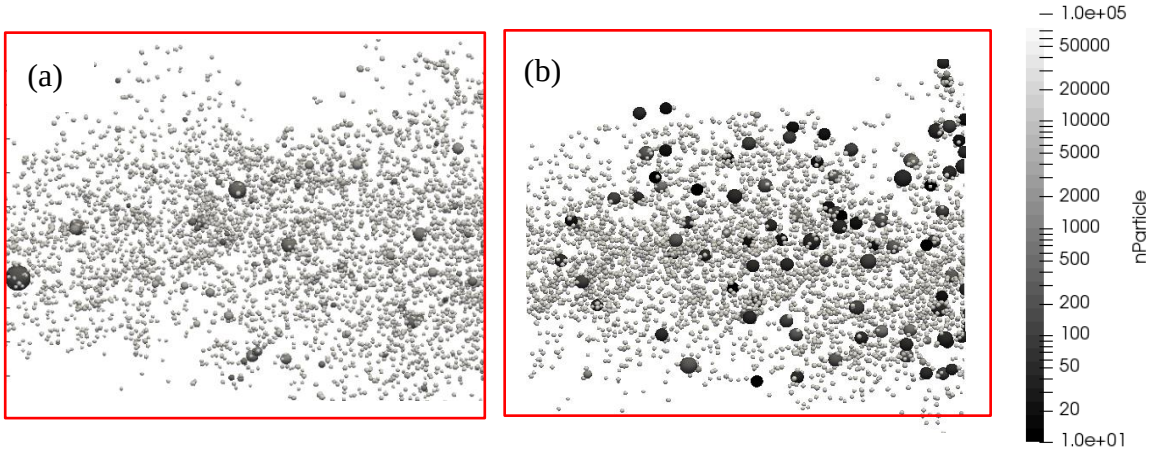

Figure 2-11: Close-up view of spray structure for (a) Fokkbreak and (b) stochastic breakup model with logarithmic scaling of the number of droplets per parcel.

Several studies (151-154) have emphasized the equivalence between a turbulent gaseous jet and high-pressure fuel sprays. In case of gaseous jets, the jet velocity should decay with axial distance z as $U \propto 1/z$. Similarly, in case of high-pressure sprays, it shown in (128) that after an initial acceleration in the gas-phase velocity due to momentum transfer from the liquid droplets, the gas-phase velocities are expected to decay rapidly along the spray centreline. Because the gas-phase is accelerated by the spray, the axial gas-phase velocity profiles in the dense-spray region are a good measure of the momentum transfer between the liquid spray and the gas-phase. So, a comparison of the filtered gas-phase jet velocities for different breakup models is shown in *Figure 2-12*. The centreline gas-phase velocities of Stochastic and Fokkbreak models reflect the strong acceleration of spray which reaches a maximum approximately around 5mm, followed by its rapid deceleration. In case of KH-RT model, the high initial centreline gas-phase velocities indicate much higher momentum transfer from the fuel droplets to the gas-phase. Moreover, it can be seen that the gas-phase flow retains the initial momentum all throughout the spray length without exchanging it with droplets due to entrainment process. The causal effect relationship between liquid-gas momentum transfer and the breakup in the case of KH-RT is complicated to explain because the breakup parameters and the droplet acceleration are both modelled in terms of the relative velocity of the gas and the droplet $(\bar{u} - u_p)$ which is under-resolved by LES.

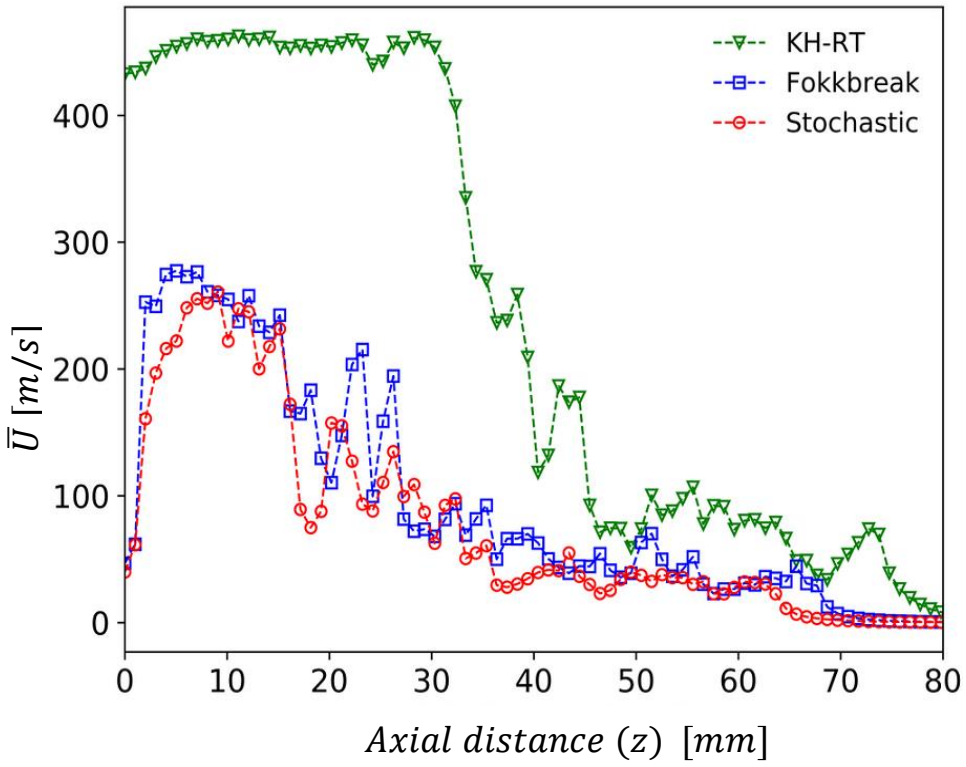

Figure 2-12: Instantaneous axial gas phase velocities along the spray centreline at time t = 1.5ms ASOI

2.3.2 Low pressure non-evaporating spray

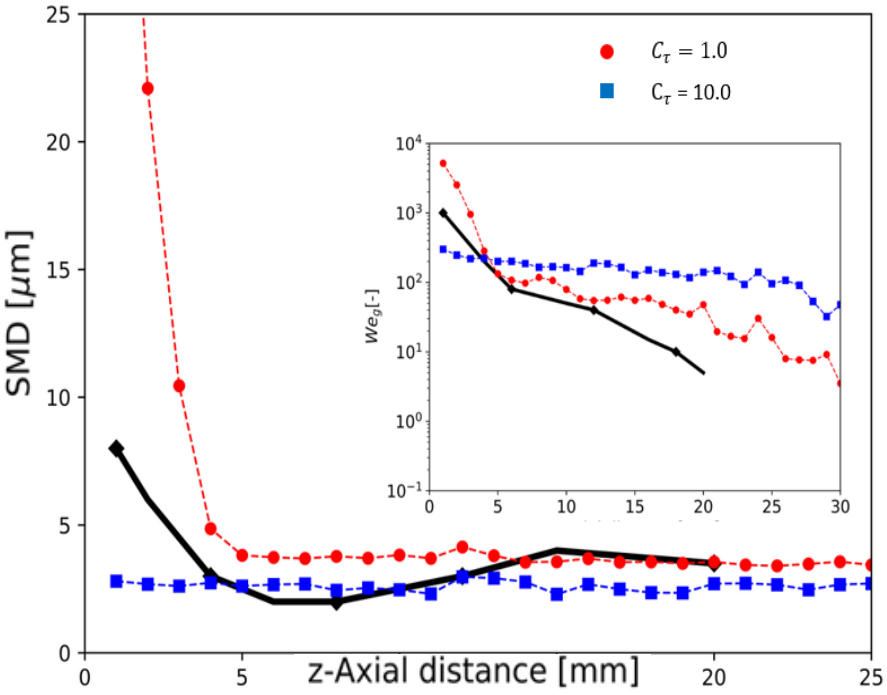

Figure 2-13: SMD and We_g profiles for different breakup time constants of stochastic model at t=1.5ms ASOI for Spray A-2 test case

In this section we present the results of spray characteristics at low injection pressures corresponding to *"Spray-A2"* experiment. The initial numerical calculations of Stochastic breakup model have shown that the model results in instantaneous atomization of the spray at the nozzle exit producing much smaller droplets than in the experiment. So, a parametric study is performed by varying the breakup time scale coefficient $\mathbf{C_\tau}$. A comparison of SMD and We_g for two different values of $\mathbf{C_\tau}$ for *F-grid* is shown in

Figure 2-13. Using $\mathbf{C_\tau} = 1$ gives instantaneous spray breakup right at the nozzle exit producing much smaller droplets with lower We_g. On the other hand, scaling the breakup time with $\mathbf{C_\tau} = 10$ reduces the breakup rate and thereby gives a much better prediction of SMD and also We_g profiles. Therefore, for all further comparisons, we used the scaled breakup time coefficient. Now a comparison of spray tip penetration for different breakup models using two grid resolutions is shown in *Figure 2-14*. Even with fine-grid resolution i.e. *Figure 2-14(b)* the breakup models over-predict the evolution of spray-tip penetration.

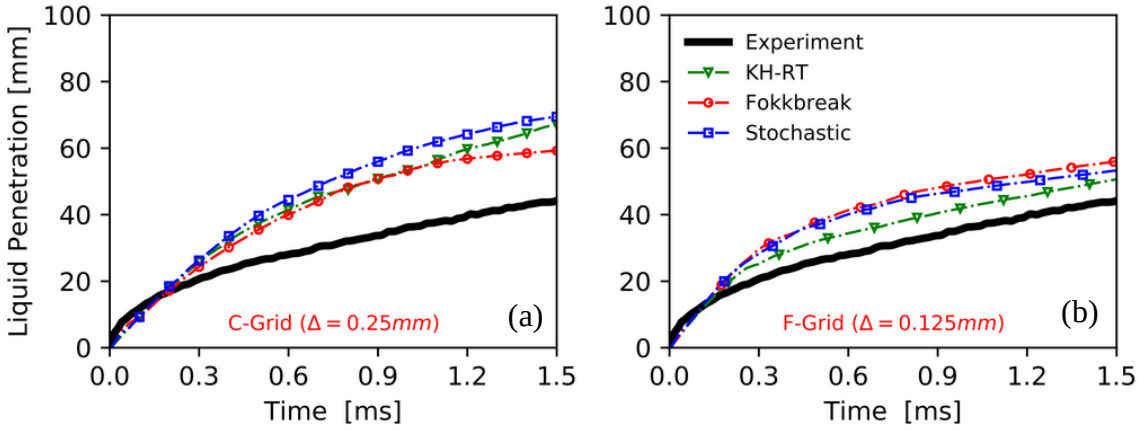

Figure 2-14: Comparison of spray tip penetration for different breakup model for two different grid sizes i.e. (a) C-grid (b) F-grid.

Figure 2-15 shows the comparison of the spatial evolution of Sauter Mean Diameter (SMD) for the fully developed spray condition. The experimental profile shows a decrease in SMD upto an axial distance of 7-8 mm and then a gradual increase again till 15 mm. This kind of increase in SMD diameter is not significant in high-pressure spray conditions. This shows that at low-injections pressures apart from spray breakup, collision and coalescence of droplets may also be significant. Since we did not take into account droplet collisions, the breakup models give flatter profiles for the SMD. While all the three models predict the steady state SMD value accurately, the stochastic and KH-

RT models show a more gradual decrease in the breakup rate compared to the Fokkbreak model.

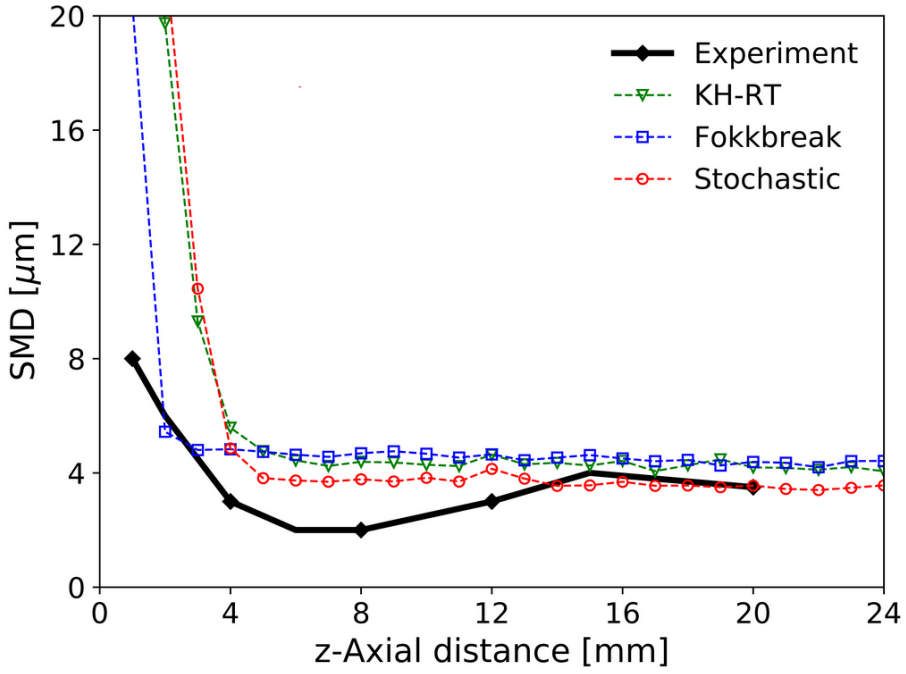

Figure 2-15: Comparison of SMD profiles for different breakup models for fully developed spray condition at time t=1.5ms ASOI for Spray A-2 test case

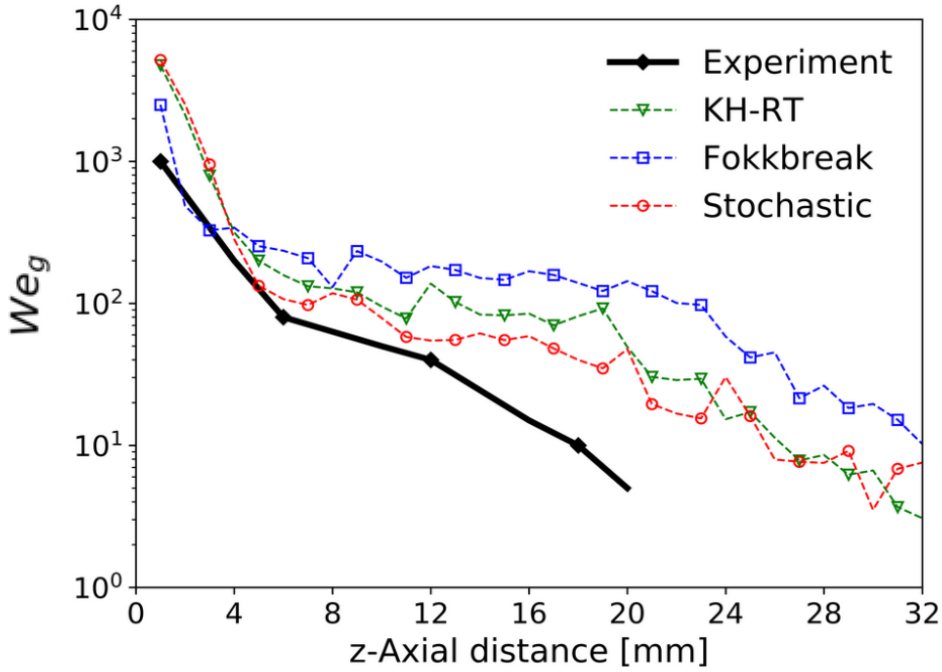

Figure 2-16: Comparison of We_g profiles for different breakup models for fully developed spray condition at time t=1.5ms ASOI for Spray A-2 test case

Next a comparison of the evolution of We_g profiles and the breakup length are shown in *Figure 2-16*. Assuming the critical weber number as defined in (145) to be around 80, the experimental breakup length is approximately around 5-7mm. Unlike at high injection pressures, KH-RT model gives similar prediction of all the spray characteristics compared to other two breakup models. Since the relative velocities are much lower compared to high-pressure injection case, the potential for breakup is much less and most of the atomization is completed within first millimetres from the nozzle exit. This shows that at lower injection pressures the important parameter controlling the global spray characteristics is the spray-turbulence interaction and not the spray breakup. And the same can be observed from the spray tip penetration profiles. All the three breakup models over-predicted the spray tip penetration even on finer grid, since they do not explicitly account for the influence of SGS turbulence on droplet motion.

2.3.3 Evaporating sprays

In case of non-evaporating sprays, the spray structure is characterized by the momentum exchange between the two-phases in the near-nozzle region and by turbulent dispersion of droplets in the far-field region. The effect of atomization on ensuing spray dynamics is characterized by the droplet-size distribution which determines the nature of spray-turbulence interaction as noted in earlier sections. On the other hand, in high temperature ambient environments the spray structure is also determined by the rate of evaporation of the liquid droplets. As both the atomization and evaporation processes contribute to droplet-size distribution, dynamics of the liquid-spray interaction could be completely different from the non-evaporating sprays. Therefore, in this section the capability of the breakup models to model the spray-characteristics in evaporating spray conditions is studied. Since the different spray parameters for non-evaporating spray conditions are well predicted using the *F-grid*, the influence of spray-breakup on evaporation and local mixture formation process for *Spray-Av1* experiment are also characterized using the *F-grid*. The spray tip penetration is a direct measure of the overall vaporization rate. Unlike in non-evaporating sprays, the penetration length reaches a steady state value where the rate of vaporization is balanced by the spray momentum. A comparison of the liquid-penetration length predicted by different breakup models with the experimental value is presented in *Figure 2-17*. The experimental steady state liquid penetration length is around 10mm. Even on a fine grid resolution it can be noticed that all the three breakup models over-predict the penetration length. While KH-RT and Stochastic models predict

a spray penetration length of 20 mm, the Fokkbreak model predicts much higher value of around 50mm. This shows that all the breakup models under-represent the vaporization rate even on the finer grid resolution.

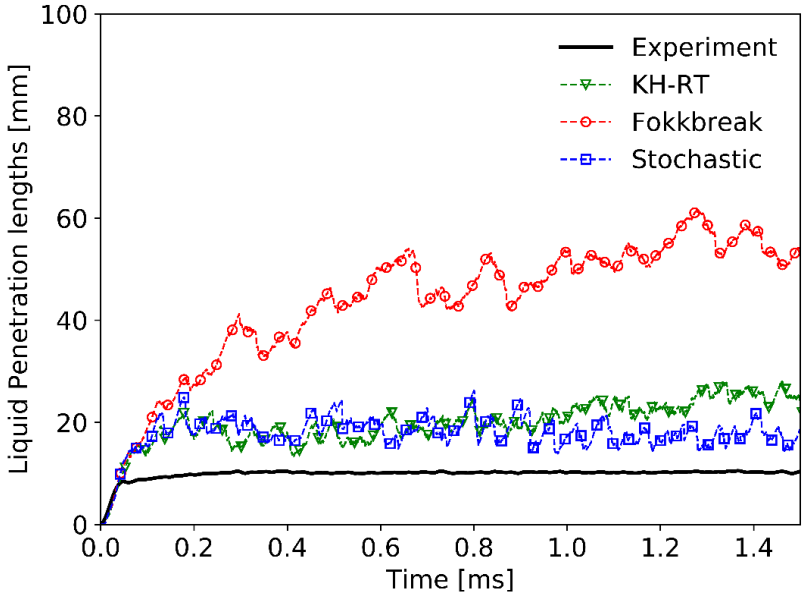

Figure 2-17: Comparison of the evolution of Liquid penetration length

Usually experiments provide ensemble average of gas-phase flow statistics over 30-40 repetitions of the same experimental condition. Since LES provides instantaneous filtered flow field variables, roughly speaking an LES simulation is equivalent to a single realization of spray experiment. In order to compare the LES results with statistically averaged spray parameters of experiment, different realizations of LES has to be obtained. To this end, a random seeding procedure (155) is used in the Lagrangian spray solver. Using a different random seed number for each LES simulation with exactly same initial and boundary conditions, produces a completely different realization of both Lagrangian and Eulerian flow statistics. For each breakup model 5 different realizations of the spray are obtained to calculate the averaged statistics. *Figure 2-17* shows the different realizations of gas-phase velocity and vapor-mass fraction distribution at a cross-section 30 mm downstream of the nozzle exit. These profiles are obtained from the Stochastic breakup model. Because of the significant variation in flow statistics, more realizations are required to accurately represent the standard deviation of the fluctuations in the flow variables in comparison to the experiments. So, only the mean flow statistics are used in this study to characterize the influence of spray breakup models on evaporation.

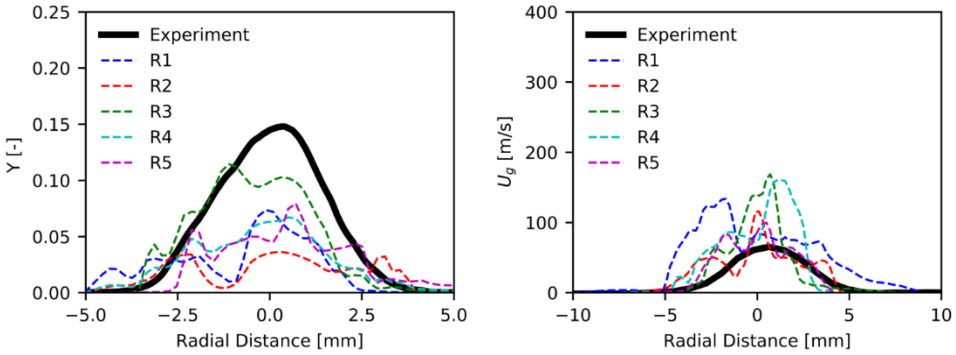

Figure 2-18: Multiple realizations of vapor mass fraction profiles at an axial distance z=30mm for stochastic breakup model at t=1.5ms ASOI

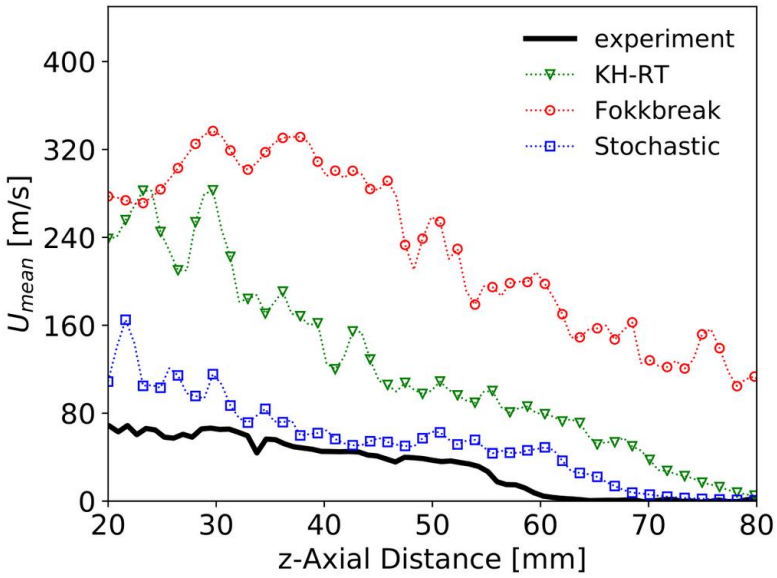

Figure 2-19: Comparison of ensemble averaged axial gas-phase velocity profiles along the spray centreline at t=1.5ms ASOI for different breakup models

Figure 2-19 provides a comparison of the ensemble averaged axial gas-phase velocity statistics obtained for a fully developed spray condition i.e. 1.5ms ASOI. As is the case with non-evaporating sprays, KH-RT model overpredicts the momentum transfer to the gas phase resulting in higher gas-phase velocities. But in case of Fokkbreak, even though it predicts similar decay of velocity profiles as stochastic model for non-evaporating sprays, very high axial velocities are observed for the evaporating spray conditions. In case of Fokkbreak, it is difficult to identify the causal effect relationship between evaporation, breakup and gas-phase turbulence which result in such differences in spray structure. But it signifies the non-linear interaction between different spray sub-processes and its importance in assessment of performance of spray sub-models. On the other hand, both the maximum value of the axial velocity in the near-nozzle region and the rate of

decay of velocity is more accurately predicted by the stochastic breakup model. As Fokkbreak model does not accurately predict the evaporating spray characteristics, for further comparison of local flow statistics only the KH-RT and stochastic models are used. *Figure 2-20* shows a comparison of variation in the axial gas-phase velocity in the radial direction at two different cross-sections i.e. 20 and 30 mm downstream of the injector nozzle. Even-though the centreline velocities are over-predicted, the stochastic breakup model gives a much better prediction of the radial spread in the velocity profile.

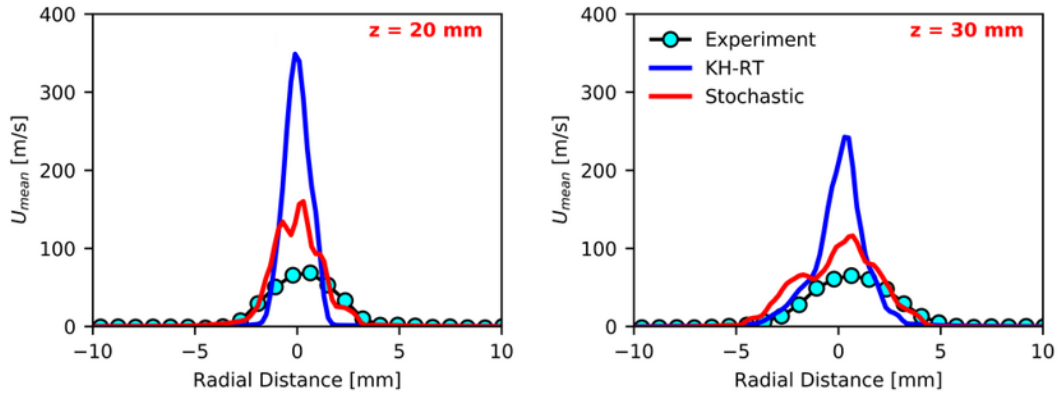

Figure 2-20: Comparison of ensemble averaged axial gas-phase velocity profiles at two different cross-sections z= 20mm and z=30mm downstream of the nozzle exit

Similarly, a comparison of the axial and radial ensemble averaged vapor mass fraction profiles is provided in *Figure 2-21* and *Figure 2-22* respectively.

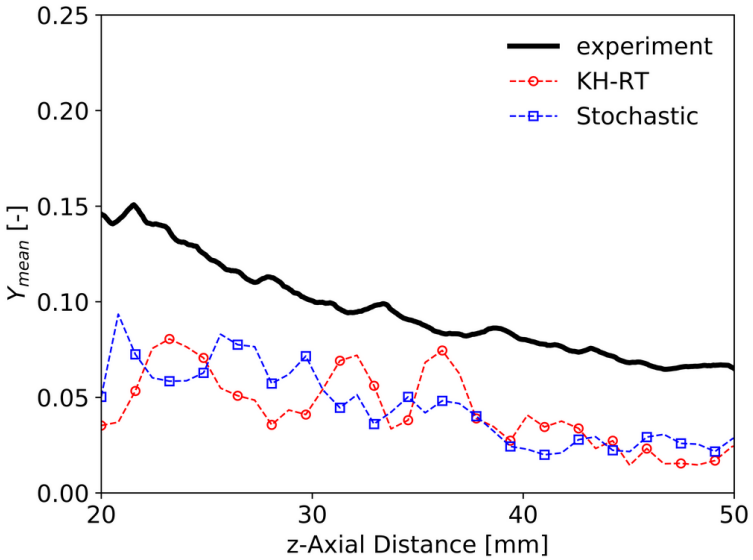

Figure 2-21: Comparison of ensemble averaged vapor-mass fraction profiles along the spray centreline at t=1.5ms ASOI for different breakup models

While from *Figure 2-22* it is evident that the stochastic model predicts a wider spray than the KH-RT model, both the models under-predict the magnitude of vapor mass fraction. Even though the stochastic model accurately predicts the spray breakup characteristics and the gas-phase velocities which characterize the spray-turbulence interaction, the intensity of vaporization is still under-represented.

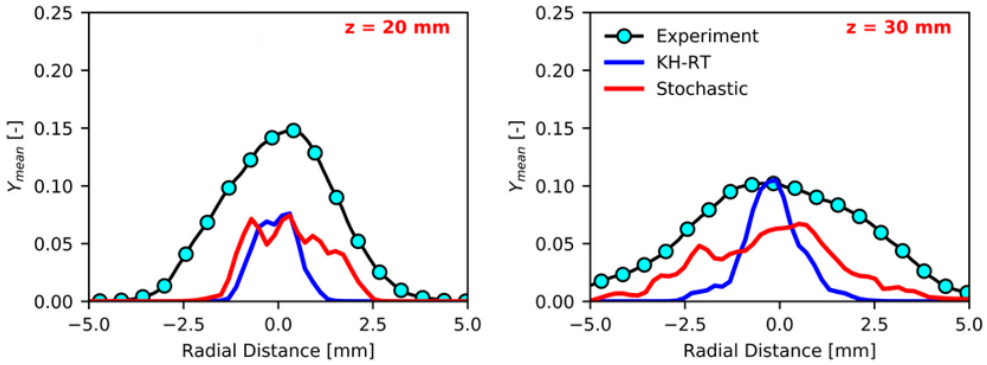

Figure 2-22: Comparison of ensemble averaged vapor-mass fraction profiles at two different cross-sections z= 20mm and z=30mm downstream of the nozzle exit

Finally, a qualitative comparison of the overall spray structure predicted by KH-RT and stochastic breakup models is presented in *Figure 2-23*. In case of KH-RT model because of the presence of an elongated liquid core, there is no vaporization upto 5mm and the maximum intensity of the vaporization rate is observed at the tip of liquid penetration length for both the cases. Since the stochastic model predicts more accurately the turbulent features of the spray it shows more radial dispersion compared to KH-RT.

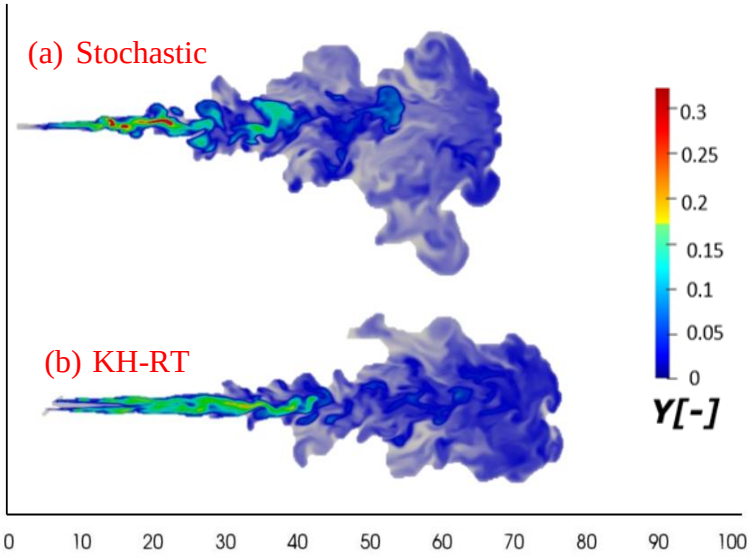

Figure 2-23: Instantaneous spray structure coloured by the vapor mass fraction field at time t=1.5ms ASOI for KH-RT and Stochastic breakup models

2.4 Conclusions

In this chapter we characterized the performance of three lagrangian spray breakup models namely, the deterministic KH-RT model, Fokkbreak model based on fragmentation under scaling symmetry at frequency independent of droplet size and a new stochastic breakup model accounting for the intermittency effects of unresolved turbulent scales. First the ECN non-evaporating spray experimental data for two different injection pressures i.e. 150MPa and 50MPa were used to assess the predictive capabilities of different breakup models. The global spray characteristics like the spray tip penetration length, sauter mean diameter (SMD) and the breakup length calculated from the spatial evolution of mean gaseous weber number (We_g) are used to evaluate the breakup models. From the investigations of spray breakup characteristics at high injection pressure conditions it was observed that, as expected the high momentum of liquid spray and atomization process control the spray evolution. In case of KH-RT model, even on the finer grid resolution the model predicts the global spray characteristics like near-nozzle gas phase velocities, breakup rate and rate of spray penetration in a way probably against the physical intuition and observations of experimental studies. The spray structure predicted by KH-RT model has a prolonged liquid core with larger droplets in the near-nozzle region and fastly penetrating smaller droplets in the far-field region compared to the experimental findings. Compared to KH-RT model, Fokkbreak and Stochastic breakup models present a better representation of global spray characteristics in comparison with the experiments with the finer-grid resolution. But the Fokkbreak model predicts much smaller spectrum of parcel sizes, with high probability of parcel size concentrated around the SMD of 1.25μm. On the other hand, the stochastic breakup model predicts a spray with much broader spectrum of parcel sizes within the range of 1-10 μm producing a more statistically realistic representation of the spray. Analysing the statistics of liquid-gas phase velocities and liquid droplet sizes, the differences in results for the three models may be attributed to the complex interactions between three physical parameters namely, the momentum exchange between the liquid spray and ambient gas in the near-nozzle region, the droplet size distribution resulting from the breakup and turbulent spray dispersion in the far field region. Since the breakup parameters in KH-RT model are expressed explicitly in terms of the filtered gas phase velocities discarding the contributions of SGS turbulent fluctuations, the effect of liquid-gas interactions on the spray breakup characteristics are seen more explicitly. Therefore, in case of deterministic models like KH-RT accurate modelling of spray characteristics require either to resolve

the smaller turbulent scales using grid sizes as small as 32μm as reported in (117) or to model the effects of unresolved scales on droplet motion correctly. On the other hand, stochastically modelling the breakup rate in terms of dissipation rate field, which is an important parameter characterizing the small-scale turbulence, the effects of unresolved scales are implicitly accounted. Therefore, the Fokkbreak and stochastic breakup models are able to provide a more accurate description of spray statistics on much coarse grid sizes of 125 μm. On the other hand, at low injection pressures it was observed from the experimental profiles of We_g that the atomization is completed within the first few millimetres from nozzle exit. It was noticed that the stochastic breakup model predicts instantaneous breakup of spray at the nozzle exit producing much smaller droplets compared to the experiment. So, the breakup time is scaled by modelling coefficient c_τ to obtain a more realistic breakup rate in comparison with the experiment. Because of the lower injection velocities, the potential for spray breakup is lower and the spray evolution is characterized by turbulent dispersion and not much by spray breakup. This was reflected in the results predicted by the breakup models. Even while accurately predicting the spray breakup characteristics, all the three models over-predict the spray tip penetration rate even on a finer-grid resolution. In the second part of this study, the influence of spray breakup modelling on structure of evaporating sprays is analysed. The differences in the gas-phase velocity field predicted by Fokkbreak model for non-evaporating and evaporating conditions, signifies the non-linear interaction between different spray sub-processes and its importance in assessment of performance of individual spray sub-models. On the other hand, even though the stochastic breakup model accurately predicts both the lagrangian spray statistics and the turbulence characteristics of the gas-phase, it still underpredicts the intensity of vaporization. This indicates that the classical d^2-law under-represents the evaporation rate. Therefore, in addition to modelling the SGS effects on droplet motion and breakup, accurate modelling of evaporating spray characteristics requires explicit modelling of the SGS effects on the droplet evaporation rate. Keeping in view, the relative importance of spray-turbulence interaction we attempt to analyse and develop stochastic models accounting for the effects of un-resolved scales on droplet motion and evaporation rate in the next chapter.

3 STOCHASTIC MODELS FOR SPRAY DISPERSION & EVAPORATION

3.1 Turbulent spray dispersion

3.1.1 Physics of spray-turbulence interaction

The interactions between the liquid spray and the turbulent gas phase also referred to as *"turbulent dispersion"* is characterized by different physical mechanisms which manifest themselves more profoundly due to the poly-disperse nature of the spray. Any attempts at modelling of turbulent dispersion requires a detailed understanding of these physical mechanisms and their relevance depending on two-phase flow conditions. Elgobashi (156) in his review states that the main challenge to obtain a full physical understanding of turbulent two-phase flows is marked by the presence of wide range of flow scales associated with the microscopic physics of dispersed phase in addition to those of fine and large structures of turbulence. Direct Numerical Simulations (DNS) with lagrangian particle tracking approach have been widely used to understand the physical mechanisms governing the spray-turbulence interactions in simplified flow configurations. Depending on the mass loading/volume fraction of the dispersed phase, the interaction between the two-phases is classified as *one-way* and *two-way* coupling by Elgobashi (156). At low volume fractions while particles have negligible effect on turbulence, modulation of particle motion by turbulence is significant. This is termed as *one-way coupling*. On the other hand, at higher volume fractions the dynamics of particle motion influence the turbulent flow field. This is referred to as *two-way coupling.* Even in the case of DNS, Yeung & Pope (157) showed that the accuracy of the lagrangian flow statistics is strongly dependent on the interpolation method used to interpolate the fluid velocity at the point-particle position. Their study used methods ranging from linear interpolation to lagrangian and Hermitian interpolation and also interpolation methods based on splines. It was shown that in-order to accurately describe the lagrangian velocity statistics at least a third-order interpolation scheme should be used. Studies of Squires & Eaton (158,159)

in homogenous turbulence have shown that depending on the ratio of particle to fluid inertia characterized by *Stokes number St*, the particles are preferentially concentrated either in the *convergence zones* with low vorticity, or in *eddy zones* with high vorticity. Wang & Maxey (160) showed that the preferential concentration is controlled by intense vortical structures characteristic of small-scale turbulence. So, it was argued that preferential concentration is characterized best by non-dimensionalising particle response time τ_p with Kolmogorov time scale τ_η when defining *St*.

$$\boldsymbol{St = \frac{\tau_p}{\tau_\eta}} \qquad \textbf{3-1}$$

For very small Stokes number i.e. *St <<1*, the non-inertial particles smaller than Kolmogorov length scales tend to follow all motions of the turbulence and hence they are concentrated in the eddy zones. On the other hand, at large Stokes highly i.e. *St >>1* the inertial particles experience strong centrifugal forces pushing them out of the vortices. So, they are mostly concentrated in the convergence zones. Elghobashi & Fessler (161) have explained the mechanisms of turbulence modification in two-way coupling in terms of rate of change of enegry due to particle drag force and preferrential concentration. They showed that the non-inertial particles (St << 1) being trapped in the voritcal structures tend to increases the energy content of the small scales. On the other hand, the large particles (St >> 1) traversing through different eddies tend to reduce their turbulent kinetic energy with their drag force. Bagchi & Balachander (162) and Burton & Eaton (163) studied turbulence effects on dynamics of finite-sized particles greater than Kolmogorov length scale in homogenous turbulence. They have shown the formation of wakes and vortex shedding behind the particles with Reynolds number above a certain critical value. It was argued that these turbulent structures increase the velocity fluctuations thereby enhancing the turbulence in the surrounding carrier phase. Moreover, these self-induced turbulent structures which are usually smaller than or equal to the droplet size, cause rapid variations in the instantaneous drag force acting on the particle. Recent studies of Cencini et al (164) and Volk et al (165) characterized the effects of intermittency at small scales on lagrangian acceleration statistics of particles in homogeneous statistically stationary turbulence. In addition to the non-gaussian statistics of lagrangian particle acceleration, it was shown that the norm of acceleration is correlated on large times comparable with the integral time, while the direction is correlated on short times of order of the Kolmogorov time scale. In this way the intermittency is manifested i.e., the vortical filaments of small scales are as much

energetic as the large-scale turbulent structures. And since the small non-inertial particles with *St << 1* are preferentially concentrated in high intensity vortices characterizing intermittency, they have much broader tails and shorter correlations of acceleration norm compared to the large inertial particles.

3.1.2 Sub-grid scale modelling of dispersion in context of LES

Numerical modelling of particle-laden flows should ideally treat all of the afore-mentioned physical aspects namely, particle dispersion due to the entire spectrum of turbulent fluctuations, stochastic drag force induced by vortex shedding in the wake of inertial particles at high Reynolds numbers, turbulence modulation by particle dynamics, intermittency effects and preferential concentration of particles. However, the filtered velocity field obtained from the solution of LES, provides an inaccurate estimation of the drag force in the Lagrangian particle equation of motion. These inaccuracies accumulate over time resulting in strong deviations in lagrangian particle flow statistics from the DNS or experiments. Unlike in DNS for the realistic flow simulations using LES, we generally use first order linear interpolation schemes for approximating the filtered flow velocity at the point-particle's position. This induces an additional numerical error. Over the past decade several dispersion models have been developed to account for the effects of unresolved scales thereby providing a more accurate representation of the lagrangian particle statistics. Similar to Dukowicz (73) dispersion model in RANS, Wang & Squires (166) proposed to model the effects of unresolved scales by decomposing the instantaneous velocity field into resolved and SGS components. While the former is obtained directly from the solution of LES, the latter is calculated from the subgrid kinetic energy k_{sgs} and is assumed to be piece-wise continuous in time. Each component of the SGS velocity is obtained from Eq. 3-2.

$$\boldsymbol{u'_i = \chi_i \sqrt{\frac{2}{3} k_{sgs}}} \qquad \textbf{3-2}$$

where χ_i is a random number sampled from a unit-normal distribution for each component of SGS velocity. The frequency of sampling is defined by the time taken by the droplet to traverse through an eddy, t_{turb} and is given by Eq.3-3. Owing to its simplicity this approach is widely used to model spray dispersion (167-168).

$$\boldsymbol{t_{turb} = min\left[\frac{k_{sgs}}{\varepsilon_{sgs}}, \frac{{k_{sgs}}^{1.5}}{\varepsilon_{sgs}} \frac{1}{|\bar{u} - u_p|}\right]} \qquad \textbf{3-3}$$

Shortoban & Mashayek (169) proposed to approximate the SGS velocity with a deconvolved velocity u* obtained by applying a suitable invertible filter kernel G to of the filtered velocity field $\bar{u}$ as shown in Eq. 3-4. This approach is referred to as the *Approximate Deconvolution Method (ADM).*

$$\boldsymbol{u^*}_i = \boldsymbol{G^{-1}\bar{u}_i} = \sum_{n=0}^{N}(\mathbf{1}-\boldsymbol{G})^n\,\bar{\boldsymbol{u}}_i = \bar{\boldsymbol{u}}_i + (\bar{\boldsymbol{u}}_i - \bar{\bar{\boldsymbol{u}}}_i) + (\bar{\boldsymbol{u}}_i - 2\bar{\bar{\boldsymbol{u}}}_i + \bar{\bar{\bar{\boldsymbol{u}}}}_i) + .. \quad \textbf{3-4}$$

Here G^{-1} is the inverse of the filter kernel G and is approximated by van Cittert series truncation and N is the truncation parameter representing number of terms in the series expansion to be considered. While it was found that this model gives more accurate prediction of velocity statistics at lower Reynolds numbers, it is not very efficient for high Reynolds number flows. This is because this method only reconstructs a fraction of SGS velocity field associated with wave numbers close to the filter width Δ. And given the fact that there is huge disparity in length scales, very small filter widths are required to resolve the SGS turbulence effects at high Reynolds numbers. Tsang & Rutland (170) used the two ideas presented above to the model by SGS velocity of fuel droplets in diesel sprays by decomposing it further into deterministic and stochastic components. While the former is evaluated from deconvolution method, the latter is expressed in terms of Eq 3-2. Bharadwaj and Rutland (168) accounted for the turbulence modulation by the dispersed phase by modelling the energy transfer source term in the transport equation for SGS turbulent kinetic energy in terms of the deconvolved velocity field approximated by Eq. 3-4. Pozorski and Apte (171) modelled the SGS velocity seen by the droplets using a Langevin stochastic equation of the form shown in Eq. 3-5 to study preferential concentration in particle laden flows.

$$\boldsymbol{du'} = \frac{\boldsymbol{u'}}{\boldsymbol{\tau_{sgs}}}\,\boldsymbol{dt} + \sqrt{\frac{2\boldsymbol{\sigma_{sgs}^2}}{\boldsymbol{\tau_{sgs}}}}\,\boldsymbol{dW} \quad \textbf{3-5}$$

Here dW is the vector of the increment of a standard Brownian process, $\langle dW \rangle = 0$, $\langle dW^2 \rangle = dt$. And σ_{sgs}, τ_{sgs} are the SGS velocity and time scales expressed in terms of the SGS kinetic energy as shown in Eq 3-6 and 3-7.

$$\boldsymbol{\tau_{sgs}} = \frac{\boldsymbol{\Delta}}{\boldsymbol{\sigma_{sgs}}} \quad \textbf{3-6}$$

$$\boldsymbol{\sigma_{sgs}} = \sqrt{\frac{2}{3}\boldsymbol{k_{sgs}}} \quad \textbf{3-7}$$

This approach has been successful in modelling the dynamics of only large inertial particles but did not work well with non-inertial particles. Bini & Jones (172-173)

attempted to model the non-gaussian statistics of particle acceleration by directly modelling the particle velocity increments along the particle trajectory using a Langevin equation of the form shown in Eq. 3-8.

$$\boldsymbol{du_p = \frac{\bar{u}-u_p}{\tau_p} + \sqrt{\frac{k_{sgs}}{\tau_t}}\, dW} \qquad \textbf{3-8}$$

where τ_t is turbulent time scale parameter expressed as a power function of k_{sgs}.The model has been shown to capture the broad tails in the velocity increment distribution and also accurately model the dispersion in turbulent mixing layers and dilute sprays. But the main drawback of this approach is that as filter width Δ decreases the k_{sgs} also decreases, consequently the velocity increment du_p also decreases as shown in Eq. 3-8. But it was pointed out in Zamansky & Gorokhovski (78,79) that with decreasing grid size the acceleration of the gas increases and hence the particle acceleration is also expected to increase which is contradictory to Eq. 3-8. Alternatively, as explained in Chapter-1 the correlation between the fluid velocity and the particle acceleration is best described in terms of the viscous dissipation rate ε. Therefore, in this thesis, the LES-STRIP approach introduced in Chapter-1, based on directly modelling the particle acceleration in terms of statistics of viscous dissipation rate ε "seen" along the particle trajectory is used to model the spray dispersion. But the formulations of LES-STRIP model as proposed by Zamansky & Gorokhovski (78,79) is for particle-laden flows with one-way coupling. Therefore, a new LES-STRIP formulation referred to as "*stochastic drag force"* for finite sized particles at high Reynolds numbers accounting for turbulent fluctuations in drag force induced by vortex shedding is proposed. By coupling the re-formulated LES-STRIP with the momentum source term given in Eq. 2-30, the intermittency effects of unresolved scales on the gaseous flow turbulence field can be partially accounted for. Two principle modifications in this thesis are: two-way coupling and new-model for orientation vector as proposed in (71) The details of the re-formulated LES-STRIP approach is presented in the next section.

3.1.3 Reformulated LES-STRIP model for diesel sprays

Zamansky & Gorokhovski (79) obtained the *stochastic drag force equation* for finite sized particles ($d_p > \eta$) at high Reynolds numbers, from the momentum exchange between droplet and the surrounding turbulent fluid. Let $\frac{dP}{dt}$, be the momentum exchanged per unit time between a particle and the surrounding fluid. Assuming that *dP* is

determined as the mass of the fluid entrained by the moving particle $\left(\rho_f u' \frac{\pi d_p^2}{4} dt\right)$ multiplied by the relative velocity $\bar{u} - u_p$, we can re-write Newton's law for droplet's equation of motion in the following form:

$$\frac{\pi d_p^3}{6} \rho_p \frac{du_p}{dt} = \rho_f u' \frac{\pi d_p^2}{4} C_d \left(\bar{u} - u_p\right) \quad \textbf{3-9}$$

Introducing Kolmogorov scaling ($u' = \varepsilon^{1/3} d_p^{1/3}$), the Eq.3-9 reduces to,

$$\frac{du_p}{dt} = \frac{\rho_f}{\rho_p} \frac{\varepsilon^{\frac{1}{3}}}{d_p^{\frac{2}{3}}} C_d \left(\bar{u} - u_p\right) \quad \textbf{3-10}$$

In our thesis we use the definition of $\overrightarrow{e_p} = \bar{u} - u_p / |\bar{u} - u_p|$ to obtain an equivalent form of Eq.3-10 as shown in Eq. 3-11.

$$\frac{du_p}{dt} = \frac{\rho_f}{\rho_p} C_d \frac{\varepsilon^{\frac{2}{3}}}{d_p^{\frac{1}{3}}} \overrightarrow{e_p} \quad \textbf{3-11}$$

Similar to formulation of discharge coefficient C_d , the boundary layer is assumed to be fully turbulent with vortices of different length scales being shed from the droplet for particle Reynolds number Re_p greater than a critical value of 1000. So, the re-formulated LES-STRIP model for application to diesel sprays is given by:

For $Re_p > 1000$ and $d_p > \eta$:

$$\frac{du_p}{dt} = \frac{\rho_f}{\rho_p} C_d \frac{\varepsilon^{\frac{2}{3}}}{d_p^{\frac{1}{3}}} \overrightarrow{e_p} \quad \textbf{3-12}$$

For $Re_p < 1000$

$$\frac{du_p}{dt} = \frac{\bar{u} - u_p}{\tau_p} + \sqrt{\frac{\varepsilon}{\tau_p}} \overrightarrow{e_p} \quad \textbf{3-13}$$

The evolution of the instantaneous dissipation rate ε along the particle trajectory is modelled using the stochastic equation for log-normal process (84) given by Eq. 1-74 which is re-written here for sake of consistency.

$$d\varepsilon = -\varepsilon \left(\ln\left(\frac{\varepsilon}{\bar{\varepsilon}}\right) - \frac{1}{2}\sigma^2\right) \frac{dt}{T} + \varepsilon \sqrt{\frac{2\sigma^2}{T}} dW(t) \quad \textbf{3-14}$$

And the unit directional vector is modelled using the OU-process for random walk over a unit sphere without the relaxation towards local vorticity field, making all directions

equiprobable. The Stratanoivch form of increment of unit direction vector without the relaxation term is given by Eq. 3-15 which is solved by the mid-point scheme proposed in (71).

$$\mathbf{de_i} = \sqrt{2\tau_\eta^{-1}}\epsilon_{ijk}\mathbf{dW_j} \circ \mathbf{e_k} \qquad \textbf{3-15}$$

3.2 Turbulent spray evaporation

3.2.1 Physical aspects of turbulent spray evaporation

As shown in evaporating spray experiments of Sahu et al (35), the dynamics of evaporation are coupled with the spray dispersion. The dispersion of evaporating droplets is much more complex due to the transient nature of mass and momentum transfer between the carrier gas and continuously decreasing droplet size thereby reducing droplets Stokes number. This inherent poly-disperse nature of the evaporating droplets might have more significant role on preferential concentration and turbulence modulation. Mashayek et al (174) have first studied the dispersion of evaporating droplets in isotropic turbulence using one-way coupling. For intermediate times it was shown that the initially mono-disperse spray relaxes to a Gaussian size distribution. Mashayek (175) further studied dispersion of evaporating droplets using two–way coupling with higher droplet mass loadings. The influence of initial vapor mass fraction, droplet temperature, mass loading on evaporation rates and spatio-temporal fluctuations of vapor mass fraction were investigated. It was shown that increasing the droplet mass loading reduces the evaporation rate of droplets resulting in deviation from the d^2-law. Moreover, it was shown that the temporal evolution of fluctuations in vapor mass fraction are initially determined by droplet dispersion and later by turbulent dissipation of fluctuations. Miller & Bellan (176) have studied the droplet evaporation in three-dimensional non-homogenous mixing layer using a non-equilibrium vaporization model. The mechanism of evaporation process is explained in terms of droplet statistics conditioned on the second invariant of deformation tensor used to characterize turbulent flow structures (16). With increasing mass loading, the droplets tend to concentrate preferentially in regions of high strain and low-vorticity regions. Moreover, it was demonstrated that these low vorticity regions also correspond to high gas temperature zones, which contribute further to enhancement of droplet evaporation. Reveillon & Demoulin (177) have studied preferential concentration of droplets and its subsequent effect on the evaporation process in isotropic turbulence using one-way coupling for spray-turbulence interaction. While

the evolution of the mean vapor mass fraction is shown to be determined by the size of droplet clusters, the vapor mass fraction fluctuations are initially controlled by the evaporation rate of these droplet clusters and later by the turbulent dissipation of the fluctuations similar to Mashayek et al (174). The study has also demonstrated the presence of different evaporation modes due to the transient dynamics of droplet clustering resulting from constantly changing clustering sizes due to droplet evaporation. Recently Barba and Picano (178) considered the DNS of an evaporating turbulent spray jets. The study has shown that the instantaneous vapor concentration field 'seen' by the droplet is consistently higher than the mean vapor concentration field due to the small-scale clustering in the dense spray core and air entrainment process in more dilute regions.

3.2.2 Sub-grid scale modelling of dispersion in context of LES

Based on the experimental and DNS studies of evaporating sprays, Jenny et al (179) in their review on turbulent spray combustion summarized the spray evaporation process by three possible scenarios. The first one consists of rapidly evaporating isolated droplets in regions with little or no vapor concentration. Second scenario consists of droplet clusters with small inter-droplet distances, which result in a drastic reduction of the evaporation rate for the droplets. The third scenario deals with turbulent droplet transport between high and low vapor concentration regions. These scenarios make the vapor-mass fraction gradient "seen" by the droplets and subsequently their evaporation rates stochastic random variables. But most LES studies of diesel-like fuel sprays consider only the first scenario assuming the spray to be dilute with large inter-droplet distances. Therefore, the classical d^2-law based on assumption of rapid-mixing of the fuel vapor by the surrounding gaseous medium is used to model the droplet evaporation rate. When modelling evaporating sprays in co-axial combustor, Apte et al (180) stochastically modelled the vapor mass fraction field "seen" by the droplet from a presumed beta-pdf distribution of the mixture fraction field. The variance of mixture fraction field required for constructing the PDF was modelled dynamically in terms of the gradients of local mixture fraction field. The hypothesis of their approach is that the net evaporation rate of the droplets is controlled by the scalar-mixing time scale. This is similar to Villermaux (33,34) hypothesis for dense sprays. But in reality, as shown in experimental studies of Sahu et al (35) we have isolated droplets in the spray periphery and dense droplet clusters in the spray core. So, the evaporation process has two competing phenomena i.e. rate of diffusion of vapor from the droplet surface and a finite rate of mixing of the diffused vapor by the surrounding gaseous medium depending on the local turbulence intensity.

Accounting for this, in this thesis we attempt to develop and assess a new stochastic SGS formulation for the gradients of the vapor mass fraction "seen" along the droplet trajectory.

3.2.3 Stochastic Mixing Controlled Evaporation Model (SMICE)

In the under-resolved LES with classical d²-law model for droplet evaporation, the droplet evaporation rate is modelled in terms of the filtered vapor mass fraction field and the saturated vapor mass fraction at the droplet surface as shown in Eq 3-16.

$$\dot{m}_p = \frac{dm_p}{dt} = -2\pi d_p \rho D_{fv}\, Sh_d\, \frac{Y_{F\zeta} - \overline{Y_v}}{1 - Y_{F\zeta}} \qquad \textbf{3-16}$$

Instead of the resolved vapor mass fraction $\overline{Y_v}$,we calculate the evaporation rate from a stochastically modelled vapor mass fraction Y_v^{stoch} whose value is in between the saturated vapor mass fraction at the droplet surface $Y_{F\zeta}$ and the resolved value $\overline{Y_v}$ in the control volume in which the droplet is located. In difference with the standard evaporation model, i.e. *d^2-law*, this expression contains the multiplier $\frac{Y_{F\zeta} - Y_v^{stoch}}{1 - Y_{F\zeta}}$. The stochastic model for Y_v^{stoch} is based on the following physical assumption:

$$\frac{Y_{F\zeta} - Y_v^{stoch}}{\tau_{vap}} = \frac{Y_v^{stoch} - \overline{Y_v}}{\tau_{mix}} \qquad \textbf{3-17}$$

Here τ_{mix} is the time scale of mixing and τ_{vap} is the time scale of droplet evaporation. While τ_{vap} is evaluated locally in terms of resolved variables as shown in Eq. 3-18, the random mixing time τ_{mix} is described by stochastic lognormal process along the droplet trajectory as shown in Eq. 3-19, thereby representing the intermittency effects "seen" by the droplet.

$$\tau_{vap} = 2\pi d_p \rho D_{fv}\, \frac{1}{1 - Y_{F\zeta}}\, Sh_d\, \frac{1}{V_{cell}} \qquad \textbf{3-18}$$

$$\tau_{mix} = \frac{k_{sgs}^{0.5}}{\varepsilon} \qquad \textbf{3-19}$$

To some extent, the physical assumption is similar to the partially stirred reactor model of turbulent combustion proposed by Vulis (181), in which the chemical reaction rate, evaluated at a certain intermediate concentration follows the rate of turbulent mixing of that concentration. The random vapor mixing fraction "seen" by the moving droplet in its vicinity is expressed as:

$$Y_v^{stoch} = \overline{Y_v} \frac{\tau_{vap}}{\tau_{vap}+\tau_{mix}} + Y_{F\zeta} \frac{\tau_{mix}}{\tau_{vap}+\tau_{mix}} \qquad 3\text{-}20$$

It is seen that in the case of very weak turbulence around a droplet, $Y_v^{stoch} \sim Y_{F\zeta}$, with negligible rate of evaporation. On the other hand, a strongly turbulent environment provides an aerated condition for evaporation, and then the vapor mass fraction is characterized by resulting mixture on large resolved scales, $Y_v^{stoch} \sim \overline{Y_v}$, leading to the maximal rate of evaporation.

3.3 Experimental and Computational details

3.3.1 Co-axial spray combustor

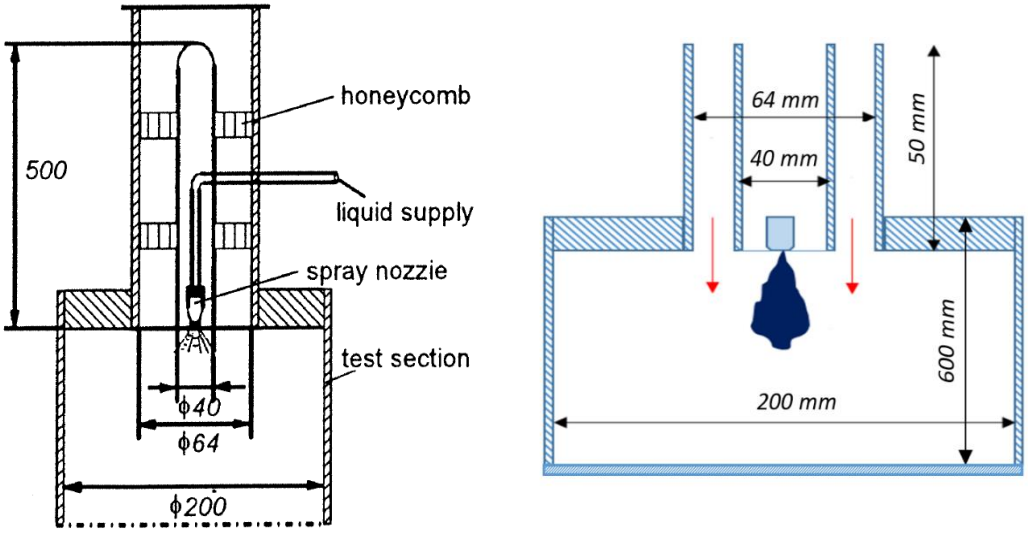

Figure 3-1 Schematic representation of (a) co-axial flow combustor experiment (left) and (b) the corresponding computational geometry used for simulations (right)

The experimental studies of Sommerfeld & Qiu (126) on isopropyl alcohol spray evaporating in a coflowing hot turbulent air flow has been used earlier (182-185) to validate the evaporation models both in the framework of RANS and LES. A schematic of the experimental set-up is shown in *Figure 3-1 (a)*. A moderately pre-heated air is blown from an annular injection tube of length 500mm and a diameter of 64 mm into a wider test section of diameter 200mm. The turbulence levels in the gas stream is changed using perforated rings of plexiglass. Into this stream of hot air, a liquid spray of isopropyl alcohol issuing from a hollow cone spray atomizer with a diameter of 20 mm, is injected at the center of the test sectio0.582n. The mass flow rates of the air and the liquid spray are 28.3 and 0.44 g/s respectively. The hot air is issued at a temperature of 373K while the liquid is injected at a temperature of 313K. The moderate temperatures of air prevent

auto-ignition of the liquid fuel and moreover the evaporation process is driven by mass transfer effects. In order to describe the initial conditions for liquid spray, detailed measurements of the droplet size distribution and correlation between droplet size, location and velocities are provided close to the nozzle exit. The well characterized inlet conditions for the liquid spray makes this configuration most suitable for studying the evaporation effects of droplets independent of spray atomization. Statistical data on spatial changes in the droplet velocities, size distribution and mass flux are measured using phase-doppler anemometry at different axial sections ranging from 25mm to 400 mm downstream of the spray atomizer.

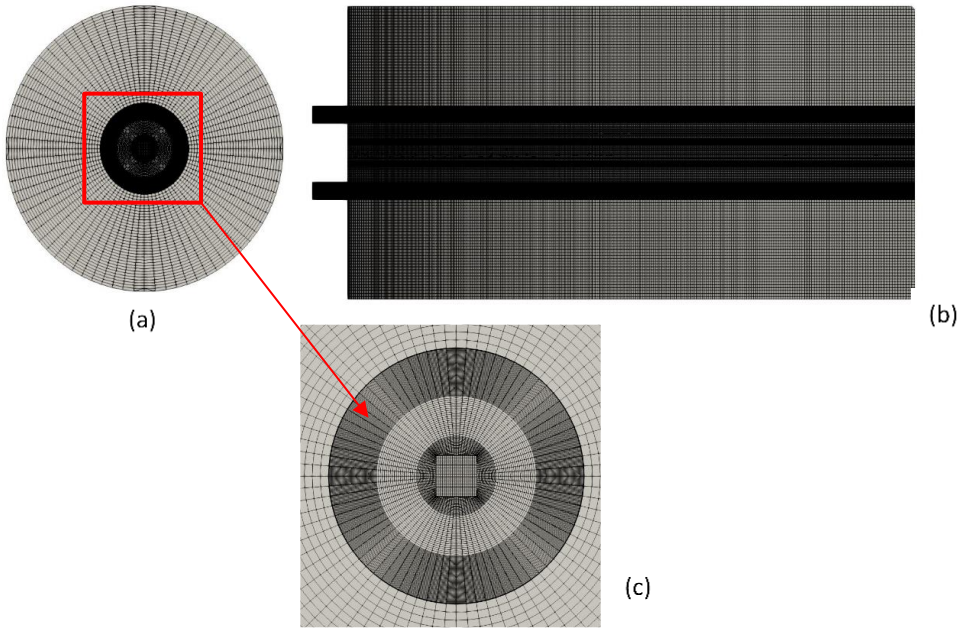

Figure 3-2 : Details of computational mesh (a) Top view (b) Cross-sectional view (c) Close up of the mesh in the annular flow region with spray

A schematic of the computational domain is shown in *Figure 3-1(b).* The bulk mean flow velocity (U_b) of air is 18 m/s. Taking the annular radius of the co-flow as a reference length scale, the bulk flow Reynolds number for the flow can be approximated to be around $2e4$. In order to reduce the computational effort, the turbulent fluctuations at the exit of the annular pipe are generated from a priori periodic flow simulation. An artificial body-force term is added to the momentum equation to drive the flow by correcting the pressure gradient across the pipe length and its magnitude is calculated from the bulk mean flow velocity. The inflow data is generated and stored over several flow through times, for every few computational time steps of the channel flow simulation. The velocity profiles are then mapped onto the gas flow inlet located 50 mm above the

atomizer. The velocity profiles are linearly interpolated for time steps between any two consecutive time intervals of mapping. Since only a finite sized domain of 600 mm is used instead of simulating the entire test section, a convective boundary condition is applied at the outlet in order to ensure conservation of mass flow leaving the domain. No-slip and adiabatic boundary conditions are used for velocity and temperature at the walls. *Figure 3-2* shows the computational grid. The O-grid technique is used to generate a structured hexahedral mesh with increasing grid density in the spray injection and annular gas flow regions. The grid size varies from 0.25 mm in the regions closer to the spray atomizer to 2.5 mm in the outer wall regions both in the axial and radial directions. The droplets are injected from a plane 3mm downstream of the atomizer where the measurements of the spray size and velocity correlations are available. The number of droplets injected per time step is calculated based on the liquid mass flow rate. The position of each droplet is randomly sampled over a radial distance of 10mm around the center. The droplet size distributions are experimentally measured over 10 discrete radial zones each with a size of 1mm. Depending on the droplet position, the droplet diameter is then sampled from the size distribution corresponding to the radial zone containing the droplet. Then the velocity of the droplet is calculated based on the velocity-size correlations. The axial and radial velocity components of the droplet determine the angle at which the it is injected into the domain. A first order Euler scheme is used for temporal discretization, while second order central differencing scheme is used for spatial discretization of terms in filtered Navier Stokes equations. Also, a first order linear-interpolation scheme is used for interpolating the Eulerian flow field variables at particle position.

3.3.2 ECN constant volume spray combustor

First in-order to characterize the influence of dispersion models on spray breakup and global spray structure, we use the same experimental conditions for non-evaporating ECN Spray-A that are used in Chapter-2. The spray penetration lengths, SMD and gaseous Weber number profiles are used as metrics to evaluate the performance of two dispersion models. For evaluating the performance of evaporation models, in addition to the vaporizing ECN Spray-A condition we use another ECN spray experiment referred to as *Spray-H*. The *Spray-H* experiment uses a fuel injector with a sharp edged, non-hydroground nozzle without any taper from inlet to the exit. The nozzle has a diameter of 100µm and n-Heptane is used a surrogate of diesel fuel in this experiment. More specific details of the two evaporating spray experimental configurations are provided in the *Table*

3-1.While *Spray-A* experiment provides the ensemble-averaged statistics of gas-phase velocity measurements, *Spray-H* experiment provides the ensemble-averaged statistics of vapor mass-fraction profiles at different time instances of spray evolution. In addition to these experimental measurements, the liquid/vapor penetration lengths and instantaneous spray. Similar to the studies performed in Chapter-2, two computational grids are used to study the sensitivity of models to grid size. The base coarse mesh referred to "*C-Grid"* consists of a uniform cell size of 250µm both in axial and radial directions. Another finer mesh referred to as *"F-Grid"* with a cell size linearly varying from 125µm to 250µm both in axial and radial directions is used to study the effects of mesh resolution. The implementation of the numerical discretization schemes, initial/boundary conditions for the Lagrangian spray and Eulerian gas are the same as those used in Chapter-2 and hence are not illustrated here again.

Evaporating spray conditions		
Experiment name	Spray-A	Spray-H
Injection pressure (MPa)	150	150
Ambient pressure (MPa)	6	4
Fuel temperature (K)	363	363
Ambient temperature (K)	900	1000
Injected mass (mg)	3.46	17.6
Injection duration (ms)	1.5	6
Nozzle diameter (µm)	90	100
Fuel	n-dodecane	n-Heptane

Table 3-1 : Non-evaporating spray experimental conditions

3.4 Results – comparison of measurements

In this section we try to validate the performance of two sets of models for different experimental conditions described in earlier section. For non-evaporating conditions we compare the Wang & Squares (166) *"standard"* dispersion model with LES-STRIP approach. For evaporating conditions, the *"standard"* approach refers to Wang & Squires (166) dispersion model with d^2-law for droplet evaporation. On the other hand, the *"stochastic"* approach refers to LES-STRIP dispersion model with SMICE evaporation model.

3.4.1 Co-axial spray combustor

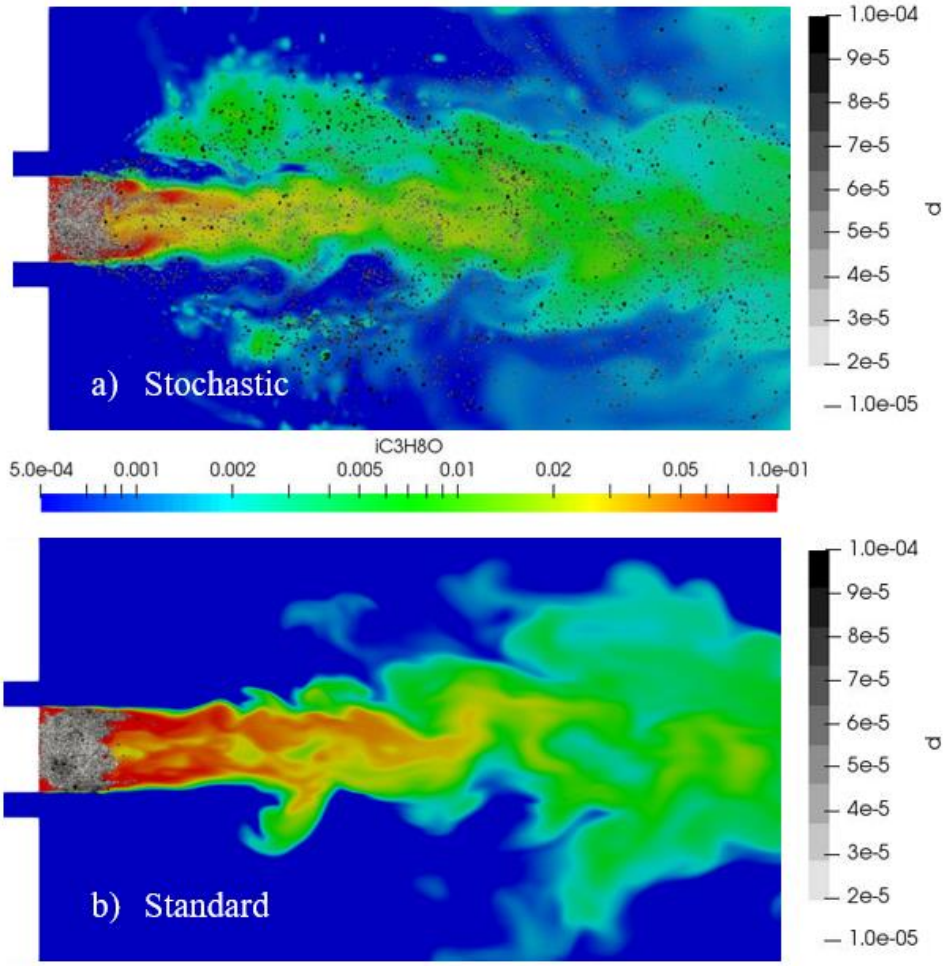

Figure 3-3 : Cross-sectional view of steady state spray structure predicted by (a) Stochastic approach (b) Standard approach

Figure 3-3 shows the cross-sectional view of steady state spray structure for the two modelling approaches. Generally, the initially injected droplets tend to evaporate much quickly due to the strong gradients in the vapor mass fraction fields. The fuel-vapor generated from evaporating these droplets is mixed with the hot air reducing the temperature of the mixture. At later times, the droplets are injected into this low-temperature nearly saturated gaseous flow thereby reducing their evaporation rates. Therefore, they traverse longer distances downstream where they are radially dispersed by the gaseous flow turbulence. This scenario is well represented in case of the spray-structure predicted by the stochastic approach. Contrary to the experimental findings, the standard approach over-predicts the vaporization rates resulting in liquid spray droplets completely being evaporated in first 100mm of injection. So, for further comparison of the droplet statistics only the results from stochastic approach are presented.

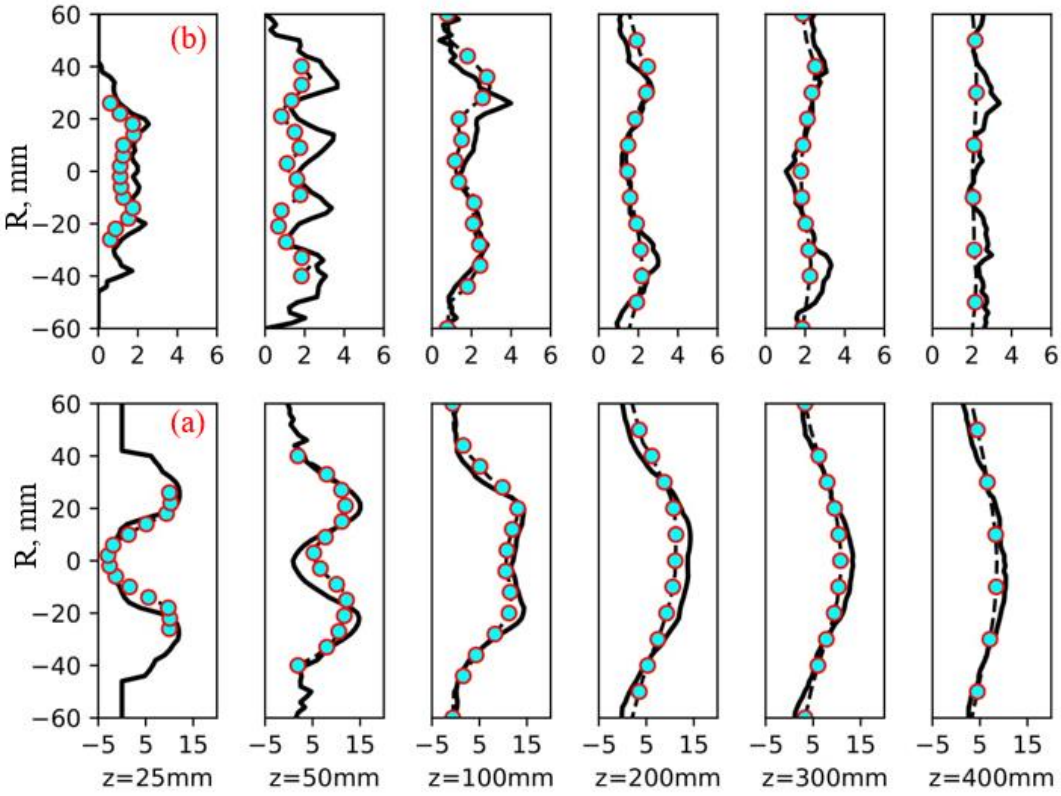

Figure 3-4 Comparison of (a) mean and (b) rms axial velocity averaged over all droplet sizes at different axial locations starting from 25mm upto 400mm

Figure 3-4 shows the radial profiles of the mean and root mean square (RMS) values of axial velocity fields for droplets at different cross-sections. It is seen that except the profile of RMS fluctuations at z=50mm, the statistical distributions of the axial velocity of droplets are predicted relatively well. The velocity profiles reproduce the entrainment of injected droplets by the high-speed co-flow; droplets move downstream spreading radially, and their velocity profile takes a form similar to that of the gaseous flow. Therefore, the negative velocities of droplets at z=25mm are a result of the recirculation zones in the gas flow generated by sudden expansion of the gas-flow entering the combustion chamber from the co-flow annulus. In the simulation the recirculation zones are extended upto 50mm as can be seen from the mean axial velocity comparison. A good comparison of the droplet velocity statistics reflects the accuracy of the LES-STRIP approach for modelling spray dispersion.

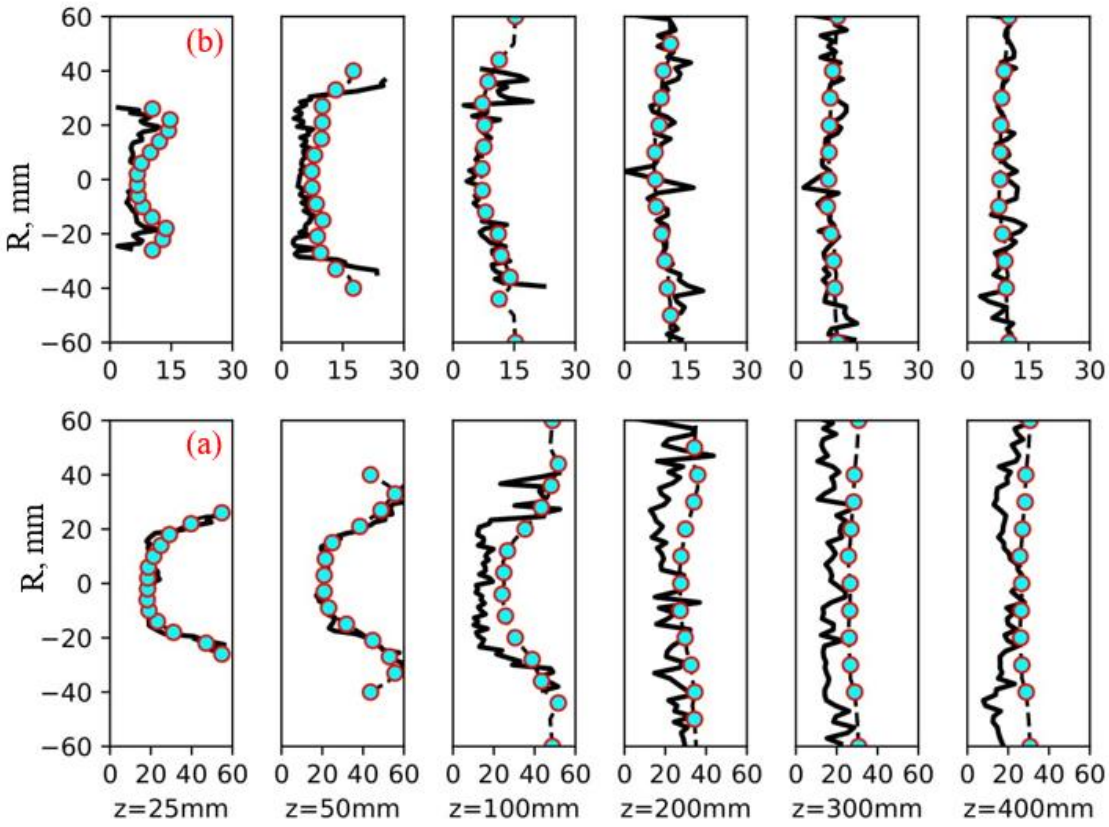

Figure 3-5 Comparison of (a) mean and (b) rms droplet diameter averaged over all droplet at different axial locations

Figure 3-5 shows the mean and rms of the droplet diameter at different axial locations. Since the injection model provides the nozzle capability with continuous hollow cone spray, wherein smaller size droplets are entrained in the core, whereas the larger droplets travel to the edge of the spray, these are subjected to the hot coflow and evaporate more intensively than droplets in the core. Consequently, the mean droplet size profile flattens in the downstream direction. It is seen that while rms profiles of the droplet diameter at all locations and the mean diameter in the near field are well predicted, the profiles of the mean diameter in the far-field of the spray are predicted less satisfactory, being at the same time not far from measurements: at 300mm and 400mm, the computed diameter is around 20μm against measured 30μm. While there are large fluctuations in the droplet statistics because of the averaging over discrete time samples, better prediction of the general trends indicates the capability of SMICE model for predicting the spray evaporation process.

3.4.2 Non-evaporating diesel spray conditions

All through this study the KH-RT breakup model is used, as the effects of unresolved scales on the atomization and resulting spray characteristics are more profoundly seen. *Figure 3-6* and *Figure 3-7* show the comparison of the spray tip penetration lengths

predicted by the two dispersion models for the non-evaporating ECN spray experimental conditions corresponding to injection pressures of 150MPa and 50MPa respectively.

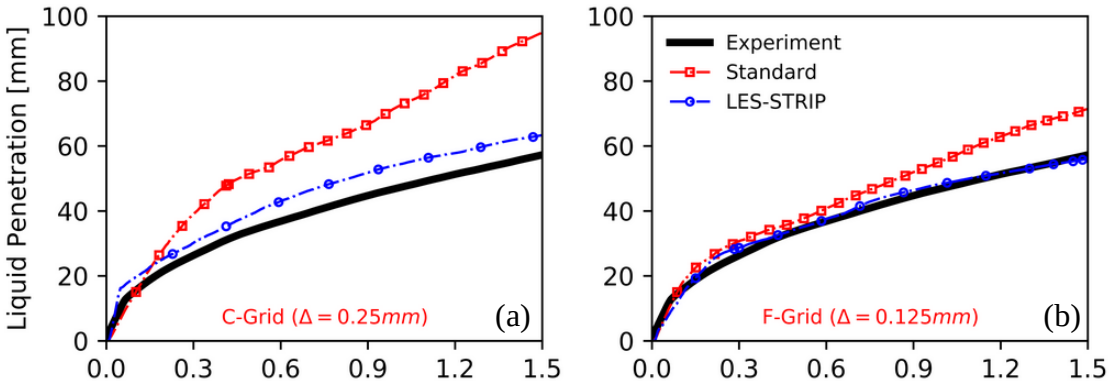

Figure 3-6: Comparison of spray tip penetration length evolution for *Spray-A1* experiment with $P_{inj} = 150MPa$ for two grid sizes i.e. (a) C-grid (b) F-grid

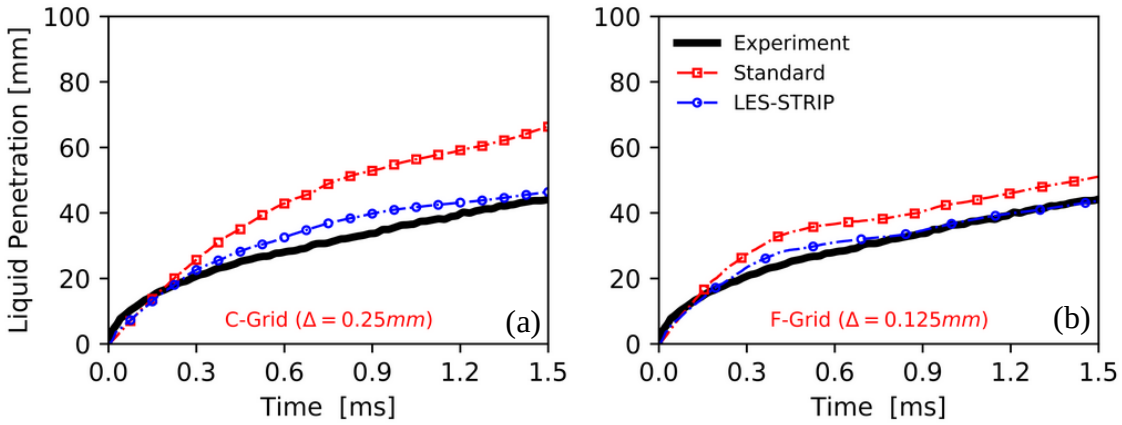

Figure 3-7: Comparison of spray tip penetration length evolution for *Spray-A2* experiment with $P_{inj} = 50MPa$ for two grid sizes i.e. (a) C-grid (b) F-grid

The results show that the standard SGS model requires much finer grid resolution to capture the evolution of penetration length compared to the LES-STRIP model. As grid resolution is increased, more and more scales are directly resolved by LES through the filtered velocity $\bar{u}$ and the modelled sub-grid scale velocity contributions ($u' \sim \sqrt{k_{sgs}} \sim 0$) in negligible. On the other hand, the STRIP model gives a much better prediction of penetration length evolution compared to stochastic breakup models even on a coarse grid for both injection pressures. Moreover, the penetration length predicted by the STRIP model is less sensitive to the variations in grid size. For all further comparisons of spray statistics, the results from *F-grid* are used. First a comparison of the spatial evolution of the SMD predicted by different models for the high injection pressure *Spray-A1*

experiment is shown in *Figure 3-8*. While the standard model predicts a slower breakup rate with large steady state SMD values, the STRIP model predicts a much faster breakup rate similar to the stochastic breakup model but produces smaller steady state SMD values compared to stochastic breakup model.

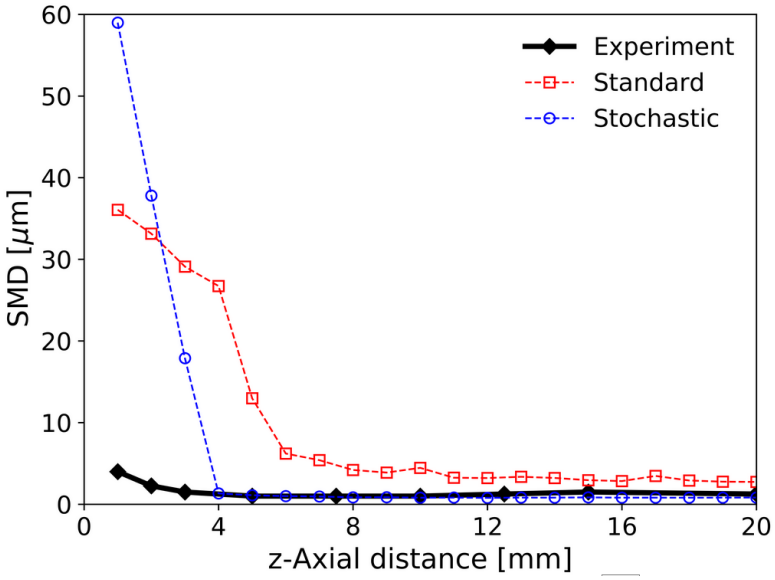

Figure 3-8: Evolution of the Sauter mean diameter (SMD) axially along the centreline of the spray at time t=1.5ms ASOI for Spray A-1 test case – comparison of dispersion models

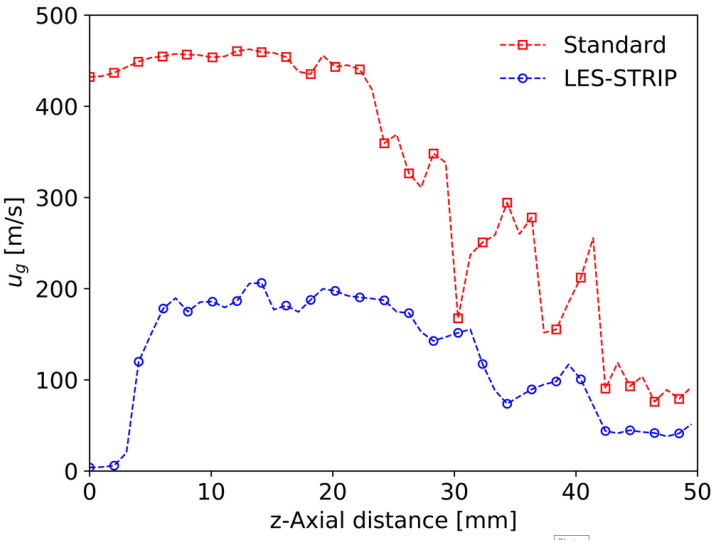

Figure 3-9: Instantaneous gas phase velocity profile along spray axis at t=1.5ms ASOI for Spray A-1 test case – comparison of dispersion models

The comparison of the instantaneous axial gas-phase velocity profiles along the spray centreline shown in *Figure 3-9*, shows that the standard dispersion model predicts very high gas-phase velocities which are retained over the spray length. This indicates that it

overpredicts the turbulence production by the momentum transfer from the liquid spray in the high-shear near-nozzle region. On the other hand, the STRIP model shows a quick acceleration followed deceleration of the gas which is in line with the gas jet analogy of the sprays.

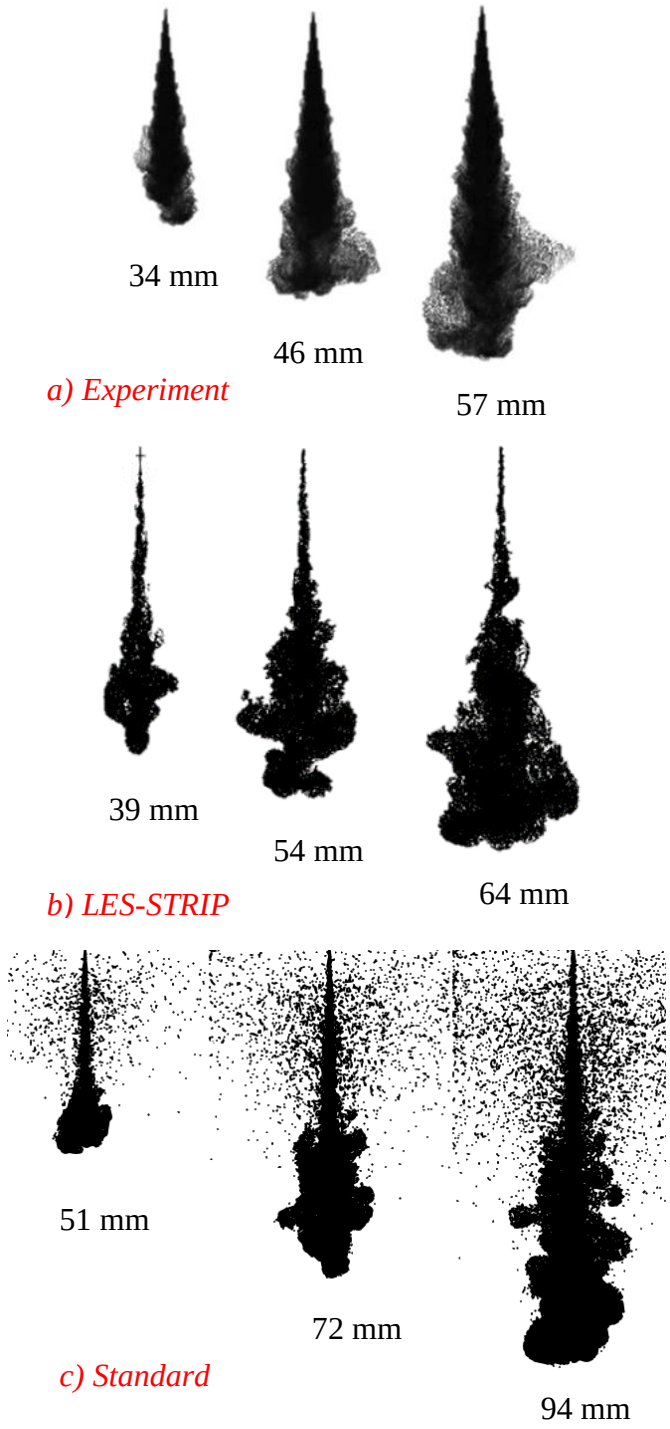

Figure 3-10: Instantaneous spray structure images of (a) Experiment (b) LES-STRIP and (c) Standard dispersion model at times 0.5ms, 1.0ms and 1.5ms ASOI. The results shown here are for the *C-grid* ($\boldsymbol{\Delta = 0.25mm}$).

In order to qualitatively illustrate the differences in the spray physics predicted by different dispersion models, a comparison of the instantaneous spray structure with the experiment for time instances of 0.5ms, 1.0ms and 1.5ms is provided in *Figure 3-10*. While the spray structure predicted by LES-STRIP model are similar to the schlieren images of the experiment, the standard model predicts a spray with highly penetrative spray core surrounded by large number of parcels dispersed radially close to the injector. Such differences in the spray structure between the two dispersion models are explained in terms of the short correlation of components of acceleration vector compared to its norm, manifested by intermittency effects of small scales. The auto-correlation function of the droplet acceleration is calculated using Eq. 3-21.

$$\boldsymbol{\rho_{a_p}(\tau)} = \frac{\langle a_{p,k}(t+\tau)a_{p,k}(t)\rangle}{\langle a_{p,k}(t)a_{p,k}(t)\rangle} \qquad \textbf{3-21}$$

Here k = 1, 2 represents the axial and the radial components of acceleration respectively and the brackets indicate averaging over all particles. A comparison of the auto-correlation of different components of the acceleration vector for the both models is presented in *Figure 3-11*. The correlation time (τ) is normalized by the Kolmogorov time scale (τ_η).

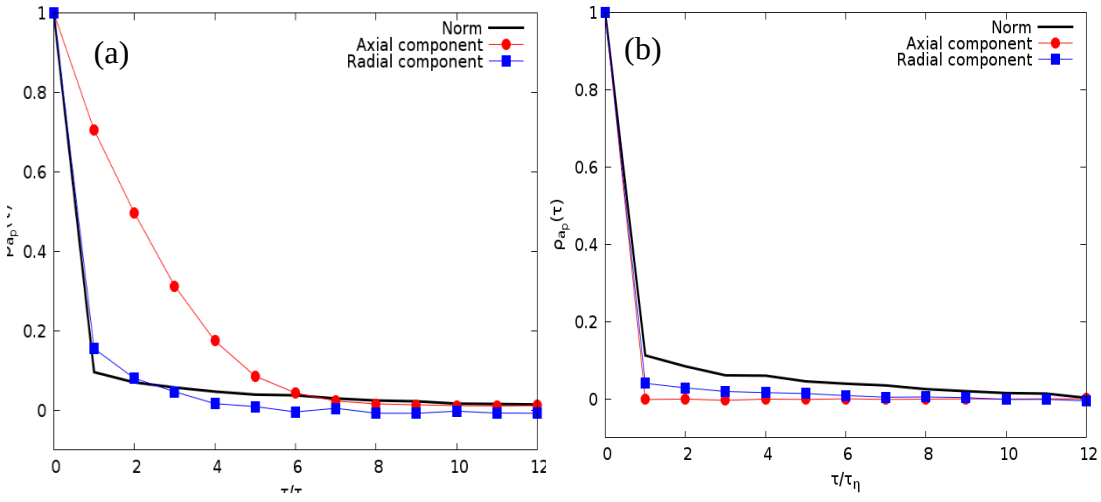

Figure 3-11: Comparison of autocorrelation of the droplet acceleration norm, axial and radial components for (a) Standard model (left) (b) LES-STRIP (right)

It can be seen from *Figure 3-11(a)* that for standard dispersion model, the droplet acceleration components have longer correlation than its norm. Long correlations of axial component indicate that droplets retain their axial direction of motion for a long time without radial dispersion. This is the consequence of the model used in Eq. 3-2, where the norm of acceleration sampled from turbulent velocity u' is non-correlated in time. At

the same time the direction of acceleration is retained on times defined by large scale structures in Eq. 3-3. Therefore, a large number of droplets in the spray core only penetrate axially without any radial dispersion. Moreover, only the secondary droplets from stripped from the blobs which acquire an additional radial velocity component are dispersed radially as shown in *Figure 3-10 (c)*. On the other hand, for LES-STRIP it can be seen from *Figure 3-11(b)* that both the axial and radial components of droplet acceleration have smaller correlation compared to its norm. The shorter time correlations of the components are because of the stochastic model, where the frequency of the fluctuations in orientation vector of droplet acceleration are scaled with the Kolmogorov time scale, thereby manifesting the effects of intermittency i.e. vortical structures on small scales are as much energetic as the large-scale structures. Therefore, the LES- STRIP model shows higher radial dispersion of droplets thereby accurately predicting the spray structure as shown in *Figure 3-10 (b)*.

3.4.3 Evaporating diesel spray conditions

3.4.3.1 ECN Spray-H experiment

Figure 3-12 shows the comparison of the liquid and penetration lengths predicted by the two modelling approaches for different grid resolutions. The liquid spray tip penetration attains steady state value, where the total evaporation rate is equal to the fuel injection rate, characterizing the overall spray vaporization rate. On the other hand, vapor penetration length defined as the farthest downstream location of 0.1 % fuel mass fraction, continues to progress with time. The vapor penetration length characterizes the rate of vapor/air mixing, thereby characterizing the overall spray dispersion. It is clearly seen that the stochastic approach predicts both the liquid and vapor penetration lengths accurately even on coarser grids. Moreover, the results predicted with the stochastic approach are less sensitive to the grid resolution for the two-grid sizes compared in this study i.e. $\Delta = 0.125mm$ and $\Delta = 0.25mm$. On the other hand, the standard approach overpredicts both the liquid and vapor penetration lengths even on the fine grid size $\Delta = 0.125mm$. An explained in Chapter-2 the experiments provide ensemble-averaged statistics of 20-40 realizations of each spray experiment. In order to replicate the same numerically 20 realizations each for the two approaches are preformed using the random-seeding technique explained in Chapter-2. For the two different grid resolutions, an assessment of accuracy in prediction of the ensemble averaged mean vapor mass fraction on the spray centreline and its radial profile at longitudinal position of 30 mm downstream at time t= 0.5ms ASOI is shown in *Figure 3-13*.

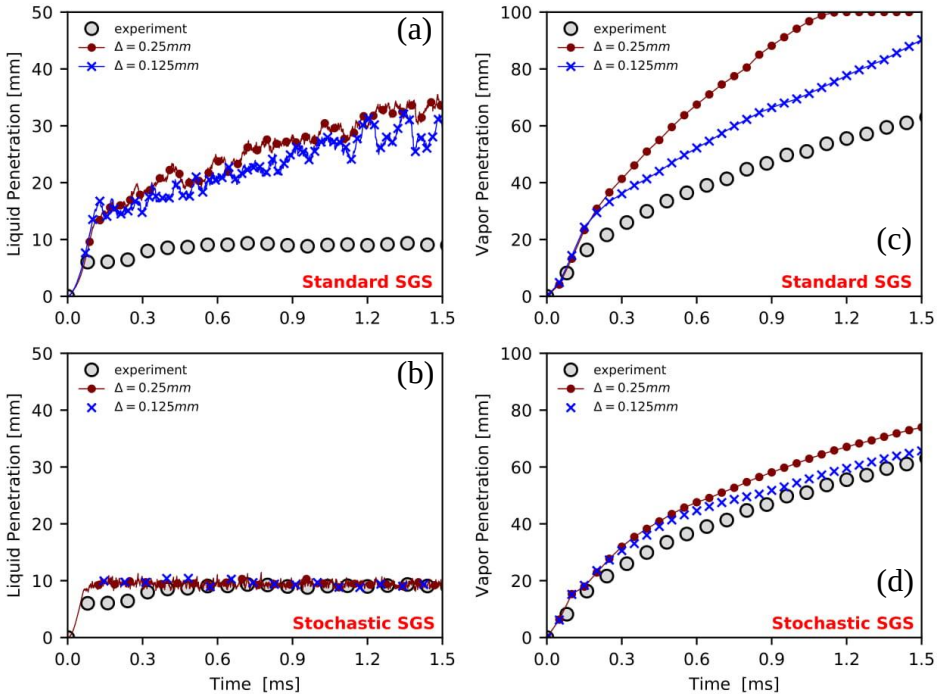

Figure 3-12 : Mesh sensitivity analysis of Liquid Penetration length: (a) Standard (b) Stochastic approach. Mesh sensitivity analysis of Vapor Penetration length : (c) Standard (d) Stochastic approach.

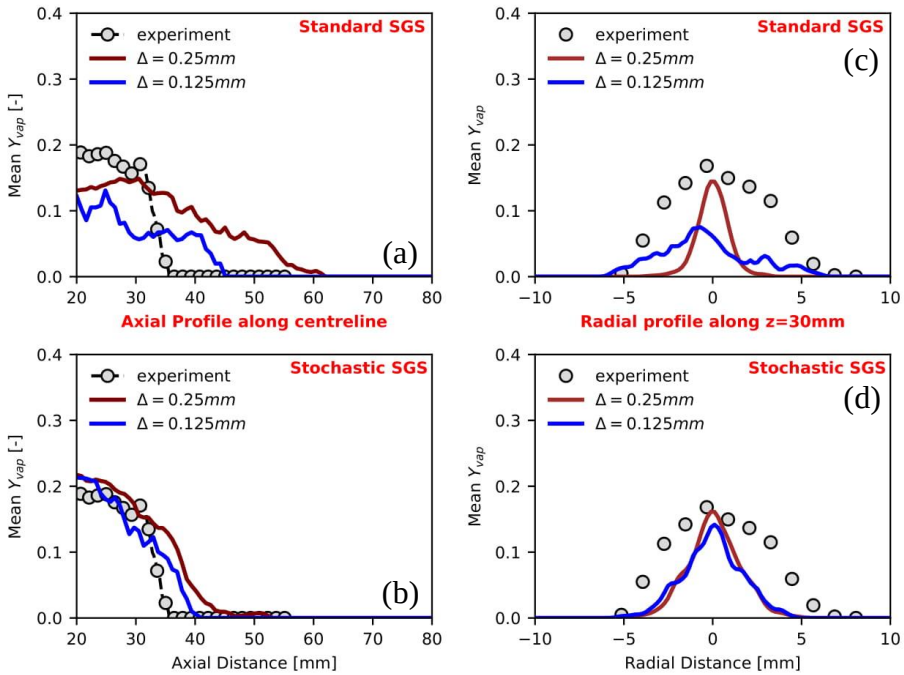

Figure 3-13 : Mesh sensitivity analysis of mean vapor mass fraction along the spray centreline (a) Standard (b) Stochastic. Mesh sensitivity analysis of mean vapor mass fraction at a cross-section of 30 mm downstream (c) Standard (d) Stochastic. The results correspond to the time t= 0.5ms ASOI

It can be seen that while the stochastic approach gives a fairly good prediction of the spray-centreline vapor-mass fraction profiles even on coarse grid, the standard approach under-predicts the centre-line vapor mass fraction profiles even on the finer grid. On the other hand, while the stochastic approach gives a better prediction of the radial spread of the mass fraction field compared to standard approach, the experimental spray plume is relatively broader than that predicted from the stochastic approach. Similar to the penetration length profiles, the local vapor mass fraction profiles predicted using stochastic approach are less sensitive to the grid size compared to the standard approach. Since the finer mesh provides better spray statistics, especially for the standard approach for all further comparisons, the statistics obtained from finer grid are presented. Next a comparison of the mass fraction field along the spray centreline and its radial profiles at three different longitudinal positions i.e. at 20, 30 and 40mm downstream for two different time instances i.e. t= 0.68ms and t= 1.13ms ASOI are shown in *Figure 3-14* and *Figure 3-15*. From the results it can be seen that for different times, the stochastic approach gives a better prediction of mean vapor mass fraction compared to the standard approach. But the stochastic approach tends to over-predict the centreline vapor mass fraction in the near-nozzle dense spray region while correctly predicting the radial spread in the mass fraction profiles as can be seen from the radial mass fraction distribution at longitudinal distance of 20mm. On the other hand, the standard approach continues to under-predict the both the centreline and radial vapor mass fraction distributions even at alter times. Since the standard approach does not provide a good comparison of the mean vapor mass fraction field, it is also incapable to match the variance of the vapor mass fraction. So, a comparison of the variance of mass fraction distribution along the spray centreline and its radial profiles for three different longitudinal positions i.e. at 20mm, 30mm and 40mm are shown in *Figure 3-16* and *Figure 3-17* for the stochastic approach at two different times t=0.68ms and 1.1 ms ASOI. From the results it can be concluded that the stochastic approach seems to provide a fairly good representation of the variance of mass fraction distribution, even though it predicts slightly higher values along the spray axis and also slightly narrow spray plume compared to the experiment. Next a comparison of the instantaneous spray structure predicted by a single realization of the stochastic approach with a single realization of the experiment at four different time instances of spray evolution are shown in *Figure 3-18*. The mass fractions statistics corroborate the spray snapshots. While the spray structure is well represented by the stochastic approach, the initial spray plume in the experiments is wider than that predicted by the stochastic approach.

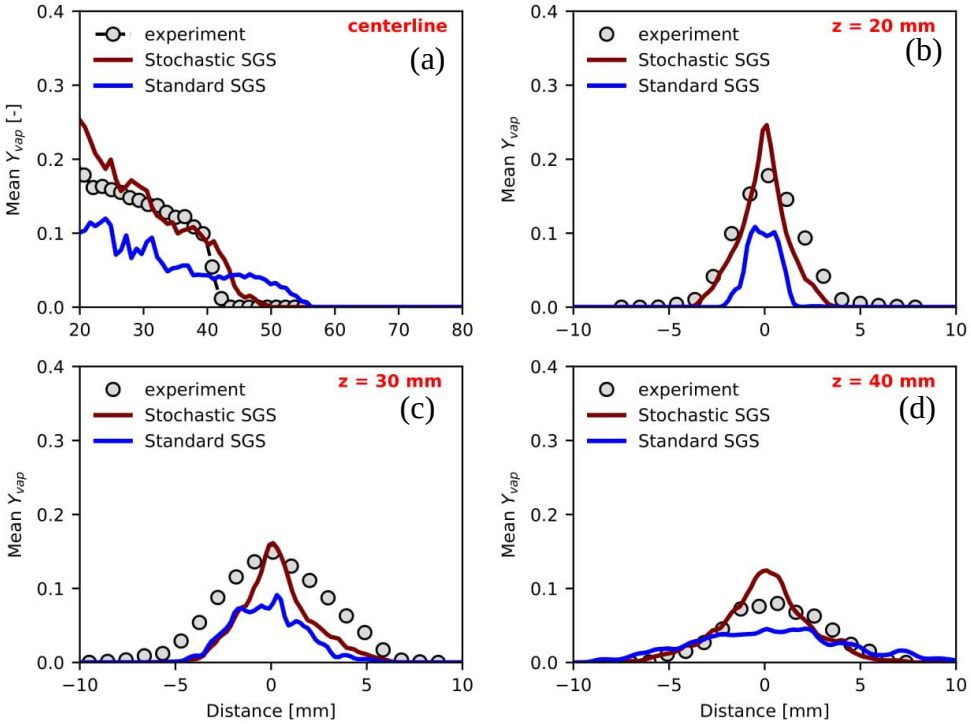

Figure 3-14 : Mean vapor mass fraction profiles (a) along the spray centreline (b) at cross section of 20mm, (c) at cross section of 30 mm and (d) at a cross section of 40mm downstream of nozzle exit. The results correspond to a time t= 0.68ms ASOI.

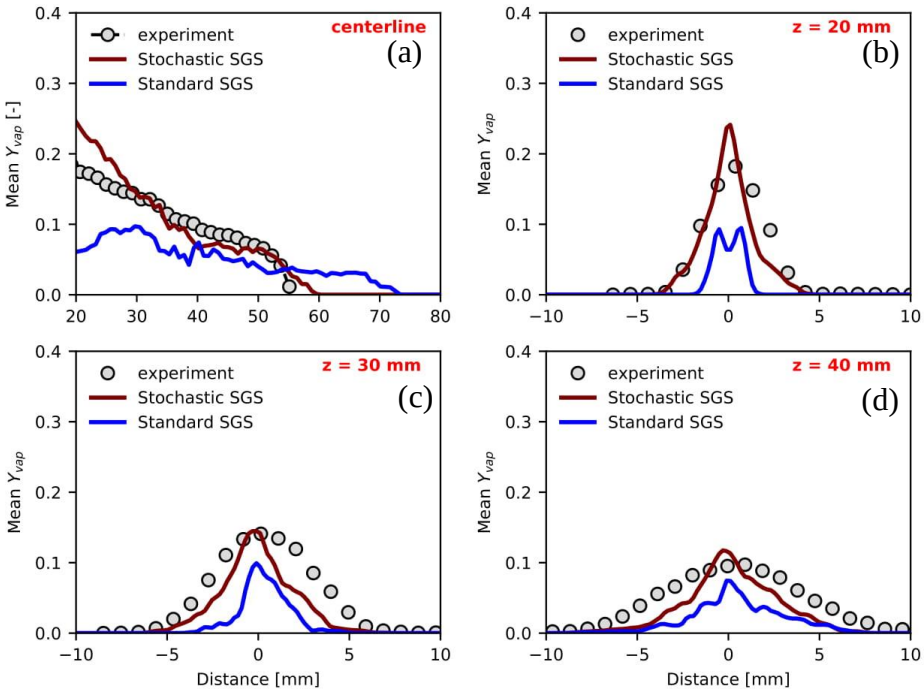

Figure 3-15 : Mean vapor mass fraction profiles (a) along the spray centreline (b) at cross section of 20mm, (c) at cross section of 30 mm and (d) at a cross section of 40mm downstream of nozzle exit. The results correspond to a time t= 1.1ms ASOI.

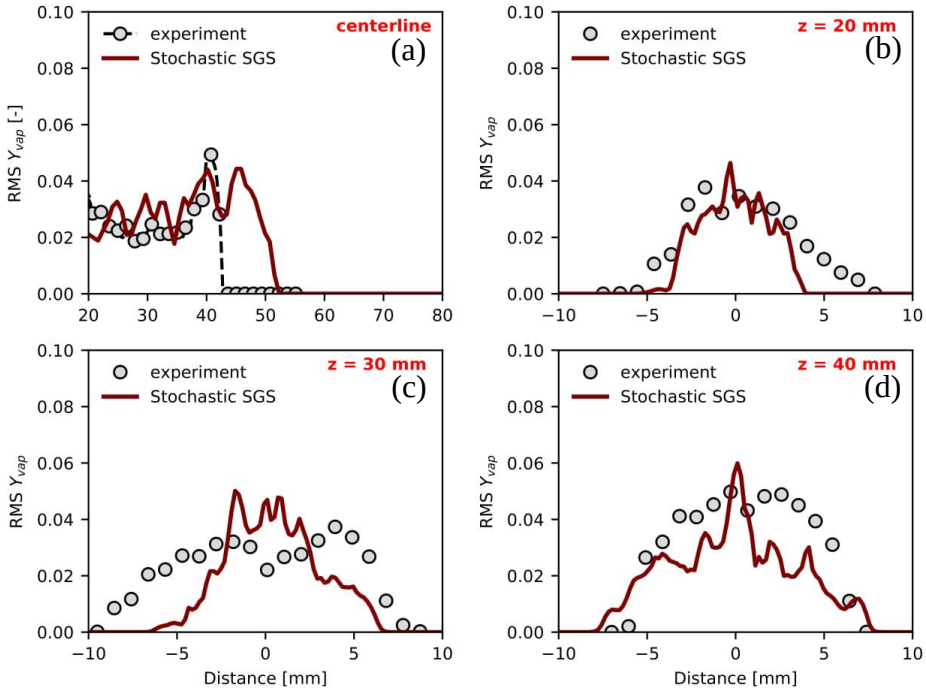

Figure 3-16 : RMS of vapor mass fraction profiles (a) along the spray centreline (b) at cross section of 20mm, (c) at cross section of 30 mm and (d) at a cross section of 40mm downstream of nozzle exit. The results correspond to a time t= 0.68ms ASOI.

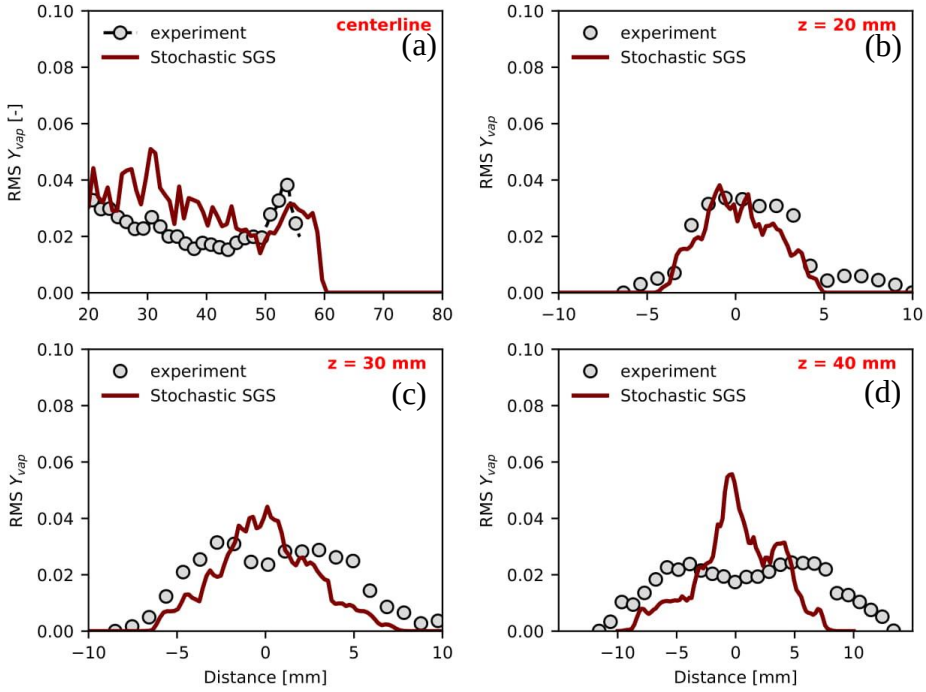

Figure 3-17 : RMS of vapor mass fraction profiles (a) along the spray centreline (b) at cross section of 20mm, (c) at cross section of 30 mm and (d) at a cross section of 40mm downstream of nozzle exit. The results correspond to a time t= 1.1ms ASOI.

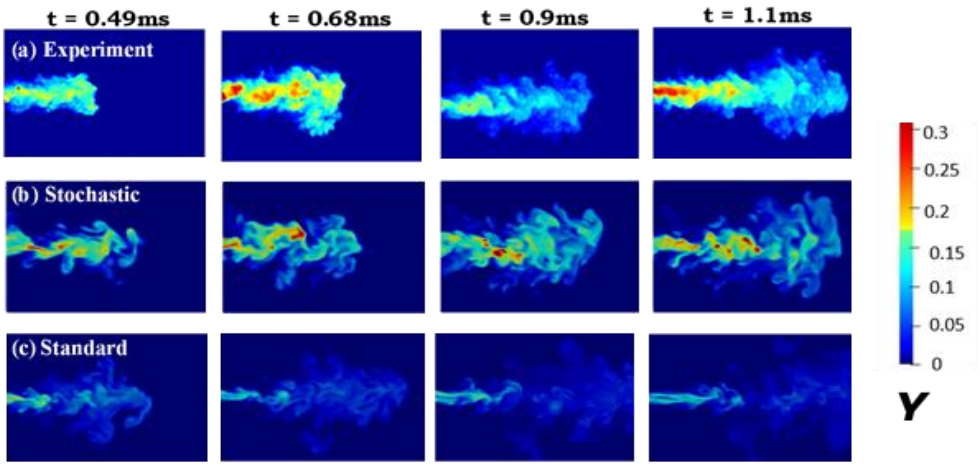

Figure 3-18 : Comparison of the instantaneous vapor mass fraction profiles of (a) Experiment (b) Stochastic (c) Standard at different time instances of t= 0.49ms, 0.68ms, 0.09ms and 1.1ms ASOI.

3.4.3.2 ECN Spray-A experiment

While *Spray-H* experiments provide the time varying statistics of evaporating spray dynamics, ECN *Spray-A* experiments provide vapor mass fraction statistics reflective of a steadier state condition. Similar to *Spray-H*, multiple realizations of *Spray-A* experiment are simulated using the random seeding technique to accurately represent the mean and variance statistics of velocity mass fraction statistics. Moreover, having shown the grid sensitivity of the two approaches for *Spray-H* only the results of statistics obtained for the finer grid resolution i.e. *F-grid* are shown in this section. The axial and radial profiles of the ensemble averaged mean vapor mass fraction profiles for *Spray-A* experiment at the end of the simulation i.e. t=1.5ms ASOI are shown in *Figure 3-19*. From the *Spray-A* condition, the stochastic approach gives a very good prediction of both the centreline and radial mean mass fraction distributions compared to *Spray-H*. On the other hand, even on fine grid the standard approach under-predicts the centreline values and also the radial spread of the mass fraction distributions similar to the results seen in *Spray-H* experiment. Therefore, a comparison of the variance of mass fraction of only the stochastic approach with the experiment is shown in *Figure 3-20*. Even the variance of mass fraction distributions is much better predicted for the ECN Spray-A steady state spray condition. In hindsight the better performance of the stochastic approach in general for the *ECN Spray-A* conditions compared to *Spray-H* experiment could be because for the *Spray-H* experiment we used a approximated mass flow rate profile filtering out the variations in the steady state mass flow rate, while for *Spray-A* experiment we used the experimental rate shape profile for mass flow rate.

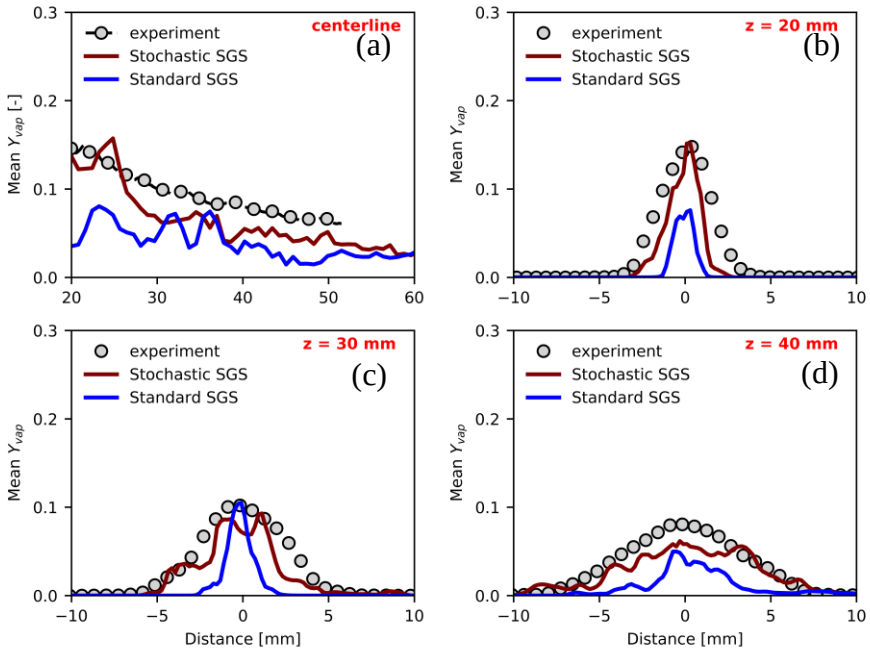

Figure 3-19 : Mean vapor mass fraction profiles (a) along the spray centreline (b) at cross section of 20mm, (c) at cross section of 30 mm and (d) at a cross section of 40mm downstream of nozzle exit.

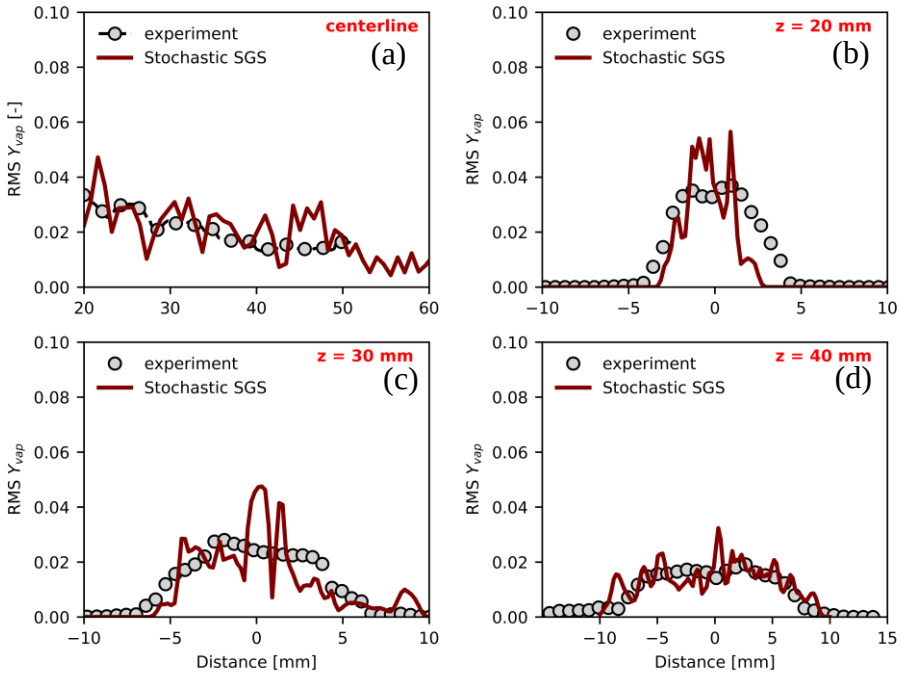

Figure 3-20 : RMS of vapor mass fraction profiles (a) along the spray centreline (b) at cross section of 20mm, (c) at cross section of 30 mm and (d) at a cross section of 40mm downstream of nozzle exit.

While the centreline vapor mass fraction profiles reflect the intensity of vaporization process and the radial distribution of mass fraction implicitly the turbulent fuel-air mixing process. But a direct measure of the momentum transfer from the liquid spray to the surrounding gaseous medium and also the air-entrainment by the spray is quantified better in terms of the velocity statistics of gas-phase provided. So, the ensemble averaged gas-phase velocity statistics for the *Spray-A* at different time instances measured by Payri et al (45) is used for assessing the two approaches. The mean axial velocity on the spray centreline and its radial profile at longitudinal position of 30 mm downstream at time t= 0.5ms ASOI is shown in *Figure 3-21*.

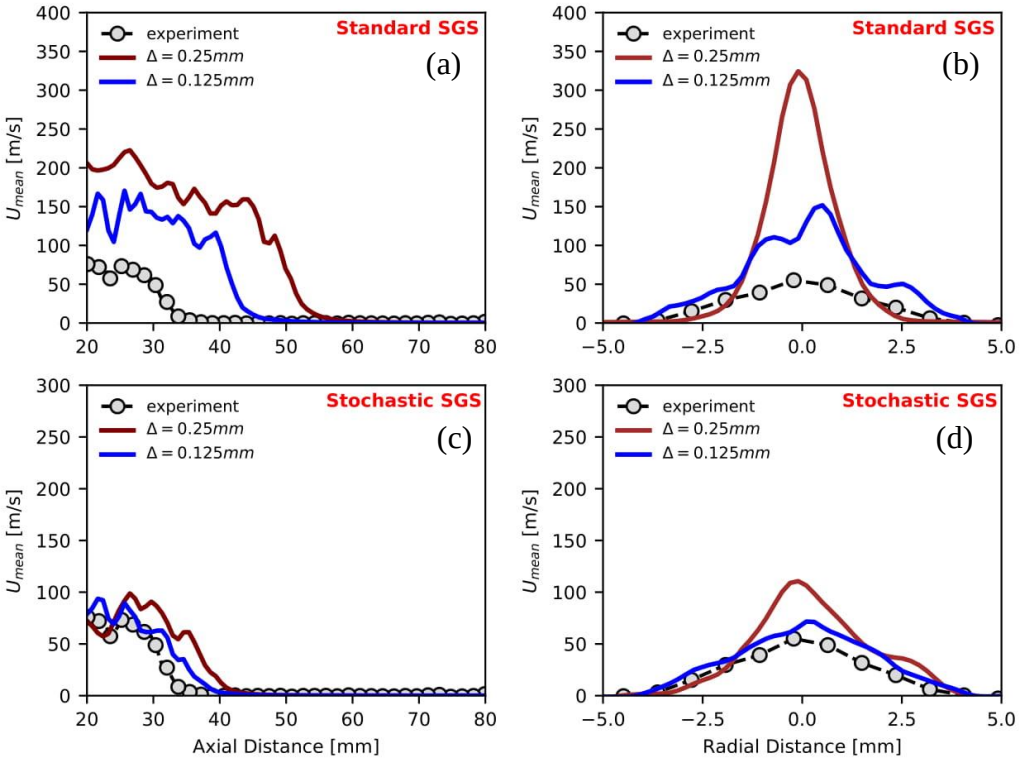

Figure 3-21 : Mesh sensitivity analysis of mean axial velocity along the spray centreline (a) Standard (b) Stochastic. Mesh sensitivity analysis of mean axial velocity at a cross-section of 30 mm downstream (c) Standard (d) Stochastic.

In *Figure 3-21*, grid sensitivity of the two approaches in predicted the gas-phase velocity is shown. From the results it can be clearly seen that the standard approach over-predicts the gas-phase velocity by factor of 3-4 even on the finer grid resolution. The over-prediction of the gas velocities by the standard approach reflects that the momentum transfer from the liquid spray droplets to the surrounding gaseous medium in the near nozzle region is over-predicted. Also, it can be seen that the gas retains this momentum for long distances downstream indicating that the air-entrainment process is also not well accounted for. On the

other hand, stochastic approach while slightly over-predicting the centreline axial gas velocities on the coarse grid, it provides a fairly good representation of the gas velocities on the finer grid. Since the standard approach does not represent the mean velocity statistics accurately, it cannot give good prediction of the variance of velocity profiles as well. So, a comparison of the mean and variance of axial velocity components for the stochastic approach on fine grid for time t=1.5ms ASOI is shown in *Figure 3-22* and *Figure 3-23*. The results show that the mean velocity profiles are predicted reasonably well except the near-field of the spray, corresponding to from the nozzle exit 20mm. The results also show that while the stochastic approach accurately predicts the mean velocity profiles, it still tends to over-predict the variance of the axial velocity profiles.

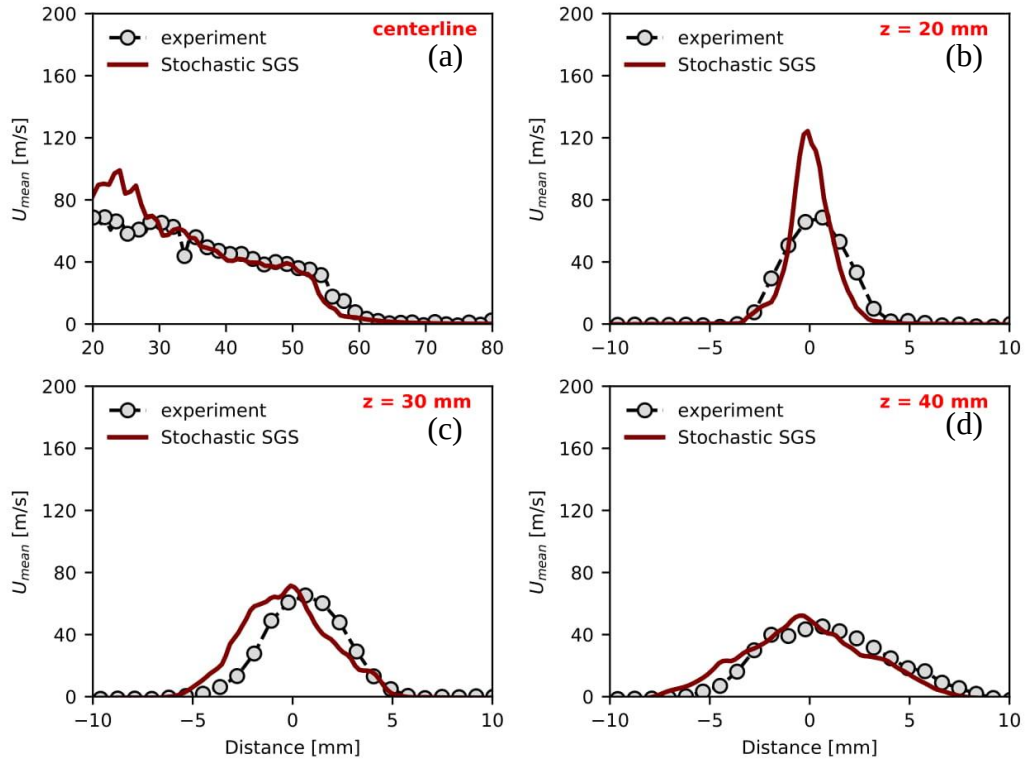

Figure 3-22 : Mean axial gas velocity (a) along the spray centreline (b) at cross section of 20mm, (c) at cross section of 30 mm and (d) at a cross section of 40mm downstream of nozzle exit.

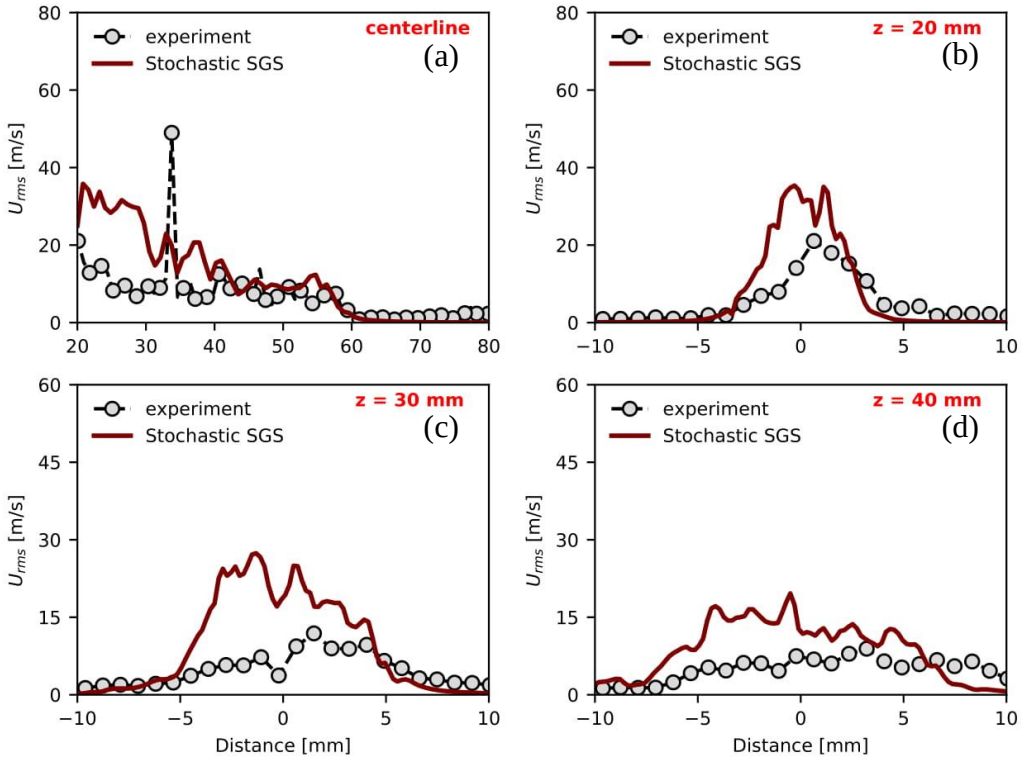

Figure 3-23 : RMS axial gas velocity (a) along the spray centreline (b) at cross section of 20mm, (c) at cross section of 30 mm and (d) at a cross section of 40mm downstream of nozzle exit. The profiles are for time t=1.5ms ASOI.

3.5 Discussion – Numerical simulations and relevant physics of spray vaporization

Even though a numerous DNS studies have been performed to characterize the vaporization effects in terms of droplet clustering and scalar mixing in simplified flow configurations, the physical parameters controlling the spray vaporization in a high Reynolds number condition is an open problem. Having obtained satisfactory prediction of different flow statistics in comparison to the experiments of high-speed vaporizing sprays motivates us to discuss the physical aspects of spray vaporization predicted by the stochastic approach for the two-configurations used in this study i.e. the co-axial combustor and high-pressure fuel injected into relatively high temperature environments like in ECN sprays. Since our results not from DNS, our observations are only qualitative in nature and have to be seen as an attempt to further the understanding of complex spray evaporation dynamics in realistic flow-configurations.

3.5.1 Co-axial spray combustor

Figure 3-25 shows the local concentration of the droplets marked as point particles mapped on the normalized local vorticity field at two different longitudinal positions z= 50mm and z=250mm. From the plots it can be seen that the droplets are concentrated in clusters formed outside of the high intensity vorticity regions at both locations.

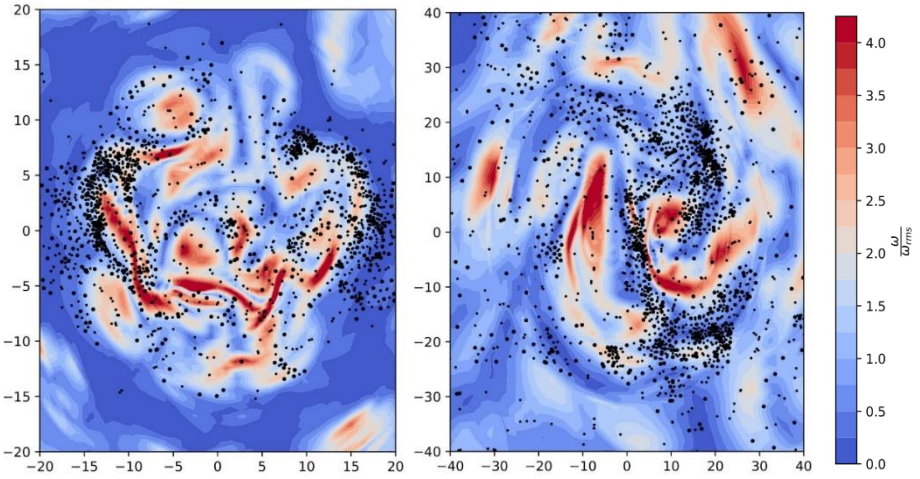

Figure 3-24 : Concentration of droplets marked as point particles mapped onto the Eulerian vorticity field at two longitudinal sections corresponding to z=50mm (left) and z=250mm (right) downstream of injection.

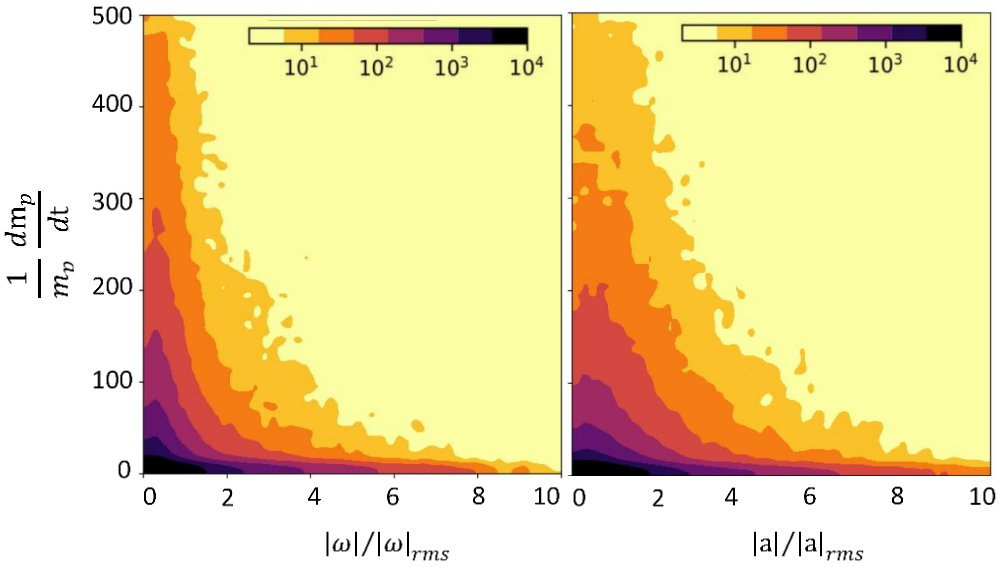

Figure 3-25 : Joint-PDF of droplet vaporization intensity and vorticity (left) and acceleration (right). The statistics are obtained over all the droplets in the domain at a steady state condition

Next in-order to understand the correlation of intensity of droplet evaporation with different gaseous flow parameters like vorticity, acceleration and strain rate, we plot the

joint-PDF of droplet vaporization intensity i.e. $\frac{1}{m_p}\frac{dm_p}{dt}$ and the gaseous flow parameters interpolated at the droplets positions. *Figure 3-25* show the joint-PDF of droplet vaporization intensity and gas acceleration and vorticity fields for all the droplets in the computational domain. The inensity of the joint-PDF is on an log-scale and is colored by the number of particles epxeriencing a certain magnitude of flow-field for a given intensity of vaporization. From the first view of the joint-PDF results it can be seen that droplets with high vaporization rates are seen in low-acceleration and low-vorticity regions. But taking a second look accounting for the number density, it becomes evident that a large number of droplets (dark purple color) are concentrated in low-vorticity and acceleration zones experience very low-vaporization rates while only fewer droplets experience higher vaporization rates. As seen earlier in *Figure 3-24*, there are droplet clusters in low-vorticity zones in the spray centre while some isolated droplets dispersed radially away from the center also are located in low-vorticity and nearly stagnant flow regions. Since clustering of droplets reduces the vaporization rate, it can be assumed that the large number of non-evaporating droplets at low-vorticity and low-acceleration seen in the joint-PDF's coresspond to the droplet clusters. On the other hand, the high vaporization intensities of droplets in low-vorticity and low-acceleration can be because of two scenarios. The first is the dispersed isolated droplets in the spray periphery are also located in relatively low-vorticity zones and can evaporate more intensely compared to the clusters. This explains the intermediate vaporization intensities. Second entrainment of hot air by the spray in the region enclosed by the annular coflow results in high temperature spots corresponding to the regions where droplets are clustered in the spray centre. Given the low droplet mass flow rates and the large dimensions of the injector the vapor mass fractions are very low in the combustion chamber as shown in *Figure 3-3*. Therefore the clusters are not saturated to restrict evaporation. So the droplets clustered in these high temperature zonse tend to evaporate very intensively. To illustrate this in *Figure 3-26* we plot the cross-sectional view of spray on the longitudinal plane at z=50mm with lagrangian particles mapped onto the Eulerian temperature field. Here while the droplet size is scaled by their size, the intensity of their vaporization rate is colored on gray-scale. The closely-packed droplet clusters in *Figure 3-26* correspond to the low-vorticity zones shown in *Figure 3-24*. And it is clearly evident that because of the high temperatures in these regions, the intensity of droplet vaporization of some of the droplets is also very high (colored in black).

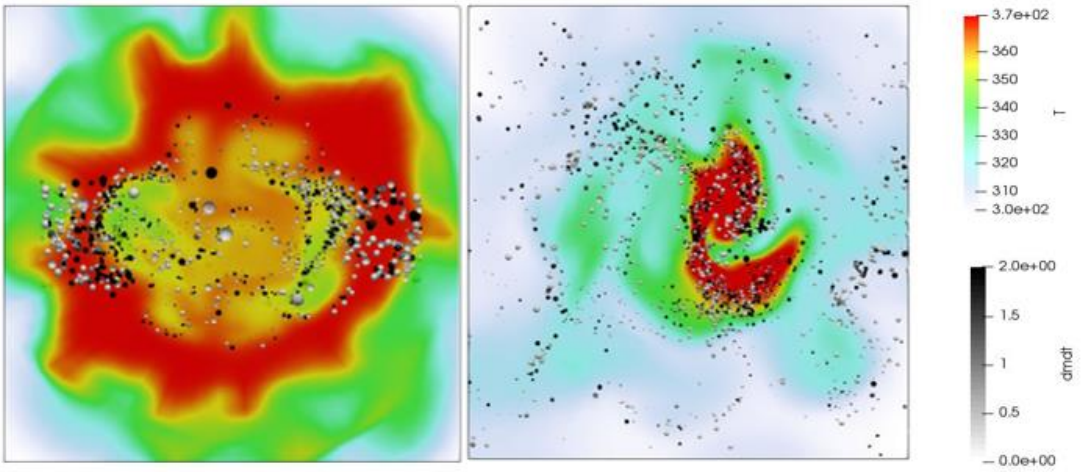

Figure 3-26 : Cross sectional view of spray structure at z= 50mm (left) and z=250mm (right). Droplets are scaled by their size and coloured by intensity of vaporization. The Eulerian flow field shows the gas temperature

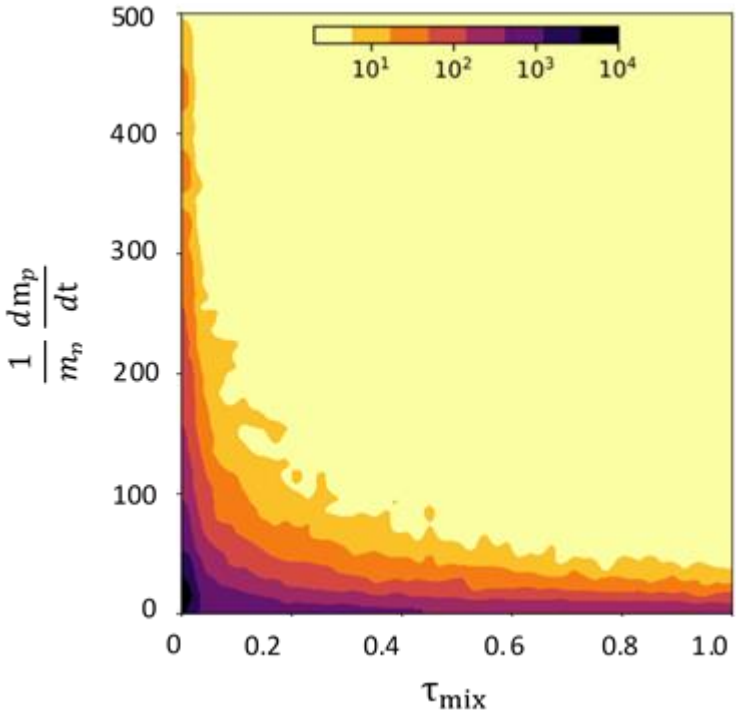

Figure 3-27 : Joint-PDF of droplet vaporization intensity and mixing time scale

Another important parameter controlling the vaporization rate is the rate of of vapor surrounding the droplet surface by the turbulence of the gaseous flow, which in our model is represented by the mixing time scale on energetic scales $\tau_{mix} = k_{sgs}/\varepsilon$. The joint-PDF of the droplet turbulent mixing time scale and intensity of vaporization is shown in *Figure 3-27*. Smaller the mixing time-scale more rapid is the mixing of saturated vapor at the droplet surface by the turbulence. Therefore the vapor mass fraction 'seen" by the droplet

approaches the filtered vapor mass fraction resulting in higher vaporization rates. resulting in large mixing time scales. Again similar hypothesis can be used to explain the correlation of clustering and mixing time scales and their vaporization intensities. From *Figure 3-27* it can be seen that small number of droplets have very high vaporization intensities and their mixing time scales are relatively very small $\tau_{mix} \sim 0$. This probably corresponds to the dispersed-isolated droplets in the spray periphery. The intermediate mixing time scales with intermediate vaporization intensities can probably correspond to clustered droplets in hot zones. And finally, the high number of droplets with very small vaorization intensities and long mixing time scales can correspond to the droplet clusters.

3.5.2 Evaporating direct injection fuel sprays

Unlike the co-axial combustor, the fuel sprays in engines are injected from a very small injector nozzles with much higher mass flow rates into a stagnant ambient flow at higher temperatures. Given the relatively small droplet sizes and higher Reynolds numbers the turbulence and preferential concentration effects on droplet evaporation can be more significant. But the evaporating ECN-Spray experiments used in this study are at very high temperatures where most of the spray is evaporated in first few millimeters of injection. So we considered an hypothetical condition of spray injection for *Spray-A* injector with lower injection pressure with injection velocity of 200m/s and a lower ambient temperature of 600K, so that the spray tip penetration length is prolonged upto a distance of approximately 45 mm. All the statistics presented in this section correspond to a quasi-steady state spray obtained at end of simulation i.e. t=1.5ms ASOI. In case of direct injection fuel sprays, the lquid spray generates the turbulence in the gaseous flow field. The structure of the turbulence in the gaseous jet is similar to the the spray structure. This is shown by plotting the iso-surface of the Q-factor representing the to the symmetric part of the local resolved velocity gradient tensor in *Figure 3-28*. A positive value of Q shows the local rotational motion of the fluid was chosen for plotting the iso-surfaces to visualize coherent vortices. A large number of small atomized liquid droplets are trapped in these vortical structures resulting in clustering of droplets which reduce the evaporation rate of these droplets. On the other hand, the highly vaporizing droplets are located in zones where the acceleration in the gas is low. These droplets are withdrawn by entrainment eddies to the low-acceleration zones located in periphery of the spray which is also characterized by high gas temperatures. This is illustrated by the *Figure 3-29* and *Figure 3-30*. *Figure 3-29* shows the plots of droplets scaled by their vaporization intensity

mapped on the Eulerian flow acceleration and vorticity fields. Figure 3-30shows the plot of droplets scaled by their vaporization intensity mapped on the Eulerian flow temperature field. Both the plots are for a transverse cross section at 30mm downstream of the nozzle exit.

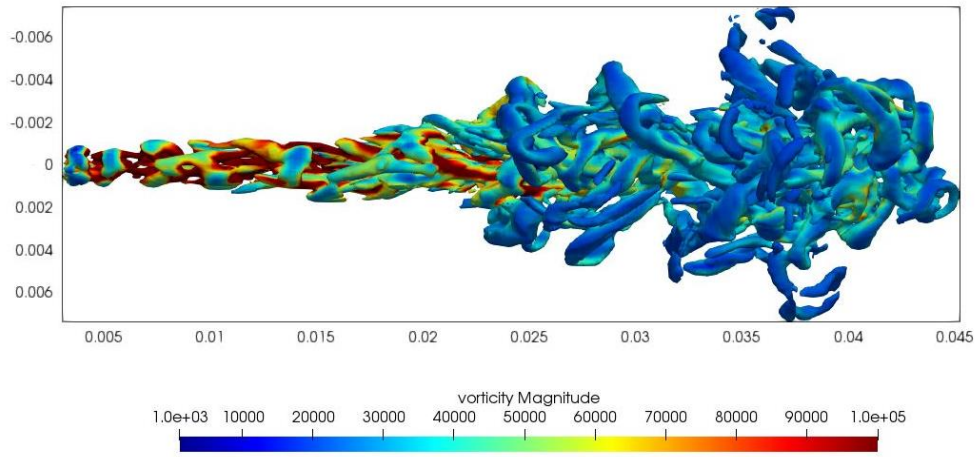

Figure 3-28 : Iso-surface of Q-factor with iso-value of Q= $1e^{8}\ s^{-2}$ coloured by intensity of vorticity.

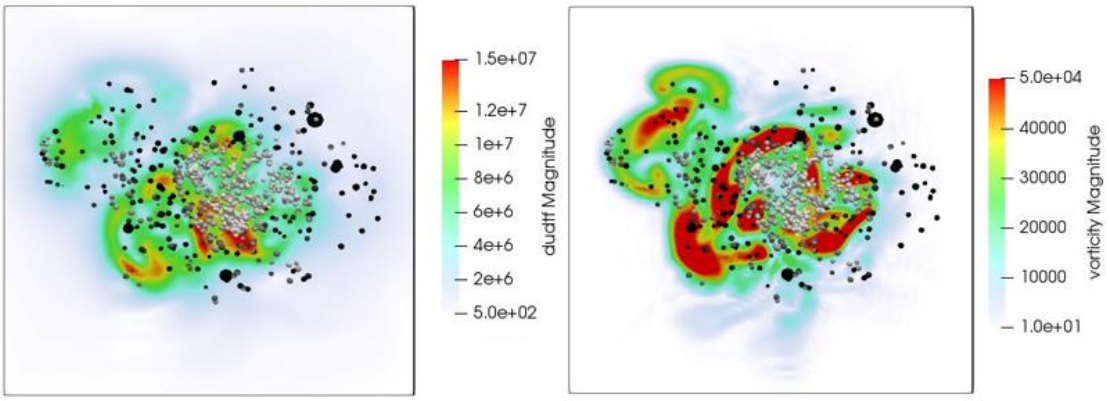

Figure 3-29 : Cross sectional view of spray structure at z= 30mm. Droplets coloured by intensity of vaporization. The Eulerian flow field shows the gas flow field variables (a) acceleration (left) (b) vorticity (right).

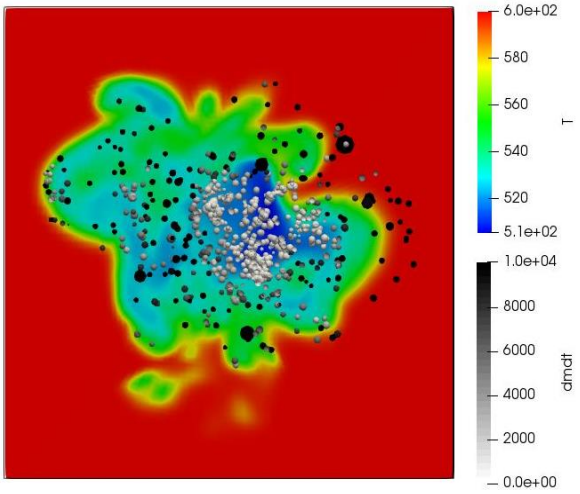

Figure 3-30 : Cross sectional view of spray structure at z= 30mm. Droplets by intensity of vaporization. The Eulerian flow field shows the gas flow temperature.

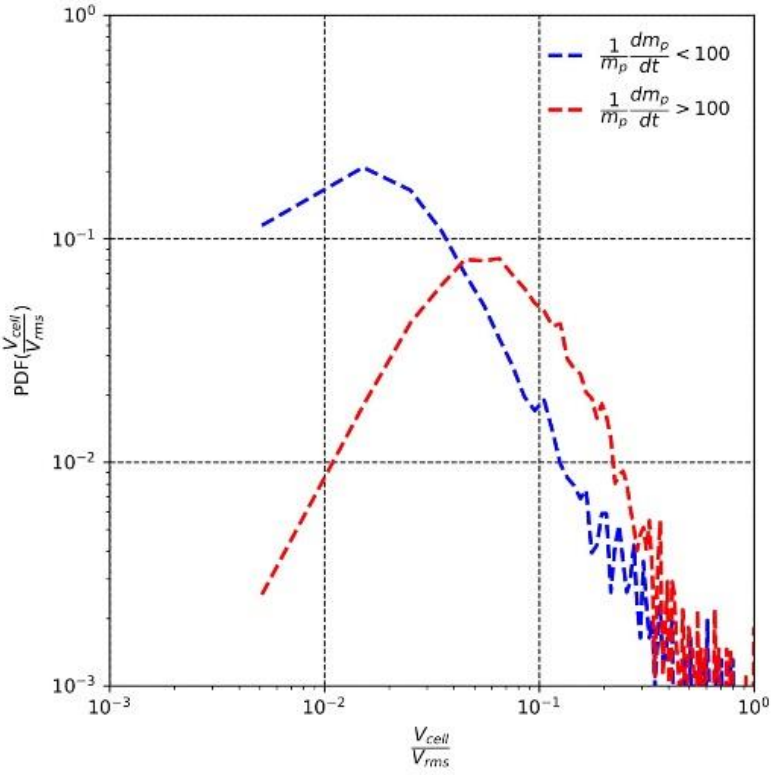

Figure 3-31 : PDF of normalized Voronoi cell volume conditioned on the intensity of droplet vaporization. A reference value of 100 is chosen for the vaporization intensity to get sufficient statistics for the two classes.

In order to statistically show the effect of droplet clustering in the spray core on the vaporization rate for all the droplets present in the computational domain we used the Voronoi tesselation conditional on droplet evaporation rate. Voronoi tesselation is used earlier for characterizing the clustering of particles by Monchaux et al (36) and Barge &

Gorokhovski (78,79). Smaller the volume of tesselated cells higher is the local concentration of particles. So we plot the PDF of voronoi cell volumes predicted for all the droplets in the spray domain conditional on their vaporization rate. This is shown in *Figure 3-31*. From the PDF it can be seen that droplets with higher vaporization intensity correspond to higher concentration of droplets i.e. higher probablilty of finding small voronoi cells. So it can be argued that clustering reduces the intensity of vaporization rate for the fuel sprays. Next we compare in *Figure 3-32* the joint-PDF statistics of droplet vaporization intensity with flow acceleration and vorticity fields "seen" by the droplet. The results show similar physics compared to co-axial combustor i.e. most of the droplets are concentrated in low-vorticity and low-acceleration regions and expereince low vaporization rates. On the other hand, very few droplets experience high vaporization rates in the low-acceleration and vorticity zones. The statistics can be explained by using the hypthesis used for co-axial combustor.

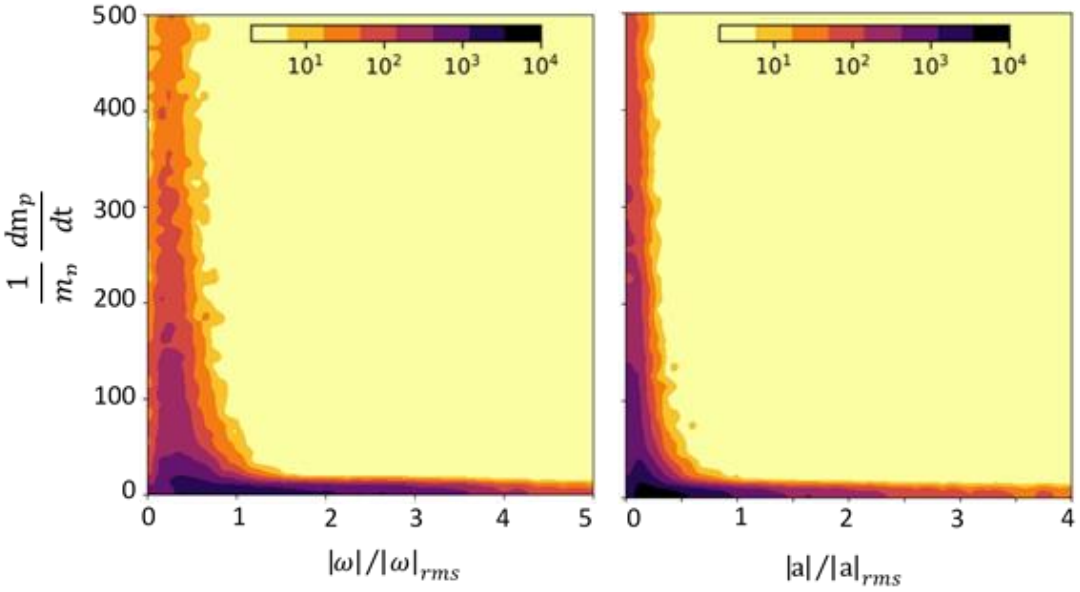

Figure 3-32 : Joint-PDF of droplet vaporization intensity and Eulerian gas flow field variables: vorticity (right) and acceleration (left). The statistics are obtained over all the droplets in the domain at t=1.5ms ASOI.

3.6 Conclusions

In this chapter we proposed new stochastic models for droplet dispersion and evaporation accounting for the intermittency effects on unresolved scales. The LES-STRIP approach is reformulated into a "*stochastic drag force"* for finite sized particles at high Reynolds numbers accounting for turbulent fluctuations in drag force induced by vortex shedding.

Also, a new stochastic vaporization model referred to as "*Stochastic Mixing controlled Evaporation (SMICE)"* is proposed. Instead of assuming that vaporization is either controlled completely by diffusion process or completely by turbulent mixing, the vaporization rate is modelled in terms of these two competing phenomena. In order to account for the intermittency effects of unresolved scales, the statistics of turbulent mixing time is expressed in terms of the instantaneous dissipation rate modelled using the log-normal process. The stochastic models are compared with standard dispersion (Wang & Squires (166)) and evaporation (d^2-law (55)) models used in the literature. In order to study the effects of spray dispersion and evaporation independent of the atomization process, the models are first assessed using the evaporating co-axial spray combustor experiments of Sommerfeld and Que (126). It was shown that the d^2-law evaporation model over-predicts the vaporization rate and all the droplets are evaporated within first 100mm, in contradiction to the experimental observations. On the other hand, the stochastic models have shown fairly good comparison of the droplet velocity and size statistics. Next, we assessed the performance of the dispersion models using the non-evaporating *Spray-A* experiments. As explained in Chapter-2, we used the KH-RT breakup model in conjunction with the dispersion models to evaluate their influence on spray breakup characteristics. It was shown that the standard dispersion model does not correctly account for the effects of momentum transfer in the near-nozzle spray region resulting in very high axial gas velocities, slower breakup rate and higher spray penetration lengths. Comparing the spray structure with the experimental spray images show that standard model gives unphysical spray with large number of droplets excessively dispersed radially. On the other hand, LES-STRIP model fairly good prediction of the spray penetration lengths and spray structure even on course-grids for both high and low injection pressures. The differences between the two models are explained in terms of the temporal correlations of droplet acceleration. The shorter correlation of droplet acceleration components represents large fluctuations in orientation of droplet acceleration due to intermittency effects of small scales. By correlating the acceleration orientation vector with the Kolmogorov time scale, LES-STRIP accounts for the intermittency effects of small scales resulting in larger radial dispersion of spray and slower penetration lengths. On the other hand, the higher spray penetration and unphysical spray structure with standard dispersion model is attributed to longer correlation of the droplet acceleration components. Also, it was shown that the LES-STRIP model gives similar spray breakup characteristics like the stochastic breakup

model. This corroborates with our hypothesis in Chapter-2 that by accounting for the unresolved scale turbulence on droplet motion, the KH-RT breakup model also produces similar spray breakup characteristics of stochastic breakup models. Next, we assessed the performance of the stochastic models using the evaporating ECN spray experiments. It was shown that the stochastic models while accurately predicting the global spray characteristics of liquid/vapor penetration lengths, also give a fairly good representation of the ensemble averaged statistics of the local vapor mass fraction and velocity fields. Also, the grid-sensitivity analysis for both non-evaporation and evaporating conditions have shown that the stochastic models are less sensitive to the grid-resolution. Therefore, it can be concluded that accounting for the intermittency effects of unresolved scales on dispersion and evaporation processes is essential for accurately modelling turbulent spray dynamics at engine relevant conditions. Having obtained satisfactory prediction of different flow statistics in comparison to the experiments of high-speed vaporizing sprays, we attempted to understand the physical parameters controlling the vaporization process in high Reynolds number flows. Even though the fuel injection and the gas flow flow-conditions are different for the direct injection fuel sprays and co-axial spray combustor configuration, it was shown that the intensity of evaporation is controlled by air-entrainment and the presence of clusters in both the cases. It was shown that while clustering of droplets reduces the intensity of vaporizations, the air-entrainment process withdraws the droplets into low-acceleration zones with high temperatures in the spray periphery resulting in faster evaporation. The effects of clustering are more explicitly seen in case of direct injection fuel sprays because of the high mass flow rates.

4 STOCHASTIC MODELS FOR INTERNAL AND NEAR NOZZLE SPRAY

4.1 LES modelling of nozzle internal flow

Assuming the flow inside the injector nozzle to be incompressible, the filtered Navier Stokes equations for the single-phase incompressible turbulent flow is given by Eq. 4-1 and 4-2.

$$\nabla . \bar{\mathbf{u}} = 0 \tag{4-1}$$

$$\frac{\partial \bar{\mathbf{u}}}{\partial t} + \bar{\mathbf{u}} \nabla . \bar{\mathbf{u}} = -\frac{1}{\rho} \nabla . \bar{\mathbf{p}} - \frac{1}{\rho} \nabla \boldsymbol{\tau} + (\nu + \nu_{sgs}) \nabla . (\nabla \bar{\mathbf{u}} + \nabla \bar{\mathbf{u}}^{\mathbf{T}}) \tag{4-2}$$

4.1.1 Near-wall treatment for LES subgrid scale turbulence models

Nicoud et al (186) argued that in the wall normal direction the turbulent viscosity should scale with $O(y^3)$ as $y \to 0$ and should vanish at the wall boundary. But the classical eddy-viscosity models do not provide this scaling and therefore do not vanish near the wall boundary. Therefore, they proposed an eddy viscosity model based on second invariant to the symmetric part of the local resolved velocity gradient tensor S_{ij}^d and the local resolved strain rate S_{ij} which provides the correct scaling for turbulent viscosity required in the near wall region. This model is widely used for modelled wall-bounded flows and is referred to as *Wale Adapting Local Eddy (WALE)* viscosity model.

$$\nu_{sgs} = C_s \Delta^2 \frac{\left(S_{ij}^d S_{ij}^d\right)^{1.5}}{\left(S_{ij} S_{ij}\right)^{2.5} + \left(S_{ij}^d S_{ij}^d\right)^{1.25}} \tag{4-3}$$

$$S_{ij}^d = \frac{1}{2}\left(\frac{\partial \overline{u_k}}{\partial x_i}\frac{\partial \overline{u_j}}{\partial x_k} + \frac{\partial \overline{u_k}}{\partial x_j}\frac{\partial \overline{u_i}}{\partial x_k}\right) - \frac{1}{3}\delta_{ij}\frac{\partial \overline{u_k}}{\partial x_l}\frac{\partial \overline{u_l}}{\partial x_k} \tag{4-4}$$

Another common approach for providing correct scaling for turbulent viscosity is based on Wang & Moin (187) idea to apply wall damping functions for the mixing length scale used in eddy viscosity model in the near-wall region as shown in Eq. 4-5. While in the

near-wall region the turbulent length scale is assumed to be proportional to the wall distance y, in the outer layer the mixing length scale is assumed to be proportional to filter width.

$$\boldsymbol{\nu_{sgs}} \;=\; \boldsymbol{min}\left(\boldsymbol{\kappa y}\left(\mathbf{1}-\boldsymbol{e}^{-y/\delta_v A^+}\right), \boldsymbol{C_s}\,\boldsymbol{\Delta}\right)|\bar{\boldsymbol{S}}|^2 \qquad \textbf{4-5}$$

Where y is the wall-normal distance, δ_v is the viscous length scale, κ and A^+ are the model constants assumed to take the values of 0.41 and 26 respectively. This model is hereafter referred to as the "*wall-damping"* model.

4.1.2 LES-SSAM model for wall-bounded flows

The momentum equation for the surrogate velocity field obtained by forcing the SGS acceleration on the filtered momentum equation (Eq. 4-2) is given by Eq. 4-6.

$$\frac{\partial \bar{\mathbf{u}}}{\partial \mathbf{t}} + \bar{\mathbf{u}}\nabla.\bar{\mathbf{u}} = -\frac{1}{\rho}\nabla.\bar{\mathbf{p}} - \frac{1}{\rho}\nabla\boldsymbol{\tau} + (\boldsymbol{\nu} + \boldsymbol{\nu_{sgs}})\nabla.(\nabla\bar{\mathbf{u}} + \nabla\bar{\mathbf{u}}^{\mathbf{T}}) + |\boldsymbol{a}|\vec{\mathbf{e}} \qquad \textbf{4-6}$$

Since the LES is under-resolved across the channel, the forcing of SGS acceleration is applied for the full domain and not just in the near-wall region. As explained in Section 1.7.2 the norm of the SGS acceleration is based Kolmogorov's scaling of acceleration in terms of resolved dissipation rate $\bar{\varepsilon}$ and viscosity ν as shown in Eq. 4-7.

$$|\boldsymbol{a}| \;=\; \left(\frac{\bar{\varepsilon}^3}{\upsilon}\right)^{\mathbf{0.25}} \qquad \textbf{4-7}$$

In this thesis, we analyzed two different formulations for viscosity υ. The first model uses the laminar flow viscosity, while the second formulation uses a turbulent viscosity. Turbulent viscosity is obtained using the mixing-length eddy viscosity model with wall damping as shown by Eq. 4-5. The first model is referred to *SSAM-v1* and the second formulation is referred to as *SSAM-v2*.

4.2 LES modelling of near nozzle spray atomization

4.2.1 Geometrical VOF - Iso-advection method

A summary of the iso-advection scheme as described by Roenby et al (122) is presented briefly in this section. The starting point of the *isoAdvector* method is the continuity equation for the density field $\rho(x,t)$ integrated over the volume of an interface cell:

$$\frac{\boldsymbol{d}}{\boldsymbol{dt}}\iiint \boldsymbol{\rho(x,t)dV} + \sum_f \iint \boldsymbol{\rho(x,t)u(x,t)}\,.\,\boldsymbol{dS} = \mathbf{0} \qquad \textbf{4-8}$$

Here *V* is the cell volume, *S* is the surface of one of the faces compromising the cell boundary and Σ_f is the sum over all the cell's faces. Let ρ_l and ρ_g be the liquid and gas phase densities. The indicator function *H(x,t)* is given by:

$$\boldsymbol{H(x,t) = \frac{\rho(x,t) - \rho_g}{\rho_l - \rho_g}} \quad \textbf{4-9}$$

The transport equation for the indicator function as shown in Eq. 4-10 can be obtained by isolating $\rho(x,t)$ in Eq. 4-9 and rearranging Eq. 4-8.

$$\boldsymbol{\frac{d}{dt}\iiint H(x,t)dV + \sum_f \iint H(x,t)u(x,t)\,.\,dS = -\frac{\rho_g}{\rho_l - \rho_g}\sum_f \iint u(x,t)\,.\,dS} \quad \textbf{4-10}$$

Assuming ρ_l and ρ_g to be constant then both fluids are incompressible, causing the righthand side in Eq. 4-10 to vanish. The indicator function, *H(x,t)* becomes a 3-dimensional Heaviside function taking the values 0 and 1 in the region of space occupied by the gas and liquid, respectively. With these definitions the volume fraction of a cell *P* is given by Eq. 4-11.

$$\boldsymbol{\alpha_P = \frac{1}{V_P}\iiint H(x,t)\;dV} \quad \textbf{4-11}$$

Re-writing Eq. 4-10 in terms of volume fraction $\boldsymbol{\alpha_P}$ gives the transport equation for the volume fraction field.

$$\boldsymbol{\frac{d\alpha_P}{dt} + \frac{1}{V_P}\sum_f \oiint H(x,t)u(x,t)\;.dS = 0} \quad \textbf{4-12}$$

This equation is exact for incompressible fluids. The key to accurate interface advection is to realise that the discontinuous nature of the problem demands geometric modelling involving considerations of the shape and orientation of the face, as well as of the local position, orientation and motion of the interface. Integrating Eq. 4-12 over time from time *t* to time $t+\Delta t$ gives the incremental change in the volume fraction of a cell.

$$\boldsymbol{\alpha_P(t+\Delta t) = \alpha_P(t) - \frac{1}{V_P}\sum_f \Delta V_f(t,\Delta t)} \quad \textbf{4-13}$$

Here $\Delta V_f(t,\Delta t)$ denotes the volume of liquid phase transported through the face *f* during the time step $[t, t+\Delta t]$ and is given by Eq. 4-14.

$$\boldsymbol{\Delta V_f(t,\Delta t) = \int_t^{t+\Delta t}\int_f H(x,\tau)u(x,\tau)\,.\,dSd\tau} \quad \textbf{4-14}$$

While for faces *f* completely immersed in the liquid during the entire time step, $\Delta V_f(t,\Delta t)$ will just be averaged flux over the face in a given time step i.e. $\Delta V_f(t,\Delta t) = \phi_f \Delta t$ and if

the face was in the gaseous medium throughout the time step, $\Delta V_f(t, \Delta t)$ would be zero. But in general, the faces can be fully or partially swept by the interface during a time step.

In contrast to the geometric advection methods based on calculation of flux polyhedral and their intersection with the grid cell, the *isoAdvector* method models the face-interface intersection line sweeping the face during a given time step. The first step in *iso-advection* is to realise that the rapid changes in ΔV_f during a time step is typically not due to an abruptly varying velocity field but due to the passage of the interface through the cell face. Hence, we will assume that the term (*u (x, t). dS*) in Eq. 4-14 can be written in terms of an averaged flux over the face and over the time step as shown in Eq. 4-15.

$$\boldsymbol{u(x,t).dS \approx \overline{u_f}.n_f dA = \overline{\phi_f} dA} \qquad \textbf{4-15}$$

Here $\overline{u_f}$ *and* $\overline{\phi_f}$ can be thought of as averages over both time step and face area. At the beginning of the algorithm, stepping forward from time *to*, we may use the available $\phi_f(t)$ as the estimate of the average flux over the time step, $\overline{\phi_f}$. However, over multiple iterations in a single time step, the averaged flux is obtained from $\phi_f(t + \Delta t)$. In any case, inserting Eq. 4-15 into Eq. 4-14 we can write:

$$\boldsymbol{\Delta V_f(t, \Delta t) \approx \overline{\phi_f} \int_t^{t+\Delta t} \alpha_f^+(\tau) d\tau} \qquad \textbf{4-16}$$

where we have defined the quantity,

$$\boldsymbol{\alpha_f^+(t) = \frac{1}{A_f} \int_f H(x,t) dA} \qquad \textbf{4-17}$$

which is the instantaneous "*Area-Of-Fluid*" of face *f*, i.e. the fraction of the face area submerged in the liquid. If the velocity field is constant in space and time and the face is planar, the approximation in Eq. 4-16 becomes exact. To progress, we now assume that the interface has been reconstructed within the interface cell from which face *f* receives fluid (upwind cell). The reconstructed interface is represented by an internal polygonal face, referred to as an *isoface*. The *isoface* cuts the cell into two disjoint sub–cells occupied by the liquid and gas, respectively, as illustrated in *Figure 4-1(a)*. The *isoface* will intersect some cell faces, cutting them into two subfaces immersed in heavy and light fluid, respectively, while others will be fully immersed in one of the two fluids. This is the state at time *t*. However, Eq. 4-16 requires α_f^+ for the whole interval [*t*, *t*+Δt]. To obtain an estimate of this, we first note that the isoface will have a well-defined face centre, x_S and a well-defined unit normal, n_S, the latter by convention pointing away from

the denser liquid phase. We may then interpolate the cell averaged velocity field, u_P to the isoface centre, x_S, to obtain the isoface velocity u_S. If the fluid interface is a plane with unit normal n_S starting at x_S at time *t* and moving with constant velocity u_S, then the interface will arrive at a given point x_v at time:

$$\mathbf{t_v = t + \frac{x_v - x_S}{u_S . n_S}} \qquad \textbf{4-18}$$

In particular, this holds true for all points on the general polygonal (N–sided) face *f*, including its vertices x_1, ..., x_N , and therefore defines the face-interface intersection line at any $\tau \in [t, t + \Delta t]$ as required in Eq. 4-16. We will now use this to explicitly calculate the time integral in Eq. 4-16. First note that a planar polygonal face may be triangulated in a number of ways, with the triangles lying exactly on the surface of the face. For a non-planar polygonal face, we must define its surface, which we do by estimating a face centre and using that as the apex for N triangles with the N face edges as base lines. The face surface is then defined by the union of these N triangles. In other words, any polygonal face may be represented as a union of triangles. Our analysis can therefore be confined to a triangular subface since the contribution from these can subsequently be accumulated to obtain the time integral in Eq. 4-16 for the whole face. Therefore, we consider a triangle with vertices $x_1, x_2, and\ x_3$. The interface arrival times can be calculated from Eq. 4-18 and we may assume without loss of generality that the points are ordered such that $t_1 \leq t_2 \leq t_3$. The interface enters the triangle at time t_1 at the point x_1, and then sweeps the triangle reaching $x_2\ at\ time\ t_2$, where it also intersects the edge $x_1 - x_3$ at a point we shall call x_4, as illustrated in Figure 4-1 (b). In what follows, we denote an edge between $x_i\ \ and\ x_j$ as $x_{ij} = x_i - x_j$. Then for $x_4\ we\ have$:

$$\boldsymbol{x_{41} = \frac{x_{21} . n_S}{x_{31} . n_S} x_{31}} \qquad \textbf{4-19}$$

Finally, at time t_3, the interface leaves the face through x_3. We note that in general the three times $t_1, t_2\ and\ t_3$and the two times *t* and $t + \Delta t$ can be distributed in various ways. For instance, if $t < t_1 < t_2 < t + \Delta t < t_3$, then the triangle is completely immersed in the gaseous medium from time t to time t_1 at which point the isoface will enter the triangle sweeping it and ending up on the triangle at time $t + \Delta t$. The correct ordering must be taken into account, when doing the time integration in Eq. 4-16. For any given time τ between t_1 and t_2, the immersed part of the triangle will have an area $A^+(\tau)$ given by Eq. 4-20.

$$\boldsymbol{A^{+}(\tau) = \frac{1}{2}|x_{41}(\tilde{t}) \times x_{21}(\tilde{t})|} \qquad \textbf{4-20}$$

where $\tilde{t} = \frac{\tau - t_1}{t_2 - t_1}$. From Eq. 4-20 and the total area of triangle $A = \frac{1}{2}|x_{31} \times x_{21}|$ the fraction of face area immersed in denser liquid phase is given by Eq. 4-21.

$$\boldsymbol{\alpha_f^{+}(\tau) = \frac{A^{+}}{A}\tilde{t}^2} \qquad \textbf{4-21}$$

Similarly, for time τ between t_2 and t_3 the immersed area $A^{+}(\tau)$ ***and*** α_f^{+} are given by Eq. 4-22 and 4-23.

$$\boldsymbol{A^{+}(\tau) = \frac{1}{2}|x_{43}(\tilde{t}) \times x_{23}(\tilde{t})|} \qquad \textbf{4-22}$$

$$\boldsymbol{\alpha_f^{+}(\tau) = \alpha_f^{+}(t_2) + \frac{A^{+}}{A}\tilde{t}^2} \qquad \textbf{4-23}$$

where $\tilde{t} = \frac{\tau - t_3}{t_3 - t_1}$. From Eq. 4-21and Eq. 4-23 it is evident that α_f^{+} for the sub-triangles of a polygonal face are quadratic polynomials in τ whose coefficients change at the intermediate time t_2. These coefficients are uniquely determined by the face vertex positions, t_1, t_2 and t_3, the isoface velocity, u_S, the unit normal, n_S, and the *isoface* centre at the beginning of the time step, x_S. *Figure 4-1 (c)* and *Figure 4-1 (d)* shows the time evolution of $\alpha_f^{+}(t)$ for a polygonal face as it is swept by a planar interface. If we name the polynomial coefficients for the first sub time interval of an polygons i^{th} triangle as $\boldsymbol{A_{i,1}}$, $\boldsymbol{B_{i,1}}$ and $\boldsymbol{C_{i,1}}$ and the coefficients for its second sub-interval as $\boldsymbol{A_{i,2}}$, $B_{i,2}$ and $\boldsymbol{C_{i,2}}$, then the time integral in Eq. 4-16 takes the form:

$$\boldsymbol{\int_t^{t+\Delta t} \alpha_f^{+}(\tau) d\tau \approx \sum_{i=1}^{N} \sum_{j=1}^{2} \frac{1}{3} A_{i,j} \left(t_{i,j+1}^3 - t_{i,j}^3\right) + \frac{1}{2} B_{i,j} \left(t_{i,j+1}^2 - t_{i,j}^2\right) + C_{i,j} \left(t_{i,j+1} - t_{i,j}\right)} \qquad \textbf{4-24}$$

Here $t_{i,1}$, $t_{i,2}$ and $t_{i,3}$ are the arrival times for the i^{th} triangle of a polygonal face calculated from Eq. 4-18. This concludes the description of the advection step. Next the reconstruction step is used to obtain the *isoface* at the beginning of a time step including its centre x_S and unit normal, n_S. As suggested by the name, this is done by representing the *isoface* as the intersection between the cell and a numerically calculated iso-surface of the volume fraction field, $\alpha_P(t)$. To calculate such iso-surface, the volume fraction field is first interpolated from the cell centres to the vertices of the cell. With a volume fraction value associated with each cell vertex, we can now for a given iso–value, α_0, determine for each cell edge, if α_0 lies between the two vertex values of that edge. If this

is the case, we mark a cut point on the edge by linear interpolation. Doing this for all the cell's edges and connecting the cut points across the cell faces, we obtain the isoface. Its centre and normal can be calculated by triangulation as for any other polygonal face. It is important to choose for each interface cell a distinct iso–value giving rise to an isoface cutting the cell into sub–cells of volumetric proportions in accordance with the volume fraction of the cell. The search algorithm for finding the iso-value to within a user specified tolerance has been optimized by exploiting the known functional form of a sub–cell volume as a function of the iso–value. The final element in the *isoAdvector* algorithm is a heuristic bounding step. It is introduced to correct volume fractions ending up outside the meaningful interval, [0, 1], if the isoAdvector algorithm is stressed beyond its formal region of validity by taking time steps so large that the underlying geometric assumptions break down.

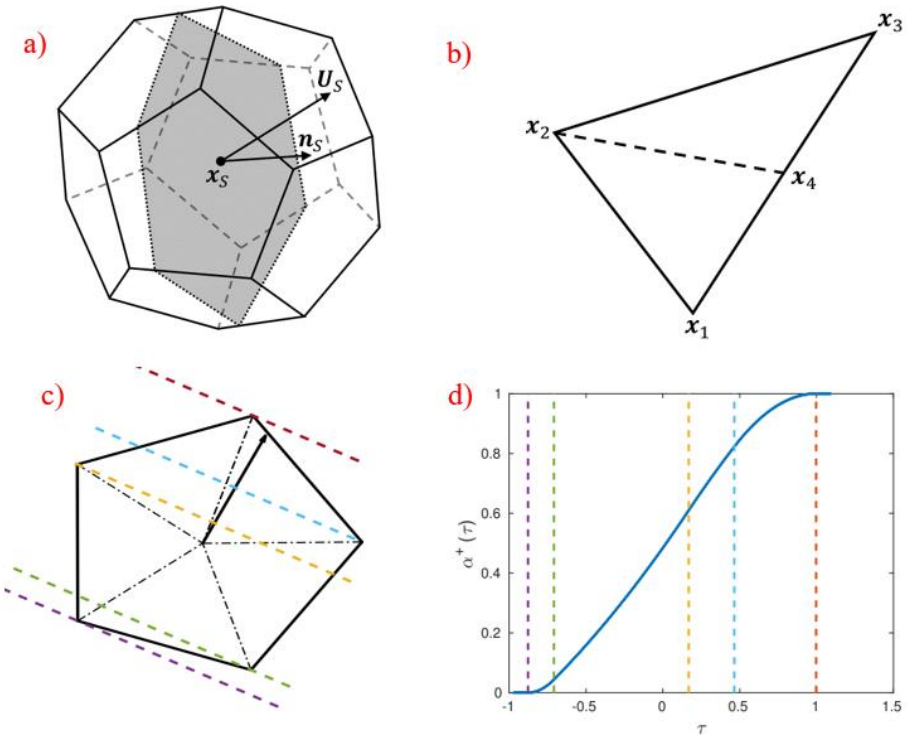

Figure 4-1 (a) Reconstructed isoface in a polyhedral interface cell (b) Triangular subface cut by planar isoface at face-interface intersection line (c) Face-interface intersection line sweeping a polygonal face and passing by its vertices (d) The evolution of the area–of–fluid as the face is swept showing quadratic dependency on τ with different coefficients on each subinterval

4.2.2 LES-SSAM formulation for VOF modelling

For the sake of brevity, the formulations of LES-SSAM method for two-phase flow as described in Section 1.7.2 is revisited here. The momentum equation for the surrogate velocity field obtained by forcing the SGS acceleration on filtered Navier Stokes Equation is given by Eq. 4-25.

$$\frac{\partial \overline{\rho \mathbf{u}}}{\partial t} + \overline{\mathbf{u}} \nabla . \overline{\rho \mathbf{u}} = -\nabla . \overline{\mathbf{p}} - \nabla(\overline{\boldsymbol{\tau}} + \boldsymbol{\tau}_{sgs}) + \overline{\mathbf{T}_{\sigma}} + \overline{\rho} . \mathbf{a}^{*} \vec{\mathbf{e}} \qquad \textbf{4-25}$$

Following the decomposition of the SGS acceleration into two stochastic variables one for the norm and another for the orientation vector, the acceleration norm is modelled by the log-normal process given by Eq. 4-26.

$$d\mathbf{a}^{*} = -\mathbf{a}^{*} \left(\ln\left(\frac{\mathbf{a}^{*}}{\mathbf{a}_{\eta}}\right) - \frac{3}{16}\boldsymbol{\sigma}^{2} \right) \frac{dt}{T} + \frac{3}{4}\mathbf{a}^{*} \sqrt{\frac{2\sigma^{2}}{T}}\, d\mathbf{W}(t) \qquad \textbf{4-26}$$

where $dW(t)$, is the increment of a standard Brownian process,$\langle dW \rangle$=0, $\langle dW^2 \rangle$=dt. The dispersion term σ^2 is dependent on the local Reynolds number $\mathrm{Re}_{\Delta} = \frac{\nu_t}{\nu}$, through the Kolmogorov length scale η. The relaxation time T is correlated to the integral flow time scale.

$$\boldsymbol{\sigma}^{2} = \ln \frac{\Delta}{\eta} \quad \textbf{and} \quad \mathbf{T}^{-1} = \frac{\nu_t}{\Delta^{2}} \qquad \textbf{4-27}$$

The orientation vector in this study is modelled using the Ornstein-Ulhenbeck process of Sabelnikov, Barge & Gorokhovski (71) without the relaxation towards local vorticity field. The solution of the momentum equation is obtained via a PISO iteration procedure. A predictor velocity is first constructed and then corrected to ensure momentum balance and mass continuity. Explicit formulation of the predictor velocity is a twostep process, where first the viscous, advective and temporal terms in the momentum equation are used to generate a cell centered vector field, which is then projected to cell faces using a second order scheme. Contributions from surface tension and gravity terms are then added, concluding the predictor formulation. This procedure enforces a consistent discretization of surface tension and pressure gradient terms and therefore ensures numerical stability of the solver (187). A similar approach is followed when adding the contribution of the SGS acceleration term to the momentum equation. The SGS acceleration is calculated at the cell-centres and then added to the predictor formulation along with the surface tension forces and pressure gradient term.

4.3 Results & discussion

Given the small dimensions and high Reynolds numbers in fuel injectors determining the turbulence velocity statistics either using the DNS or experiments is not possible for the real-nozzles. Ignoring the needle transients, at high-lift steady state conditions the in-nozzle flow can be assumed to be driven by a uniform pressure gradient and the flow Reynolds numbers are usually in the range of 10^4-10^5. Since the fully developed channel flow problem is also driven by a uniform pressure gradient, the DNS data for channel flow with flow Reynolds numbers in the range of injector nozzle flow Reynolds numbers are used to validate the performance of LES-SSAM approach in comparison with standard wall-turbulence models. The details of the computational setup and the results for channel flow LES calculations are provided in Section 4.3.1. In section 4.3.2 the description of ECN Spray-A injector nozzle geometry and experiments results concerning primary atomization and corresponding validation of the numerical models is presented.

4.3.1 Turbulent Channel flow

A schematic of a typical channel flow configuration driven by a constant pressure gradient between two parallel planes is shown in *Figure 4-2*. In a cartesian co-ordinate system the streamwise flow is assumed to be aligned with *x*-axis, while the wall normal and the transverse flow directions are aligned with *y*- and *z*- axis respectively. Since the walls are of infinite size, the geometry of channel flow is fully characterized by the half channel width, *h*. However, the computational domain is assumed to be bounded with periodic flow boundary conditions applied in both the streamwise and spanwise directions. This artificial truncation introduces two more geometrical parameters, the streamwise truncation length, l_x, and the spanwise truncation length, l_z. The values of l_x and l_z should be large enough to fit the largest existing turbulent structures inside the domain. And no-slip conditions are used at the top and bottom walls. Apart from the flow viscosity ν,other important parameter commonly used to characterize the channel flow is the bulk flow velocity U_b given by Eq 4-28.

$$\boldsymbol{U_b = \frac{1}{h}\int_0^h \bar{u}\, dy} \qquad \textbf{4-28}$$

The bulk flow velocity is used in the simulations instead of defining the pressure gradient, because it becomes easy to characterize the flow behavior in terms of flow Reynolds number $Re_b = \frac{U_b h}{\upsilon}$. On the other hand, the near-wall turbulent length and velocity scales are characterized in terms of viscosity and wall shear stress τ_w. The total shear stress is

the sum of viscous stress and the Reynolds stress. When a no-slip boundary condition is used at the wall, the Reynolds stresses are zero. Therefore, the wall shear stress is entirely due to the viscous contribution i.e.

$$\boldsymbol{\tau_w} = \boldsymbol{\nu}\frac{d\bar{u}}{dy}\Big|_{y=0} \qquad \textbf{4-29}$$

Then the wall friction velocity u_τ and the viscous length scale δ_v are defined as,

$$\boldsymbol{u_\tau} = \sqrt{\frac{\tau_w}{\rho}} \textbf{ and } \boldsymbol{\delta_v} = \frac{\nu}{u_\tau} \qquad \textbf{4-30}$$

Here $\boldsymbol{\rho}$ is the fluid density. And finally, the wall friction Reynolds number defined by,

$$\boldsymbol{Re_\tau} = \frac{u_\tau h}{\nu} \qquad \textbf{4-31}$$

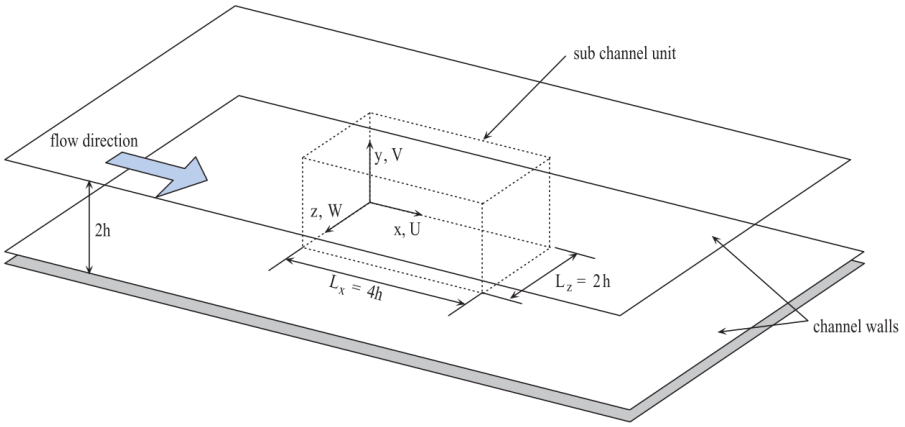

Figure 4-2: Schematic representation of the channel flow problem and periodic computational domain (adapted from 63).

In this study three different DNS cases with varying Re_τ values of 395, 1000 and 5200 are used. Hereafter, they are referred to as *Re395*, *Re1000* and *Re5200* respectively. In all the cases the dimensions of the computational domain used is $8\pi h \times 2h \times 3\pi h$, where the channel half width h is assumed to be 1m. The flow is driven by a uniform pressure gradient varying in time, which ensures constant mass flux through the domain. The channel flow parameters and the computational details used in these DNS studies is listed in *Table 4-1*. In *Table 4-1*, the grid spacing is expressed in terms of wall scale units l^+, which is obtained by non-dimensionalising the length scale *l* by the viscous length scale i.e. $l^+ = \mathrm{l}/\delta_v$. While the bulk flow velocity is equal to 0.1335m/s for *Re395* test case, it is set to a value of 1m/s for other two test cases.

Parameter	$\boldsymbol{Re_b}$	$\boldsymbol{\nu}$	$\boldsymbol{\delta_v}$	$\boldsymbol{\Delta x^+ \times \Delta y^+ \times \Delta z^+}$	$\boldsymbol{N_x \times N_y \times N_z}$
Units	[-]	[m²/s]	[m]	[-]	[-]
Re395(188)	$1.33e^{04}$	$2.0e^{-05}$	$2.5e^{-03}$	$12 \times (0.02 - 6) \times 6$	256 ×192 ×192
Re1000 (189)	$2.25e^{04}$	$5.0e^{-05}$	$1.0e^{-03}$	$12 \times (0.02 - 6) \times 6$	2048 ×512 ×1536
Re5200 (190)	$1.25e^{05}$	$8.0e^{-06}$	$2.0\ e^{-04}$	$12\times (0.5 - 10) \times 6.4$	10240 ×1536×7380

Table 4-1: Channel flow DNS data parameters

As explained earlier, in-order to correctly resolve the near-wall statistics the streamwise and spanwise lengths should be large enough to resolve the largest turbulent structures. The DNS results have shown that the length scales of the streaks in near-wall regions are typically of the order of $100-1000y^+$, where *y* is the wall normal distance. So, in-order to minimize the computational costs, following Fureby's (51) minimal channel approach a much smaller computational domain than DNS but sufficiently large enough to resolve multiple streak lengths is used. In the LES simulations the bulk flow velocity is imposed and the pressure gradient is computed. In order to maintain a uniform pressure gradient an additional external body force term is introduced into the momentum equation. This artificial force drives the flow, and the magnitude of the force is determined by the prescribed bulk velocity. At each time step, the actual $\boldsymbol{U_b}$ is re-calculated, and an adjustment to the magnitude of the external force is made, to correct the value. It was shown (51) that for a good resolution of turbulent statistics the grid spacing in wall units should be of the following order $\boldsymbol{\Delta x^+ \sim 40}$, $\boldsymbol{\Delta z^+ \sim 20}$ and $\boldsymbol{\Delta y^+ \sim 2\ to\ 20.}$ For *Re395* and *Re1000* case, the aforementioned optimal grid scaling is used. On the other hand, given very small viscous length scales for *Re5200* case, the optimal grid spacing would be computationally very expensive even on smaller computational domains. Therefore, for Re5200 case, the comparison between SGS models is made on relatively coarse meshes. Specific details concerning the computational domain size and grid spacing for each of the test cases are provided in *Table 4-2*. A second order backward differencing scheme is used for the time integration in conjunction with second order schemes for spatial discretization.

Parameter	$L_x \times L_y \times L_z$	$\Delta x^+ \times \Delta y^+ \times \Delta z^+$	$N_x \times N_y \times N_z$
Units	[m]	[-]	[-]
Re395 (188)	4h×2h×2h	$40 \times (2-20) \times 20$	40×50 ×40
Re1000 (189)	4h×2h×2h	$40 \times (2-20) \times 20$	100×128 ×100
Re5200 (190)	2h×2h×2h	$100\times (2-100) \times 50$	100 ×200×200

Table 4-2 Channel flow LES computational domain size and grid resolution

4.3.1.1 Low-Reynolds number flow – model comparison

First a general comparison of the two formulations of LES-SSAM approach with WALE and Wall-damping models for the low-Reynolds number flow conditions corresponding to the Re395 test case. *Figure 4-6 (a)* shows the log-plot of mean streamwise velocity component normalized by the wall friction velocity ($U^+ = U/u_\tau$) along the wall-normal direction for different wall-turbulence models in comparison with the DNS. On the other hand, *Figure 4-3 (b)* shows the root mean square (RMS) profiles for streamwise velocity components variation along the wall-normal direction for different wall-turbulence models.

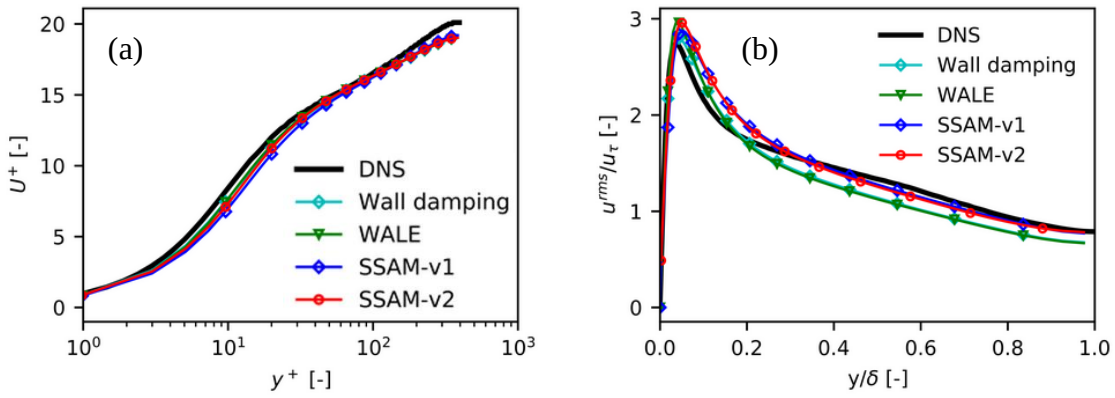

Figure 4-3 Comparison of different wall turbulence models for Re395 case: (a) Log-plot showing variation of the mean value of streamwise velocity component along the wall-normal direction (b) RMS of streamwise velocity component variation along the wall-normal direction

It can be seen from the results that all the models predict similar profiles for statistics of streamwise velocity component. And following Bose et al's (92) assertion all the models over-predict the streamwise velocity fluctuations in the near-wall region. But the LES-

SSAM formulations provide a better prediction of the streamwise velocity fluctuation in the outer-layer compared to standard models i.e. WALE and Wall-Damping. Next a comparison of the streamwise and spanwise velocity fluctuations for different wall turbulent models is shown in *Figure 4-4*. From the results, it can be noticed the LES-SSAM approach gives a better prediction of both wall-normal and spanwise velocity fluctuations in comparison to the standard models. Even though both LES-SSAM formulations provide similar spanwise velocity fluctuations, the *SSAM-v2* model where the SGS acceleration is modelled with turbulent viscosity is producing higher fluctuation in the wall-normal velocity component compared to the *SSAM-v1*. So, for further comparison of the wall turbulence statistics we used *SSAM-v2* and is referred to as *LES-SSAM*.

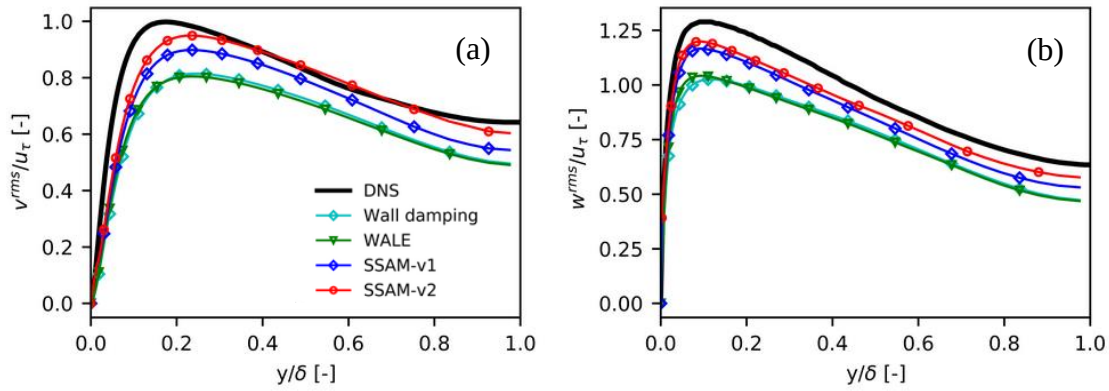

Figure 4-4 Comparison of different wall turbulence models for Re395 case: (a) RMS of wall-normal velocity component variation along the wall-normal direction (b) RMS of spanwise velocity component variation along the wall-normal direction

4.3.1.2 High-Reynolds number flow – model validation

The typical flow Reynolds number for the injector nozzle flow is of the order $0.5 - 1.0e^5$, whereas the bulk flow Reynolds number for the *Re395* case is around $1.0e^4$. So, in-order to characterize the performance of LES-SSAM approach at flow Reynolds numbers reflective of diesel fuel injection, we performed channel flow simulations for two high-Reynolds number flows. For further comparisons, we use only *SSAM-v2* (referred to as LES-SSAM) and the WALE model. In case of wall-bounded flows the source of turbulence is the recurring streak ejection and breakup process. This near-wall turbulence cycle is naturally initiated by the growth of small initial perturbations or imperfections on the wall boundary. Since the numerical calculations do not have such initial perturbations, it takes long time for the turbulence initialization in case of WALE model. While at low-

Reynolds numbers, given the large time steps and a smaller number of grid-points the turbulence initialization is not a big problem. But at high Reynolds numbers, with large number of grid points and very small-time steps turbulence initialization can pose a serious problem from view point of computational costs. Several methods (63,191-193) have been developed in recent times to artificially impose the velocity fluctuations at the inlet to initialize the turbulence at a much faster rate. In contrast to artificially imposing the velocity fluctuations at the inlet, LES-SSAM forces the acceleration at unresolved scales which characterize the turbulence generation process in the near-wall region. Therefore, the LES-SSAM method implicitly generates turbulence in the flow in a more physically consistent manner and at a much faster rate. To illustrate this, Figure 4-5 shows the temporal evolution of the wall friction velocity over time for the two models for Re1000 case. The friction velocity is normalized by the DNS friction velocity value and the time is normalized by the flow-through time (t_f). As shown in *Figure 4-5* for the wall-turbulence to develop the WALE model requires approximately 200 flow through times while the transition to turbulent flow for LES-SSAM requires 4-5 flow times only.

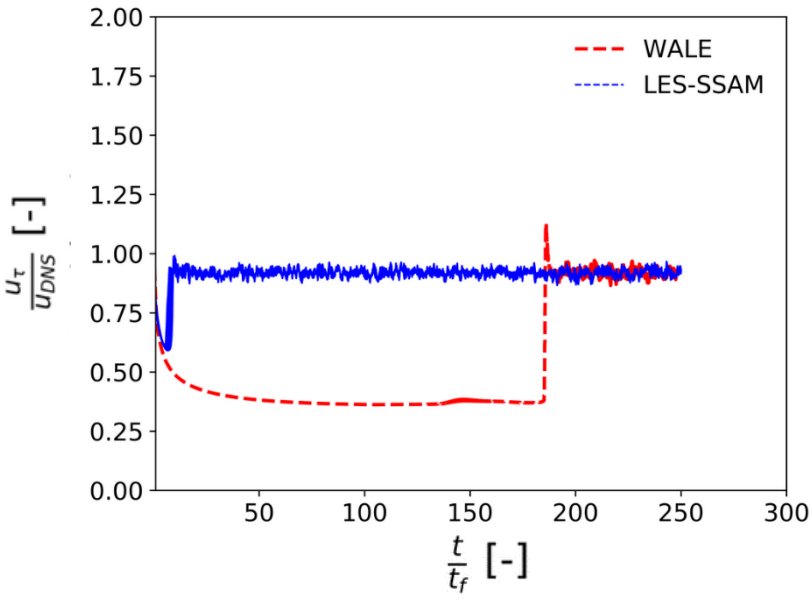

Figure 4-5 Time evolution of the wall friction velocity for Re1000 case

Figure 4-6 shows the log-plot of mean streamwise velocity component normalized by the wall friction velocity ($U^+ = U/u_\tau$) along the wall-normal direction for the two test cases. It can be seen that for *Re1000* case, the velocity profiles match very well with the DNS both in the near-wall region and in the outer layer. On the other hand, for *Re5200* case compared to the DNS, the velocities are under-predicted in the near-wall region for both the cases. And the velocity profiles of LES-SSAM method shows more-deviation

from DNS compared to WALE model for *Re5200*. *Figure 4-7* shows the root mean square (RMS) value of the streamwise velocity profiles along the wall-normal direction. Both the models tend to over-predict the peak intensity of the fluctuations in the near-wall region. With increasing Reynolds number, the WALE model largely under-predicts the velocity fluctuations in log-law and outer layer regions as seen for Re5200 case.

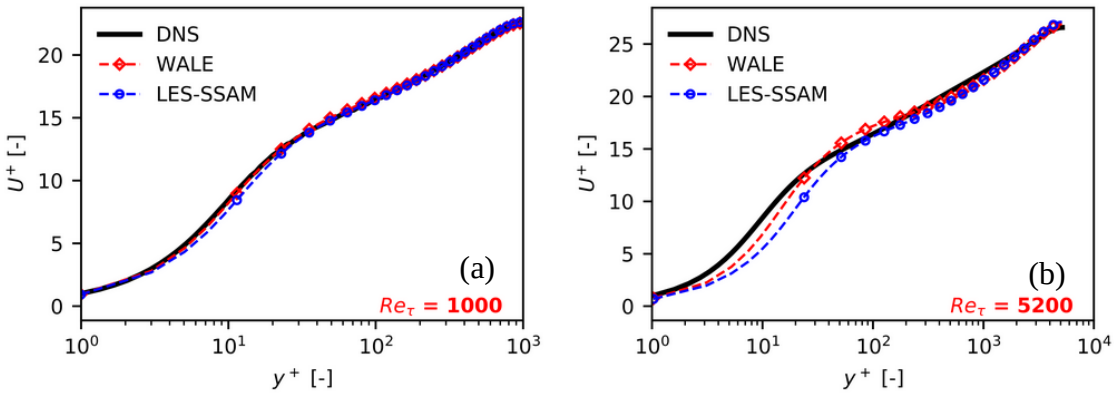

Figure 4-6 Log-plot of mean velocity profiles along the wall-normal direction for (a) Re1000 (left) and (b) Re5200 (right).

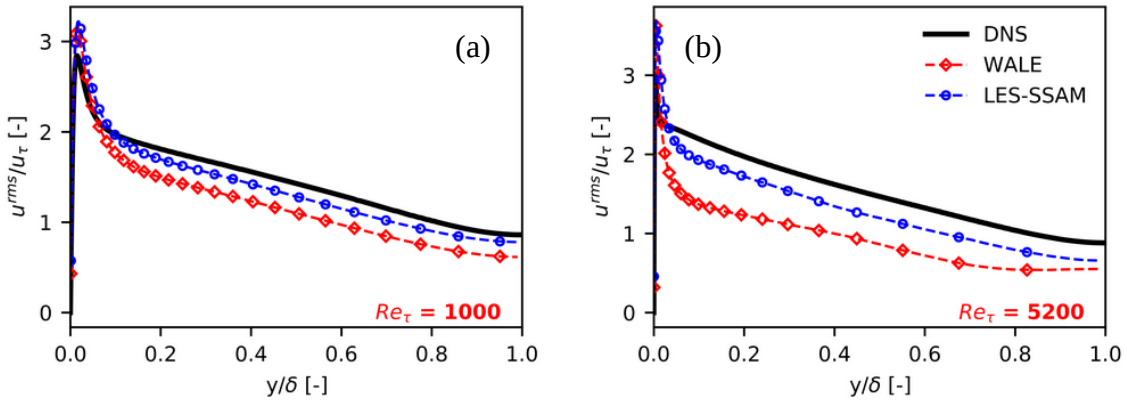

Figure 4-7 RMS of streamwise velocity components along the wall-normal direction for Re1000 (left) and Re5200 (right).

Next a comparison of the wall-normal and cross-stream velocity fluctuations i.e. v^{rms} and w^{rms} in both *Figure 4-8* and *Figure 4-9*. In general WALE turbulence model underpredicts the peak intensity of fluctuations. With increasing flow Reynolds number, the intensity of peak is largely underpredicted by WALE model. On the other hand, the LES-SSAM model predicts more accurately both the peak intensity of the velocity fluctuations and also the overall profile.

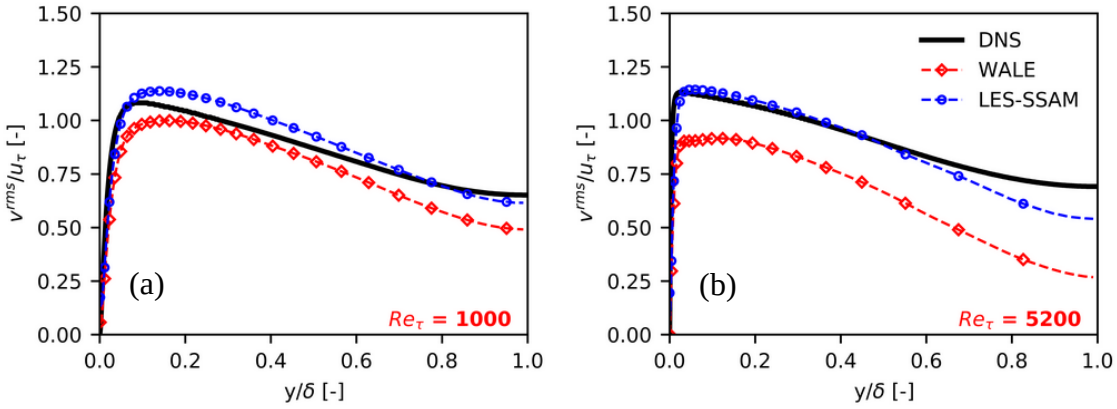

Figure 4-8 RMS of wall-normal velocity components along the wall-normal direction for Re1000 (left) and Re5200 (right).

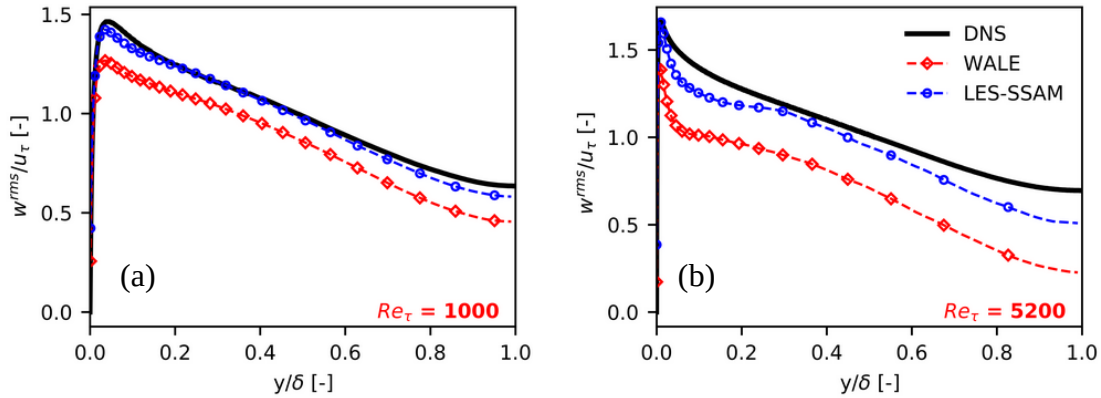

Figure 4-9 RMS of cross-stream velocity components along the wall-normal direction for Re1000 (left) and Re5200 (right).

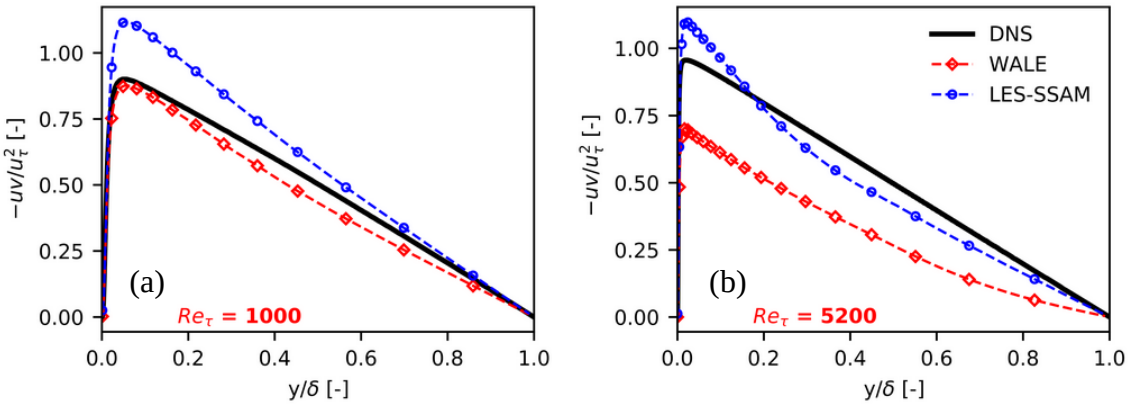

Figure 4-10 Wall-shear stress components along the wall-normal direction for Re1000 (left) and Re5200 (right).

Figure 4-10 shows the total shear stress profiles for both the cases. For *Re1000* case, since the grid spacing in both stream-wise direction and wall-normal directions are optimized,

the WALE model correctly predicts the total shear stress profile. But for *Re5200*, because of the coarse grid the WALE model underpredicts the shear stresses. On the other hand, we notice that LES-SSAM over-predicts the near-wall shear stress for both the cases. Finally, a schematic of the vorticity and the instantaneous streamwise velocity profile predicted by LES-SSAM for Re5200 case are shown in *Figure 4-11*.

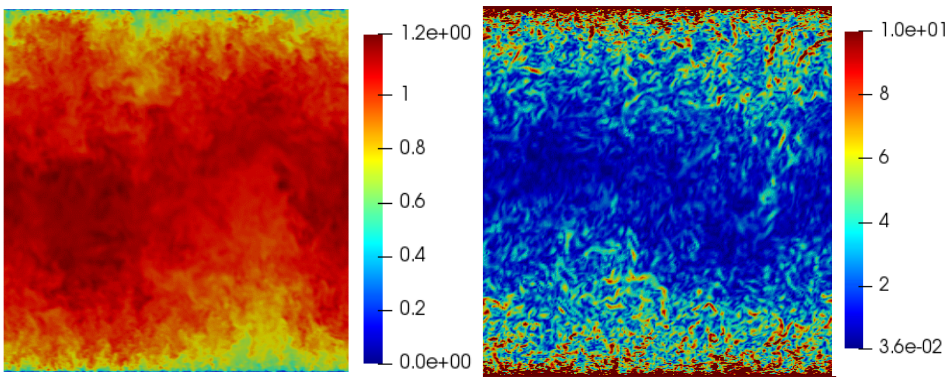

Figure 4-11 Instantaneous velocity (left) and vorticity (right) field predicted by LES-SSAM for Re5200 on a coarse grid.

4.3.2 Preliminary simulation of ECN Spray-A injector nozzle flow and near-nozzle spray atomization

The *Spray-A* injector has a convergent hydro-ground nozzle with a taper ratio of 1.5 and a nozzle diameter of 90 µm. Kastengren et al (45) made detailed measurements of the nozzle geometry for four different *Spray-A* injectors using different experimental technqiues like X-ray tomography, X-ray phase-contrast imaging, silicone molding, and optical microscopy. It was pointed out that due to the manufacturing challenges associated with the small dimensions of the nozzles, the actual nozzle profiles deviate from the nominal specifications. From multiple X-ray tomography measurements, the authors have reconstructred a representative nozzle geometry to be used for numerical modelling. While processing the X-ray images, the surface irregularities are removed generating a much smoother finish to the nozzle geometry. A schematic of the final processed nozzle geometry reconstructed from images is shown in *Figure 4-12*. The nozzle centerline is offset from the sac region centerline. In addition, the two inlet turning angles $\boldsymbol{\theta_1}, \boldsymbol{\theta_2}$ are different. More specific details of ECN Spray-A nozzle geometry and the operating conditions are provided in *Table 4-3*. Using liquid density, injection and ambient pressures and the nozzle outlet diameter, the bulk flow velocity at the nozzle exit can be estimated to be around 605m/s using Bernoulli's formula. From the nozzle exit velocity and the nozzle outlet diameter the flow Reynolds number is expected to be

around $\mathbf{6.0e4}$. This is in the same range of bulk flow Reynolds numbers studied in channel flow in the previous section.

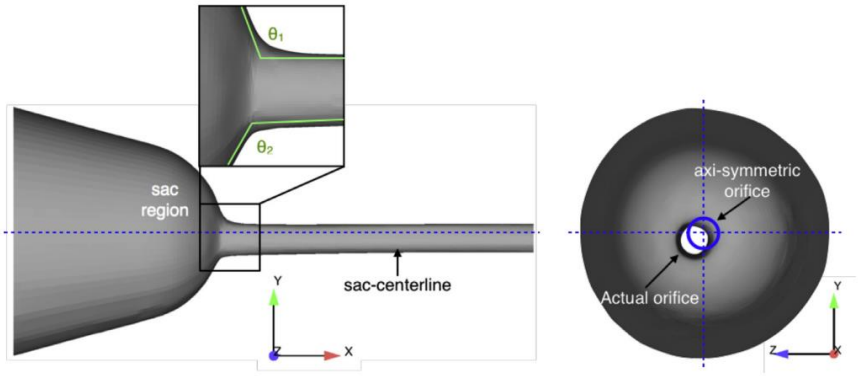

Figure 4-12 ECN Spray-A injector geometry highlighting the flow asymmetry

Outlet diameter	µm	89.4
Inlet diameter	µm	116
Nozzle length	µm	1030
Velocity coefficient C_v	-	0.96
Fuel injection pressure	MPa	150
Ambient pressure	MPa	2
Kinematic Viscosity	m^2/s	1e-06
Fuel density	kg/m^3	750
Surface tension	N/m	0.021

Table 4-3 Nozzle geometry parameters and operating conditions for LES

An unstructured tetrahedral mesh with a total of 4 million cells is generated for the nozzle geometry. In the nozzle the average cell size is around 2 µm in both axial and radial directions. Additionally, prism layers are used to resolve the boundary layer such that the first near wall cell has $y^+ < 5$. The schematic of the computational grid used for the injector nozzle is shown in *Figure 4-13*. At the nozzle inlet and outlet fixed pressure boundary condition is applied. A no-slip boundary condition is applied at the injector walls. Similar to the channel flow simulations a second order backward differencing scheme is used for the time integration with second order schemes for spatial discretization. From the bulk flow velocity at the nozzle exit the flow-through time is estimated to be around 2µs. For turbulence to develop the flow is initially simulated for

10 flow through times and then the velocity statistics at the nozzle exit are sampled once in every 10ns (nano-seconds) for over a period of 50μs. The sampled velocity profiles are imposed as inlet velocity boundary condition for the VOF simulations of primary atomization. The steady-state instantaneous velocity and vorticity fields predicted by LES-SSAM model are shown in *Figure 4-14* and *4-15*.

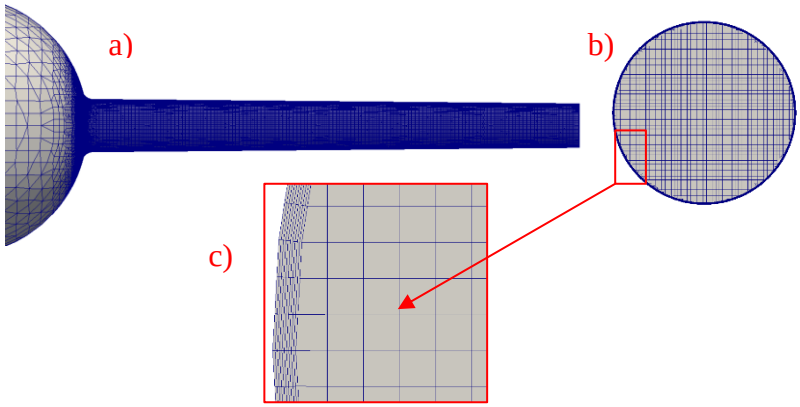

Figure 4-13 (a) Injector nozzle mesh -sideview (b) Grid resolution of the nozzle exit (c) Zoomed in view of the prism layers used to model the near-wall boundary region

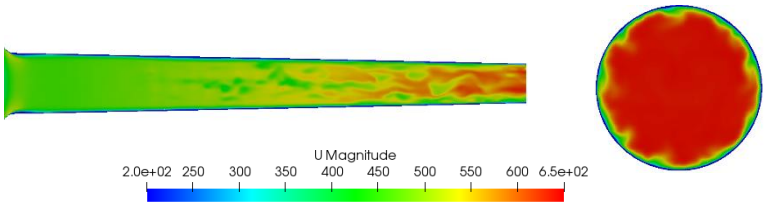

Figure 4-14 Cross-sectional view of the instantaneous velocity field along the nozzle length and at the nozzle exit.

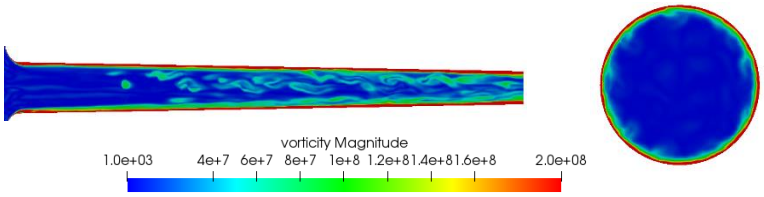

Figure 4-15 Cross-sectional view of the instantaneous vorticity field along the nozzle length and at the nozzle exit.

For simulating the near-nozzle spray atomization process a cylindrical domain of radius 1.6mm and a length of 16 mm is used. A non-uniformly discretized mesh with cell sizes varying from 2μm to 32μm are used as shown in *Figure 4-16*.

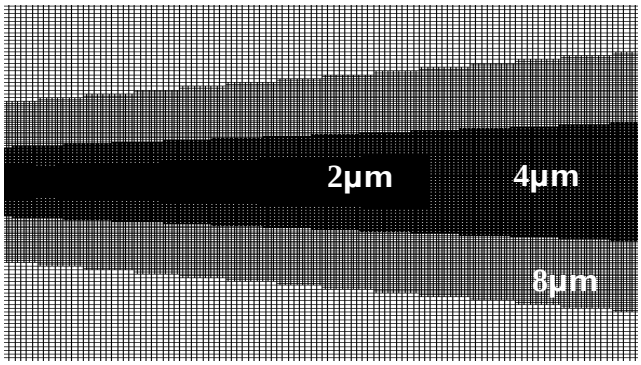

Figure 4-16 Mesh resolution of spray domain for simulating primary atomization.

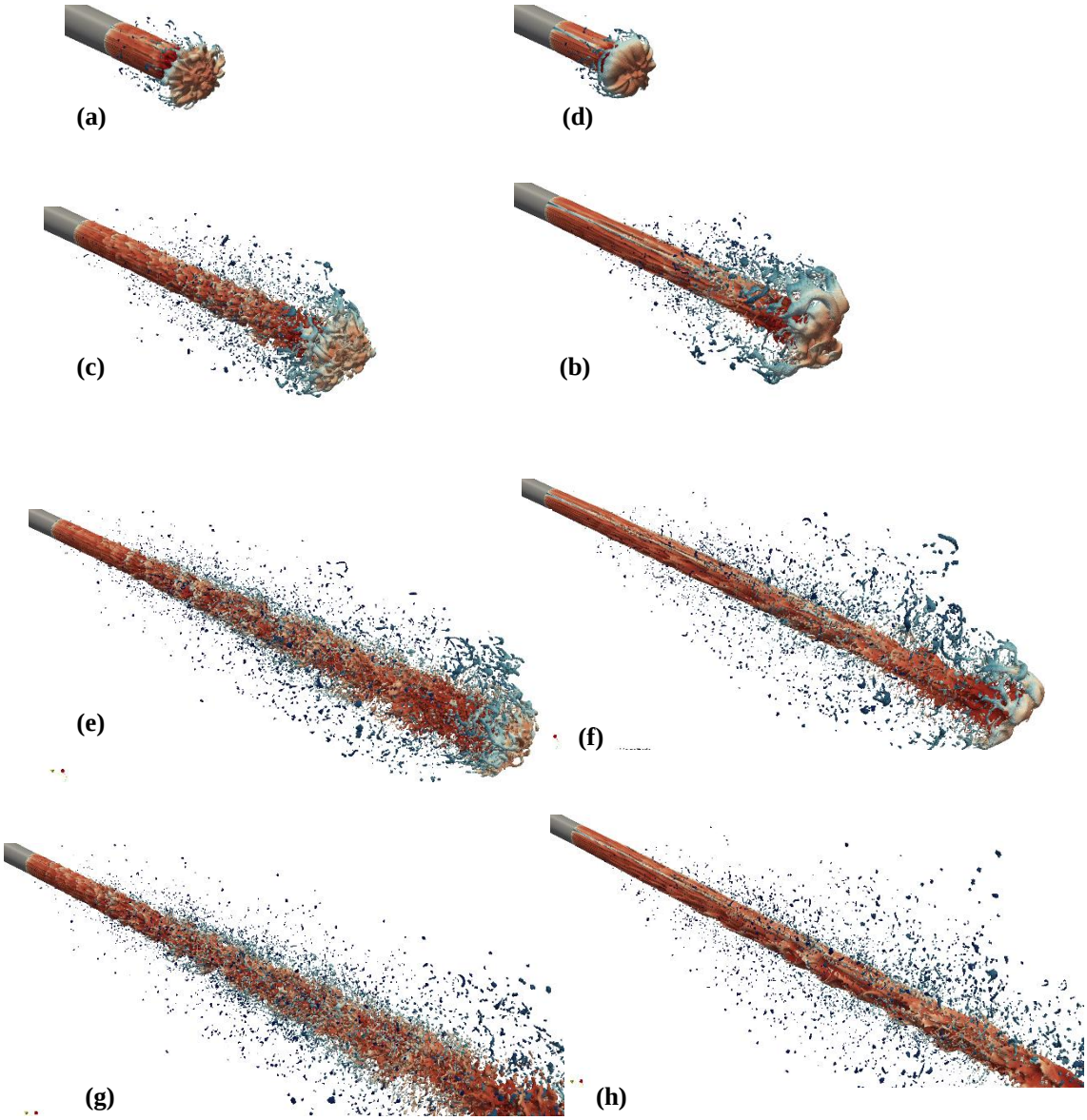

Figure 4-17 Instantaneous near-nozzle spray jet structure for different time instances of t = 1µs, 2 µs, 4µs and 8µs. The images from LES-SSAM are shown on left by (a), (c), (e) and (g). The images from Standard VOF are shown on right by (b), (d), (f) and (g).

A first order *Euler* time integration scheme is used along with second order *vanLeer* scheme for spatial discretization of the flux terms. Two computations are performed one with *standard LES* and the other with *LES-SSAM* using isoAdvector VOF method for a duration of 50 µs. The time evolution of the spray jet predicted by the two models is shown in *Figure 4-17*. Here it can be clearly seen that with the LES-SSAM approach surface instabilities/wrinkling on jet surface start much closer to the nozzle exit and subsequently faster shearing of smaller ligament structures from the jet surface. A quantitative comparison with the time averaged Projected mass density (PMD) and Transverse integrated mass profiles obtained from experimental studies of Kastengren et al (194) and Xue et al (195). In the computations the time averaging of the volume fraction fields α_l is performed over a period of 25 µs. The Projected mass density (PMD) profiles shown in *Figure 4-18* is defined as the line integral of the mean liquid mass representing the projection of the 3D liquid mass distribution on a 2D plane. PMD computed along z axes is given by

$$\boldsymbol{\phi_z(x,y) = \rho_l \int_{-\infty}^{\infty} \langle \alpha_l \rangle \; dz} \qquad \textbf{4-32}$$

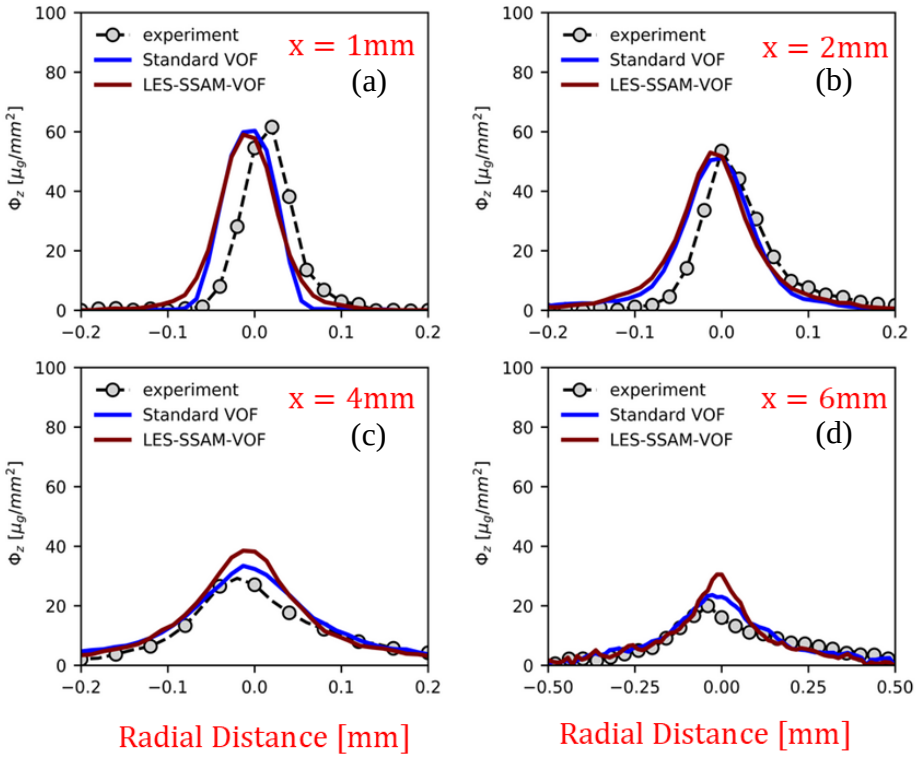

Figure 4-18 Projected Mass density profiles along a radial cross-section at axial positions of (a) x=1mm (b) x=2mm (c)x=4mm and (d) x=6mm.

Similarly, the Transverse Integrated Mass (TIM) profile shown in *Figure 2-19* is defined as the fuel mass per unit distance and is given by the surface integral of mean liquid mass at a given axial position.

$$\boldsymbol{TIM}(x) = \rho_l \oint \langle \alpha_l \rangle \;\; \boldsymbol{dy}\, dz \qquad \textbf{4-33}$$

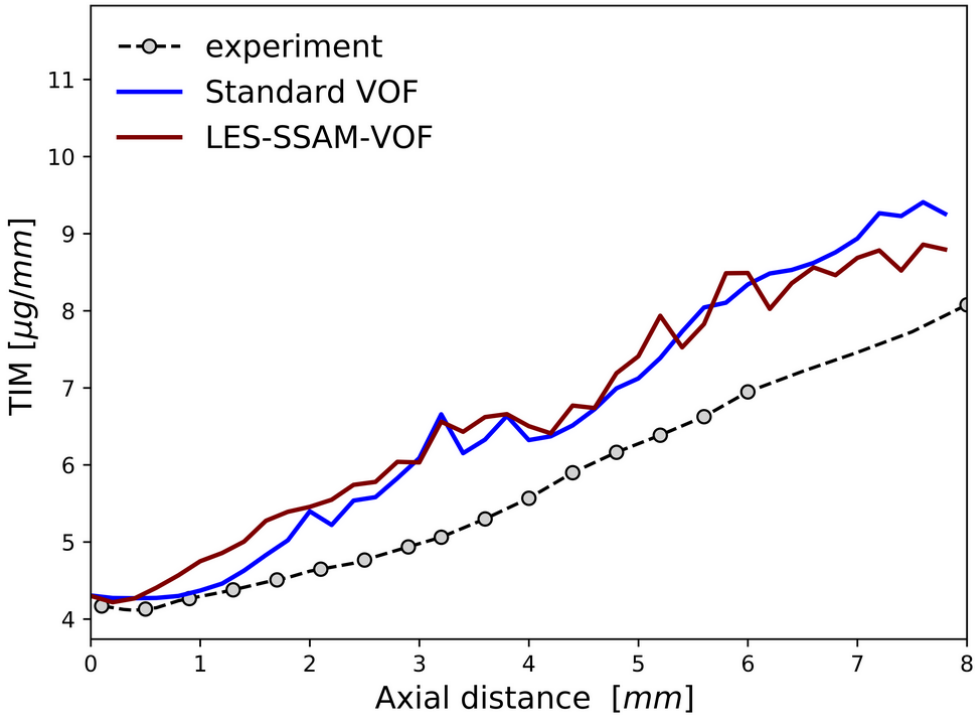

Figure 4-19 Total integrated mass profile predicted along the spray centreline.

The results show that even though the spray structures predicted by the two modelling approaches are different the mean statistical quantities predicted by both modelling approaches are similar. Further downstream of the nozzle exit i.e. at x=4mm and 6mm, the LES-SSAM over-predicts both the centreline values of the PMD while accurately predicting the radial spread of the liquid mass/volume fraction. The averaging time in this study is very smaller compared to other numerical studies of ECN Spray-A in the framework of LES (114-117). So, this study is only a preliminary study providing the LES-SSAM approach framework for modelling atomization using VOF method. The comparisons provided here are only qualitative in nature. A more detailed analysis of different parameters like droplet number density, sauter mean diameter (SMD) and interface surface density are required to quantitatively assess the performance of LES-SSAM method.

4.3.3 Conclusions

Several numerical studies characterizing the influence of nozzle flow on primary atomization have shown that the non-axial velocity fluctuations significantly contribute to the surface-instabilities leading to the breakup of the liquid spray jet. In wall-bounded flows Bose et al (92) have shown that the classical wall-modelled LES methods tend to underpredict the non-axial velocity fluctuations as they do not account for the intermittent dynamics of streak ejection and breakup occurring in the near-wall region. So, in this study the LES-SSAM approach with a new formulation for the SGS acceleration norm is analysed by comparing with DNS data of channel flow for different flow Reynolds numbers. The LES-SSAM approach is validated in comparison with widely used SGS-wall turbulence models and against the DNS data of Moser et al (188-190) for three different flow Reynolds number flows i.e. $Re_\tau = 395, 1000$ and 5200. While the standard wall-turbulence model underpredict the peak intensity of the non-axial velocity fluctuations, it was shown that LES-SSAM approach accurately predicts the velocity fluctuations even on relatively coarser grids. Another problem when modelling wall-turbulence at high Reynolds numbers pertains to turbulence initialization. It was shown that it could take more than 100 flow through times to induce turbulence for the channel flow conditions for the standard models, while LES-SSAM approach initializes turbulence in just 4-5 flow cycles. Moreover, while several methods have been developed to artificially induce turbulence at the flow inlet, LES-SSAM approach implicitly induces turbulence in a physically more consistent manner. A drawback that should be noted with the current LES-SSAM formulation is that it over-predicts the wall-shear stress. Since the primary objective of this work is accurately model the non-axial velocity fluctuations for under-resolved LES simulations, we overlook this drawback of LES-SSAM approach. The LES-SSAM method is then used to simulate the ECN Spray-A injector flow to provide the turbulent inlet boundary conditions for modelling the primary atomization process. When modelling primary atomization using LES, the unclosed term $\overline{u'\Psi'}$, correlating the SGS velocity fluctuations to the SGS fluctuations of liquid-gas interface is neglected. But Chesnel et al (118) have shown that the contribution of this term on interface dynamics is significant and hence cannot be neglected. In this thesis instead of modelling the unclosed term, we attempt to obtain a surrogate velocity field representing the fully resolved turbulent flow with forcing it on residual scales in order to represent the unresolved scale acceleration based on idea of LES-SSAM presented in Chapter-1. With the knowledge of the surrogate velocity field the interface is then re-constructed

using the iso-advector VOF method. This LES-SSAM approach is used to simulate the primary atomization of ECN Spray-A. In comparison to the classical LES approach without any SGS models, the LES-SSAM approach seems to provide highly sheared liquid jet with large number of smaller ligaments right from the nozzle exit. On the other hand, both the approaches predict similar time-averaged integral flow quantities. This study is only a preliminary attempt to evaluate the LES-SSAM method. A more detailed comparison of different spray statistics is necessary to validate the performance of the LES-SSAM method.

5 CONCLUSIONS

Given the high flow Reynolds numbers in engines, the flow is highly intermittent in nature. At the same time LES does not resolve the turbulent flow scales characterizing the intermittency effects. Sabelnikov, Chtab and Gorokhovski (74) have shown that acceleration or the forces acting on the fluid particle is the key parameter to model the intermittency effects. Further Zamansky & Gorokhovski (77) have shown that the viscous dissipation rate is the key variable which reflects the intermittent nature of flow acceleration on droplet dynamics. So, in thesis the stochastic models implemented in LES are specifically targeted on modelling the intermittency effects of residual scales on spray breakup, dispersion and evaporation processes in the context of Euler-Lagrangian modelling and internal nozzle flow and primary breakup in the context of Eulerian flow modelling.

In Chapter-2 we characterized the performance of a new stochastic breakup model accounting for intermittency effects in comparison with the deterministic *KH-RT* model and *Fokkbreak* model based on fragmentation theory. The stochastic breakup model is based on the idea presented in Gorokhovski et al (124), wherein the critical radius and breakup frequency used in the breakup rate expression are assumed to be stochastic random variables. Based on Gorokhovski (125), the definition of the critical radius is expressed by accounting for the inertial response of the droplet to turbulent fluctuations in the surrounding gas-phase. Both the critical radius and the breakup frequency are expressed in terms of the instantaneous viscous dissipation rate "seen" by the droplet, which is modelled by log-normal process of Pope & Chen (82). thereby accounting for the intermittency effects. The non-evaporating and evaporating ECN spray experiments (44,45,145,146) are used to evaluate the performance of the different breakup models. At high injection pressures, results have shown that in comparison to the experiments KH-RT breakup model predicts higher spray penetration, slower breakup rate and higher Sauter Mean Diameter (SMD) of droplets. On the other hand, the Fokkbreak and stochastic breakup model give fairly good representation of the spray evolution and breakup characteristics. However, while the Fokkbreak model predicts faster breakup and smaller SMD compared to the stochastic breakup model. Comparing the spray structures

produced by the three models, it was shown that the stochastic breakup model gives a more statistically realistic spray representation with wide-spectrum of droplet parcel sizes. The differences in spray structure predicted by the three models in explained in terms of three physical processes namely, liquid/gas momentum exchange in the near-nozzle region, the droplet size distribution resulting from the breakup and turbulent spray dispersion in the far field region. At lower injection pressures, it was shown that the spray structure is characterized by turbulent spray dispersion and not by spray breakup and hence all the three models could not accurately predict the spray evolution even on finer grid resolution. Analysing the results of spray breakup models under evaporating conditions have shown that all the three breakup models under-represent the intensity of evaporation. Even though the stochastic breakup model accurately represented the spray turbulence statistics, it could not correctly predict the vaporization intensity. From these results two hypothesis were drawn: First in case of deterministic models like KH-RT accurate modelling of spray characteristics require either modelling of the effects of unresolved scales on droplet motion correctly. Second is that the classical d^2-law under-represents the vaporization rate and we need a sub-grid scale model to accurately account for the effects of unresolved scales on spray evaporation.

In Chapter-3 we attempted to account for the intermittency effects of unresolved scales on spray dispersion and evaporation using stochastic models for droplet acceleration and vapor mass fraction "seen" by the droplet. The idea for droplet dispersion is based on Zamansky & Gorokhovski (77), wherein the droplet lagrangian equation of motion is coupled with the stochastic properties of the instantaneous dissipation rate field 'seen' by the particle along its trajectory. This approach was referred to as Stochastic Response of Inertial Particles (STRIP). In this thesis two modifcations were made to the *LES-STRIP* method proposed by Zamansky & Gorokhovski (77). While the original *LES-STRIP* model (77) is applied for particle-laden flows with one-way coupling, in this thesis we use two-way coupling. Secondly, the improved approach for solving the random walk over a unit sphere using Ornstein Uhlenbeck process proposed by Sabelnikov, Barge and Gorokhovski (75) is used for modelling the fluctuations in the droplet acceleration orientation vector. A new vaporization model is developed in this thesis. The basic idea of the model is that the evaporation rate is controlled by two competing phenomenon namely diffusion of vapor from droplet surface and the turbulent mixing of vapor by surrounding gas-phase. So, the actual vapor mass fraction "seen" by the droplet is modelled in terms of the statistics of rate of diffusion and the rate of turbulent mixing on

energetic scales. This approach is referred to as *Stochastic mixing-controlled evaporation* (SMICE) model. The performance of these two-stochastic models is assessed in comparison to two different experiments. First in order to study the effects of dispersion and evaporation independent of spray atomization coaxial-spray combustor experiment of Sommerfeld and Que (126) with well -defined initial conditions for droplet size is used. It was shown that the stochastic models given a fairly good prediction of the droplet size and velocity statistics. On the other hand, the classical d^2-law evaporation model over-predicted the evaporation rate. Next a detailed assessment of the two models is performed in comparison with the non-evaporating and evaporating spray experiments (44,45,145,146). The results have shown the LES-STRIP dispersion model with KH-RT breakup model gives breakup characteristics similar to stochastic breakup model. This corroborates our earlier hypothesis that in case of deterministic breakup models accounting for the unresolved scale effects on droplet motion improves the spray breakup characteristics. It was also shown that unlike stochastic breakup model, the LES-STRIP dispersion model accurately predicts the spray evolution even for low-injection pressures even on coarser grids. On the other hand, for evaporating spray conditions it was shown that the TSMC evaporation model gives a fairly good prediction of the local vapor mass fraction statistics, while the classical d^2-law underpredicts the vapor mass fraction distributions all throughout the spray length. Having obtained good comparison of the spray statistics for high Reynolds number flows we attempted to analyze the physical parameters controlling the vaporization rate for the two experimental conditions. In both the cases it was shown that while clustering of droplets reduces the intensity of vaporization, the air-entrainment process withdraws the droplets into low-acceleration zones with high temperatures in the spray periphery resulting in faster evaporation. The effects of clustering are more explicitly seen in case of direct injection fuel sprays because of the high mass flow rates.

In Chapter 4, we made a preliminary attempt to model the intermittency effects on in-nozzle flow turbulence and the interface dynamics of primary atomization process based on the idea of Sabelnikov, Chtab and Gorokhovski (74). The basic idea is to provide in the filtered momentum equation of the Eulerian phase an access to the fluid acceleration on residual scales. This approach based on the stochastic forcing of filtered momentum equations, is often referred to as stochastic subgrid acceleration model or *LES-SSAM*. While Zamansky, Vinkovic & Gorokhovski (99) have developed the *LES-SSAM* approach for near-wall turbulence, their model was constructed for rectilinear geometries

and is difficult to extend it for complex nozzle geometry. Therefore, another approach for modelling the near-wall sub-grid acceleration is proposed in this thesis. The new LES-SSAM approach is first assessed using high Reynolds number channel flows. Even for flow Reynolds numbers as high as $1e^5$, the LES-SSAM method has given a fairly good prediction of velocity fluctuations on coarse grids while the standard wall-turbulence models under-predict the velocity fluctuations. Moreover, since the *LES-SSAM* induces the acceleration at small unresolved scales, which characterize the turbulence production in wall bounded flows, the *LES-SSAM* approach implicitly generate turbulence at much faster rate compared to standard wall-turbulence models. This also eliminates the need for using any artificial methods for turbulence generation. The drawback of the LES-SSAM formulation used in this thesis is that it over-predicts the wall-shear stress. But since our primary objective is to generate higher turbulent fluctuations, we overlook this drawback. This approach is used to model the in-nozzle flow turbulence which is used to generate initial conditions for the primary atomization simulations. Next a first attempt is made to model the SGS interface dynamics using LES-SSAM approach with geometric interface capturing VOF method. The model is used to simulate the near-nozzle spray atomization process of ECN Spray-A injector. While LES-SSAM method generates surface instabilities much closer to the nozzle exit resulting in much faster shearing of liquid ligaments for the jet compared to classical LES-VOF method, both the approaches predict similar time-averaged integral flow quantities. A further detailed investigation in terms of droplet-size statistics and liquid volume fraction is necessary to arrive at a conclusive evidence about the better performance of LES-SSAM approach.

In this thesis we made a first attempt to model the intermittency effects of unresolved scales on different spray sub-processes like spray atomization, dispersion, evaporation and in-nozzle flow turbulence. The detailed assessment of the different models show that we have been able to model the spray physics at engine relevant conditions with good accuracy. The future scope of this work is to further develop the LES-SSAM approach for modelling of primary atomization and also extending these ideas to modelling of in-nozzle flow cavitation.

6 REFERENCES

1. **Senecal, P.K**. and **Leach, F.**, 2019. Diversity in transportation: Why a mix of propulsion technologies is the way forward for the future fleet. *Results in Engineering*, *4*, p.100060.
2. **Kalghatgi, G.**, 2018. Is it really the end of internal combustion engines and petroleum in transport? *Applied energy*, *225*, pp.965-974.
3. **Serrano, J.R., Novella, R.** and **Piqueras, P.,** 2019. Why the development of internal combustion engines is still necessary to fight against global climate change from the perspective of transportation.
4. **Dec, J.E.**, 2009. Advanced compression-ignition engines—understanding the in-cylinder processes. *Proceedings of the combustion institute*, *32*(2), pp.2727-2742.
5. **Kalghatgi, G.T.**, 2014. The outlook for fuels for internal combustion engines. *International Journal of Engine Research*, *15*(4), pp.383-398.
6. **Kalghatgi, G.,** 2019. Development of fuel/engine systems—the way forward to sustainable transport. *Engineering*, *5*(3), pp.510-518.
7. **Reitz, R.D.**, 2013. Directions in internal combustion engine research. *Combustion and Flame*, *160*(1), pp.1-8.
8. **Dempsey, A.B., Curran, S.J**. and **Wagner, R.M**., 2016. A perspective on the range of gasoline compression ignition combustion strategies for high engine efficiency and low NOx and soot emissions: Effects of in-cylinder fuel stratification. *International Journal of Engine Research*, *17*(8), pp.897-917.
9. **Baumgarten, C.**, 2006. *Mixture formation in internal combustion engines*. Springer Science & Business Media.
10. **Fansler, T.D.** and **Parrish, S.E**., 2014. Spray measurement technology: a review. *Measurement Science and Technology*, *26*(1), p.012002.
11. **Reitz, R.D.** and **Bracco, F.V**., 1982. Mechanism of atomization of a liquid jet. *The physics of Fluids*, *25*(10), pp.1730-1742.
12. **Reitz, R.D.** and **Chigier, N**., 1996. Regimes of jet breakup and breakup mechanisms (physical aspects). *Prog. Astronaut. Aeronaut*, *166*, p.109.
13. **Lin, S.P.** and **Reitz, R.D**., 1998. Drop and spray formation from a liquid jet. *Annual review of fluid mechanics*, *30*(1), pp.85-105.

14. **Lefebvre, A.H.**, 1989. Atomization and sprays, (1989). ISBN 0-89116-603-3.
15. **Faeth, G.M., Hsiang, L.P.** and **Wu, P.K.**, 1995. Structure and breakup properties of sprays. *International Journal of Multiphase Flow*, *21*, pp.99-127.
16. **Wu, P.K., Miranda, R.F.** and **Faeth, G.M.**, 1995. Effects of initial flow conditions on primary breakup of nonturbulent and turbulent round liquid jets. *Atomization and sprays*, *5*(2).
17. **Wu, P.K., Tseng, L.K.** and **Faeth, G.M**., 1992. Primary breakup in gas/liquid mixing layers for turbulent liquids. *Atomization and Sprays*, *2*(3).
18. **Wu, P.K.** and **Faeth, G.M.**, 1993. Aerodynamic effects on primary breakup of turbulent liquids. *Atomization and Sprays*, *3*(3).
19. **Hiroyasu, H.**, 1991. Break-up length of a liquid jet and internal flow in a nozzle. In *Proc. 5th. ICLASS* (pp. 275-282).
20. **Arai, M.**, 1988. Break-up length and spray formation mechanism of a high-speed liquid jet. In *Proceedings of the 4th International Conference on Liquid Atomization and Spray Systems*.
21. **Kim, J.H., Nishida, K.** and **Hiroyasu, H.**, 1997. Characteristics of the internal flow in a diesel injection nozzle. *International Journal of Fluid Mechanics Research*, *24*(1-3).
22. **Andriotis, A., Gavaises, M.** and **Arcoumanis, C.,** 2008. Vortex flow and cavitation in diesel injector nozzles. *Journal of Fluid Mechanics*, *610*, pp.195-215.
23. **Dumouchel, C.**, 2008. On the experimental investigation on primary atomization of liquid streams. *Experiments in fluids*, *45*(3), pp.371-422.
24. **Pilch, M.** and **Erdman, C.A**., 1987. Use of breakup time data and velocity history data to predict the maximum size of stable fragments for acceleration-induced breakup of a liquid drop. *International journal of multiphase flow*, *13*(6), pp.741-757.
25. **Hsiang, L.P.** and **Faeth, G**., 1992. Secondary drop breakup in the deformation regime. In *30th Aerospace Sciences Meeting and Exhibit* (p. 110).
26. **Guildenbecher, D.R., López-Rivera, C.** and **Sojka, P.E.**, 2009. Secondary atomization. *Experiments in Fluids*, *46*(3), p.371.
27. **Shavit, U.** and **Chigier, N**., 1995. Fractal dimensions of liquid jet interface under breakup. *Atomization and sprays*, *5*(6).

28. **Grout, S., Dumouchel, C., Cousin, J.** and **Nuglisch, H.**, 2007. Fractal analysis of atomizing liquid flows. *International Journal of Multiphase Flow*, *33*(9), pp.1023-1044.
29. **Dumouchel, C., Cousin, J.** and **Triballier, K**., 2005. Experimental analysis of liquid–gas interface at low Weber number: interface length and fractal dimension. *Experiments in fluids*, *39*(4), pp.651-666.
30. **Birouk, M.** and **Gökalp, I**., 2006. Current status of droplet evaporation in turbulent flows. *Progress in Energy and Combustion Science*, *32*(4), pp.408-423.
31. **Verwey, C.** and **Birouk, M**., 2017. Experimental investigation of the effect of droplet size on the vaporization process in ambient turbulence. *Combustion and Flame*, *182*, pp.288-297.
32. **Verwey, C.** and **Birouk, M**., 2018. Fuel vaporization: Effect of droplet size and turbulence at elevated temperature and pressure. *Combustion and Flame*, *189*, pp.33-45.
33. **Villermaux, E**., **Moutte, A., Amielh, M.** and **Meunier, P.**, 2017. Fine structure of the vapor field in evaporating dense sprays. *Physical Review Fluids*, *2*(7), p.074501.
34. **De Rivas, A.** and **Villermaux, E.**, 2016. Dense spray evaporation as a mixing process. *Physical Review Fluids*, *1*(1), p.014201.
35. **Sahu, S., Hardalupas, Y.** and **Taylor, A.M.K.P**., 2018. Interaction of droplet dispersion and evaporation in a poly-dispersed spray. *Journal of Fluid Mechanics*, *846*, pp.37-81.
36. **Monchaux, R., Bourgoin, M.** and **Cartellier, A.**, 2010. Preferential concentration of heavy particles: a Voronoi analysis. *Physics of Fluids*, *22*(10), p.103304.
37. **Lian, H., Charalampous, G.** and **Hardalupas, Y**., 2013. Preferential concentration of poly-dispersed droplets in stationary isotropic turbulence. *Experiments in fluids*, *54*(5), p.1525.
38. **Sahu, S., Hardalupas, Y.** and **Taylor, A.M.K.P**., 2016. Droplet–turbulence interaction in a confined poly-dispersed spray: effect of turbulence on droplet dispersion. *Journal of Fluid Mechanics*, *794*, pp.267-309.
39. **Naber, J.D.** and **Siebers, D.L.**, 1996. Effects of gas density and vaporization on penetration and dispersion of diesel sprays. *SAE transactions*, pp.82-111.

40. **Desantes, J.M., Payri, R., Garcia, J.M.** and **Salvador, F.J**., 2007. A contribution to the understanding of isothermal diesel spray dynamics. *Fuel*, *86*(7-8), pp.1093-1101.
41. **Payri, R., Viera, J.P., Gopalakrishnan, V.** and **Szymkowicz, P.G.**, 2017. The effect of nozzle geometry over the evaporative spray formation for three different fuels. *Fuel*, *188*, pp.645-660.
42. **Siebers, D.L**., 1998. Liquid-phase fuel penetration in diesel sprays. *SAE transactions*, pp.1205-1227.
43. **Siebers, D.L**., 1999. Scaling liquid-phase fuel penetration in diesel sprays based on mixing-limited vaporization. *SAE transactions*, pp.703-728.
44. **Idicheria, C.A.** and **Pickett, L.M**., 2007. Quantitative mixing measurements in a vaporizing diesel spray by Rayleigh imaging. *SAE Transactions*, pp.490-504.
45. **Payri, R., Viera, J.P., Wang, H.** and **Malbec, L.M.**, 2016. Velocity field analysis of the high density, high pressure diesel spray. *International Journal of Multiphase Flow*, *80*, pp.69-78.
46. **Meijer, M., Somers, B., Johnson, J., Naber, J., Lee, S.Y., Malbec, L.M.C., Bruneaux, G., Pickett, L.M., Bardi, M., Payri, R. and Bazyn, T**., 2012. Engine Combustion Network (ECN): Characterization and comparison of boundary conditions for different combustion vessels. *Atomization and Sprays*, *22*(9).
47. **Bardi, M., Payri, R., Malbec, L.M.C., Bruneaux, G., Pickett, L.M., Manin, J., Bazyn, T. and Genzale, C.L**., 2012. Engine combustion network: comparison of spray development, vaporization, and combustion in different combustion vessels. *Atomization and Sprays*, *22*(10).
48. **Kastengren, A.L., Tilocco, F.Z., Powell, C.F., Manin, J., Pickett, L.M., Payri, R.** and **Bazyn, T.**, 2012. Engine combustion network (ECN): measurements of nozzle geometry and hydraulic behavior. *Atomization and Sprays*, *22*(12), pp.1011-1052.
49. **N. Mordant, P. Metz, O. Michel**, and **J.-F. Pinton**. Measurement of lagrangian velocity in fully developed turbulence. Phys. Rev. Lett., 87 :214501, Nov 2001.
50. **N. Mordant, L. Leveque**, and **J.-F. Pinton**. Experimental and numerical study of the lagrangian dynamics of high Reynolds turbulence. New Journal of Physics, 6 :116, 2004.
51. **G. A. Voth, K. Satyanarayan,** and **E. Bodenschatz**. Lagrangian acceleration measurements at large Reynolds numbers. Physics of Fluids, 10 :2268, 1998.

52. **G. A. Voth, A. La Porta, A. M. Grawford, J. Alexander,** and **E. Bodenschatz**. Measurement of particle accelerations in fully developed turbulence. Journal of Fluid Mechanics, 469 :121–160, 2002.
53. **Dukowicz, J.K.**, 1980. A particle-fluid numerical model for liquid sprays. Journal of computational Physics, 35(2), pp.229-253.
54. **Amsden, A.A., O'Rourke, P.J. and Butler, T.D.**, 1989. KIVA-II: A computer program for chemically reactive flows with sprays (No. LA-11560-MS). Los Alamos National Lab. (LANL), Los Alamos, NM (United States).
55. **Spalding, D. B.** 1953 The combustion of liquid fuels. In 4th Symp. (Int.) on Combustion, pp. 847–864. The Combustion Institute, Pittsburgh. 128, 130, 131, 200.
56. **Frossling, N**. 1938 Über die Verdunstung fallender Tropfen (On the evaporation of falling drops). Gerlands Beitr. Geophys. 52, 170–216. 128, 132.
57. **Ranz, W. E. & Marshall, W. R.** 1952 Evaporation from drops. Chem. Eng. Prog. 48 (4), 173. 127, 132, 146.
58. **Reitz, R. D.** and **Diwakar, R.**, Structure of high-pressure fuel sprays, SAE Paper 870598, 1987.
59. **Pilch, M.** and **Erdman, C.A.**, 1987. Use of breakup time data and velocity history data to predict the maximum size of stable fragments for acceleration-induced breakup of a liquid drop. International journal of multiphase flow, 13(6), pp.741-757.
60. **Smagorinski J.** General circulation experiments with the primitive equations. Mon. Weather Rev., Vol. 91, p. 99, 1963.
61. **Kolmogorov AN.** Dissipation of energy in the locally isotropic turbulence. 1991.
62. **Kolmogorov A. N.** The local structure of turbulence in incompressible viscous fluid for very large Reynolds numbers. Dokl. Akad. Nauk., Vol. 30, pp. 301 – 305, 1941. Reprinted Proc. Royal Soc. London; 434; 9; 1991.
63. **Eugene de Villiers**, 2006, The Potential of Large Eddy Simulation for the Modeling of Wall Bounded The Potential of Large Eddy Simulation for the Modelling of Wall Bounded Flows, *PhD thesis, Imperial College London*.
64. **Yoshizawa, A.** and **Horiuti, K**., 1985. A statistically-derived subgrid-scale kinetic energy model for the large-eddy simulation of turbulent flows. *Journal of the Physical Society of Japan*, *54*(8), pp.2834-2839.

65. **Kim, W.W., Menon, S.** and **Mongia, H.C**., 1999. Large-eddy simulation of a gas turbine combustor flow. *Combustion Science and Technology*, *143*(1-6), pp.25-62.
66. **Fureby C, Gosman A.D., Tabor G., Weller H.G, N. Sandham** and **Wolfshtein M.** Large eddy simulation of turbulent channel flows. Turbulent shear flows, Vol. 11, 1997.
67. **Sone, K. and Menon, S., 2003**. Effect of subgrid modeling on the in-cylinder unsteady mixing process in a direct injection engine. *J. Eng. Gas Turbines Power*, *125*(2), pp.435-443.
68. **Brusiani, F. and Bianchi, G. M.** LES simulation of ICE non-reactive flows in fixed grids. SAE paper 2008-01-0959, 2008.
69. **Bellan, J**., 2000. Perspectives on large eddy simulations for sprays: issues and solutions. *Atomization and Sprays*, *10*(3-5).
70. **Landau LD.** Course of Theoretical Physics. Fluid Mech Pergamon Press 1987. Volume 6.
71. **Kuo, A.Y.S.** and **Corrsin, S.**, 1971. Experiments on internal intermittency and fine-structure distribution functions in fully turbulent fluid. *Journal of Fluid Mechanics*, *50*(2), pp.285-319.
72. **A. N. Kolmogorov.** A refinement of previous hypotheses concerning the local structure of turbulence in a viscous incompressible fluid at high Reynolds number. Journal of Fluid Mechanics, 13 :82–85, 1962
73. **A. M. Obukhov.** Some specific features of atmospheric turbulence. Journal of Fluid Mechanics, 13(01) :77–81, 1962.
74. **Sabel'nikov V, Chtab-Desportes A, Gorokhovski M**. New sub-grid stochastic acceleration model in les of high-Reynolds-number flows. Eur Phys J B. 2011;80(2):177–87.
75. **Sabelnikov, V., Barge, A.** and **Gorokhovski, M.**, 2019. Stochastic modeling of fluid acceleration on residual scales and dynamics of suspended inertial particles in turbulence. *Physical Review Fluids*, *4*(4), p.044301.
76. **Barge, A.** and **Gorokhovski, M.A.**, 2020. Acceleration of small heavy particles in homogeneous shear flow: direct numerical simulation and stochastic modelling of under-resolved intermittent turbulence. *Journal of Fluid Mechanics*, *892*.
77. **Gorokhovski, M.** and **Zamansky, R.**, 2014. Lagrangian simulation of large and small inertial particles in a high Reynolds number flow: Stochastic simulation of subgrid turbulence/particle interactions. In *Center for Turbulence Research, Proceedings of the Summer Program* (pp. 37-46).

78. **Gorokhovski, M.** and **Zamansky, R.**, 2018. Modeling the effects of small turbulent scales on the drag force for particles below and above the Kolmogorov scale. *Physical Review Fluids*, *3*(3), p.034602.viera
79. **Barge. A,** 2018**,** Propriétés lagrangiennes de l'accélération turbulente des particules fluides et inertielles dans un écoulement avec un cisaillement homogène : DNS et nouveaux modèles de sousmaille de LES, PhD thesis Ecole Centrale de Lyon.
80. **Kuznetsov, V. & Sabel'nikov, V.** 1990 Turbulence and Combustion. Hemisphere Publishing Corporation.
81. **Bec, J., Biferale, L., Boffetta, G., Celani, A., Cencini, M., Lanotte, A., Musacchio, S. and Toschi, F.**, 2005. Acceleration statistics of heavy particles in turbulence.
82. **Pope, S.B. and Chen, Y.L.,** 1990. The velocity-dissipation probability density function model for turbulent flows. *Physics of Fluids A: Fluid Dynamics*, *2*(8), pp.1437-1449.
83. **Jiao, D., Zhang, F., Du, Q., Niu, Z. and Jiao, K.,** 2017. Direct numerical simulation of near nozzle diesel jet evolution with full temporal-spatial turbulence inlet profile. *Fuel*, *207*, pp.22-32.
84. **Bode, M., Diewald, F., Broll, D.O., Heyse, J.F., Le Chenadec, V. and Pitsch, H.**, 2014. *Influence of the injector geometry on primary breakup in diesel injector systems* (No. 2014-01-1427). SAE Technical Paper.
85. **Agarwal, A. and Trujillo, M.F.,** 2020. The effect of nozzle internal flow on spray atomization. *International Journal of Engine Research*, *21*(1), pp.55-72
86. **Shi, J., Aguado Lopez, P., Gomez Santos, E., Guerrassi, N., Dober, G., Bauer, W., Lai, M.C. and Wang, J**., 2017, July. Evidence of vortex driven primary breakup in high pressure fuel injection. In Ilass Europe. 28th European conference on Liquid Atomization and Spray Systems (pp. 10-17). Editorial Universitat Politècnica de València.
87. **Shi, J., Lopez, P.A., Santos, E.G., Guerrassi, N., Bauer, W., Lai, M.C. and Wang, J.,** 2018, July. High pressure diesel spray development: the effect of nozzle geometry and flow vortex dynamics. In *14th triennial international conference on liquid atomization and spray systems, Chicago, IL* (pp. 22-26).
88. **Lai, M.C., Wang, F., Xie, X., Shi, J., Dober, G., Guerrassi, N., Meslem, Y., Gao, Y., Wang, J., Durfresne, E. and Moon, S**., 2014. Correlating the Nozzle

Flow to Spray and Primary Breakup using Visualization and Multi-phase Simulation. *SIA Powertrain.*

89. **Jiménez, Javier**. "Coherent structures in wall-bounded turbulence." *Journal of Fluid Mechanics* 842 (2018).
90. **D. R. Chapman**, "Computational aerodynamics development and outlook," AIAA J. 17, 1293 (1979).
91. **Piomelli, U., Balaras, E., Squires, K. and Spalart, P.**, 2002, December. Zonal approaches to wall-layer models for large-eddy simulations. In *3rd Theoretical Fluid Mechanics Meeting* (p. 3083).
92. **Bose, S.T. and Park, G.I.**, 2018. Wall-modeled large-eddy simulation for complex turbulent flows. *Annual review of fluid mechanics*, *50*, pp.535-561
93. **Larsson, J., Kawai, S., Bodart, J. and Bermejo-Moreno**, I., 2016. Large eddy simulation with modeled wall-stress: recent progress and future directions. *Mechanical Engineering Reviews*, *3*(1), pp.15-00418.
94. **Nicoud, F. and Ducros, F.**, 1999. Subgrid-scale stress modelling based on the square of the velocity gradient tensor. *Flow, turbulence and Combustion*, *62*(3), pp.183-200.
95. **Yeo, K., Kim, B.-G. & Lee, C.** 2010 On the near-wall characteristics of acceleration in turbulence. J. Fluid Mech. 659, 405–419.
96. **Chen, L., Coleman, S. W., Vassilicos**, J. C. & HU, Z. 2010 Acceleration in turbulent channel flow. J. Turbul. 11 (N41).
97. **Lee, C., Yeo, K. & Choi, J.-I**. 2004 Intermittent nature of acceleration in near-wall turbulence. Phys. Rev. Lett. 92 (14), 144502.
98. **Zamansky, R., Vinkovic, I. and Gorokhovski, M.,** 2013. Acceleration in turbulent channel flow: universalities in statistics, subgrid stochastic models and an application. *Journal of Fluid Mechanics*, *721*, pp.627-668.
99. **Hoyas, S. & Jiménez, J.** 2008 Reynolds number effects on the Reynolds-stress budgets in turbulent channels. Phys. Fluids 20 (10), 101511.
100. **Moser, R. D., Kim, J. & Mansour, N. N**. 1999 Direct numerical simulation of turbulent channel.
101. **Hermann, M.** and **Gorokhovski, M**., 2008. Modeling primary atomization. *Annu. Rev. Fluid Mech*, *40*, pp.343-366.

102. **Harlow, F.H.** and **Welch, J.E**., 1965. Numerical calculation of time-dependent viscous incompressible flow of fluid with free surface. *The physics of fluids*, *8*(12), pp.2182-2189.

103. **Tryggvason, G., Bunner, B., Esmaeeli, A., Juric, D., Al-Rawahi, N., Tauber, W., Han, J., Nas, S. and Jan, Y.J.**, 2001. A front-tracking method for the computations of multiphase flow. *Journal of computational physics*, *169*(2), pp.708-759.

104. **Sussman, M., Smereka, P. and Osher, S**., 1994. A level set approach for computing solutions to incompressible two-phase flow.

105. **Hirt, C.W. and Nichols, B.D.**, 1981. Volume of fluid (VOF) method for the dynamics of free boundaries. *Journal of computational physics*, *39*(1), pp.201-225.

106. **Mirjalili, S., Jain, S.S. and Dodd, M**., 2017. Interface-capturing methods for two-phase flows: An overview and recent developments. *Center for Turbulence Research Annual Research Briefs, 2017*, pp.117-135

107. **Brackbill, J.U., Kothe, D.B. and Zemach, C**., 1992. A continuum method for modeling surface tension. *Journal of computational physics*, *100*(2), pp.335-354.

108. **M´enard, T., Beau, P.-A., Tanguy, S., Demoulin, F.-X.**, and **Berlemont, A**., Primary break-up: DNS of liquid jet to improve atomization modelling, Comput. Meth. Multiphase Flow III, pp. 343–352, 2005.

109. **M´enard, T., Tanguy, S., and Berlemont, A.**, Coupling level set/VOF/ghost fluid methods: Validation and application to 3D simulation of the primary break-up of a liquid jet, Int. J. Multiphase Flow, vol. 33, no. 5, pp. 510–524, 2007

110. **Lebas, R., Menard, T., Beau, P. A., Berlemont, A.,** and **Demoulin, F. X**., Numerical simulation of primary break-up and atomization: DNS and modelling study, Int. J. Multiphase Flow, vol. 35, no. 3, pp. 247–260, 2009.

111. **Herrmann, M.**, Detailed numerical simulations of the primary breakup of turbulent liquid jets, in Proc. of the 21st Annual Conf. ILASS Americas, Orlando, FL, May, 2008.

112. **Desjardins, O., McCaslin, J., Owkes, M.** and **Brady, P**., 2013. Direct numerical and large-eddy simulation of primary atomization in complex geometries. *Atomization and Sprays*, *23*(11).

113. **De Villiers, E., Gosman, A.D. and Weller, H.G.**, 2004. Large eddy simulation of primary diesel spray atomization. *SAE transactions*, pp.193-206.

114. **Arienti, M., Sussman, M.**, 2015. A high-fidelity study of high-pressure diesel injection. SAE 2015-01-1853.

115. **Agarwal, A. and Trujillo, M.F.**, High Fidelity Simulations of Nozzle Internal Flow and its Effect on Breakup Behavior.

116. **Bianchi, G.M., Minelli, F., Scardovelli, R. and Zaleski, S**., 2007. 3D large scale simulation of the high-speed liquid jet atomization. *SAE Transactions*, pp.333-346.

117. **Anez, J., Ahmed, A., Hecht, N., Duret, B., Reveillon**, J. and Demoulin, F.X., 2019. Eulerian–Lagrangian spray atomization model coupled with interface capturing method for diesel injectors. *International Journal of Multiphase Flow*, *113*, pp.325-342.

118. **Chesnel, Jeremy, Thibaut Menard, Julien Reveillon, and Francois-Xavier Demoulin**. "Subgrid analysis of liquid jet atomization." *Atomization and Sprays* 21, no. 1 (2011).

119. **Herrmann, M. and Gorokhovski, M.**, 2008. An outline of a LES subgrid model for liquid/gas phase interface dynamics. Proceedings of the 2008 CTR Summer Program, pp.171-181.

120. **Roenby, J., Bredmose, H.** and **Jasak, H.**, 2019. IsoAdvector: Geometric VOF on general meshes. In *OpenFOAM*® (pp. 281-296). Springer, Cham.

121. **Roenby, J., Bredmose, H. and Jasak, H.,** 2016. Isoadvector: Free, fast and accurate VOF on arbitrary meshes. In *The 4th OpenFOAM User Conference*.

122. **Vukcevic, V., Keser, R., Jasak, H., Battistoni, M., Im, H. and Roenby**, J., 2019. Development of a CFD Solver for Primary Diesel Jet Atomization in FOAM-Extend (No. 2019-24-0128). SAE Technical Paper.

123. **Jasak, H., Jemcov, A. and Tukovic, Z.**, 2007, September. OpenFOAM: A C++ library for complex physics simulations. In International workshop on coupled methods in numerical dynamics (Vol. 1000, pp. 1-20). IUC Dubrovnik Croatia.

124. **Gorokhovski, M., Chtab-Desportes, A., Voloshina, I. and Askarova**, **A.**, 2010, March. Stochastic simulation of the spray formation assisted by a high pressure. In AIP Conference Proceedings (Vol. 1207, No. 1, pp. 66-73). American Institute of Physics.

125. **Gorokhovski, M., 2001.** The stochastic Lagrangian model of drop breakup in the computation of liquid sprays. *Atomization and Sprays*, *11*(5).

126. **Sommerfeld, M., and H-H. Qiu.** Experimental studies of spray evaporation in turbulent flow. International journal of heat and fluid flow 19, no. 1 (1998): 10-22.

127. **Beale, J.C. and Reitz, R.D.**, 1999. Modeling spray atomization with the Kelvin-Helmholtz/Rayleigh-Taylor hybrid model. *Atomization and sprays*, *9*(6).

128. **Wehrfritz, A., Kaario, O., Vuorinen, V. and Somers, B.**, 2016. Large eddy simulation of n-dodecane spray flames using flamelet generated manifolds. *Combustion and Flame*, *167*, pp.113-131.

129. **Gorokhovski, M.A. and Saveliev, V.L.**, 2003. Analyses of Kolmogorov's model of breakup and its application into Lagrangian computation of liquid sprays under air-blast atomization. *Physics of Fluids*, *15*(1), pp.184-192.

130. **Gorokhovski, M.A. and Saveliev, V.L.,** 2008. Statistical universalities in fragmentation under scaling symmetry with a constant frequency of fragmentation. *Journal of Physics D: Applied Physics*, *41*(8), p.085405.

131. **A. N. Kolmogorov**, ''On the log-normal distribution of particles sizes during break-up process,'' Dokl. Akad. Nauk SSSR 31,99-1941.

132. **Apte, S.V., Gorokhovski, M. and Moin, P.**, 2003. LES of atomizing spray with stochastic modeling of secondary breakup. *International Journal of Multiphase Flow*, *29*(9), pp.1503-1522.

133. **Apte, S.V., Mahesh, K., Gorokhovski, M. and Moin, P.,** 2009. Stochastic modeling of atomizing spray in a complex swirl injector using large eddy simulation. *Proceedings of the Combustion Institute*, *32*(2), pp.2257-2266.

134. **Habchi, C.,** 2011. The energy Spectrum Analogy Breakup (SAB) model for the numerical simulation of sprays. *Atomization and Sprays*, *21*(12).

135. **Jones, W.P. and Lettieri, C.,** 2010. Large eddy simulation of spray atomization with stochastic modeling of breakup. *Physics of fluids*, *22*(11), p.115106

136. **J. C. Lasheras, C. Eastwood, C. C. Martínez-Bazán, and J. L. Montañés**, "A review of statistical models for the break-up of an immiscible fluid immersed into a fully developed turbulent flow," Int. J. Multiphase Flow 28, 247 2002.

137. **Monin, A.S. and Yaglom, A.M., 2013**. *Statistical fluid mechanics, volume II: mechanics of turbulence* (Vol. 2). Courier Corporation.

138. **Rayleigh, J.W.S.**, "On the instability of Jets," Proc. Lond. Math. Soc., Vol. 10, No. 4, 1878.

139. **Weber, C.**, Zum Zerfall eines Flussigkeitsstrahles, Z. Angew. Math. Mech., Vol. 11, pp. 138-245, 1931.

140. **Sterling, A.M. and Sleicher, C.A.**, "The instability of Capillary Jets," J. Fluid Mech., Vol. 68, No. 3, pp. 477-495, 1975.

141. **Sirignano, W.A. and Mehring, C.**, 2000. Review of theory of distortion and disintegration of liquid streams. *Progress in energy and combustion science*, *26*(4-6), pp.609-655.
142. **Hwang, S.S., Liu, Z. and Reitz, R.D.**, 1996. Breakup mechanisms and drag coefficients of high-speed vaporizing liquid drops. *Atomization and Sprays*, *6*(3).
143. **Bellman, R. and Pennington, R.H.**, 1954. Effects of surface tension and viscosity on Taylor instability. *Quarterly of Applied Mathematics*, *12*(2), pp.151-162.
144. **Kitaguchi, K., Hatori, S., Hori, T.** and **Senda, J.**, 2012. Optimization of breakup model using LES of diesel spray. *Atomization and Sprays*, *22*(1).
145. **Kastengren, A., Ilavsky, J., Viera, J.P., Payri, R., Duke, D.J., Swantek, A., Tilocco, F.Z., Sovis, N.** and **Powell, C.F.**, 2017. Measurements of droplet size in shear-driven atomization using ultra-small angle x-ray scattering. *International Journal of Multiphase Flow*, *92*, pp.131-139.
146. **Abraham, J.P. and Pickett, L.M.,** 2010. Computed and measured fuel vapor distribution in a diesel spray. *Atomization and sprays*, *20*(3).
147. **Jasak, H.**, 1996. Error analysis and estimation for the finite volume method with applications to fluid flows.
148. **Vogiatzaki, K., Crua, C., Morgan, R.** and **Heikal, M.**, 2017, July. A study of the controlling parameters of fuel air mixture formation for ECN Spray A. In *Ilass Europe. 28th european conference on Liquid Atomization and Spray Systems* (pp. 2-9). Editorial Universitat Politècnica de València.
149. **Kitaguchi, K., Fujii, T., Hatori, S., Hori, T. and Senda, J.**, 2014. Effect of breakup model on large-eddy simulation of diesel spray evolution under high back pressures. *International Journal of Engine Research*, *15*(5), pp.522-538.
150. **Zhao, H., Liu, H.F., Cao, X.K., Li, W.F., Xu, J.L.**, 2011. Breakup characteristics of liquid drops in bag regime by a continuous and uniform air jet flow. Int. J. Multiphase Flow 37, 530–534.
151. **S. Post, V. Iyer,** and **J. Abraham**, A Study of Near-Field Entrainment in Gas Jets and Sprays under Diesel Conditions, ASME *J. Fluids Eng.*, vol. 122, pp. 385–395, 2000.
152. **Desantes, J.M., Arregle, J., Lopez, J.J.** and **Cronhjort, A.**, 2006. Scaling laws for free turbulent gas jets and diesel-like sprays. *Atomization and Sprays*, *16*(4).

153. **Vuorinen, V., Hillamo, H., Kaario, O., Larmi, M.,** and **Fuchs, L.**, Large eddy simulation of droplet Stokes number effects on turbulent spray shape, *Atomization Sprays*, vol. 20, no. 2, pp. 93– 114, 2010a.

154. **Vuorinen, V., Hillamo, H., Kaario, O., Nuutinen, M., Larmi, M.,** and **Fuchs, L.**, Large eddy simulation of droplet Stokes number effects on mixture quality in fuel sprays, *Atomization Sprays*, vol. 20, no. 5, pp. 435–451, 2010b.

155. **Senecal, P.K., Pomraning, E., Xue, Q., Som, S., Banerjee, S., Hu, B., Liu, K.** and **Deur, J.M.,** 2014. Large eddy simulation of vaporizing sprays considering multi-injection averaging and grid-convergent mesh resolution. *Journal of Engineering for Gas Turbines and Power*, *136*(11).

156. **Elghobashi, S.**, 1994. On predicting particle-laden turbulent flows. *Applied scientific research*, *52*(4), pp.309-329.

157. **Yeung, P.K.** and **Pope, S.B.**, 1988. An algorithm for tracking fluid particles in numerical simulations of homogeneous turbulence. *Journal of computational physics*, *79*(2), pp.373-416.

158. **Squires, K.D.** and **Eaton, J.K.,** 1990. Particle response and turbulence modification in isotropic turbulence. *Physics of Fluids A: Fluid Dynamics*, *2*(7), pp.1191-1203.

159. **Squires, K.D.** and **Eaton, J.K**., 1991. Preferential concentration of particles by turbulence. *Physics of Fluids A: Fluid Dynamics*, *3*(5), pp.1169-1178.

160. **Wang, L.P.** and **Maxey, M.R**., 1993. Settling velocity and concentration distribution of heavy particles in homogeneous isotropic turbulence. *Journal of fluid mechanics*, *256*, pp.27-68.

161. **Ferrante, A.** and **Elghobashi, S.**, 2003. On the physical mechanisms of two-way coupling in particle-laden isotropic turbulence. *Physics of fluids*, *15*(2), pp.315-329.

162. **Bagchi, P.** and **Balachandar, S.**, 2004. *Response of the wake of an isolated particle to isotropic turbulent cross-flow*. Department of Theoretical and Applied Mechanics (UIUC).

163. **Burton, T.M**. and **Eaton, J.K.,** 2005. Fully resolved simulations of particle-turbulence interaction. *Journal of Fluid Mechanics*, *545*, p.67.

164. **Cencini, M., Bec, J., Biferale, L., BOFFETTA, G., Celani, A., Lanotte, A.S., Musacchio, S.** and **Toschi, F.**, 2006. Dynamics and statistics of heavy particles in turbulent flows. *Journal of Turbulence*, (7), p.N36.

165. **Volk, R., Calzavarini, E., Verhille, G., Lohse, D., Mordant, N., Pinton, J.F.** and **Toschi, F.,** 2008. Acceleration of heavy and light particles in turbulence: comparison between experiments and direct numerical simulations. *Physica D: Nonlinear Phenomena*, *237*(14-17), pp.2084-2089.

166. **Wang, Q. and Squires, K.D.**, 1996. Large eddy simulation of particle-laden turbulent channel flow. *Physics of Fluids*, *8*(5), pp.1207-1223.

167. **Bharadwaj N., Rutland C.J., Chang S.M.** (2009) Large eddy simulation modelling of spray-induced turbulence effects, Int. J. Engine Res. 10,2, 97–119.

168. **Bharadwaj N., Rutland C.J.** (2010) A large-eddy simulation study of sub-grid two-phase interaction in particle-laden flows and diesel engine sprays, Atomization Sprays 20,8

169. **Shotorban, B.** and **Mashayek, F.,** 2005. Modeling subgrid-scale effects on particles by approximate deconvolution. *Physics of Fluids*, *17*(8), p.081701.

170. **Tsang, C.W., Trujillo, M.F.** and **Rutland, C.J.**, 2014. Large-eddy simulation of shear flows and high-speed vaporizing liquid fuel sprays. *Computers & Fluids*, *105*, pp.262-279.

171. **Pozorski, J. and Apte, S.V.**, 2009. Filtered particle tracking in isotropic turbulence and stochastic modeling of subgrid-scale dispersion. *International Journal of Multiphase Flow*, *35*(2), pp.118-128.

172. **Bini, M. and Jones, W.P.**, 2007. Particle acceleration in turbulent flows: A class of nonlinear stochastic models for intermittency. *Physics of Fluids*, *19*(3), p.035104.

173. **Bini, M. and Jones, W.P.**, 2008. Large-eddy simulation of particle-laden turbulent flows. *Journal of Fluid Mechanics*, *614*, pp.207-252.

174. **Mashayek, F., Jaberi, F.A., Miller, R.S.** and **Givi, P.**, 1997. Dispersion and polydispersity of droplets in stationary isotropic turbulence. International journal of multiphase flow, 23(2), pp.337-355.

175. **Mashayek, F.,** 1998. Direct numerical simulations of evaporating droplet dispersion in forced low Mach number turbulence. International journal of heat and mass transfer, 41(17), pp.2601-2617.

176. **Miller, R.S.** and **Bellan, J.**, 1999. Direct numerical simulation of a confined three-dimensional gas mixing layer with one evaporating hydrocarbon-droplet-laden stream. Journal of Fluid Mechanics, 384, pp.293-338.

177. **Reveillon, J.** and **Demoulin, F.X**., 2007. Effects of the preferential segregation of droplets on evaporation and turbulent mixing. Journal of Fluid Mechanics, 583, pp.273-302.

178. **Dalla Barba, F.** and **Picano, F.,** 2018. Clustering and entrainment effects on the evaporation of dilute droplets in a turbulent jet. Physical Review Fluids, 3(3), p.034304.

179. **Jenny, P., Roekaerts, D.** and **Beishuizen, N.,** 2012. Modeling of turbulent dilute spray combustion. *Progress in Energy and Combustion Science*, *38*(6), pp.846-887.

180. **Apte, S.V., Mahesh, K.** and **Moin, P.**, 2009. Large-eddy simulation of evaporating spray in a coaxial combustor. *Proceedings of the Combustion Institute*, *32*(2), pp.2247-2256.

181. **Vulis, L., A.**, 1961, Thermal regime of combustion. McGraw-Hill, Inc, N-Y, 290p.

182. **Apte, S.V., Mahesh, K. and Moin, P.,** 2009. Large-eddy simulation of evaporating spray in a coaxial combustor. Proceedings of the Combustion Institute, 32(2), pp.2247-2256.

183. **Hahn, F., Olbricht, C. and Janicka, J.**, 2008. Large eddy simulation of an evaporating spray based on an Eulerian–Lagrangian approach. *Proceedings of ILASS, Como Lake, Italy,. ILASS, Italy*.

184. **Cuenot, B., Boileau, M., Pascaud, S., Mossa, J.B., Riber, E., Poinsot, T. and Bérat, C**., 2006. Large eddy simulation of two-phase reacting flows.

185. **Sommerfeld, M., Kohnen, G. and Qiu, H.H.**, 1993. Spray evaporation in turbulent flow: numerical calculations and detailed experiments by phase-doppler anemometry. *Revue de l'Institut français du pétrole*, *48*(6), pp.677-695.

186. **Ducros, F., Nicoud, F. and Poinsot, T.**, 1998. Wall-adapting local eddy-viscosity models for simulations in complex geometries. *Numerical Methods for Fluid Dynamics VI*, pp.293-299.

187. **Wang, M. and Moin, P.,** 2002. Dynamic wall modeling for large-eddy simulation of complex turbulent flows. *Physics of Fluids*, *14*(7), pp.2043-2051.

188. **Moser, R.D., Kim, J. and Mansour, N.N.,** 1999. Direct numerical simulation of turbulent channel flow up to Re τ= 590. *Physics of fluids*, *11*(4), pp.943-945.

189. **Lee, M., Malaya, N. and Moser, R.D.,** 2013, November. Petascale direct numerical simulation of turbulent channel flow on up to 786k cores. In *SC'13: Proceedings of the International Conference on High Performance Computing, Networking, Storage and Analysis* (pp. 1-11). IEEE.

190. **Lee, M. and Moser, R.D.,** 2015. Direct numerical simulation of turbulent channel flow up to 5200. *Journal of Fluid Mechanics*, *774*, pp.395-415.

191. **Markus Klein, Amsini Sadiki, and Johannes Janicka.** A digital filter-based generation of inflow data for spatially developing direct numerical or large eddy simulations. *Journal of computational Physics*, 186(2):652–665, 2003.

192. **Di Mare, L., Klein, M., Jones, W.P. and Janicka, J.**, 2006. Synthetic turbulence inflow conditions for large-eddy simulation. *Physics of Fluids*, *18*(2), p.025107.

193. **Poletto, R., Revell, A., Craft, T.J. and Jarrin, N.**, 2011. Divergence free synthetic eddy method for embedded LES inflow boundary conditions. In *Seventh international symposium on turbulence and shear flow phenomena*. Begel House Inc.

194. **Kastengren, A., Tilocco, F.Z., Duke, D., Powell, C.F., Zhang, X. and Moon, S.,** 2014. Time-resolved X-ray radiography of sprays from engine combustion network spray a diesel injectors. *Atomization and Sprays*, *24*(3).

195. **Xue, Q., Battistoni, M., Powell, C.F., Longman, D.E., Quan, S.P., Pomraning, E., Senecal, P.K., Schmidt, D.P. and Som, S.,** 2015. An Eulerian CFD model and X-ray radiography for coupled nozzle flow and spray in internal combustion engines. *International Journal of Multiphase Flow*, *70*, pp.77-88.